

University of Alberta

*Cyclic Performance of Soft Ground*

by

*Ardeshir DehmoobedSharifabadi*



A thesis submitted to the Faculty of Graduate Studies and Research in partial fulfillment of the

requirements for the degree of *Doctor of Philosophy*

*in*

*Mining Engineering*

Department of *Civil and Environmental Engineering*

Edmonton, Alberta

Spring 2007



Library and  
Archives Canada

Bibliothèque et  
Archives Canada

Published Heritage  
Branch

Direction du  
Patrimoine de l'édition

395 Wellington Street  
Ottawa ON K1A 0N4  
Canada

395, rue Wellington  
Ottawa ON K1A 0N4  
Canada

*Your file* *Votre référence*  
*ISBN: 978-0-494-29665-3*  
*Our file* *Notre référence*  
*ISBN: 978-0-494-29665-3*

#### NOTICE:

The author has granted a non-exclusive license allowing Library and Archives Canada to reproduce, publish, archive, preserve, conserve, communicate to the public by telecommunication or on the Internet, loan, distribute and sell theses worldwide, for commercial or non-commercial purposes, in microform, paper, electronic and/or any other formats.

The author retains copyright ownership and moral rights in this thesis. Neither the thesis nor substantial extracts from it may be printed or otherwise reproduced without the author's permission.

#### AVIS:

L'auteur a accordé une licence non exclusive permettant à la Bibliothèque et Archives Canada de reproduire, publier, archiver, sauvegarder, conserver, transmettre au public par télécommunication ou par l'Internet, prêter, distribuer et vendre des thèses partout dans le monde, à des fins commerciales ou autres, sur support microforme, papier, électronique et/ou autres formats.

L'auteur conserve la propriété du droit d'auteur et des droits moraux qui protègent cette thèse. Ni la thèse ni des extraits substantiels de celle-ci ne doivent être imprimés ou autrement reproduits sans son autorisation.

---

In compliance with the Canadian Privacy Act some supporting forms may have been removed from this thesis.

Conformément à la loi canadienne sur la protection de la vie privée, quelques formulaires secondaires ont été enlevés de cette thèse.

While these forms may be included in the document page count, their removal does not represent any loss of content from the thesis.

Bien que ces formulaires aient inclus dans la pagination, il n'y aura aucun contenu manquant.

  
**Canada**

## **Dedication**

This thesis is dedicated to my parents who have supported me all the way since the beginning of my studies as well as my wife who has been a great source of motivation, inspiration and patient during my study.

## **Abstract**

The strain softening of oil sand in the underfoot, due to the loading action of large mobile mining equipment such as trucks and shovels, yields a highly unstable condition for the operation of this ultra-class equipment. High maintenance costs as a result of truck and shovel frame failures are a frequent result of this instability. Increasing our knowledge about the behaviour of oil sand due to its dynamic interactions with equipment would enhance the long-term equipment design strategy for OEM's (Original Equipment Manufacturers) and provide mine operators with improved operational guidelines for planning and maintaining this equipment.

This thesis will focus on evaluating the oil sand's behaviour under cyclic loading of large mobile mining equipment. I propose a cyclic plate load test for evaluating ground performance established and performed in both field and laboratory tests and a pseudo-elastic model is proposed that increases the ability to predict, within a reasonable error, ground deformation under ultra-class mining equipment. I will explain the empirical relationships for the pseudo-elastic model build to predict deformation under cyclic and static loading conditions. The model's average error for deformation prediction for the shovel underfoot test was approximately 5%. The mining-induced confinement during the plate load test and equipment activities using the elastic model using Boussinesq's approach was estimated.

In the laboratory tests, the cyclic and static unconsolidated undrained triaxial test under low confining pressure was performed. Also, the cyclic plate load tests were performed in big box of oil sand (large scale). The large scale laboratory tests were used to build a relationship between the load level, number of cycles and deformation. The numerical modeling was carried out to predict and compare the field cyclic plate load test results.

The underfoot shovel test (P&H shovel 4100 BOSS) was performed to understand the equipment and ground interaction. Also, ground deformation results during underfoot shovel test was predicted and compared by pseudo-elastic model.

## **Acknowledgements**

I thank my supervisor, Dr. Tim G. Joseph, for his guidance and enthusiasm and his continual encouragement throughout this endeavour. He was more than a supervisor for me. Also, his support throughout the research and writing of this thesis is gratefully appreciated. Dr. Douglas R. Schmitt, thank you for helping me throughout the geophysical data analysis and for providing theoretical support. Thanks to Dr. Dave Chan, for helping me to understand the big picture of the problem.

I thank the JPI Company, especially Laura Joseph, the Chief Operating Officer, for financial and technical support throughout this project. I thank Syncrude Research and Caterpillar Research for their financial support for this research. Also, I gratefully acknowledge Syncrude Ltd. for providing oil sand samples for my laboratory tests. I thank Suncor Energy Inc. for helping and cooperating during the field experiments.

I thank Steve Gamble for helping with the laboratory work and for providing the laboratory research facilities. Also thanks to Richard Helfrich and Larry Burden for helping with some of the laboratory apparatus.

I would also like to thank my friends who helped me throughout graduate school, especially my good friends, Hasan Ozturk and Arash Eshraghian, for their help in the laboratory and their encouragement throughout my studies. My discussions with them were an excellent source of information and constructive criticism.

Also, I thank Marek Welz for helping me to understand the geophysical aspect of my research and for providing technical support.

I would like to acknowledge the financial support provided by NSERC and the University of Alberta. I am grateful to the University of Alberta and the Department of Civil and Environmental Engineering for teaching and research-assistance opportunities during my graduate studies.

In addition, I would like to express my deepest appreciation and love for my wife, Shirin Modami, who has been patient and encouraging throughout the course of this study. Her gentle manner and warm humour inspire me to be a better person.

Finally, the writer wishes to express his sincere appreciation for all the help received throughout his years of work at the University of Alberta.

## Table of Contents

<b>1</b>	<b>INTRODUCTION .....</b>	<b>1</b>
1.1	OVERVIEW.....	1
1.2	STATEMENT OF THE PROBLEM.....	2
1.3	OBJECTIVES AND THE SCOPE OF THE STUDY.....	7
1.4	RESEARCH METHODOLOGY.....	10
1.5	REMARKS .....	11
<b>2</b>	<b>BACKGROUND .....</b>	<b>14</b>
2.1	OIL SAND INTRODUCTION:.....	14
2.2	MINING.....	15
2.2.1	OIL SAND MINING SPECIFICATIONS.....	17
2.3	ULTRA-CLASS MINING EQUIPMENT AND CAUSES OF CYCLIC LOADING 18	
2.4	GEOLOGY .....	20
2.4.1	MINERALOGY .....	22
2.4.2	MORPHOLOGY .....	24
<b>3</b>	<b>MATERIAL PROPERTIES .....</b>	<b>27</b>
3.1	GEOPHYSICS.....	27
3.1.1	PASSIVE SEISMIC DATA ANALYSIS .....	27
3.1.1.1	Introduction.....	27
3.1.1.2	Refraction data for summer and winter conditions .....	27
3.1.1.2.1	Refraction.....	27
3.1.1.2.2	Characterization of the site using refraction method .....	29
3.1.1.2.3	Summer refraction data.....	30
3.1.1.2.4	Forward and reversal refraction analysis.....	31
3.1.1.2.5	Winter refraction data.....	34
3.1.1.3	Passive data acquisition.....	35
3.1.1.3.1	Winter passive data analyses.....	37
3.1.1.3.2	Summer passive data .....	43
3.1.2	DETERMINATION OF GROUND STIFFNESS BY USING A GEOPHYSICAL TECHNIQUE.....	49
3.1.2.1	Introduction.....	49
3.1.2.2	Body and surface waves .....	50
3.1.2.3	Dispersion.....	51

3.1.2.4	Determination of stiffness with Rayleigh waves .....	53
3.1.2.5	$\tau$ -p and f-p transformation for summer and winter data .....	56
<b>4</b>	<b>LITERATURE REVIEW .....</b>	<b>59</b>
4.1	INTRODUCTION .....	59
4.2	GENERAL SOIL PARAMETERS .....	59
4.2.1	COEFFICIENT OF VOLUME COMPRESSIBILITY .....	59
4.2.2	COEFFICIENT OF COMPRESSIBILITY .....	60
4.2.3	COMPACTION .....	61
4.2.4	MODULUS OF DEFORMATION OR YOUNG'S MODULUS .....	61
4.2.5	PRE-CONSOLIDATION RATIO .....	61
4.3	PHYSICAL PROPERTIES OF OIL SANDS .....	62
4.4	CYCLIC LOADING OF MATERIALS .....	73
4.4.1	ROCK .....	75
4.4.2	CLAY .....	77
4.4.3	SAND .....	81
4.4.4	ASPHALT .....	82
4.4.5	OTHER MATERIALS .....	83
4.4.5.1	Concrete .....	83
4.4.5.2	Wood .....	84
4.4.5.3	Metals .....	84
4.5	DAMAGE MECHANICS AND SURFACE BOUNDING MODELLING .....	85
<b>5</b>	<b>INITIAL FIELD AND LABORATORY TESTS .....</b>	<b>94</b>
5.1	INTRODUCTION .....	94
5.2	HYPOTHESIS AND ASSUMPTIONS .....	94
5.3	LABORATORY TRIAXIAL TESTS .....	96
5.3.1	CONVENTIONAL AND CYCLIC TRIAXIAL TESTS .....	96
5.3.2	SET-UP AND PROCEDURE .....	97
5.3.3	LABORATORY TESTS .....	98
5.3.3.1	Material properties of tested Oil sand .....	106
5.4	FIELD TESTS .....	107
5.4.1	THE PLATE LOAD CYCLIC FIELD TEST .....	108
5.4.2	SET-UP AND PROCEDURE .....	110
5.5	MODELING OF A PLATE LOAD TEST WITH FLAC .....	118
5.5.1	BACKGROUND OF FLAC SOFTWARE .....	118
5.5.2	MODELING .....	119

5.6	VERTICAL AND HORIZONTAL STRESS MODELING BENEATH FOR FIELD PLATE LOAD TEST VIA BOUSSINESQ'S APPROACH.....	126
5.7	REMARKS .....	131
<b>6</b>	<b>LARGE-SCALE LABORATORY TESTS.....</b>	<b>133</b>
6.1	INTRODUCTION.....	133
6.2	DENSITY AND COMPACTION.....	134
6.3	OIL SAND WATER CONTENT .....	140
6.4	CONFINING STRESSES .....	141
6.5	COMPRESSIBILITY .....	142
6.6	COMPACTION TEST IN THE LARGE-SCALE LABORATORY TEST .....	143
6.7	PLATE LOAD CYCLIC LABORATORY TEST SET-UP .....	144
6.8	THE EQUIPMENT OF LABORATORY CYCLIC PLATE LOAD TEST.....	144
6.9	TEST SET-UP AND PROCEDURE .....	145
6.10	COMPACTION OF OIL SAND (SAMPLE PREPARATION).....	148
6.11	LARGE-SCALE LABORATORY PLATE LOAD TEST RESULTS .....	150
6.12	BEARING CAPACITY FAILURE TYPES.....	152
6.12.1	BACKGROUND: .....	152
6.12.2	FAILURE TYPE OF CYCLIC PLATE LOAD TEST:.....	153
6.13	REMARKS .....	153
<b>7</b>	<b>ANALYSING THE LARGE-SCALE LABORATORY TESTS.....</b>	<b>155</b>
7.1	INTRODUCTION.....	155
7.2	GENERAL PRESSURE-DEFORMATION OVERVIEW .....	156
7.3	INITIAL LOADING ANALYSIS .....	157
7.3.1	DEFORMATION.....	157
7.3.2	PRESSURE STIFFNESS .....	159
7.3.3	LOADING RATE.....	164
7.3.4	DENSITY .....	165
7.4	CYCLING ANALYSIS .....	167
7.4.1	DEFORMATION.....	167
7.4.2	PRESSURE STIFFNESS .....	170
7.4.3	DENSITY .....	173
7.5	TOTAL DEFORMATION.....	175
7.6	PREDICTION OF COEFFICIENT FACTOR FOR CYCLIC PLATE LOAD TESTS	176
7.7	EFFECT OF CYCLES ON TOTAL DEFORMATION .....	178
7.8	REMARKS .....	180

<b>8</b>	<b>P&amp;H 4100 BOSS SHOVEL UNDERFOOT TESTING AND DEFORMATION PREDICTION.....</b>	<b>181</b>
8.1	INTRODUCTION.....	181
8.2	TEST SET-UP, EQUIPMENT AND METHODS.....	181
8.3	TEST PROCEDURE .....	184
8.3.1	UNLOADED STATIC TESTS.....	186
8.3.2	MOCK DIGGING UNLOADED.....	186
8.3.3	LOADED STATIC TESTS.....	187
8.3.4	MOCK WORKING FACE LOAD ACTIVITY .....	187
8.3.5	TRUCK AND SHOVEL OPERATION.....	187
8.3.6	THE END OF THE LOADED STATIC TEST END.....	188
8.4	GROUND AND CLIMATE CONDITIONS.....	188
8.5	TEST RESULTS.....	189
8.6	VERTICAL AND HORIZONTAL STRESS MODELING BENEATH SHOVEL TRACK VIA BOUSSINESQ'S APPROACH .....	191
8.7	DEFORMATION PREDICTION .....	195
8.8	REMARKS .....	200
<b>9</b>	<b>SUMMARY.....</b>	<b>201</b>
<b>10</b>	<b>CONCLUSION AND RESEARCH CONTRIBUTION OF NEW KNOWLEDGE ACHIEVED .....</b>	<b>203</b>
<b>11</b>	<b>RECOMMENDATIONS FOR FUTURE WORK.....</b>	<b>205</b>
11.1	GEOTECHNICAL WORK IN BOTH THE LABORATORY AND FIELD.....	205
11.2	GEOPHYSICAL WORK.....	206
11.3	SOFTWARE DEVELOPMENT.....	207
	<b>REFERENCES.....</b>	<b>208</b>
	<b>APPENDIX 1- TRIAXIAL TEST RESULTS.....</b>	<b>208</b>
	<b>APPENDIX 2 – SUMMARY OF FIELD PLATE LOAD TEST .....</b>	<b>226</b>
	<b>APPENDIX 3 – FIELD PLATE LOAD TEST .....</b>	<b>229</b>
	<b>APPENDIX 4 – NUMERICAL MODELING RESULT FOR LARGE AND SMALL PLATES.....</b>	<b>236</b>
	<b>APPENDIX 5 – NUMERICAL MODELING USING BOUSSINSEQ'S EQUATION FOR TRUCK.....</b>	<b>242</b>

<b>APPENDIX 6 – LARGE-SCALE LABORATORY PLATE LOAD TEST .....</b>	<b>253</b>
<b>APPENDIX 7 – P&amp;H 4100 UNDERFOOT BOSS TEST RESULTS.....</b>	<b>259</b>

## Figures

Figure 1: Stiffness of oil sand in different seasons (after Joseph et al. 2003).....	3
Figure 2: Ground condition and corresponding velocity profile (after Welz 2001)	4
Figure 3: Excavating action (after Harnischfeger 2001).....	5
Figure 4: Shovel duty cycle (after Joseph et al. 2003).....	6
Figure 5: Cyclic ground pressure under shovel (after Joseph 2002).....	6
Figure 6: Stiffness change of oil sands (after Joseph 2002).....	8
Figure 7: Oil sand stiffness change under cyclic loading (after Joseph 2003).....	9
Figure 8: Flow chart of methodology and tests .....	13
Figure 9: The Alberta oil sands (National Energy Board 2000).....	14
Figure 10: Overburden of Athabasca oil sands (after Dusseault 1977).....	15
Figure 11: Current mining operations in northern Alberta (from Imperial 2004)..	16
Figure 12: The truck and shovel operation in open-pit mining method (after Harnischfeger 2001).....	18
Figure 13: The calculated rack of an ultra-class truck (after Joseph 2003).....	19
Figure 14: Oil sand formation in Alberta area (after Plewes 1987).....	21
Figure 15: McMurray formation in mining area (after Kosar 1989).....	22
Figure 16: In situ structure of oil sands (from Dusseault 1977 & Grant 1980)....	23
Figure 17: Grain-size distribution of oil sands (after Kosar 1989).....	24
Figure 18: Stratigraphy of Athabasca oil sands (from Dusseault 1977).....	25
Figure 19: McMurray formation (from Dusseault 1977).....	26
Figure 20: Refraction from two layers (after Tezkan 1998).....	29
Figure 21: Shot gather (time-offset) in the 6% bitumen oil sand .....	30
Figure 22: Forward and reverse method.....	32
Figure 23: Forward and reverse method for summer data .....	33
Figure 24: Route of trucks .....	33
Figure 25: Winter surface and refraction data.....	34
Figure 26: Test set-up for passive winter data acquisition .....	36
Figure 27: Passive data shot gather for a single run of truck .....	36
Figure 28: Truck velocity from passive data .....	37
Figure 29: Simple truck velocity for winter passive data .....	38
Figure 30: Slow truck velocity vs. fast truck velocity .....	39
Figure 31: Sums of amplitudes for each array position.....	40

Figure 32: Relaxation time between runs .....	41
Figure 33: Comparing the amplitude normalization for different runs .....	42
Figure 34: Comparing the seismic data and VIMS data .....	42
Figure 35: Closer view of the passive data .....	43
Figure 36: Summer test set-up .....	44
Figure 37: Sum of amplitude vs. truck velocity (loaded truck on day 1).....	45
Figure 38: Kinematics energy vs. amplitude for load trucks .....	45
Figure 39: Sum of the amplitude vs. truck velocity for an unloaded truck day 1.	46
Figure 40: Changing sum of amplitudes in each geophone .....	46
Figure 41: Unloaded truck velocity vs. sum of amplitude for day 2 .....	47
Figure 42: Unloaded truck velocity vs. sum of amplitude for day 3 .....	48
Figure 43: Loaded truck velocity vs. sum of geophones amplitude for day 3 .....	48
Figure 44: Loaded and unload trucks velocity vs. sum of amplitude for the 3 days .....	49
Figure 45: Particle motion of P, S, Love and Rayleigh waves (from Shearer 1999) .....	51
Figure 46: Phase and group velocity (from Shearer 1999).....	52
Figure 47: Dispersion of waveform (from Shearer 1999) .....	53
Figure 48: Sequence of obtaining Shear Wave velocities (from Matthews et al. 2000).....	55
Figure 49: Typical waves in a shot gather (from Matthews et al. 2000).....	56
Figure 50: Summer data shot point 1st July 18 f-p and $\tau$ -p graph .....	57
Figure 51: Winter data shot point 1st Jan 31 f-p and $\tau$ -p graph.....	58
Figure 52: The coefficient of volume compressibility (after Craig 1996).....	60
Figure 53: The coefficient of compressibility (after Craig 1996) .....	60
Figure 54: Modulus of deformation (after Craig 1996) .....	61
Figure 55: Failure envelope of re-compacted rich oil sand undrained triaxial tests (from Dusseault 1977) .....	63
Figure 56: Typical drained stress strain curve for oil sand (from Plewes 1987)..	65
Figure 57: Deformation modulus for oil sand in drained triaxial testing (after Plewes 1987).....	66
Figure 58: Ultimate shear strength of oil sand in undrained triaxial (after Plewes 1987).....	67

Figure 59: Effect of strain rate on ultimate strain undrained (after Plewes 1987)	68
Figure 60: Change of Poisson's ratio with confining pressure (after Kosar 1989)	69
Figure 61: Tangent modulus of elasticity for undrained triaxial compression on oil sand (after Kosar 1989)	70
Figure 62: Disturbance of $m_v$ with depth (after Griffin 1986)	72
Figure 63: Compressibility of oil sand at different vertical effective stress (after Griffin 1986)	73
Figure 64: Number of cycles to failure N versus frequency F, at constant applied stress (after Ishizuka 1990)	76
Figure 65: Shear stress and strain behaviour during cyclic loading (after Anderson, 1988)	79
Figure 66: Shear stress, shear strain and pore pressure during cyclic loading (after Anderson, 1988)	79
Figure 67: Change of the stiffness during cyclic loading (after Butterfield and Georgiadis 1980)	80
Figure 68: Cyclic plate 50mm bearing test (after Butterfield 1980)	80
Figure 69: Schematic illustration of cyclic liquefaction (after Grozic, 1999)	82
Figure 70: Damage mechanic parameters	86
Figure 71: Creep Curve (after Kachanov 1986)	87
Figure 72: Schematic of surface bounding in general space (from Dafalias and Hermann 1982)	90
Figure 73: Path 1 ideal plastic deformation, path 2 perfectly brittle material and path 3 combination of plasticity and damage (after Al-Shayea 2003)	93
Figure 74: Changing stiffness with number of cycles	95
Figure 75: Total deformation in load-deformation curve	95
Figure 76: Schematic of triaxial test and principal stresses	98
Figure 77: Stress- strain curve for 8% bitumen at room temperature	99
Figure 78: Linear relationship between $\sigma_1$ and $\sigma_3$	100
Figure 79: Stress-strain curve for 11% bitumen	103
Figure 80: Linear relationship for 11 % bitumen between $\sigma_1$ and $\sigma_3$	104
Figure 81: Cyclic and conventional stress-stain curve comparison for 100 kPa confining pressure	104

Figure 82: Cyclic and conventional stress-strain curve comparison for 300 kPa confining pressure .....	105
Figure 83: Cyclic and conventional stress-stain curve comparison for 500 kPa confining pressure .....	105
Figure 84: Time - Strain curve for triaxial cyclic loading.....	106
Figure 85: Mohr-Coulomb envelope for 8% oil sand .....	107
Figure 86: Mohr-Coulomb envelope for 11% oil sand.....	107
Figure 87: Cyclic plate load apparatus.....	109
Figure 88: Cyclic plate load test in the field .....	111
Figure 89: Stages of a cyclic plate load test .....	113
Figure 90: Changing stiffness during loading for oil sand .....	114
Figure 91: All cyclic plate load test .....	115
Figure 92: Stress-deformation curve for a cyclic test, showing unload-reload cycles .....	116
Figure 93: Plastic and elastic deformation components.....	116
Figure 94: General calculation sequence in FLAC (after FLAC 2002) .....	119
Figure 95: Modeling of circular plate.....	121
Figure 96: Boundary condition and applied load.....	122
Figure 97: Elastic modulus change with confining pressure for 8 and 11% oil sand .....	122
Figure 98: Vertical stress under large plate .....	123
Figure 99: Horizontal stress under large plate .....	123
Figure 100: Vertical deformation under large plate .....	124
Figure 101: Confining pressure $\sigma_3$ under large plate .....	124
Figure 102: Unbalanced force for large plate.....	125
Figure 103: Summary of FLAC modeling for deformation and stresses.....	125
Figure 104: Induced confining pressure by FLAC modeling for different plate size .....	126
Figure 105: Principal, horizontal and vertical stresses on an element.....	127
Figure 106: Load and distances from surface to soil particles .....	128
Figure 107: Vertical and horizontal stresses for large plate .....	129
Figure 108: Vertical and horizontal stresses for medium plate.....	130
Figure 109: Vertical and horizontal stresses for small plate.....	130
Figure 110: Comparing Boussinesq and FLAC results .....	131

Figure 111: Percentage oil and water, wet and dry densities for a 40 m profile in oil sand compiled from original data reported by Dusseault (1977).....	134
Figure 112: Two different methods for measuring density with a Troxler (after Evett 2000).....	136
Figure 113: Density calibration curve for MC-1 densometer .....	136
Figure 114: Moisture calibration curve for MC-1 densometer .....	137
Figure 115: Data from a 7 m profile measuring SPT blow count and fluid content (Joseph, 2001) .....	138
Figure 116: Analysis of compaction data by using results reported by Lord and Cameron (1985) and higher-grade oil sand from in-pit.....	139
Figure 117: Troxler wet bulk density results vs. fluid content.....	139
Figure 118: Troxler dry bulk density results vs. fluid content.....	140
Figure 119: Relationship between oil and water content in oil sand pit.....	141
Figure 120: Rigid steel frame and oil sand box.....	146
Figure 121: Plate load laboratory test set-up.....	147
Figure 122: Original box for laboratory test.....	148
Figure 123: Compaction of oil sand by using vibratory plate and hand roller ...	149
Figure 124: Compaction of oil sand by using steel bar and measuring density with nuclear densometer.....	149
Figure 125: Plate load test results at different stresses for 2-min. loading time	151
Figure 126: Time deformation results at different stresses for 2-min. duration.	151
Figure 127: Bearing capacity failure (after Vesic 1963) .....	153
Figure 128: Local shearing failure at 10-min. loading time.....	154
Figure 129: Global and local slope (stiffness).....	156
Figure 130: General stress-deformation curve for plate load test.....	157
Figure 131: Average data method .....	160
Figure 132: Curve fit method .....	161
Figure 133: Pressure stiffness vs. time for 5-min. tests .....	162
Figure 134: Final curves for different tests based on averaging curve fit .....	163
Figure 135: Final curves for different tests based on averaging data points.....	163
Figure 136: Loading rate vs. pressure stiffness for initial loading.....	164
Figure 137: Loading rate and deformation rate for 5 Min test .....	165
Figure 138: Initial density versus initial loading deformation .....	166

Figure 139: Time deformation curve for loading and unloading at different stresses for 2 min duration test.....	167
Figure 140: Total deformation at different pressure during 20 cycles.....	169
Figure 141: Total deformation versus deformation in 20 cycles for 0-10 min. ..	169
Figure 142: Total deformation versus deformation in 20 cycles for 2-10 min. (on removing the instantaneous 0-min data).....	170
Figure 143: Pressure stiffness for different duration cycles based on averaging curve fit.....	171
Figure 144: Local pressure stiffness during cycles for 2-min. duration cycles..	172
Figure 145: Local pressure stiffness during cycles for 0-10 min. duration cycles .....	172
Figure 146: Average of values of local pressure stiffness for 0-10 min. duration cycles .....	173
Figure 147: Initial density vs. total cyclic deformation .....	174
Figure 148: Initial density vs. final density .....	175
Figure 149: Coefficient factors for different vertical pressure level.....	177
Figure 150: Coefficient factors for different curve duration 0 to 10 Min tests....	177
Figure 151: Stress Vs. deformation curve for 600 kPa and 5 Min test .....	178
Figure 152: Deformation vs. Time for 600 kPa and 5 Min test .....	179
Figure 153: Effect of two cycles on the deformation for 600 kPa and 5 Min test .....	179
Figure 154: Survey locations for ground sensors.....	183
Figure 155: Picture of total pressure cell field installation .....	183
Figure 156: Shovel and active pressure cell locations .....	185
Figure 157: Different parts of the P&H 4100 BOSS shovel (after Harnischfeger 2001).....	185
Figure 158: Different digging positions (after Joseph et al. 2003).....	186
Figure 159: Plan view of shovel unloaded and loaded static tests .....	187
Figure 160: Total pressure cell output of NLS during test .....	190
Figure 161: Total pressure cell output of LS during test.....	190
Figure 162: Ground pressures recorded at hold position .....	191
Figure 163: Sections of calculated stress for an ultra-class shovel .....	192
Figure 164: Vertical and horizontal stresses for section B .....	193
Figure 165: Principal stresses for section B.....	193

Figure 166: Vertical and horizontal stresses for section A .....	194
Figure 167: Principal stresses for section A.....	194
Figure 168: Surveying equipment location.....	195
Figure 169: Graph of ground displacement recorded at each hold position .....	195
Figure 170: Absolute deformation from survey and prediction deformation .....	198
Figure 171: Changing the absolute deformation value during empty-shovel's rotation .....	198
Figure 172: Changing the absolute deformation value during the static loading test .....	199
Figure 173: Changing the absolute deformation value during the static loading test (end of day).....	199

## Table

Table 1: Snapshots of excavating action .....	5
Table 2: P wave velocity and thickness of summer oil sand .....	31
Table 3: Results of compressibility tests.....	68
Table 4: Equipment ground pressure .....	75
Table 5: Summary of laboratory sample properties .....	102
Table 6: Maximum pressure according to truck weight.....	111
Table 7: Plate size and test information.....	112
Table 8: Time line for cyclic plate load test.....	117
Table 9: Result of vertical and horizontal stress using Boussinesq approach ..	129
Table 10: Results of large-scale laboratory tests .....	158
Table 11: Coefficient factor via each of the two analytical processes .....	159
Table 12 : Density, deformation and loading rate .....	166
Table 13: Deformation survey information for shovel-loading conditions .....	196

## Nomenclature, symbols and abbreviations

-	Negative
%	Percentage
°	Degree
"	Inch
+	Positive
2-D	2-dimensional
A	Plate of area
A'	Damage area
A <sub>0</sub>	Initial area
ASL	Above sea level
ASTM	American Society for Testing and Materials
B & L	The foundation dimensions
cm	Centimetre
C	Centigrade
Cs	Cesium
D	Plate diameter or square side length
$\delta_x$	Horizontal stress
$d\varepsilon^d$	Damage strain
$d\varepsilon^e$	Elastic strain
$d\varepsilon^p$	Plastic strain
E	Elastic modulus
e	Strain
$\dot{\varepsilon}^p$	Plastic strain rate
$\varepsilon_m^R$	Peak pseudo-strain
E'	Young's modulus of damaged material
E <sub>ps</sub>	Post-peak Modulus
F	Force
f	Frequency
FLAC	Fast Lagrangian Analysis of Continua
FEA	Finite element methods
g	The acceleration of gravity

GM	Geiger Muller
Hz	Hertz
$(\varepsilon_e^R)$	Initial pseudo-stiffness function
$k_0, k_f$	Experimentally determined stiffness
$K_e$	Elastic stiffness
kg	Kilogram
kN	Kilo Newton
kPa	Kilo Pascal
$K_{ps}$	Post-peak stiffness
$K_p$	Plastic modulus
$\bar{K}_p$	Bounding plastic modulus
$L_F$	Left front strut pressure
$L_P$	Linear Potentiometer
$L_R$	Left rear strut pressure
$L_S$	Loading side
m	Metres
MI	Millions
$m^2$	Square metre
$m^3$	Cubic metre
Mg	Million grams
Min	Minutes
Mlb	Million pounds
mm	Millimetre
MN	Million Newton's
MPa	Mega Pascal
N	Number of cycles to failure
NLS	Non-loading side
OEM	Original equipment manufacturer
psi	Pound per square inches
Q	Applied load
$Q_t$	The thermodynamic force
R	Distances

$Q_u$	Load axis intercept
$q_n$	Previous loading history
$R_F$	Rear front strut pressure
$R_R$	Rear right strut pressure
s	Seconds
$\dot{S}$	The component of the stress rate deviator
$\sigma_1$	Maximum principal stress
$\sigma_3$	Minimum principal stress
$\sigma_H$	Horizontal stress
SPT	Standard penetration test
$\sigma_V$	Vertical stress
t	Time or arrival times
$\tau_f$	Shear stress
$\tau_{rz}$	Shear stress
UCS	Uniaxial compressive strength
UU	Unconsolidated-undrained
V	Velocity
W	Weight
$\omega$	Describes damage parameters
W	Displacement
Z	Depth
$\delta$	Deformation
$\Delta q$	Change stress
$\dot{\epsilon}$	Strain rate
$\xi_g$	A global slope
$\xi_l$	A local slope
$\sigma_n$	Normal stress
$\sigma_r$	Horizontal stress
$\sigma_z$	Vertical stress
$\dot{\psi}$	Force rate
$\phi(\sigma)$	Non-negative monotonically increasing function

$\sigma_m$	Stress corresponding to $\varepsilon_m^R$
$\sigma_{ij}'$	Image of actual stress point
$\delta$	Distance between actual stress and image
$\sigma_{ij}$	Actual stress

## **1 Introduction**

### **1.1 Overview**

The excavation of ore and overburden is the primary function of surface mining, and results in a mine's greatest capital investment and operating costs. High-production bulk surface mining methods use some of the biggest loading and hauling equipment available to facilitate a decrease in the cost per tonne of the ore delivered.

When equipment needs unscheduled maintenance, production drops, and unexpected costs consequently increase. Unscheduled maintenance is more common with age and is manifested as frame fatigue and more frequent tire and suspension damage. The root cause may be poor ground conditions beneath the shovel or truck, rather than solely the age of the equipment. Uneven ground surfaces cause adverse twists, fatigue, and cracks or, at the very least, equipment sinking due to the high deformational response of soft ground under typical loads exceeding several hundred tonnes. In the northern part of Alberta, the Athabasca deposit is shallow enough to be mined by using the surface mining method. In the summer, the ground is soft and makes the underfoot unstable and the digging conditions harsh. In this condition, high maintenance costs from truck and shovel fatigue failures occur as a result of ground-stability issues.

The changing of an active open-pit operation negates the economic or logistical possibility of improving the operating surface foundation for large mobile mining equipment and necessitates the reliance on in-pit materials, most often the ore or host strata, as the construction material. In striving to increase efficiency, mining engineers are encouraged to understand ground interactions with equipment, especially where soft ground conditions are commonly encountered.

In general, truck and shovel operations dynamically load the ground, depending on the initial ground condition. Soft ground materials such as clay or oil sand have visco-elastic-plastic behaviour, which on immediate unloading, results in

considerable permanent deformation, which is somewhat alleviated after a lengthy period of relaxation.

Geotechnical field and laboratory tests were conducted under static 'snapshot' and cyclic loading conditions. The static condition was analyzed within the elastic pre-peak and residual regions of behaviour. The analysis was extended through a series of large-scale cyclic laboratory tests to evaluate oil sand behaviour under dynamic loading conditions commensurate with the loading frequency of large equipment in-pit activities. To predict ground deformation under the cyclic loading condition, a pseudo-elastic model was used. Plastic deformation was investigated and incorporated into the analysis via analytical, physical-empirical and numerical techniques. To better understand the loading action of dynamic equipment, the dynamic loading of soft ground must be first fully understood.

Improving knowledge of equipment-ground performance will inevitably lead to lower maintenance and operating costs, improved ground relationships for OEMs' (Original Equipment Manufacturers) optimized equipment design, and overall reduced risk associated with the high capital investment associated with ultra-class equipment.

## **1.2 Statement of the Problem**

The oil sand deposits of northern Alberta are mined by using large-scale bulk handling equipment in an open-pit setting. Oil sand has unique properties that allow it to perform akin to sandstone in winter and weak clay in summer, as the temperature varies from  $-30^{\circ}\text{C}$  to  $+30^{\circ}\text{C}$ , respectively. Figure 1 shows the oil sand stiffness variations for the changing seasons.

Large mobile equipment, such as the 360-tonne-capacity Caterpillar 797 truck or the P&H 4100 BOSS shovel with gross weights of 700 and 1500 tonnes, respectively, is some of the biggest equipment reported operating in an open pit anywhere. These ultra-class units such as a truck and shovel represent high capital cost investments of \$5 MI and \$19 MI, respectively, with the structural life expected to be half of these amounts. When moving to larger equipment to

decrease operating costs, the life expectancy and, hence, the higher maintenance costs are of particular concern.

Soft ground conditions in oil sand, especially in summer due to the low stiffness of the material, cause high rack, pitch and roll in trucks, leading to fatigue failure in structural components. For shovels, poor ground stability can cause twists in carboodies and undercarriages, resulting in major damage (Joseph et al. 2003).

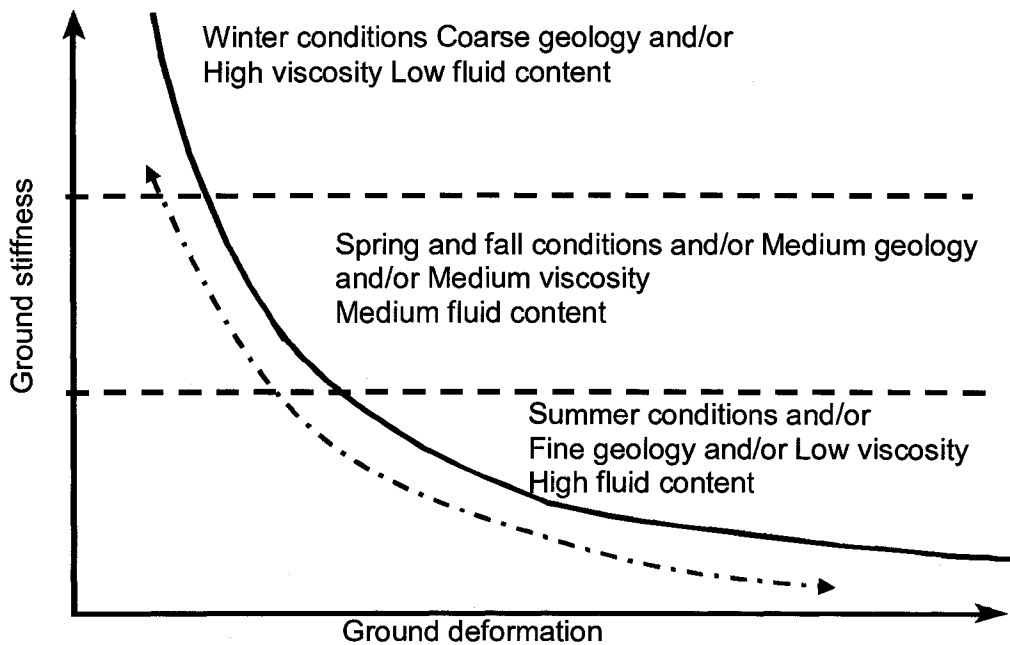


Figure 1: Stiffness of oil sand in different seasons (after Joseph et al. 2003)

Summer geophysical investigations (Welz 2001) of the ground near the surface identified mobile or soft material to around 6 to 8 metres depth, commensurate with very low velocities and a transition zone of up to 25-26 metres depth and approaching in situ oil sand below. The depth of the oil sand zones can be calculated by using the refraction analysis technique that is explained in section 2.4.1.2.1. The velocity interface near the surface, caused by the loosening of the surface material by heavy mining machinery and excavation, creates a “loss or mobility” zone. The deeper velocity changes may be due to a more compact and undisturbed nature of the material, creating “transition and in situ” zones. Figure

2 illustrates the geophones' offset versus the first arrival wave's arrival time, the loss or mobility, transition, and in situ oil sand zones.

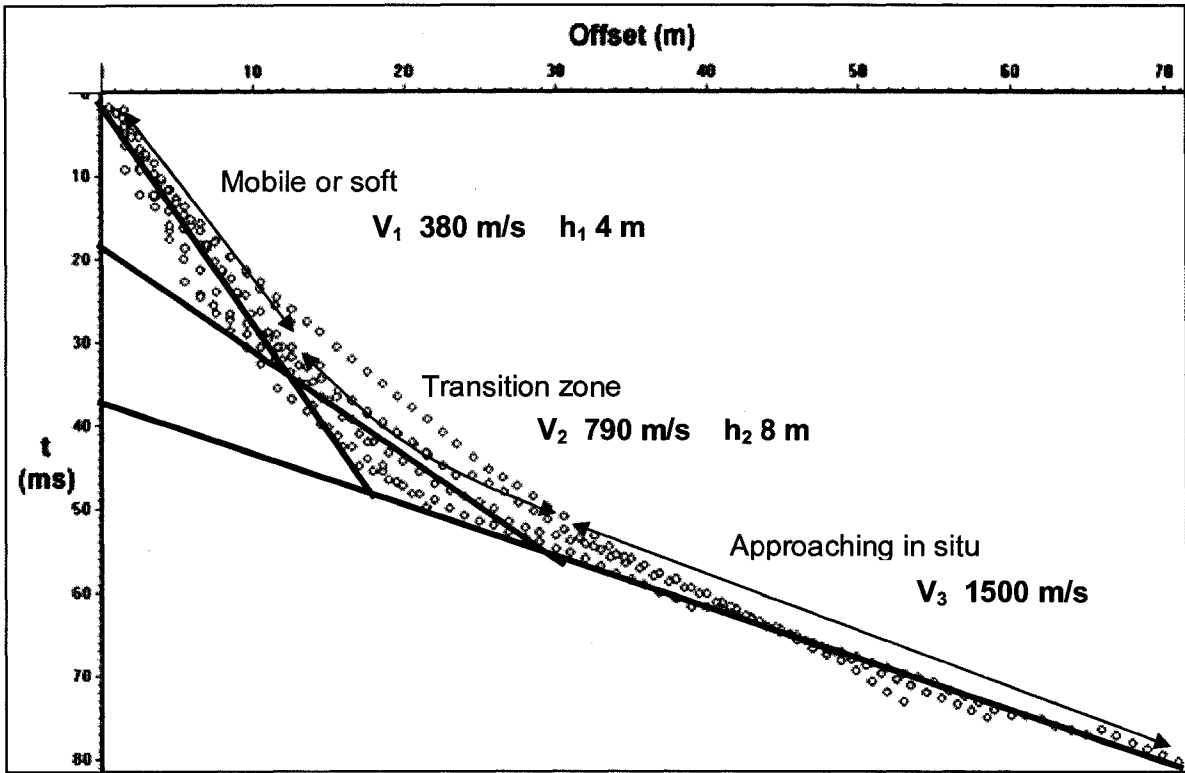


Figure 2: Ground condition and corresponding velocity profile (after Welz 2001)

Joseph et al. (2003) reported that after only a few cycles of load, trucks and shovels operating on soft ground become less stable. Because of poor rolling resistance conditions, trucks in summer are frequently loaded with less than their nominal payload. Even with lower payloads, after only a few passing trucks, the cycled ground by equipment, is unable to support the weight of a truck. In summer, the ground has a lower stiffness compared to that of the tires and suspension; consequently, ground deformation is greater than that of the tires or suspension, resulting in ground undulations. Deformed ground causes rack, roll, pitch and cumulative bounce truck motions that may be the root cause of frame, suspension and tire fatigue, as has been verified by Wohlgemuth (1997), Joseph (2001) and Trombley (2001). Rack, pitch and roll can be calculated as follows:

$$\text{Rack} = \{(L_F + R_R) - (R_F + L_R)\} \quad [1]$$

$$\text{Pitch} = \{(L_F + L_R) - (R_R + R_F)\} \quad [2]$$

$$\text{Roll} = \{(L_F + R_F) - (R_R + L_R)\},$$

[3]

where;

$L_F$ : Left front strut pressure

$R_R$ : Rear right strut pressure

$R_F$ : Rear front strut pressure

$L_R$ : Left rear strut pressure.

Shovel rocking during face activity in soft ground conditions can result in the shovel sinking after a number of cycles. In the oil sand, ground softening occurs rapidly due to cyclic track pressures. A shovel has different dipper positions or loads. The nine key snapshots are defined in Table 1 and shown in Figure 3 and Figure 4.

Table 1: Snapshots of excavating action

No.	1	2	3	4	5	6	7	8	9
Dipper	Tucked	Half in Face	Full in Face	Highest	Highest	Dump Begin	Dump End	Highest	Highest
Boom	Parallel	Parallel	Parallel	Parallel	Diagonal	Perpendicular	Perpendicular	Diagonal	Parallel
Load	Empty	Half	Full	Full	Full	Full	Empty	Empty	Empty

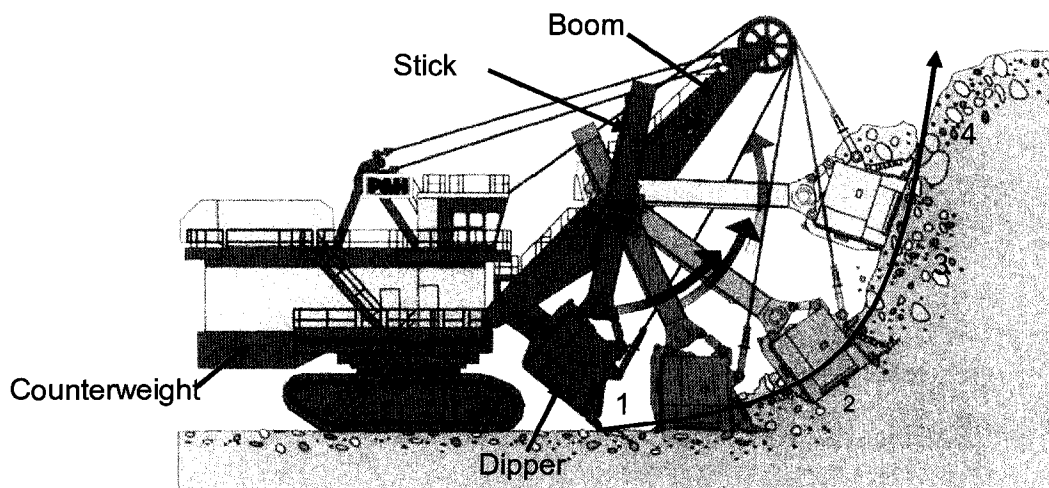


Figure 3: Excavating action (after Harnischfeger 2001)

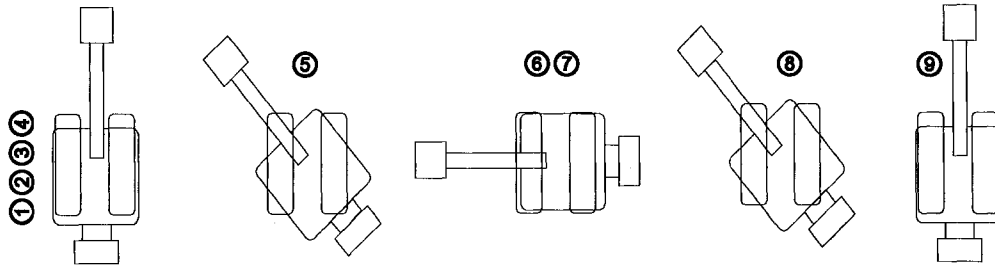


Figure 4: Shovel duty cycle (after Joseph et al. 2003)

Figure 5 shows the cyclic pressures transferred by shovels to the ground during several duty cycles (see Figure 4). Unfortunately, adding new material or grading the underfoot, cannot help to solve the problem. After a few cycles, the ground returns back to the same undulating state, due to the remaining unchanged property of in-pit oil sands compared to big zone of influence for ultra class mining equipments.

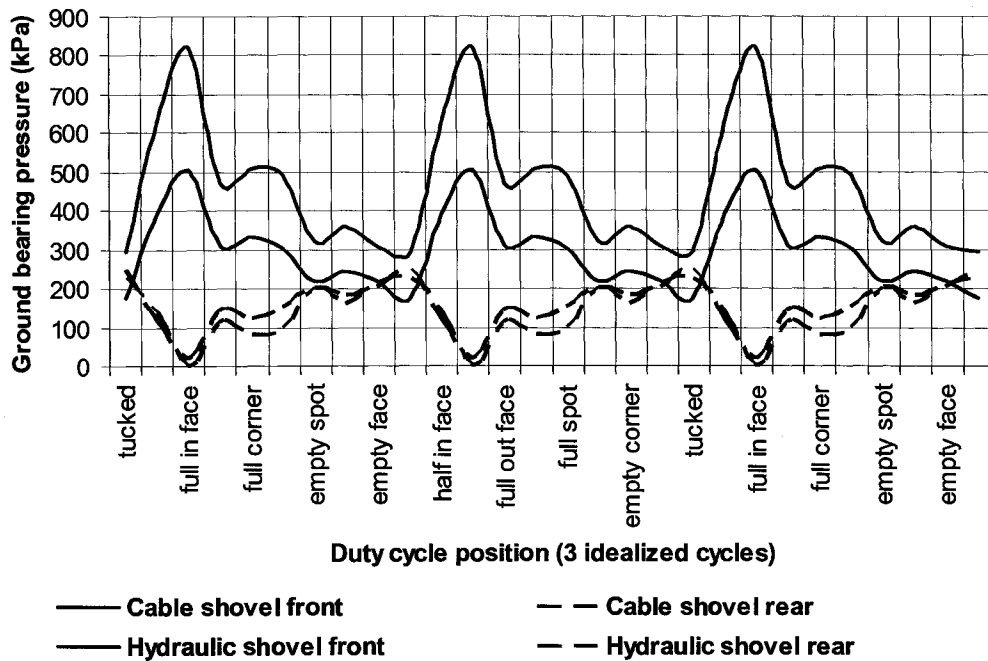


Figure 5: Cyclic ground pressure under shovel (after Joseph 2002)

Under winter conditions, depending on the extent of the cold weather, 1.5 to 3 metres of the near-surface oil sand material is firm (frozen) and overlies softer material beneath. After a few cycles of shovel activity, the oil sand beneath the firm ground softens and causes undulation similar to that of a raft structure, and the undulating ground may cause high stress in shovel structures, causing fatigue and damage. Under these conditions, trucks' tires and suspensions have low stiffness compared with that of the ground; thus, tires and suspensions deform rather than the ground. This condition can damage both the tires and the suspensions.

Understanding oil sand behaviour under dynamic loading due to equipment under varying operating conditions can lead to improved design, more durable equipment for mining operations in soft ground, and lower maintenance and operating costs.

### **1.3 Objectives and the Scope of the Study**

This study explores oil sand behaviour for a range of cyclic loading equipment under constant footprints, and investigates the corresponding ground conditions for seasons when the ground is soft. Shovel stability in terms of the ground conditions and the deformation during different boom positions is examined. Joseph et al. (2002) proposed that oil sand stiffness is a function of deformation regardless of grade, geotechnical properties, and temperature (see Figure 6). Figure 6 shows the previous peak and residual triaxial tests data on oil sand. The vertical axis is the dimensionless post-peak modulus of the strain stress curve,  $(E_{ps})$  divided by the confining stress ( $\sigma_3$ ), the horizontal axis is the strain ( $\epsilon$ ) of the stress strain curve.

Expanding on the initial work of Joseph (2002), this research proposes a simple empirical model and a methodology for analysing the stress-deformation curve of a plate load test for oil sand. This model normalizes the geotechnical variations such as grade, geological deposition, viscosity and general geotechnical properties for oil sand near the surface, to simplify the evaluation of equipment performance. This model is able to predict the deformation for a constant

footprint under mobile mining equipment by using the loading magnitude and duration.

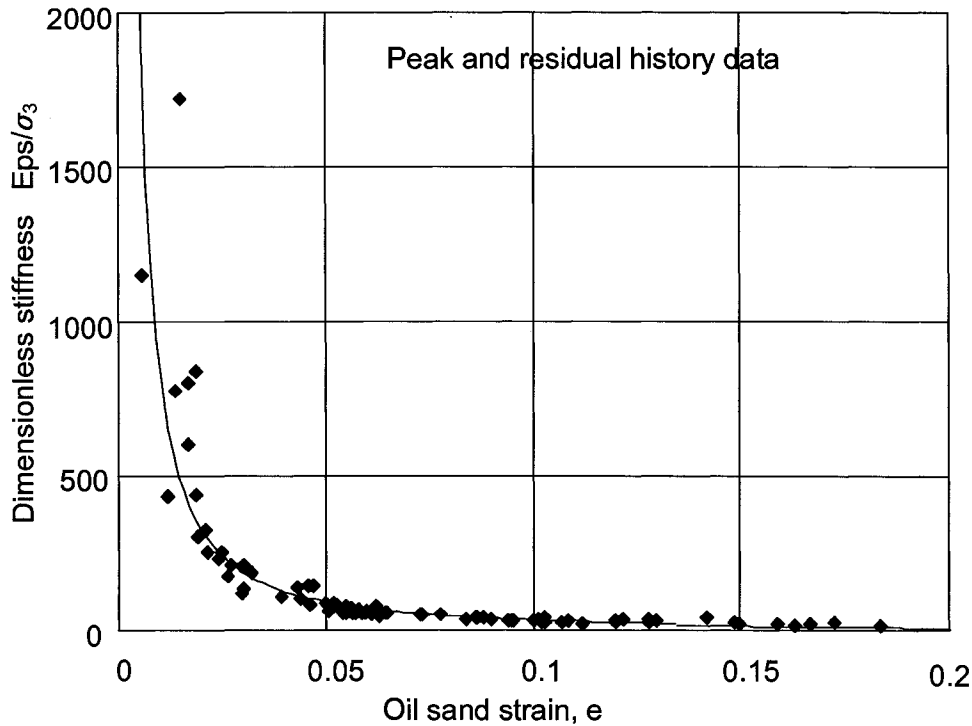


Figure 6: Stiffness change of oil sands (after Joseph 2002)

Even though oil sand has been previously studied by using a plastic or similar constitutive model (Byrne et al. 1980, Samieh and Wong 1998), these types of models require parameters that are difficult to measure for mobile equipment, such as those associated with truck and shovel mining activity. The existing models for predicting oil sand deformation, such as the plastic, elastic and visco-plastic models for predicting the ground deformation, need too many parameters that are very difficult to determine in the limited time before equipment is moved to a new mining activity area. As well, these prediction methods are very expensive because mobile mining equipment works in ever-varying ground conditions, so continuously obtaining the geotechnical parameters needed to predict exact ground deformation at each location is nearly impossible. Therefore, a more practical method and model for predicting ground deformation are required. Such a model, which can be used quickly and with reasonable error, is proposed in this thesis. The majority of previous work on oil sand behaviour has been conducted by using static loading. The objective of this

thesis is not to investigate the geotechnical properties of oil sand but to better understand its behaviour under cyclic loading. Much work has previously been done in defining oil sand properties; however, this work concentrates on the following:

- Investigation of oil sand (as an example of soft ground) under dynamic loading.
- Simplification of the factors involved in ground softening due to cyclic loading to develop a simple equation for predicting ground deformation under cyclic loading.
- Understanding of the interaction between a constant equipment footprint and the corresponding ground under nominal operating conditions.

As shown in Figure 7, oil sand softens during cyclic loading or, alternatively, the oil sand modulus decreases with an increasing number of cycles. The parameters affecting plastic and elastic deformation and stiffness change, such as magnitude and frequency of loading, number of cycles, and loading rate, have been studied. A simple field test for cyclic loading due to equipment will be proposed, including apparatus design and test procedures.

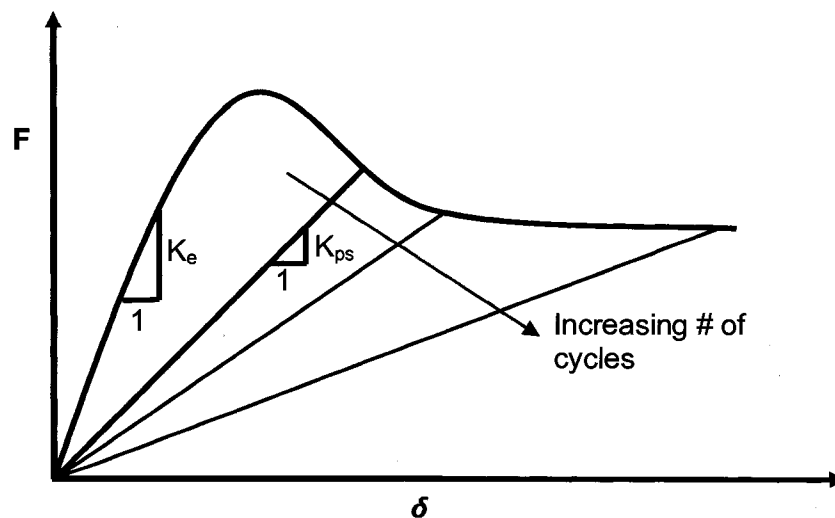


Figure 7: Oil sand stiffness change under cyclic loading (after Joseph 2003)

Static and dynamic data were gathered by using both conventional and large-scale laboratory tests and field tests for building a physical-empirical model to

asses the range of values required to predict plastic and elastic deformation (total deformation) and the stiffness change of oil sand under cyclic loading. The pseudo-elastic model was used to predict the real underfoot for P&H 4100 BOSS shovel, and the predictions were compared with the real values to evaluate the model's accuracy. Numerical modeling techniques (finite difference methods) have been used to model the ground deformation under constant footprint loading and to compare the field test results to the numerical modeling values. Also, Boussinesq's equation was used to predict the stress beneath ultra-class mining equipment.

#### **1.4 Research Methodology**

Oil sand deformation and stiffness changes under cyclic loading conditions and equipment-ground interactions were investigated. Based on the previous work on oil sand and the available data such as those for oil sand's geotechnical properties and geophysical refraction data analysis, a research methodology was developed as follows.

Very little information is available about oil sand behaviour at low confining pressure and in rich bitumen oil sand. Therefore, laboratory tests were performed to investigate rich oil sand, near-surface behaviour at low confining pressures, and to confirm previous data. Also, field tests investigating the load-deformation of in situ oil sand were performed to compare the results with laboratory results. Both kinds of tests are necessary for gathering data to build a physical-empirical load deformation model and to use this model in numerical analysis. In the laboratory, undrained, unconfined triaxial tests were run to study the stress-strain behaviour of oil sand at low confining pressures less than 500 kPa. The conventional triaxial tests were used to determine how oil sand deforms under different confining pressures. The elastic region of the stress-strain curves was analyzed to evaluate the relationship between the elastic modulus and confining pressures. This relationship was used in a FLAC (Fast Lagrangian Analysis of continua) model to simulate field plate load tests. In addition, laboratory cyclic triaxial tests were conducted under different levels of fixed confining pressure to study the behaviour of the oil sand under cyclic loading. The cyclic triaxial results

showed the differences in oil sand behaviour in the conventional and cyclic triaxial tests.

For the small-scale field test, a very simple cyclic plate load test that was quick and easy to use was developed. The results from the laboratory triaxial tests and field plate load tests were compared to infer the induced confining pressures during the field loading conditions by matching the plate load tests to the residual values of the laboratory tests.

The developed laboratory cyclic plate load tests were performed with different loads to understand the time-and-cyclic dependency of deformation under cyclic loads. The results were used to build a model for deformation with load, time and cycles for oil sand. Due to the similarity between the laboratory and field tests, which was confirmed by comparing the laboratory and field results, laboratory cyclic plate load tests were used to generalize a load-deformation equation.

In the large-scale field test, P&H 4100 Boss shovel underfoot testing was performed to investigate the real loading condition and deformation beneath the shovel. By using the generalized equation from the cyclic plate load tests, the deformation of the large-scale field test was predicted.

Numerical modeling was used to predict the stress and the ground deformation under a constant footprint, by using different software to show the possibility of ground pressure, and deformation prediction. Figure 8 presents an overview of the methodology for the various tests and shows how they are linked together.

## **1.5 Remarks**

The truck and shovel are the primary excavation equipment used extensively in most open-pit mining. Since they are key components in the overall mining performance, their operating efficiency and compatibility are crucial. Improving truck and shovel productivity will result in decreased maintenances costs and increased availability time and equipment expected life. In the northern part of Alberta, mine-equipment life is almost half of the expected life. Ground conditions are the most important factor in equipment performance. Oil sand behaviour

changes as the seasons change, this produces very hard, to very soft ground conditions. To design new equipment compatible with soft-ground conditions, understanding the ground behaviours is the key. Many factors are involved in changing oil sand behaviour, and considering all these factors in terms of day-to-day basis of equipment-ground interaction is impractical.

This thesis will initially focus on oil sand behaviours under dynamic loading from ultra-class mining equipment. The relationships among the deformation, load characteristics, and the number of cycles from both the laboratory and field tests will be identified. Numerical modeling will be used for the field tests and for comparing their results with those from real tests. The result of this research will be feedback for manufacturers designing flexible equipment for soft-ground conditions.

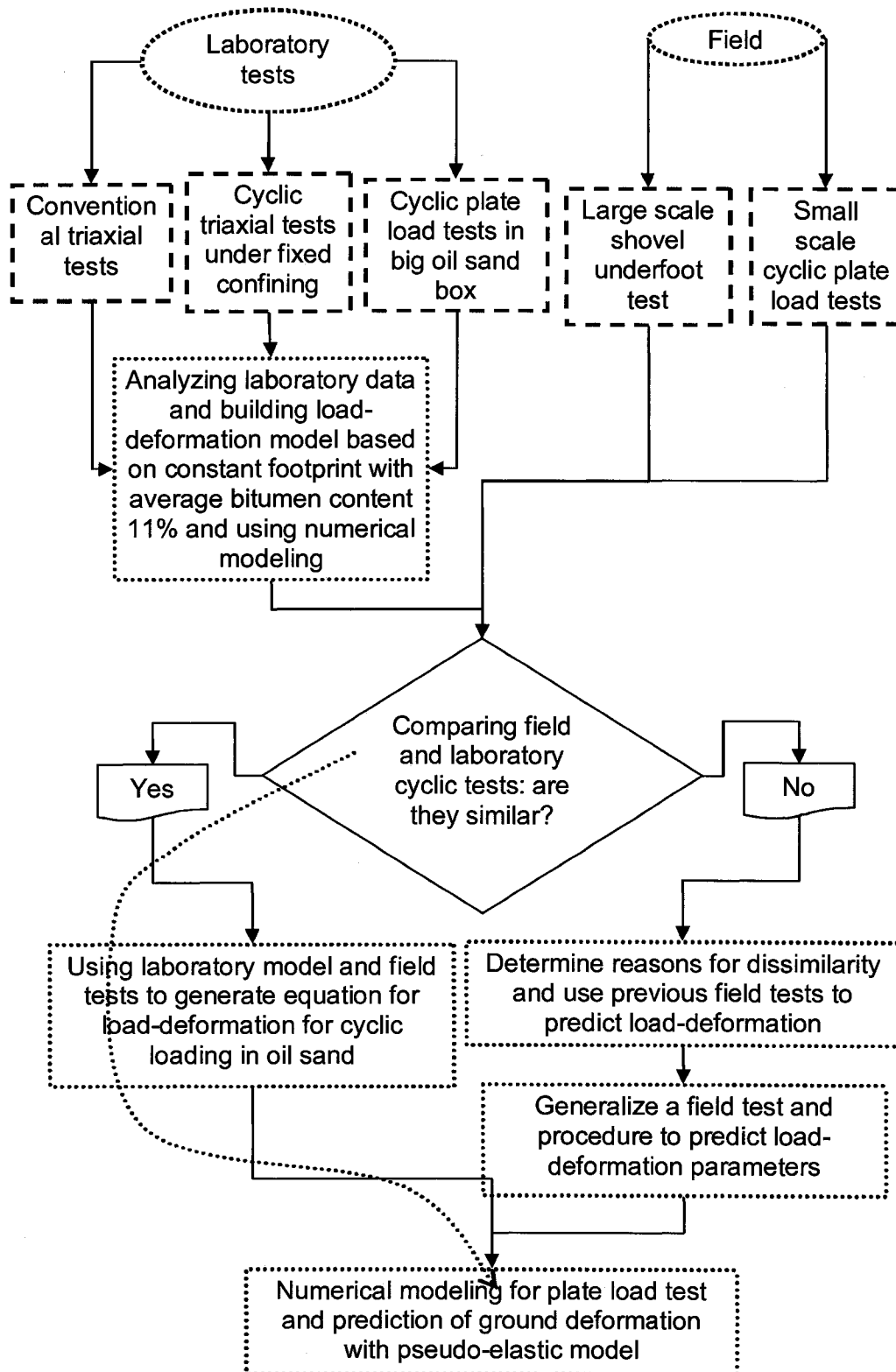


Figure 8: Flow chart of methodology and tests

## 2 Background

### 2.1 Oil sand Introduction:

Alberta's oil sand deposits are the biggest oil sand reserve in the world and represent a major source of oil. Canada's crude bitumen exists entirely within the province of Alberta and is found in sand and carbonate sedimentary formations in three regions: the Athabasca, Cold Lake, and Peace River oil sand areas. Figure 9 shows the oil sand deposits of Alberta, which are not the same as traditional oil fields. The two major differences are

- The oil sands are larger than conventional oil pools.
- The physical properties of oil sands' bitumen greatly differ from those of traditional crude oil.

The Athabasca deposit is estimated to hold 869 BB (billion barrels) or  $1.38 \times 10^{11}$  m<sup>3</sup> of heavy oil, and the total reserves of the three major Alberta oil sands are estimated to be 1350 BB. The depth of the oil sands differs. Figure 10 shows the overburden depth of the Athabasca oil sands.

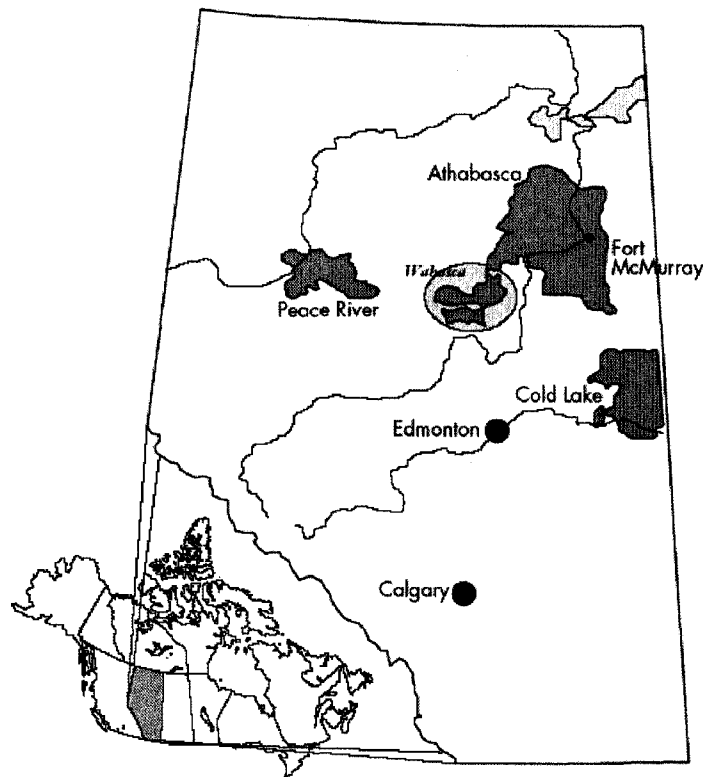


Figure 9: The Alberta oil sands (National Energy Board 2000)

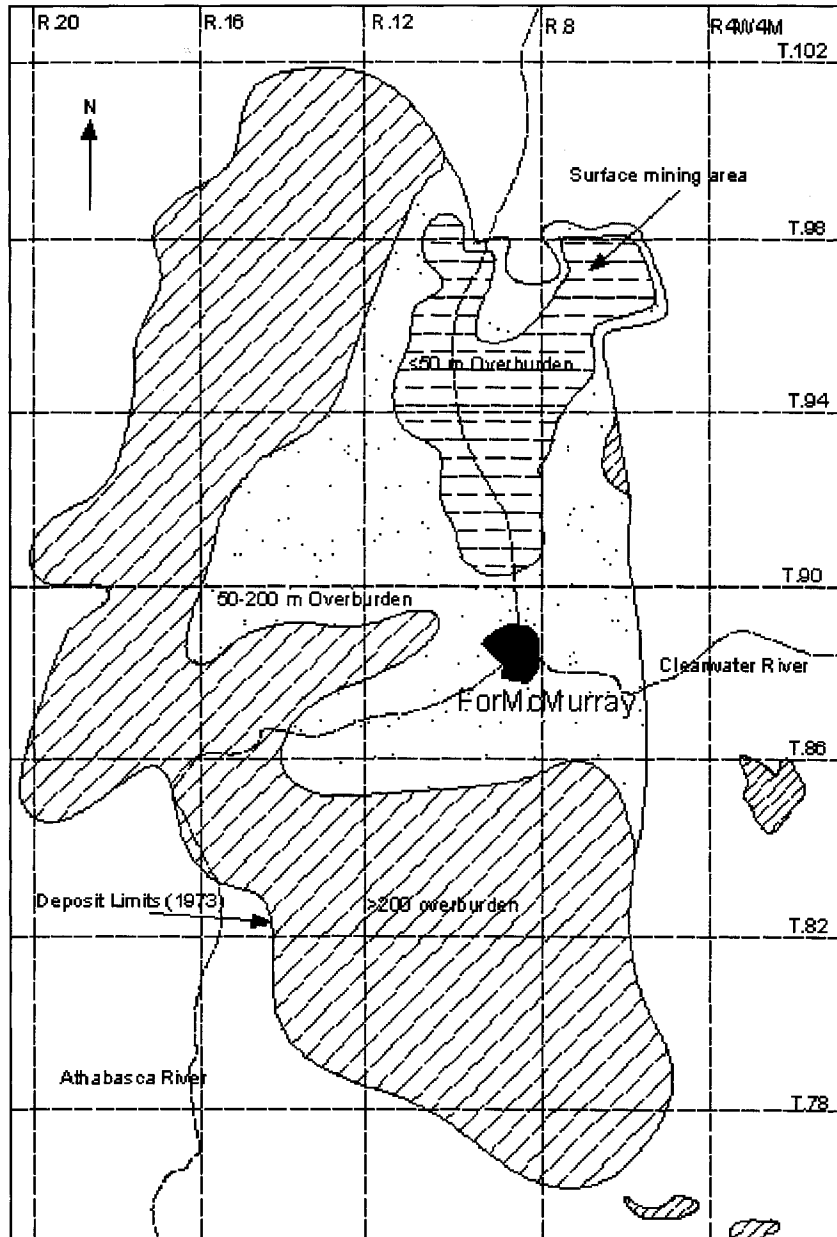


Figure 10: Overburden of Athabasca oil sands (after Dusseault 1977)

## 2.2 Mining

The Alberta Energy and Utilities Board (EUB) estimates the initial volume of crude bitumen in place to be 259.2 billion cubic metres. The EUB further estimates that the ultimate probable volume in place, is close to 400 billion cubic metres. Twenty-four billion cubic metres are categorized as amenable to surface

mining and the rest as in situ recovery. The surface-mining method is based on the thicknesses of the overburden being less than 75 metres, which is an economical thickness for surface-mining operations. Clearly, the oil sands are a tremendous Canadian resource. Canada's oil sand reserves in terms of volume are comparable to the proven conventional oil reserves of Saudi Arabia.

The bitumen content in deposits varies from 1% - 18%. More than 12% bitumen content is considered rich, and less than 6% is poor and not usually considered economically feasible to mine, although it may be mined with a blended stock of higher-grade oil sand. The typical surface-mining operation in oil sand consists of several stages. Before the oil sand can be mined, the overburden, which usually contains rock, clay and barren sand, must be removed by truck and shovel. Also, the surface vegetation and tree cover must be removed, and any suitable soil materials must be selectively excavated and used in the ongoing reclamation program. The oil sands are typically 40 to 60 metres thick and sit on top of relatively flat limestone beds. Trucks and shovels are used to mine-out in-pit oil sand. The oil sand goes to the crusher and then onto the conveyor system, which transports it to the dump pocket from where it is fed to the extraction plant. Figure 11 shows the schematic for a mining operation in the northern Alberta (Imperial 2004).

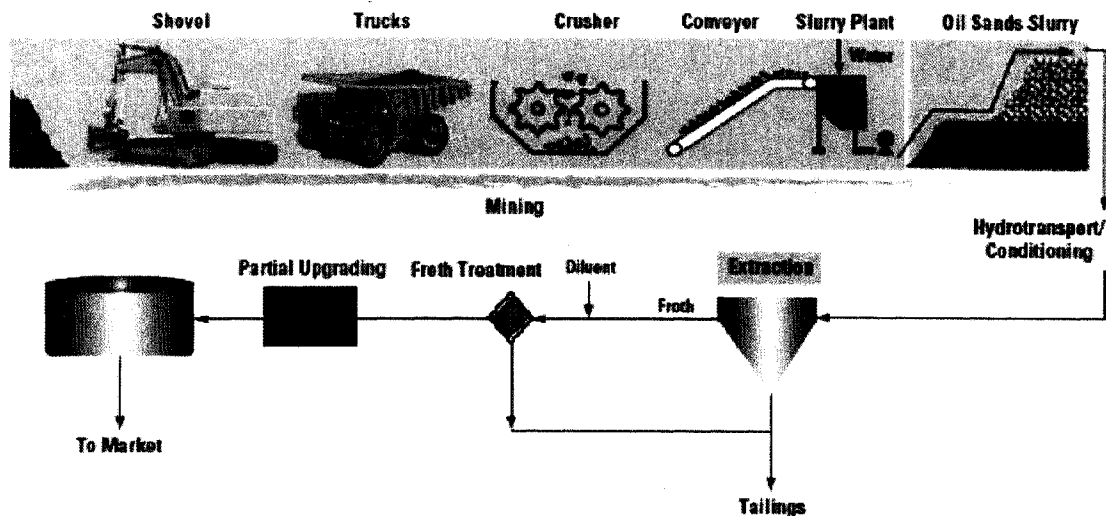


Figure 11: Current mining operations in northern Alberta (from Imperial 2004)

The truck-and-shovel method is considerably more flexible and less prone to the interruption of service than other methods. Today, the oil sands' ore is commonly moved to the dump pits by trucks capable of hauling 360 tonnes and loaded by power shovels with 45-cubic-metre (58-cubic-yard) capacity buckets (Imperial 2004).

### **2.2.1 Oil sand mining specifications**

As was mentioned previously, oil sand is extracted by using the open-pit mining method, which uses ultra-class trucks and shovels such as the 380-tonne caterpillar 797 truck, and the 45-cubic-metre dipper P&H 4100 BOSS shovel. The bench height is 15 metres, and the mining road is 30 metres wide. The angle of the working bench varies from 55 to 60 degrees. The equipment works at a 5-metre distance from the toe of the bench. Northern Alberta is a flat area that varies from being 150 to 350 metres above sea level. Most of the samples were obtained and the testing carried out at 250 to 270 metres above sea level. This project does not focus on a specific mine or location. This study investigates the cyclic performance of the surface oil sand in northern Alberta (the Athabasca oil sands). Figure 12 illustrates the schematic for shovel and truck operations in the open-pit mining method.

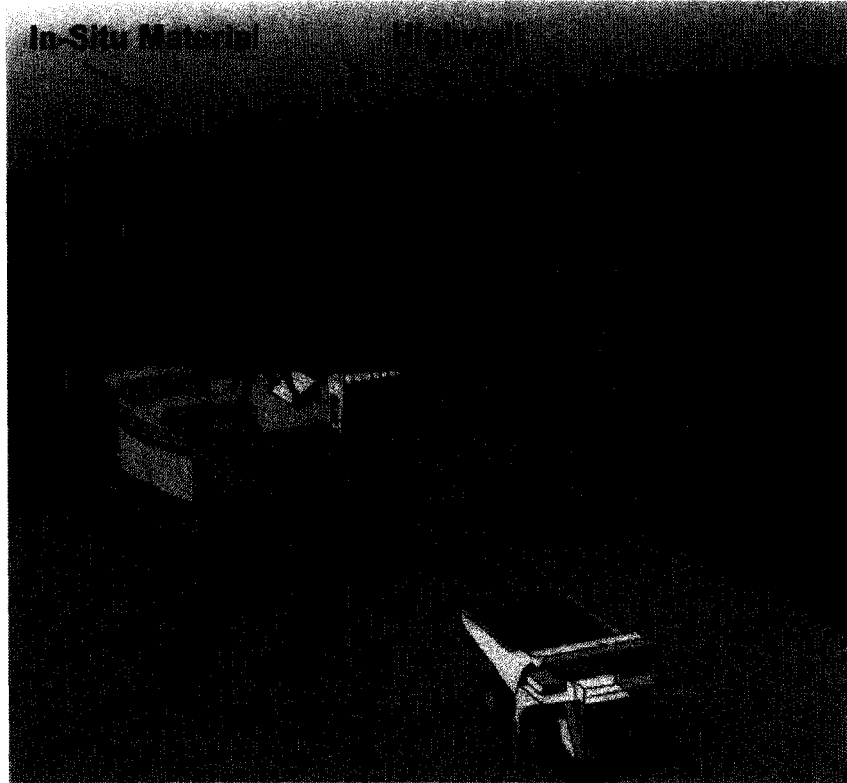


Figure 12: The truck and shovel operation in open-pit mining method (after Harnischfeger 2001)

### 2.3 Ultra-class mining equipment and causes of cyclic loading

As was explained in section 1.2, the field evidence has shown that shovels rock back and forth, with respect to the rack orientation, during face activity, and side to side during the load release into trucks. These rocking motions are caused by changing the position of the boom, stick, dipper, and counter weight (see Figure 3). This change causes a change in the shovel's centre of mass weight and the consequent cyclic loading on the ground. The frequency of the cyclic loading during the duty cycle, causes (as mentioned on 1.2) can vary and depends on the load and digging conditions.

Each tire of an ultra-class haul truck causes cyclic loading during hauling due to undulated ground. As well, due to the soft condition of oil sands, the undulating ground causes the truck to move up and down and applies cyclic force to the

ground. The frequency of the cyclic loading depends on the load profile, the truck load, the speed, and the season. The rack that can be correlated to ground cyclic loading, can yield up to 2g in some conditions. Figure 13 shows the calculated rack of an ultra-class truck.

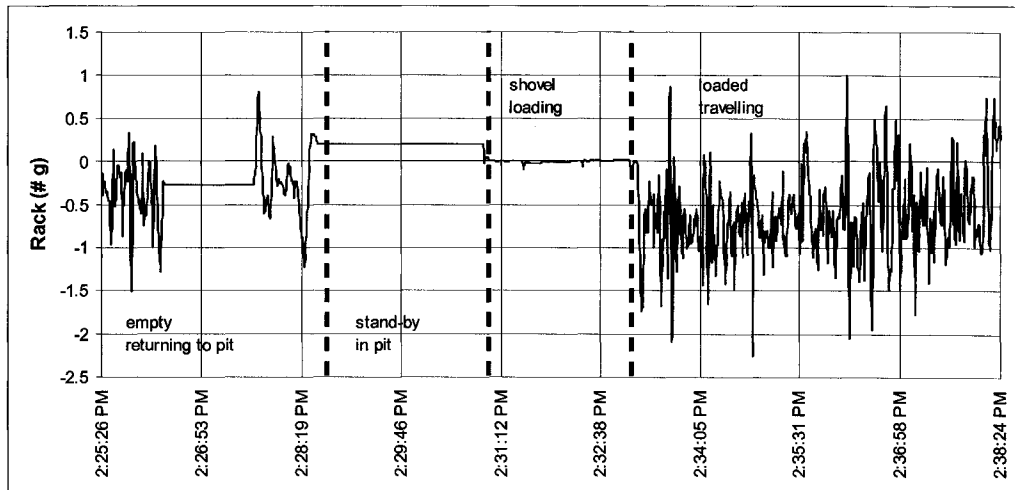


Figure 13: The calculated rack of an ultra-class truck (after Joseph 2003)

An important fact to note is that the frequency and time scale for truck and shovel operation could vary, depending on many factors. However, in simple terms, each cycle of shovel loading takes around 30 to 45 seconds. Therefore, the loading frequency could vary from 0.033 to 0.22 Hz. In the case of a truck, time scale would vary more compared to the outcome of shovel. The outcome also depends on which location is to be utilized for the loading to unloading site—either the crusher or dump areas. With all these variables considered, the average time for each cycle for truck travel is approximately 15 to 30 minutes. As illustrated in the Figure 13, the frequency of loading for mobile mining equipment varies, and depends mainly on ground profile. Because of more mobility of trucks in the mining activities, compared to the shovels, truck ground loading has a more detrimental impact on ground.

## 2.4 Geology

Most geological research on surface-mining projects (in the northern part of the deposits) has been done in areas where the researchers can predict the geometry, grade and fine content of the oil sands reservoir, and also the extension and thickness of the overlying and interbedded shale strata. The major reserves are located in the lower Cretaceous sands of the lower Mannville McMurray formation, as shown in Figure 14 (Plewes 1987, Kosar 1989). The McMurray formation is complex and highly variable and is usually divided into three units: The Upper, Middle and Lower members. The general McMurray formation in the mining area developed by Mattison is shown in Figure 15.

The McMurray formation is dominated by sands deposited in an estuarine channel complex, overlain by shale and shaley sands that are overlain by shale with interbedded sand. The uppermost facies group consists of shoal/shoreface sands overlain by a shaly-shoreface zone and the shelfal Wabiskaw of the Clearwater formation. The Wabiskaw contains oil-bearing sands in the western region and consists of three sands (Wabiskaw A (the youngest), B, and C) with interbedded shale. The Athabasca deposit is dominated by fine-to-medium-grained and uniformly graded quartz sand containing high-grade oil-bearing sands. The Athabasca oil sands have a dense interlocking grain fabric developed during the time of burial when a diagenetic process occurred with the solution and recrystallization of quartz at the grain boundaries. The Athabasca oil sands have a large number of concavo-convex and large contacts, but the typical dense sands exhibit tangential grain contacts (Kosar, 1989).

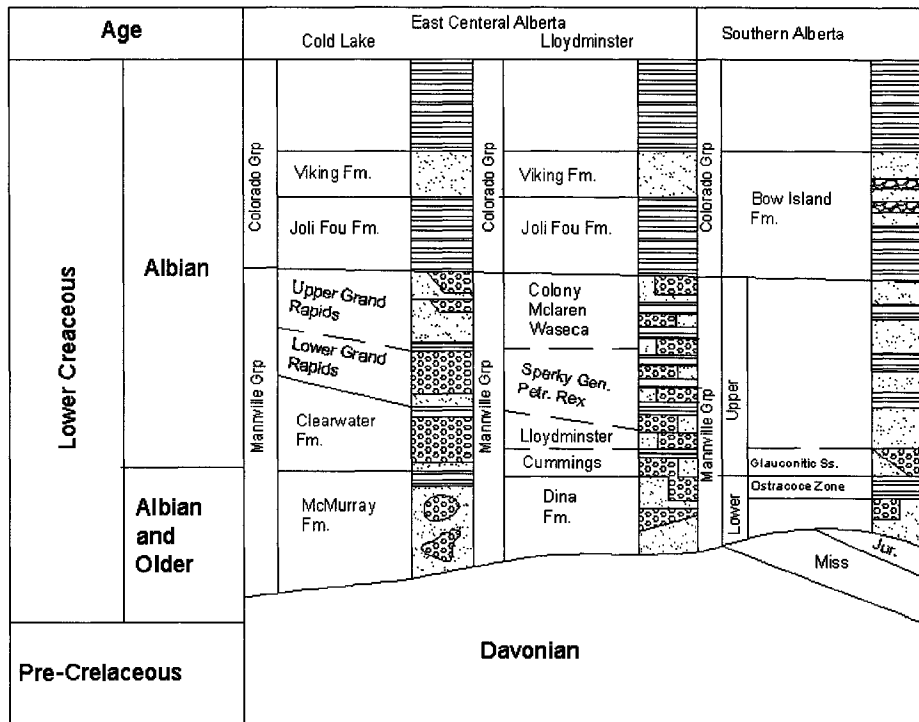
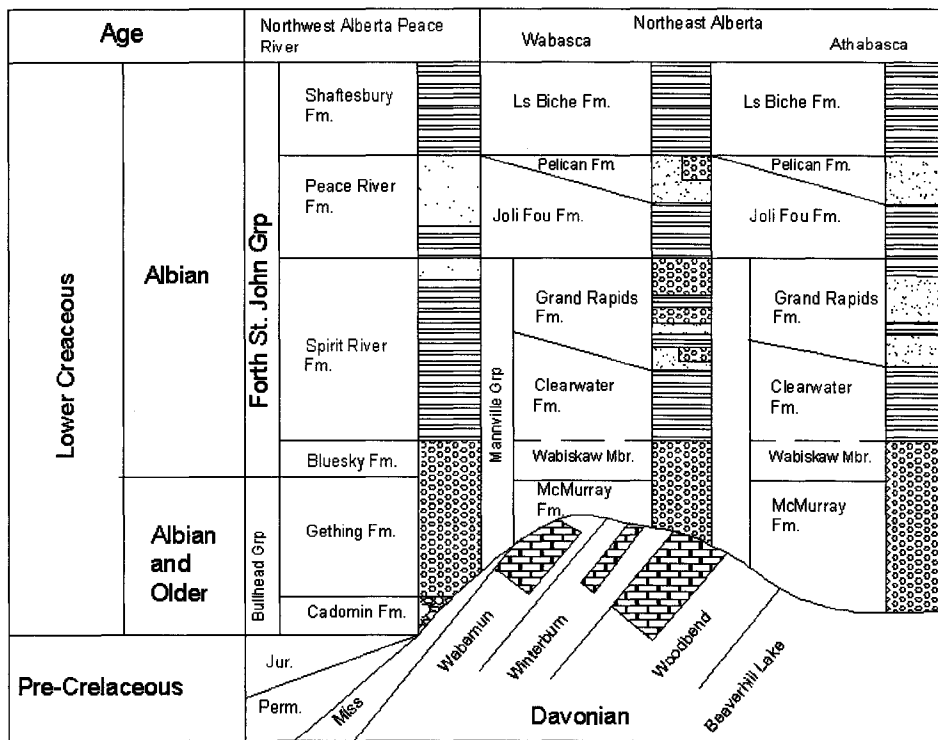


Figure 14: Oil sand formation in Alberta area (after Plewes 1987)

Age	Formation/Member	Overall Environmental Interpretation	
Early Albian	CLEARWATER - WABISKAW MBR.	Shelf	
	UPPER MCMURRAY	Transition Zone	
		Foreshore	
		SHOAL/SHORE-FACE	Upper
			Middle
Lower			
Upper Aptian and older	OSTRACODE/ CALCAREOUS SUBMEMBER	Bay-Sound	
	MIDDLE MCMURRAY	Tidal Flats	
		ESTUARINE CHANNEL COMPLEX	Channels
	LOWER MCMURRAY	Brackish Lakes and Swamps	
		Fluvial Channels	

Figure 15: McMurray formation in mining area (after Kosar 1989)

### 2.4.1 Mineralogy

Most of the rich oil sand particles with greater than 10% bitumen are fine-to-medium-grained dense sand particles (62.5 to 250 micrometers) with small silt and clay-sized material. The shale beds of the oil sands contain silt and clay-sized material and almost no oil. These shale beds of sand consist of nearly 95% quartz grains, 2 to 3 % mica flakes and clay minerals (mainly kaolinite and illite with a minor amount of montmorillonite), and traces of other minerals. The quartz grains are at least 99% water wet. Bitumen and gas are located in the remaining pore space. The bitumen is present in oil sand in a range of 0 to 18% (by weight, ~36% by volume 18%, and with water saturation 2% by weight ~ 4% by volume),

and the gas is predominately methane and nitrogen dissolved in water and bitumen. An inverse relationship exists between the amount of fine-grained material and the oil content. Figure 16 shows the in situ structure of oil sands (Dusseault 1977, Grant 1980). The grain-size distributions for the Athabasca oil sands (UTF sand) are shown in Figure 17.

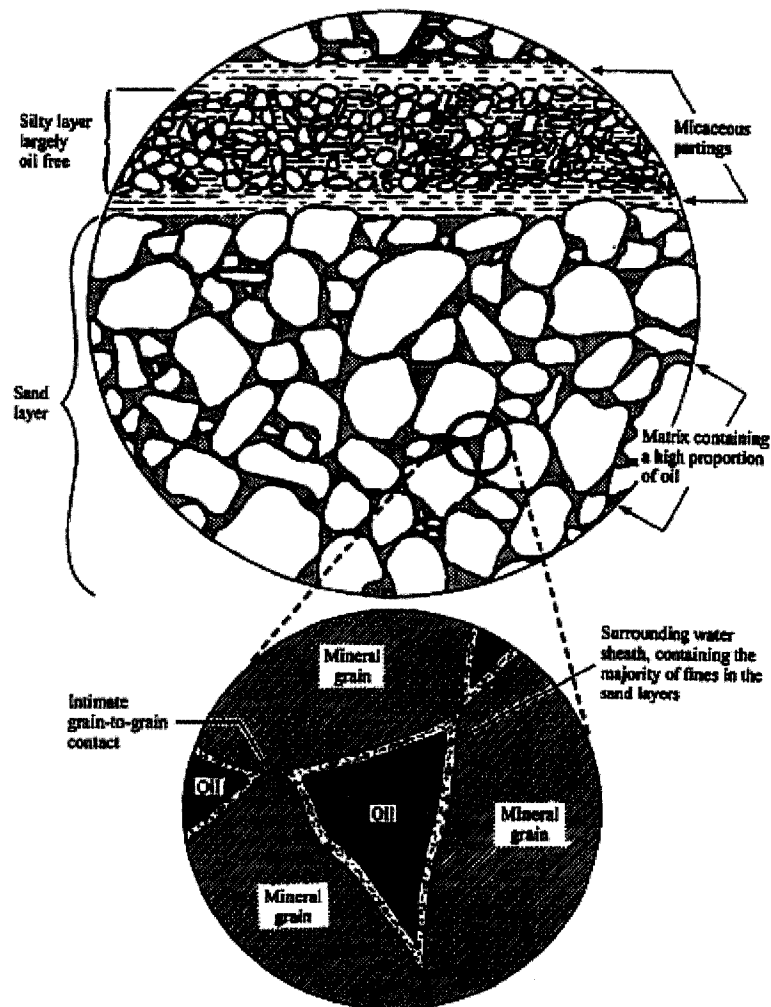


Figure 16: In situ structure of oil sands (from Dusseault 1977 & Grant 1980)

The pore liquids are saturated with gas containing 75% to 90% methane and 10% to 25% carbon dioxide under in situ conditions. The combined solubility coefficient for the combined gases is approximately 0.20 (Kosar 1989).

The porosities of the high-grade oil sand are around 25 to 35%. This high porosity shows a lack of cement in the oil sands, as well as due to increasing fine quartz in the high-grade oil sand. The permeability of the oil in the McMurray formation sand is very high, but assessing the permeability of the bitumen-saturated sand is very difficult. The viscosity of bitumen is 100,000 to 1,000,000 centipoises, and under reservoir conditions, bitumen is immobile (Grant 1980).

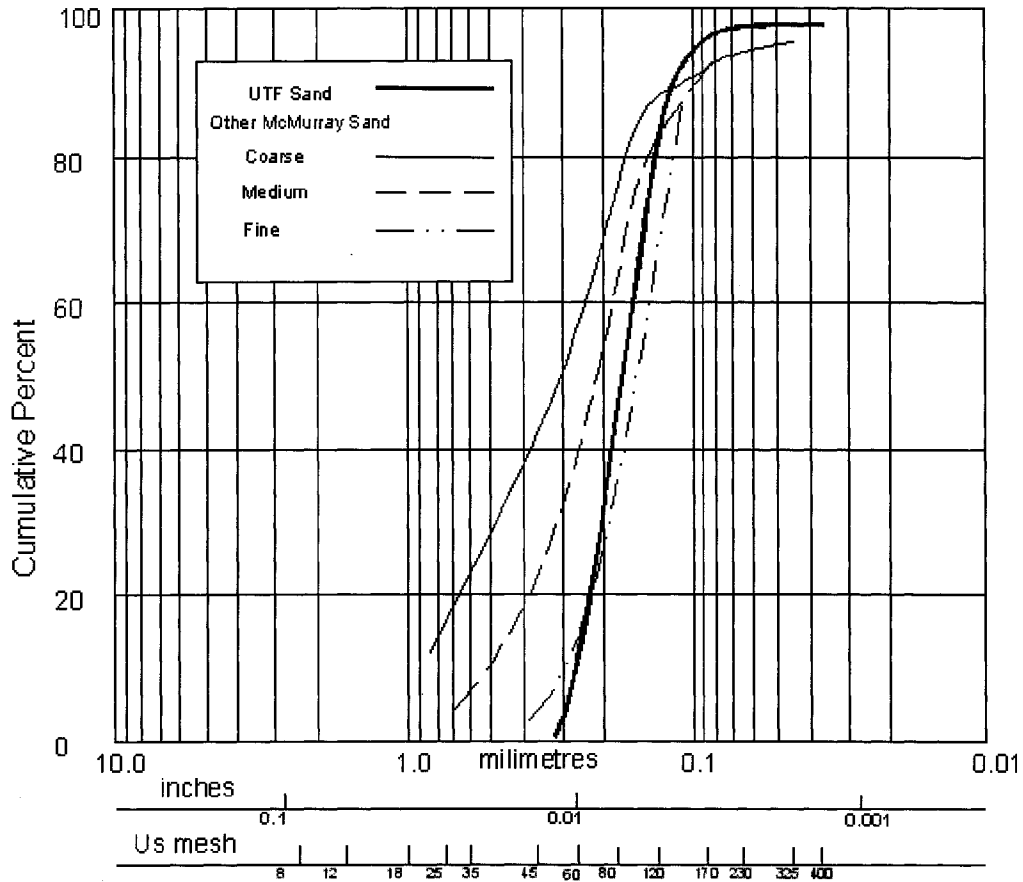


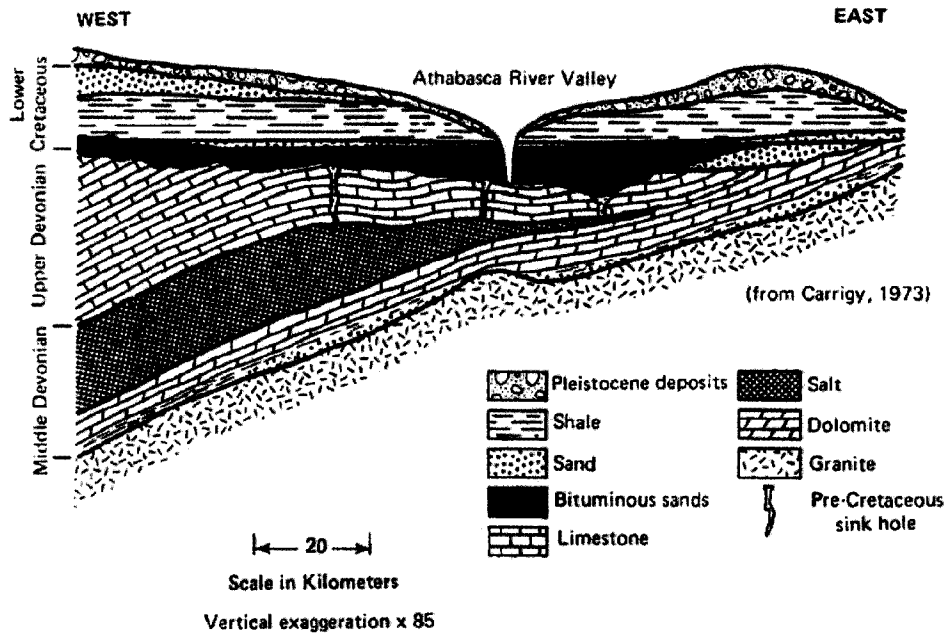
Figure 17: Grain-size distribution of oil sands (after Kosar 1989)

#### 2.4.2 Morphology

The Athabasca deposit is contained within a single reservoir (Grant 1980). The McMurray formation holds 95% of the oil reserves. Above the McMurray formation is the arenaceous portion of the Clearwater formation. Figure 18 illustrates the stratigraphy of the Athabasca oil sands. The McMurray formation is

squeezed westward into a paleotopo graphic area and grades into marine shales to the northwest. Figure 19 shows the McMurray formation (Dusseault 1977).

The McMurray oil sands have fine-to-medium-grained lean oil sand. The colour is brownish grey to black in colour. Shale interbedding was encountered from 1mm to several mm thick.



Formations	Age (millions of years) <sup>1)</sup>	Period	Rock Type
Unnamed Laurentide drift and postglacial sediments	0	Quaternary (Pleistocene)	Glacial till, proglacial lake sediments, aeolian sand
Joli Fou Fmn.	~1.5	(Post-Cretaceous erosion surface)	Shale
Grand Rapids Fmn.	~100		Sandstone
Clearwater Fmn.		Lower Cretaceous	Shale to fine-grained sand at base
Wabiskaw Mem.			Sand to basal pebble conglomerate, largely uncemented
McMurray Fmn.	~106	(Pre-Cretaceous erosion surface)	
Waterways	~360	Upper Devonian	Limestones and dolomites
Elk Point		Middle Devonian	Shale, anhydrite salt, dolomite
Unnamed Plutonic rocks	~370	(Pre-Devonian erosion surface)	Granites, gneisses,
	~1800?	Aphebian (Pre-Cambian)	Granites, gneisses, schists

Geology and Economic Minerals of Canada, 1970.

Figure 18: Stratigraphy of Athabasca oil sands (from Dusseault 1977)

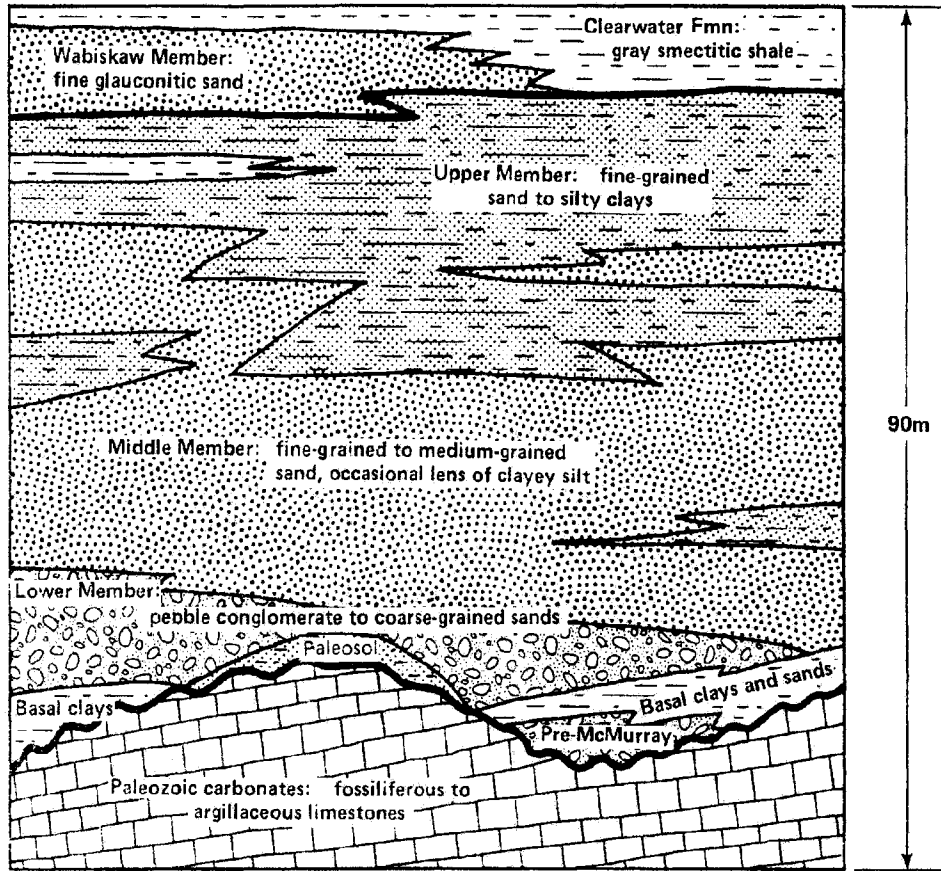


Figure 19: McMurray formation (from Dusseault 1977)

### **3 Material Properties**

#### **3.1 Geophysics**

This researcher carried out a preliminary geophysical study of the oil sands. The two following sections describe the background and the studies used to determine the ground stiffness (modulus) by using a geophysical method and passive seismic data analysis. A geophysical method can be used to evaluate the ground stiffness, as well as the changing ground stiffness during the use of ultra-class mobile mining equipment.

##### **3.1.1 Passive seismic data analysis**

###### **3.1.1.1 Introduction**

Surveying the ground via geophysical seismic methods requires ground movement to generate energy. Energy-producing sources projected into the ground can be used to generate sufficient vibrations to acquire an output.

The three most common (traditional) sources used to produce controllable energy are impact sources, gun sources and explosive sources. Uncontrollable sources or passive sources are anything that causes ground motion but over which there is little if no control, such as road traffic, wind that causes the movement of objects, people walking, or the motion of mining equipment such as trucks or shovels

###### **3.1.1.2 Refraction data for summer and winter conditions**

###### **3.1.1.2.1 Refraction**

The seismic refraction method is based on the measurement of the P waves' arrival times as a function of distance and of the travel times of the seismic waves refracted at the interfaces between the subsurface layers of different velocity. The input seismic energy is provided by a controllable seismic source.

Reflected and refracted energy from different layers is induced within a linear array of geophone sensors. Generally, only the first wave to arrive at a sensor is used, with the assumption that waves spend much of their time traveling in horizontal paths in a series of plane layers.

As travel time is proportional to distance, the procedure for determining a refraction layer's velocity is to find the slope of the travel-time-distance curve. The slope is then an inverse velocity or slowness. A travel-time-distance plot may consist of a number of separate refractions, in which case several straight line segments are fitted to the data to determine the velocities of progressively deeper layers. The basis of this method is that with increasing depth, the velocity increases. Figure 20 shows the refraction for a two-layer stratigraphy, where the physics may be described as (Tezkan 1998)

$$Z_1 = \frac{t_2 V_2 V_1}{2\sqrt{V_2^2 - V_1^2}} \quad \text{First Layer} \quad [4]$$

$$Z_2 = \frac{t_3 V_3 V_2}{2\sqrt{V_3^2 - V_2^2}} - \frac{V_3 V_2}{\sqrt{V_3^2 - V_2^2}} Z_1 \sqrt{\frac{1}{V_1^2} - \frac{1}{V_3^2}} \quad \text{Second layer} \quad [5]$$

$$Z_{n-1} = \frac{t_n V_n V_{n-1}}{2\sqrt{V_n^2 - V_{n-1}^2}} - \frac{V_n V_{n-1}}{\sqrt{V_n^2 - V_{n-1}^2}} \sum_{k=1}^{n-2} Z_k \sqrt{\frac{1}{V_k^2} - \frac{1}{V_n^2}}, n = 2,3,4,\dots \quad \text{For } n-1 \text{ layer,} \quad [6]$$

where;

- $Z_1$  thickness of first layer
- $Z_2$  thickness of second layer
- $Z_n$  the thickness of  $n^{\text{th}}$  layer
- $V_1$  velocity of first layer (reverse of first slope line)
- $V_2$  velocity of second layer (reverse of second slope line)
- $V_n$  velocity of  $n^{\text{th}}$  layer (reverse of  $n^{\text{th}}$  slope line)
- $t_1$  intersection of second line with time axis
- $t_2$  intersection of third line with time axis
- $t_n$  intersection of  $n-1$  layer with time axis.

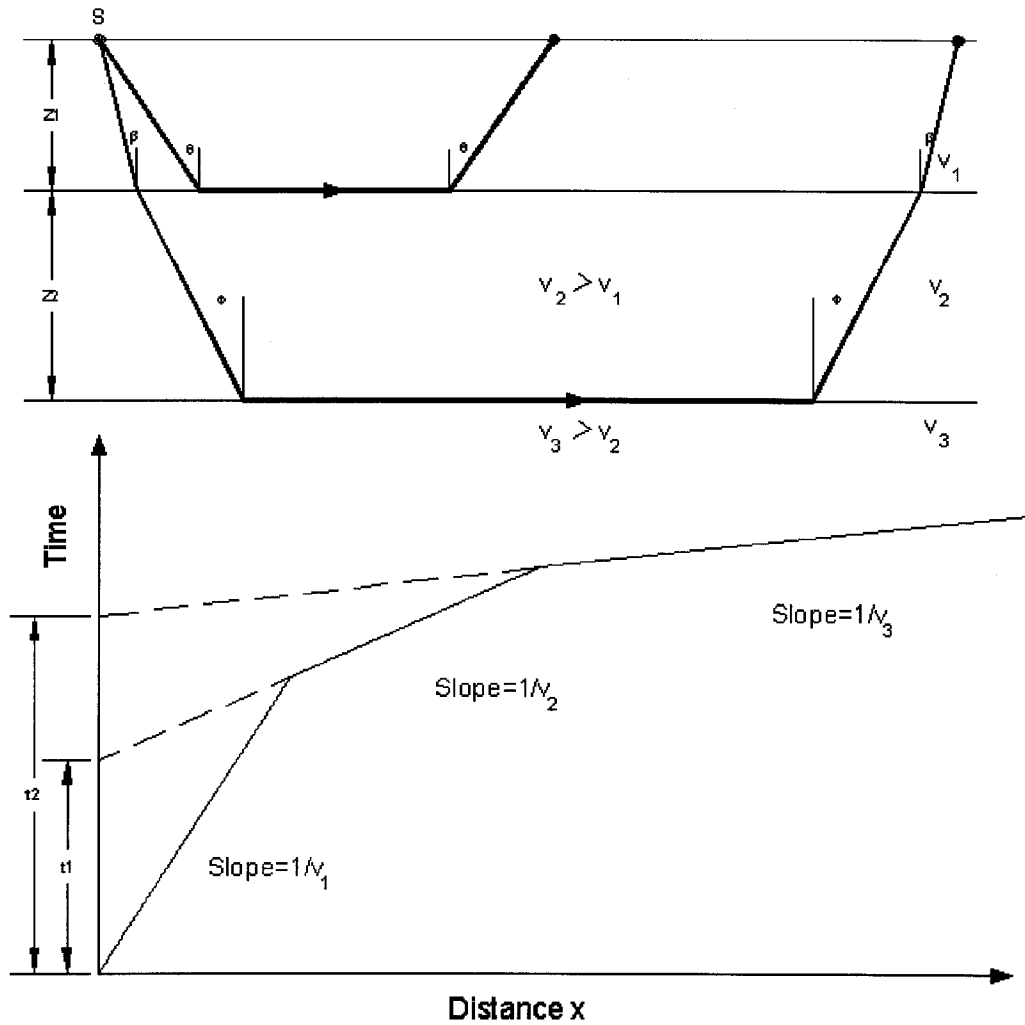


Figure 20: Refraction from two layers (after Tezkan 1998)

### 3.1.1.2.2 Characterization of the site using refraction method

In reflection, we consider the ground movement due to the reflection off the subsurface interfaces: a sophisticated version of an echo sounding. Reflection seismic processing allows us to define the subsurface from the amplitudes and shape of the ground motion. Subsurface structures may be complex in shape, but as is done with refraction method, are described in terms of the boundaries separating materials with differing elastic properties.

### 3.1.1.2.3 Summer refraction data

Seventy-two geophones were placed in a single line at 1-metre intervals, where the ambient temperature was  $\sim 30^{\circ}\text{C}$  in the active mining area, yielding high levels of noise due to heavy equipment operation. This noise proved to be a problem, so that the data had to be filtered to remove the background influence of motors, pumps and even tire treads acting on the ground. The summer data showed high attenuation commensurate with the expected more fluidic nature of the oil sand material at higher temperatures. An analysis of the refraction data showed that the attenuation usually increased with the bitumen content (increasing grade). Figure 21 shows a shot gather (time-offset) for the 6% bitumen oil sand as well as refraction analysis. Table 2 shows the results of the refraction data analysis for different area with different bitumen content.

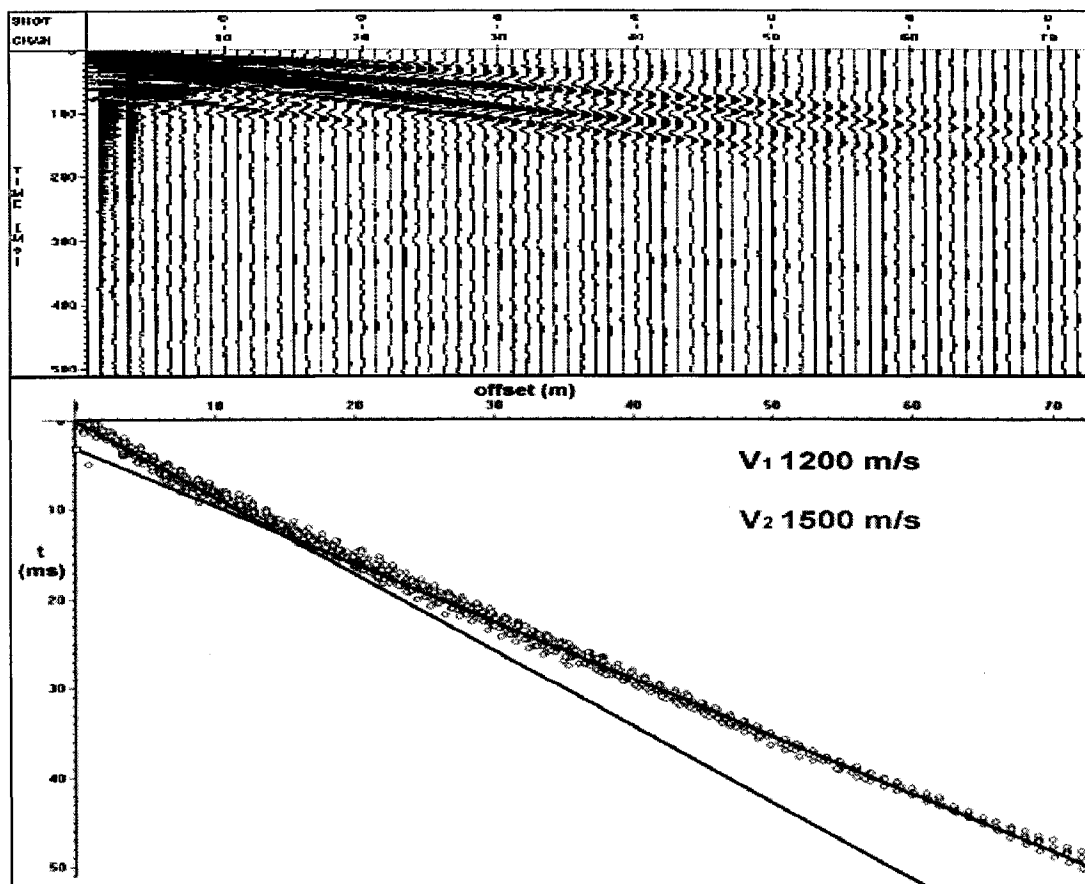


Figure 21: Shot gather (time-offset) in the 6% bitumen oil sand

Table 2: P wave velocity and thickness of summer oil sand

Changing oil sand property	Oil sand grade	Velocity (m/s)	Thickness (m)
First zone	6%	1200	2.25
Second zone		1500	Continuous
First zone	13.5	380	6.7
Second zone		790	26
Third zone		1500	Continuous
First zone	8	410	9
Second zone		1100	28
Third zone		1950	Continuous

#### 3.1.1.2.4 Forward and reversal refraction analysis

The forward and reversal refraction method will be used for measuring dipping of layers. It involves the simple process of shooting to a line of geophones from both ends,

This method works by the refraction of wave arrivals from shots offset in opposing directions (termed forward and reverse for convenience) targeting a receiver, leave the refracting surface from almost the exact lateral location. This means that for any receiver which records refracted arrivals from forward and reverse directions, refractor velocity and depth below the receiver location can be determined (see Figure 22).

During the summer refraction field test, only one day of refraction data had been shot to a line of geophones from both ends, and the first arrival waves were chosen (P wave) for both sides of the shot direction. Figure 23 shows the result of forward and reverse method of choosing first arrival time. It is obvious that the transition zone has slightly dipped to the start of the geophones line (geophone number 1). The truck routes caused the dipping, and the begging of the

geophone line was close to the truck route, compared to the end line of geophone (see Figure 24).

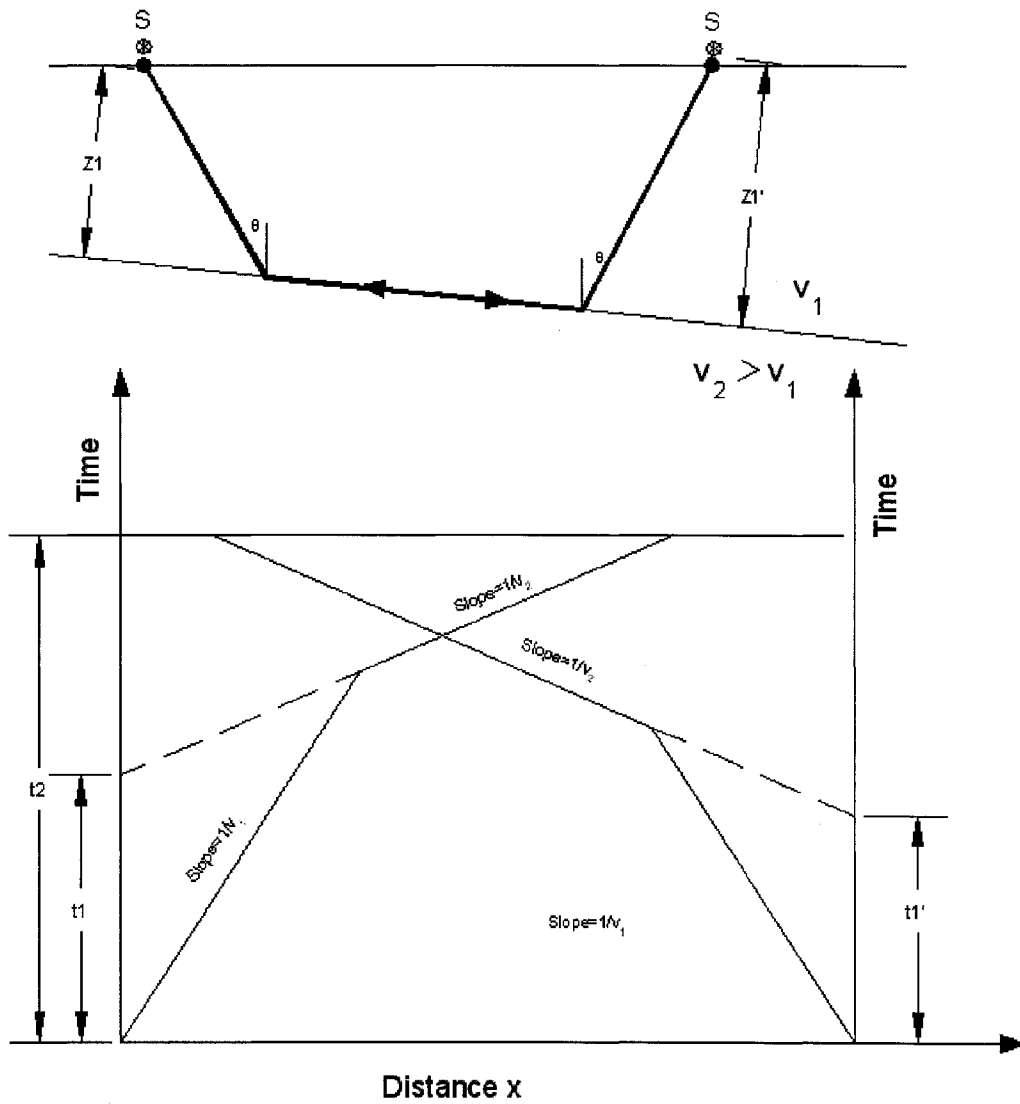


Figure 22: Forward and reverse method

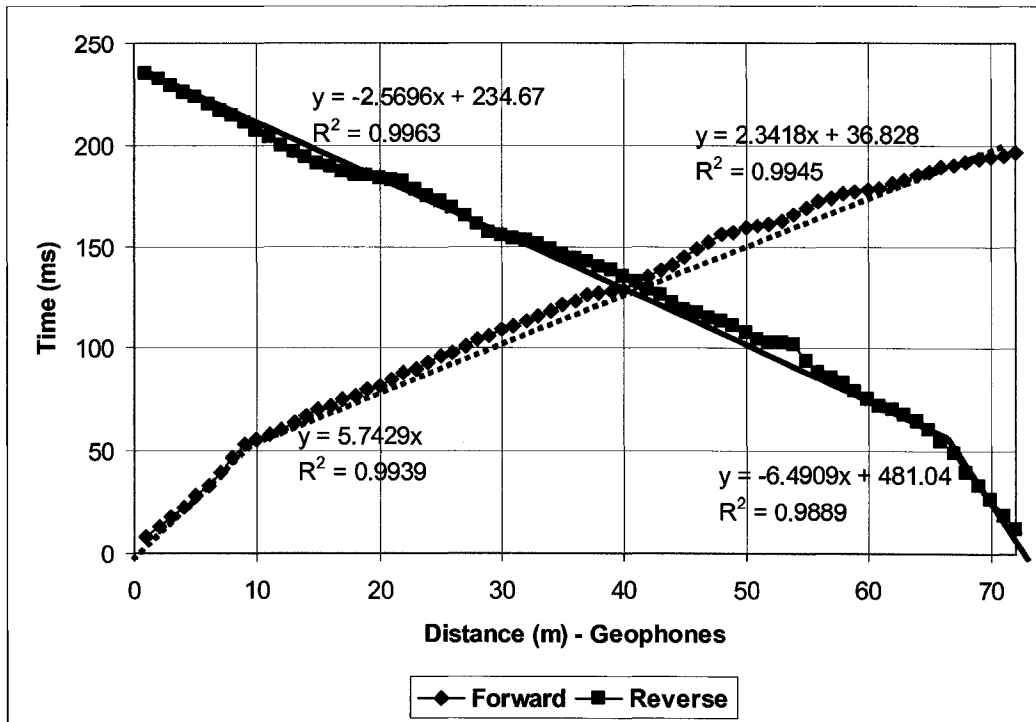


Figure 23: Forward and reverse method for summer data

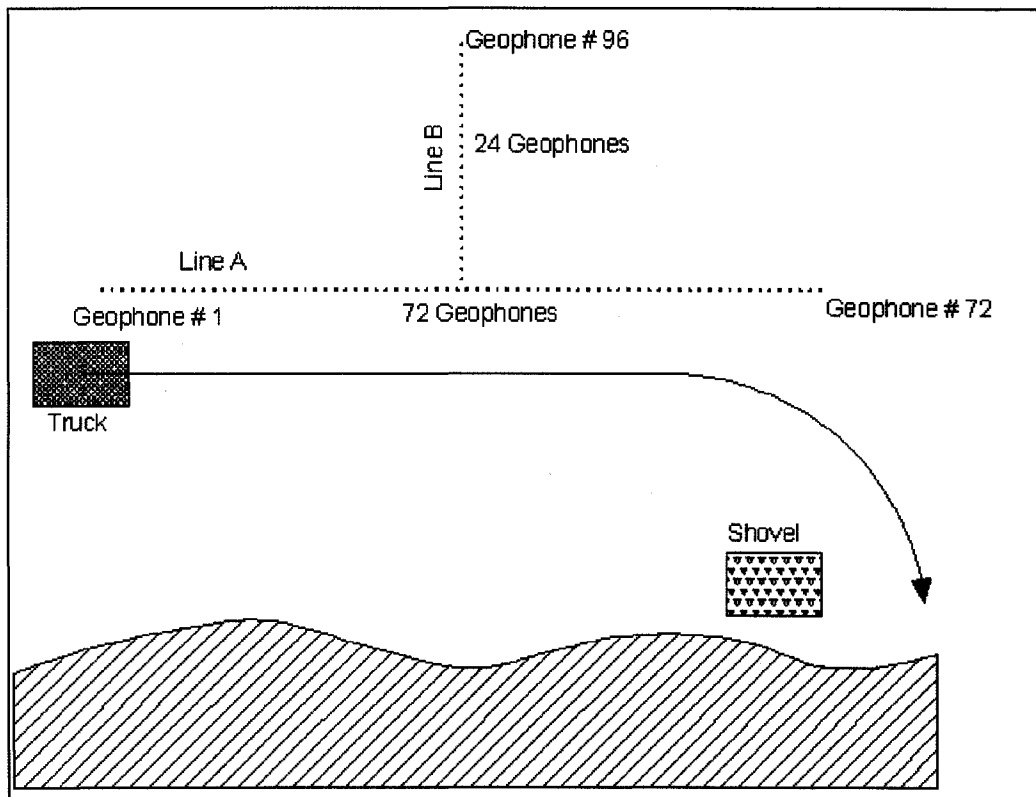


Figure 24: Route of trucks

### 3.1.1.2.5 Winter refraction data

In the case of winter data acquisition where the ambient temperature was  $\sim -38^{\circ}\text{C}$ , the top layer of oil sand was found to be frozen to a depth of several metres, yielding higher velocities compared to those beneath. No reliable refraction was discernable from this data, and the spacing of 3 parallel lines of 24 geophones at 3-metre intervals was not enough to attain refraction for the stiffer ground. Aliasing was seen in any given set of data, with high noise levels present even in the geophones farthest from the shot points. The surface waves were very strong in this frequency range, as shown in Figure 25. However, the direct waves gave a range of velocities for the frozen layer of 1500 to 1700 m/s. Figure 25 illustrates the direct wave of a winter data set.

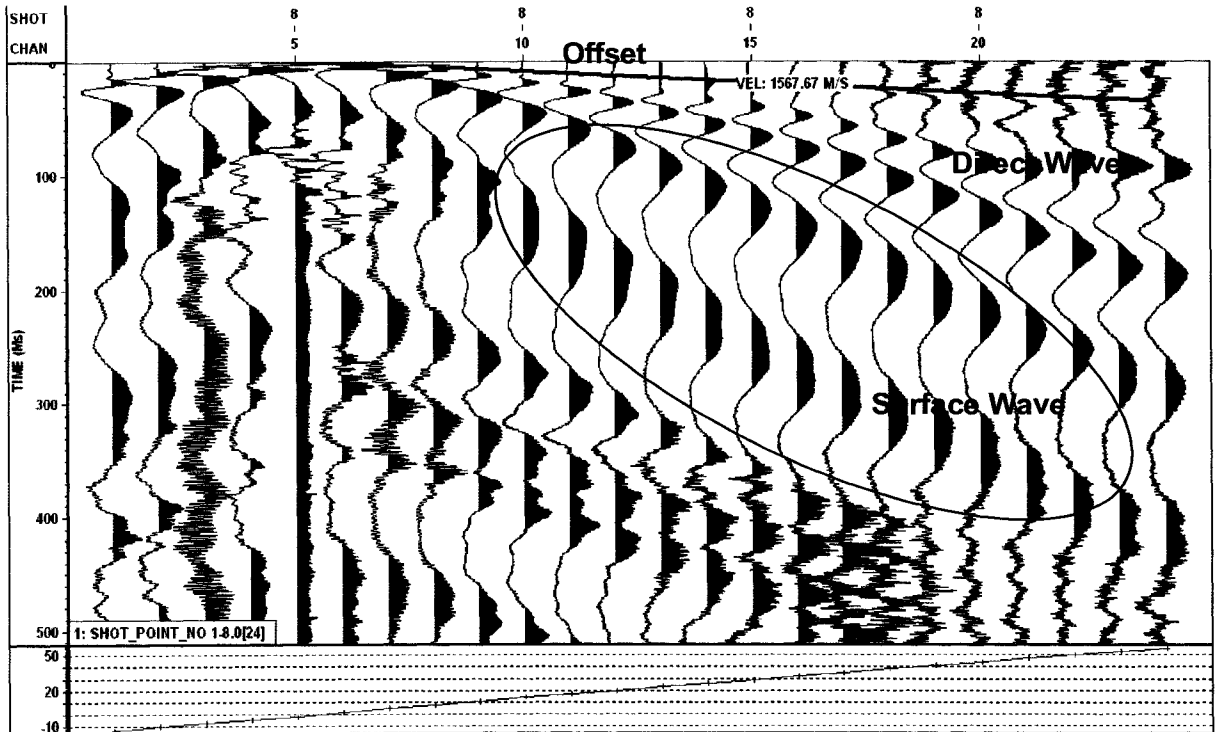


Figure 25: Winter surface and refraction data

### 3.1.1.3 Passive data acquisition

Winter ground performance data due solely to truck motion were assessed for a simple truck motion by using a 3-line array of geophones. The purpose of the test was to

- Evaluate the interaction between the ground and mobile mining equipment under firm ground conditions.
- Show that seismic equipment and seismic survey techniques were appropriate to monitor the interaction.

Figure 26 shows the winter test set-up using 3 parallel lines, each having 24 geophones with an instrument spacing of 3 metres, giving a test array of 72 metres length. The sole source of vibration was set as a single truck passing through the array, so that a few seconds before the truck reached the array, the geophones would be manually activated to start recording data. As might be expected, the middle line B had greater amplitude, compared to that of lines A and C (see Figure 27). Figure 27 shows the shot gather for single run of truck through the geophones path. The results also showed that the rear of the truck put more energy into the ground due to the truck's approximately 2/3:1/3 load distribution.

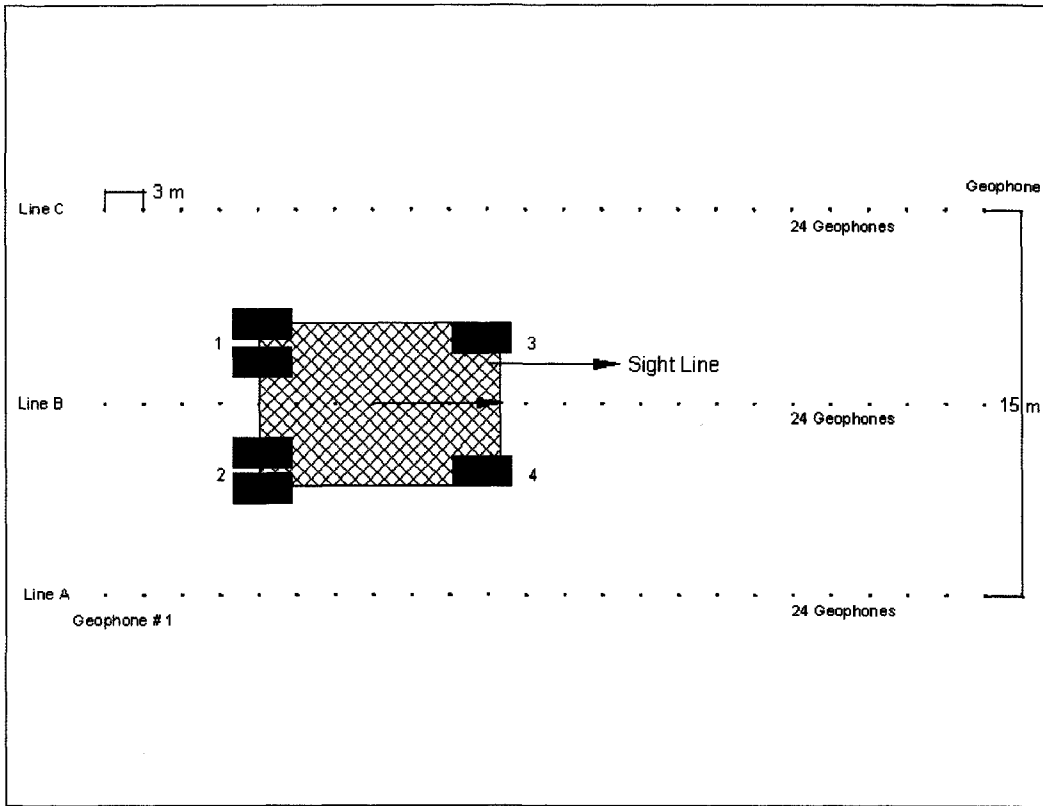


Figure 26: Test set-up for passive winter data acquisition

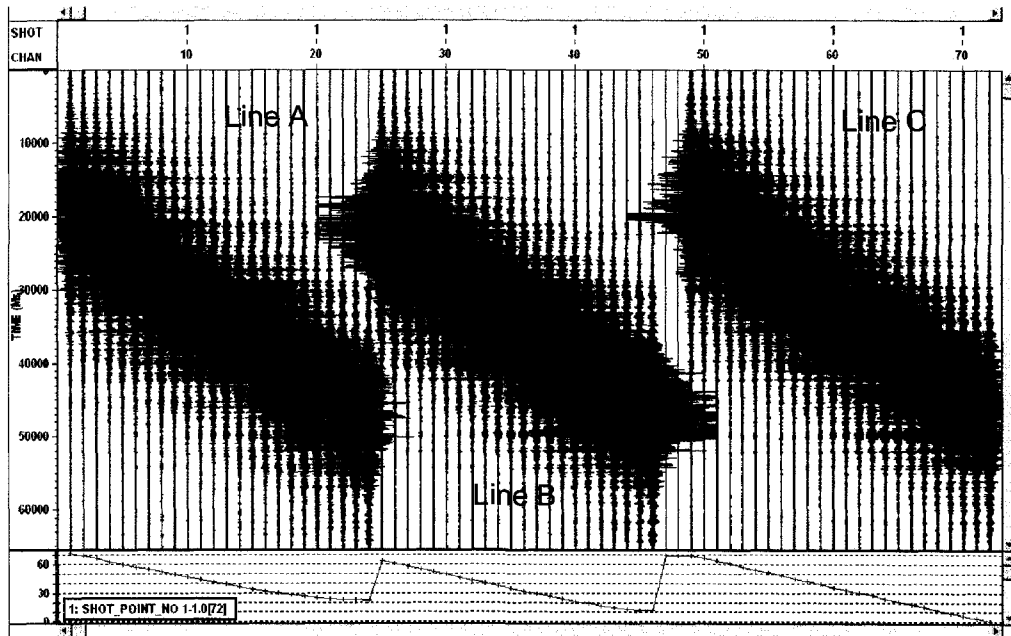


Figure 27: Passive data shot gather for a single run of truck

### 3.1.1.3.1 Winter passive data analyses

The first information evident from the passive data is the truck velocity. As Figure 28 shows, the truck velocity is the slope of the inclined line. Figure 29 illustrates the velocity of the truck for the entire test (50 runs).

As was expected, the passive data show that a truck travelling at a slow velocity has a higher band of amplitude to that of a faster truck yielding a reduced band (see Figure 30). An algorithm was written in MATLAB to normalize this width effect via summing up, the widths of the amplitudes "W" as shown in Figure 30. The geophones' amplitude from units in the same column was calculated, (e.g., 1, 25 and 49) giving an accurate correlation between the velocity of the truck, and the sum of the amplitudes. Figure 31 shows the correlation between truck velocity and the sum of the amplitudes.

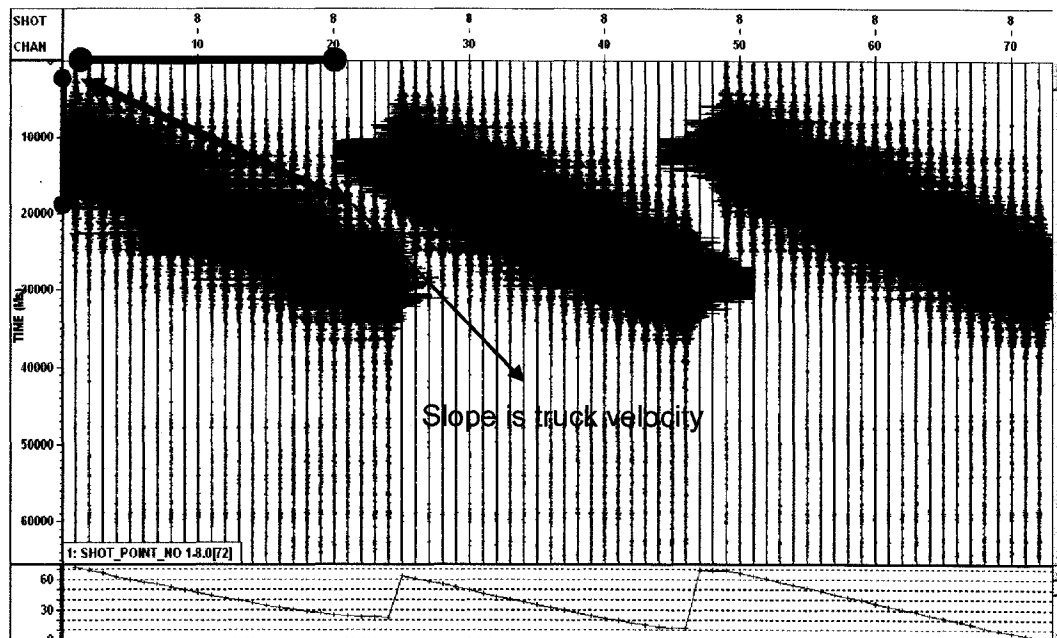


Figure 28: Truck velocity from passive data

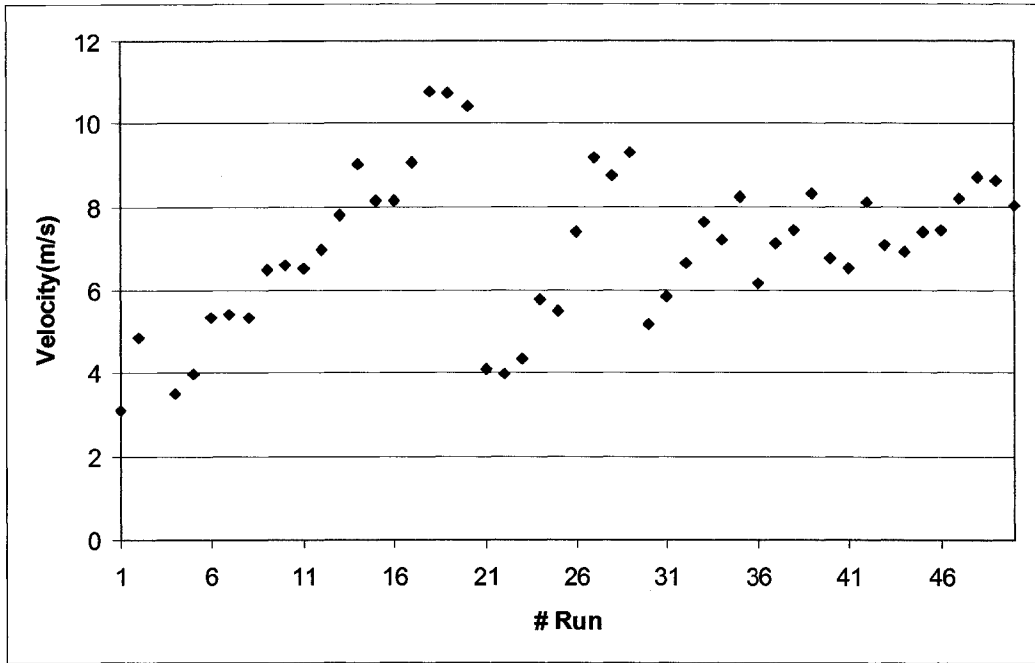


Figure 29: Simple truck velocity for winter passive data

From Figure 31, it can be concluded that trucks with higher velocity, transfer more amplitude or energy into the ground. The different time between two consecutive runs is called relaxation time. The relaxation times for 50 the runs performed for the test were not constant. Since oil sand in summer behaves like a viscous elastic material, one important parameter related to ground deformation is relaxation time. However, the tests did yield 4 levels of time gaps between runs (see Figure 32).

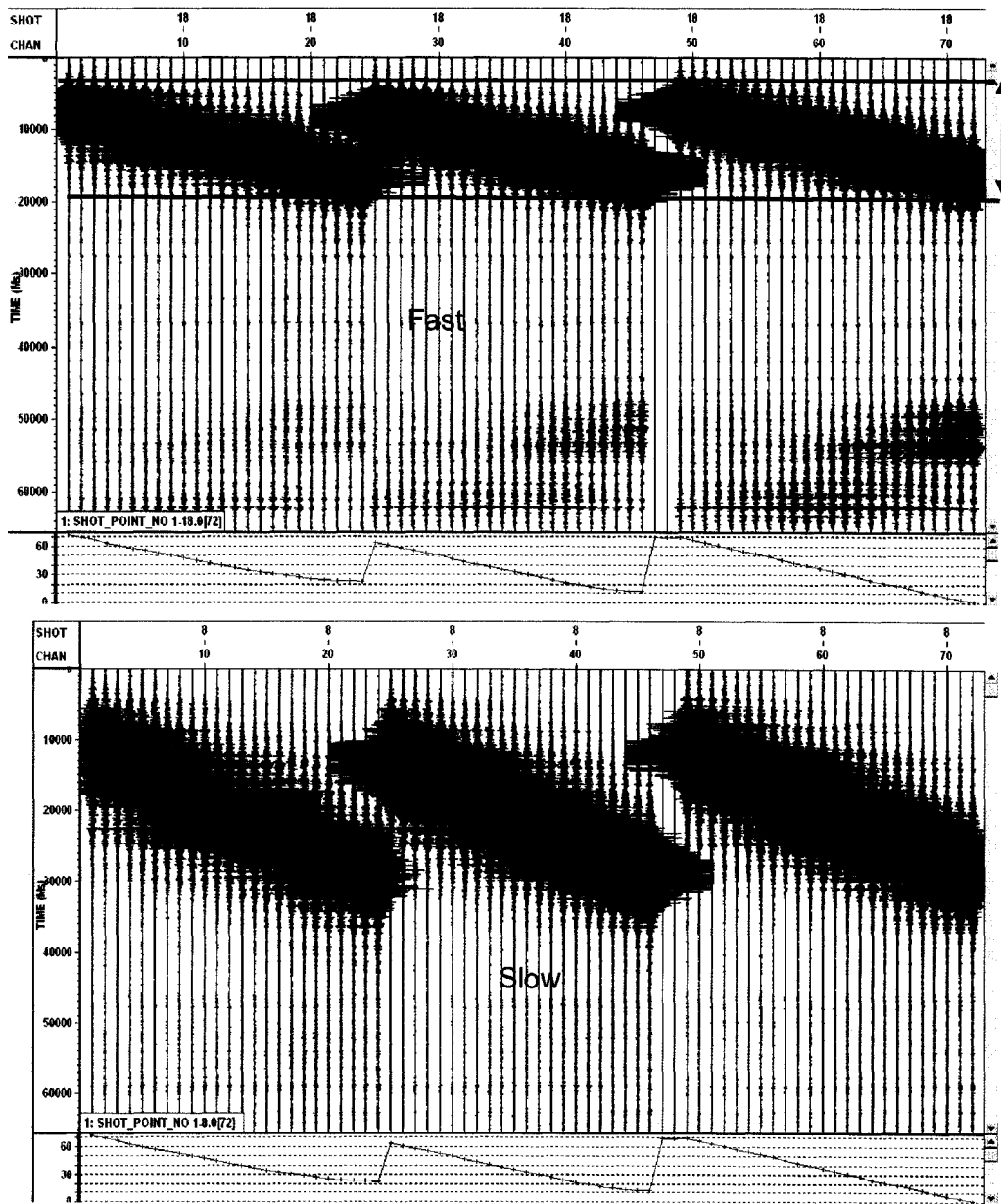


Figure 30: Slow truck velocity vs. fast truck velocity

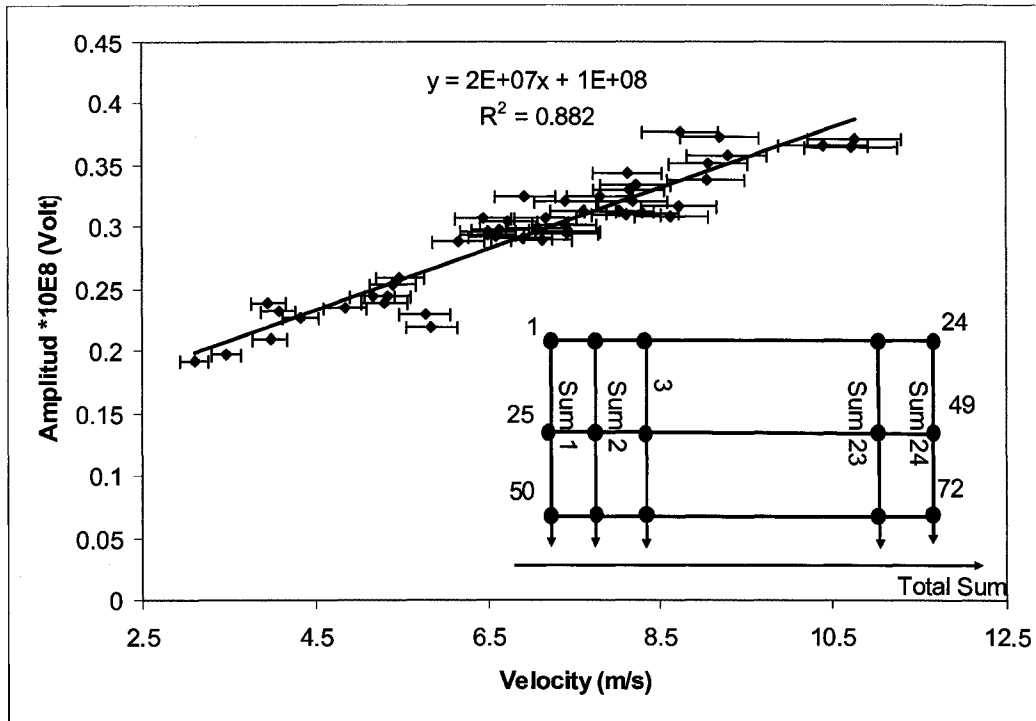


Figure 31: Sums of amplitudes for each array position

A sense of the extent of ground deformation can be achieved, by normalizing the sum of the amplitude across the width (from the summing up procedure) by sum of total amplitude for the same run. The more amplitude or energy transferred into the ground, the lower the ground stiffness. Less energy corresponds to harder ground conditions. A study compiled from each of the 4 relaxation groups shown in Figure 30, proved that after a number of runs-for each group, the total energy first increased, corresponding to the softened ground. However, after further runs, the energy suddenly dropped to a constant value. This leads to the conclusion that after several runs, the ground reached a stable condition and higher stiffness. Unlike, results of energy increase being parallel for all groups, this condition was certainly more predominant in group 4 than in group 2. In Figure 33 different lines represent different ground stiffness. Another interpretation of Figure 33 is that parameters could be important in the degree of softening are truck velocity, ground profile and relaxation time.

A major goal of this research was to try and enable the onboard truck's information system (VIMS) to predict poor ground conditions. The seismic-data-acquisition system was set at 250 Hz (1/250 Hz= 4 Ms). However, this setting

was mismatched with the OEM on-board data-acquisition system (VIMS) at 1 Hz, so that making a correlation between the two sets was difficult. However, studying the trends of the rack, pitch and roll (Joseph 2003) from the predominant truck motion provided some correlation. The difference in energy was determined via the truck's sum of front-to-back energy (amplitudes), from the seismic data. Figure 34 shows that the rack yielded a reasonable shape correlation, indicating an influence on the ground.

Figure 35 provides a closer look at the passive data. The front-to-back motion is evident. Generating a parabola that moves back and forth depends on the front-to-back truck-tire cyclic motion. However, writing an algorithm to separate the front and back motion or to distinguish the path of this apex is difficult for several reasons. The time of the front-to-back motion depends on the velocity, which may be extracted from the passive data, but only as an average value. Also, the start time is manually activated, so that distinguishing the exact time of passing adjacent to the first geophone is very difficult.

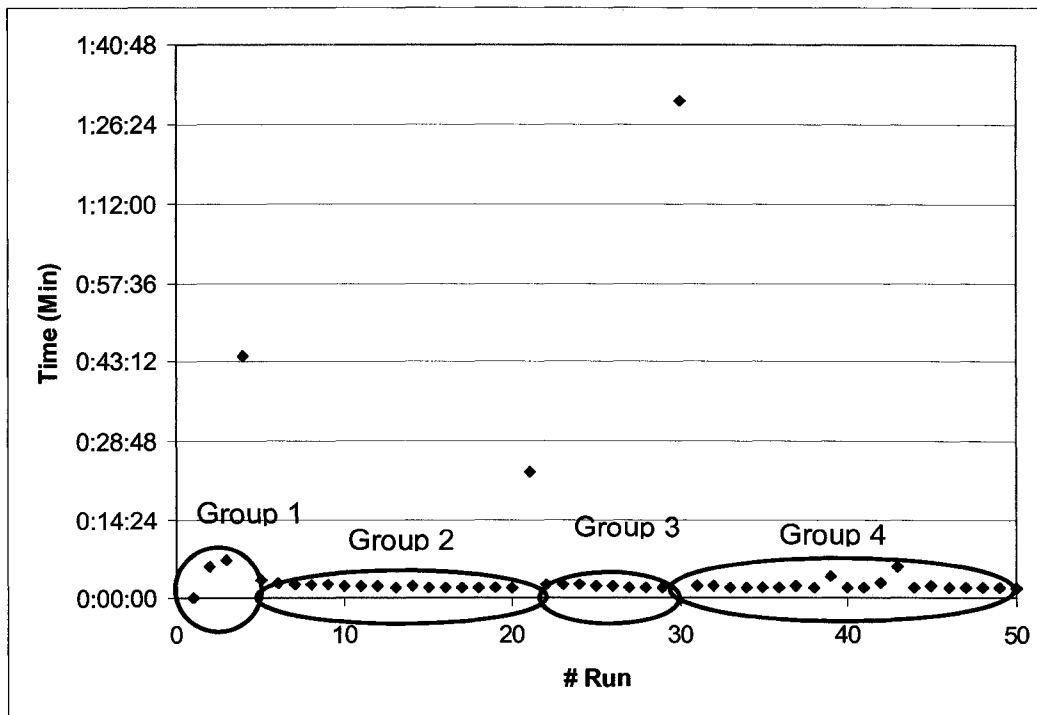


Figure 32: Relaxation time between runs

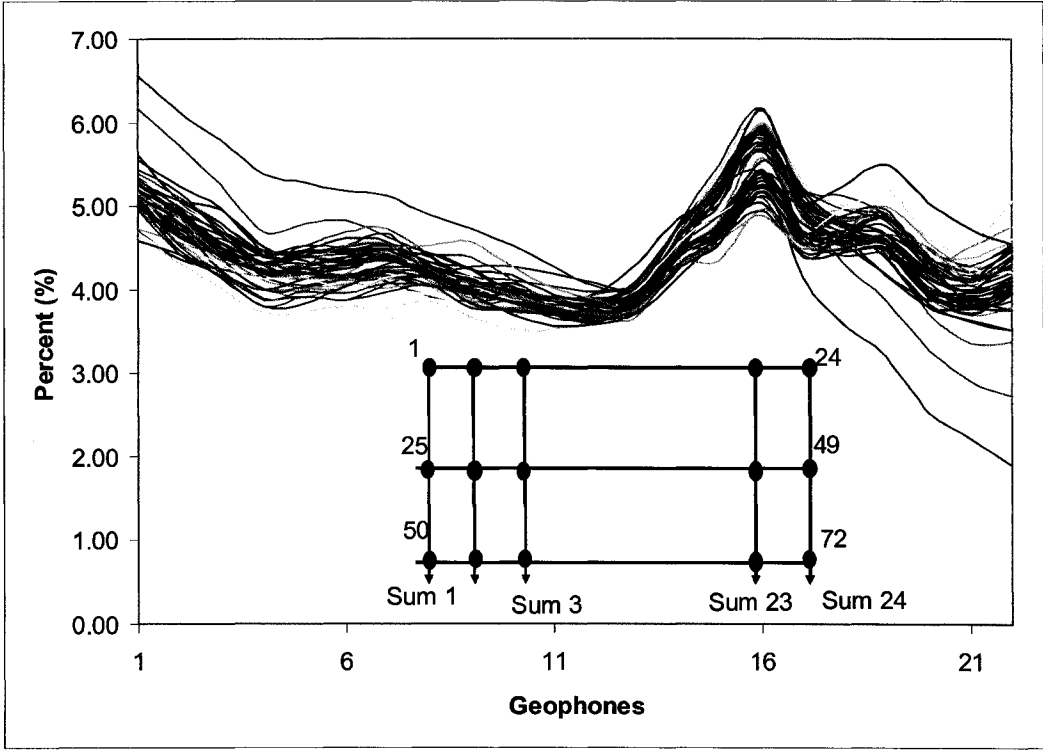


Figure 33: Comparing the amplitude normalization for different runs

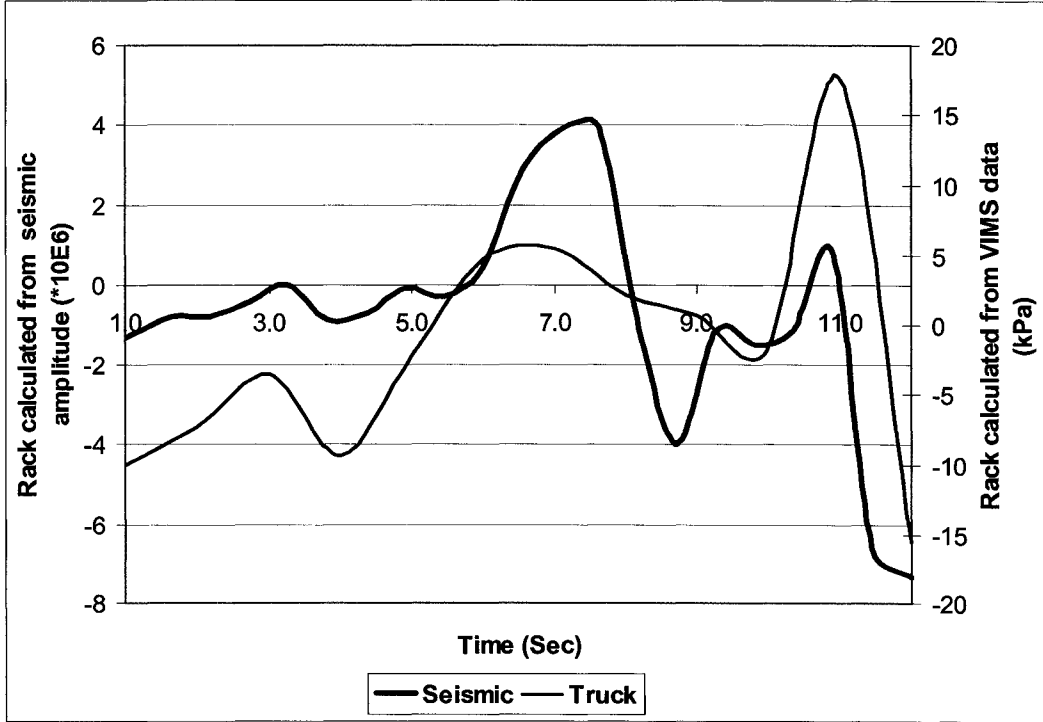


Figure 34: Comparing the seismic data and VIMS data

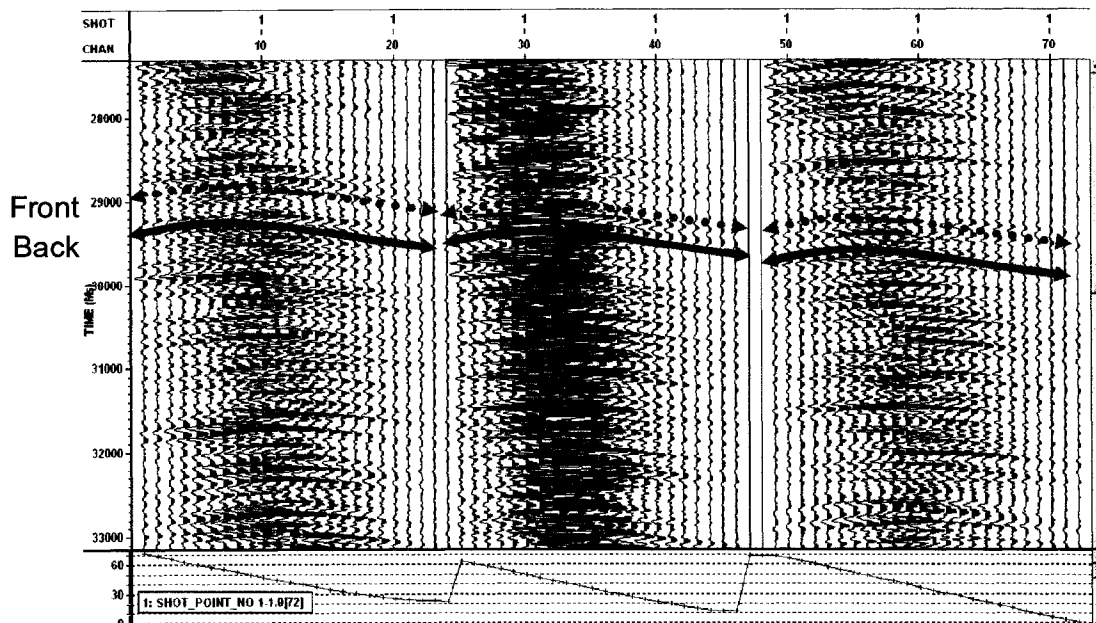


Figure 35: Closer view of the passive data

### 3.1.1.3.2 Summer passive data

Ninety-six geophones, 72 in one line and 24 in a perpendicular line were set up for passive and refraction data acquisition (see Figure 36). The distance between each geophone was set at 1 metre, with trucks passing within a 1 to 2 m distance from the line.

The mining activity adjacent to the passive data-collection site produced high levels of noise, creating additional challenge when evaluating the data. Three locations of varying soft ground conditions were evaluated. The tests on day 1 were at a location where the ground had low bitumen content (6% bitumen). The tests on day 2 were at a location with high bitumen content (13% bitumen), and on day 3 were at a location with medium bitumen content (10% bitumen). At all 3 locations, the ambient temperature reached +28°C. The low, medium, and high bitumen areas had 6-8%, 8-12%, and more than 12% bitumen content, respectively.

The sum of the amplitudes in line A of the 72 geophones for trucks passing was calculated for the different test days (see Figure 37-Figure 40). The same

phenomenon seen in the winter data was also seen in the summer data: the sum of the amplitudes increased first and then suddenly decreased after a number of passing cycles by mobile mining equipment. Also, on day 1, the sum of the amplitudes increased with increasing truck velocity.

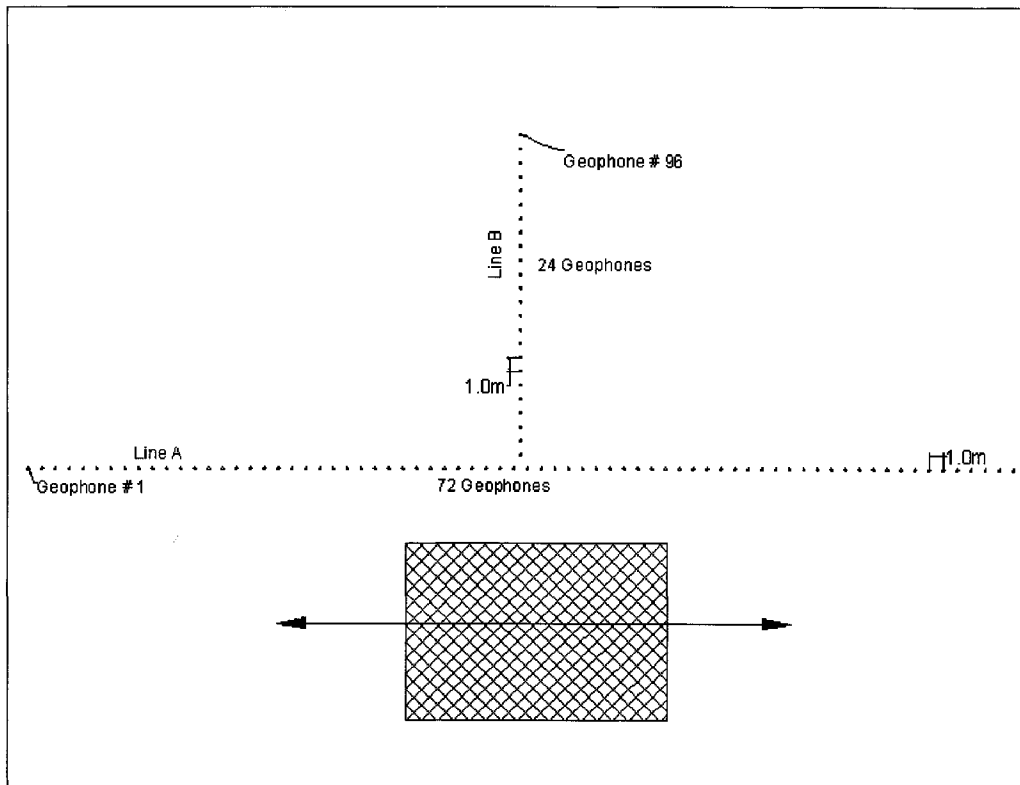


Figure 36: Summer test set-up

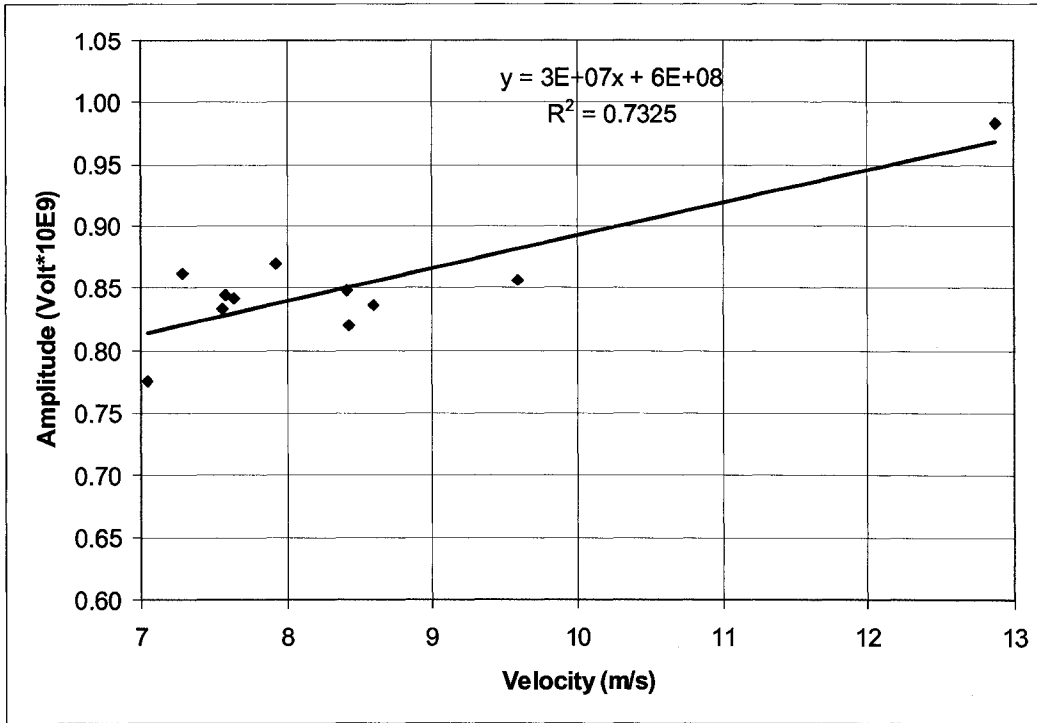


Figure 37: Sum of amplitude vs. truck velocity (loaded truck on day 1)

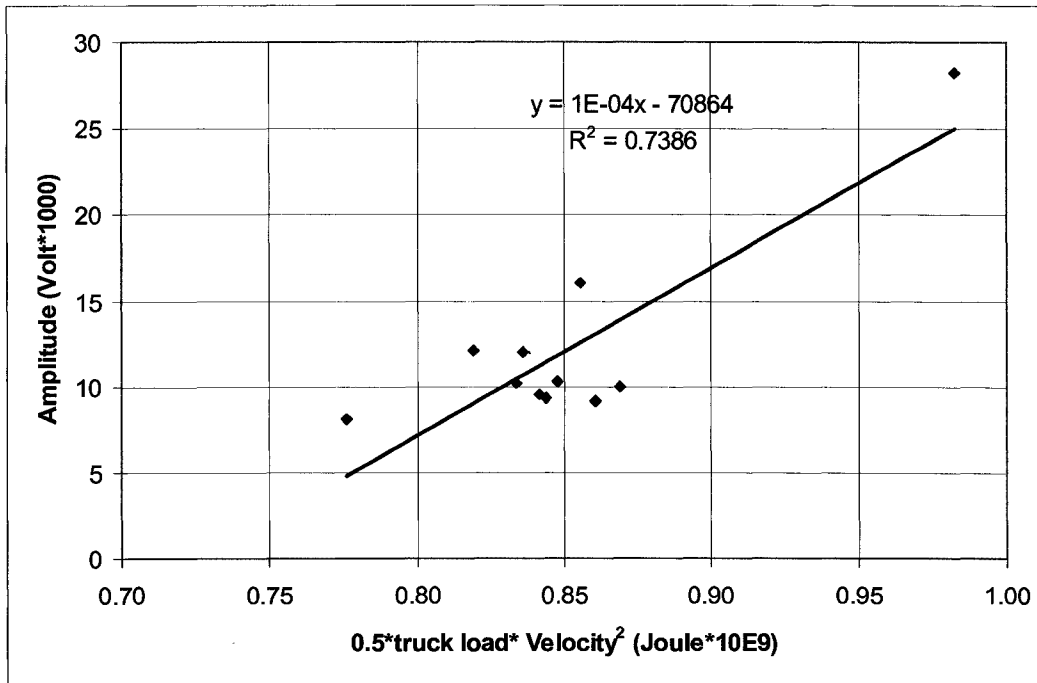


Figure 38: Kinematics energy vs. amplitude for load trucks

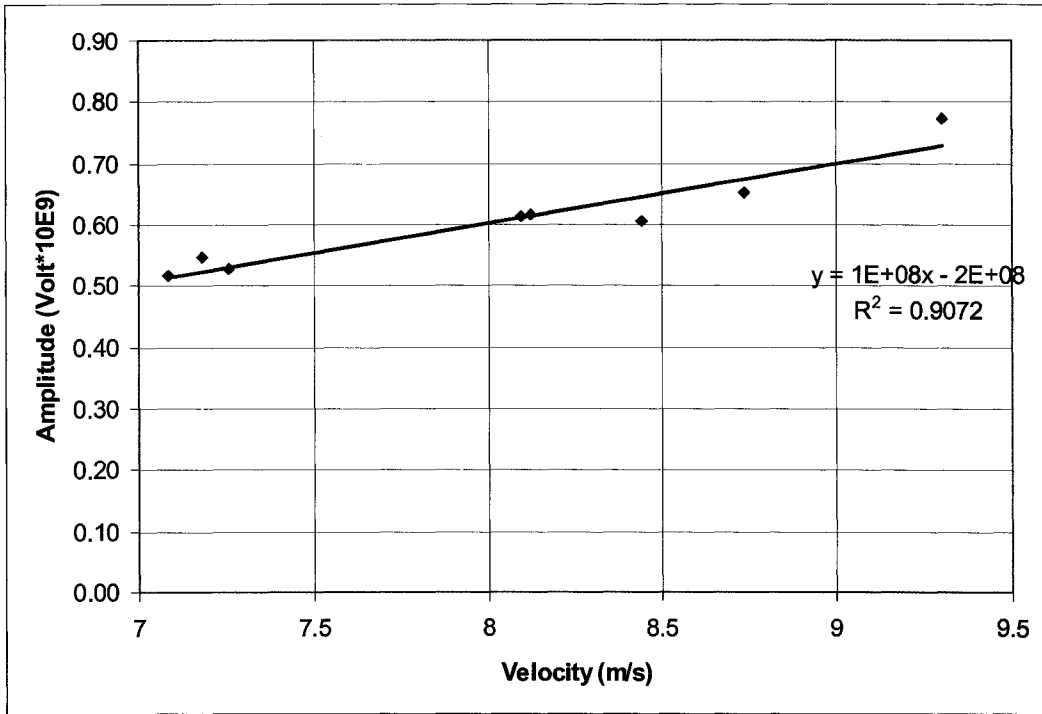


Figure 39: Sum of the amplitude vs. truck velocity for an unloaded truck day 1

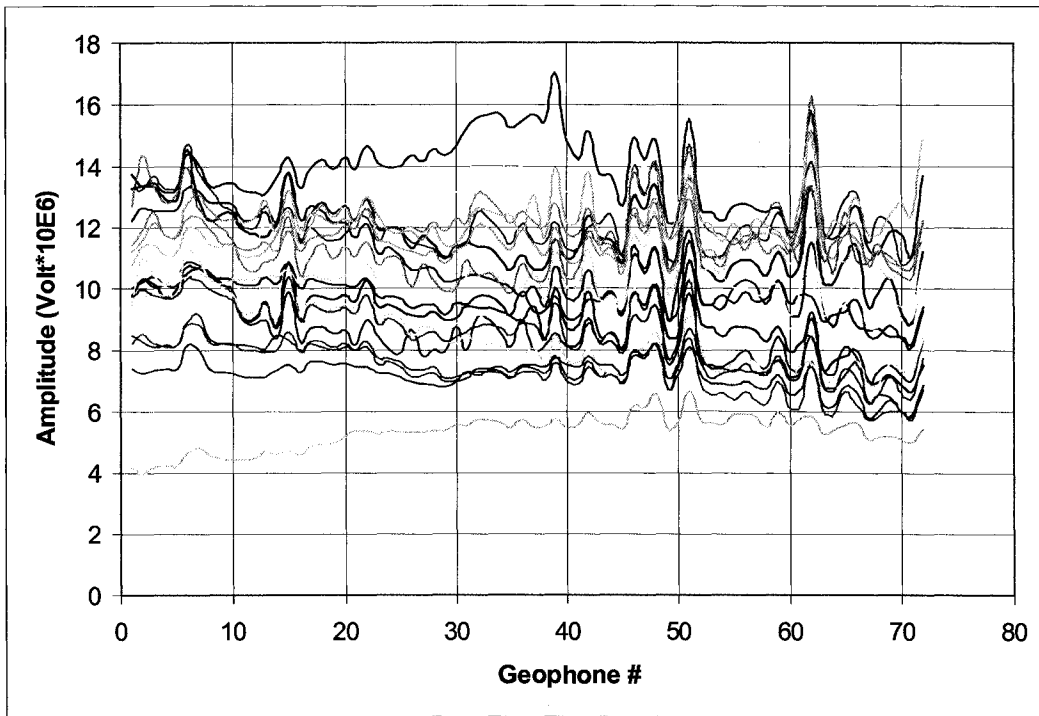


Figure 40: Changing sum of amplitudes in each geophone

On day 2, which ground had very soft conditions, the data were insufficient to identify a trend for the amplitude versus the velocity. The plot is different to the others, as a mixed fleet was operating in this area, instead of only a single truck size, as shown in Figure 41. One reason why no trend could be identified for day 2 was that before the truck reached the end of the path in order to prepare for the loading position, its distance from the geophones' line increased. For this loading truck, only two data points were available.

Figure 42 and Figure 43 show the sum of geophones amplitude versus truck velocity for day 3, which had medium ground conditions. For this day, the mixed fleet made interpretation difficult. Figure 44 shows all the data for 3 days for the loaded and unloaded trucks.

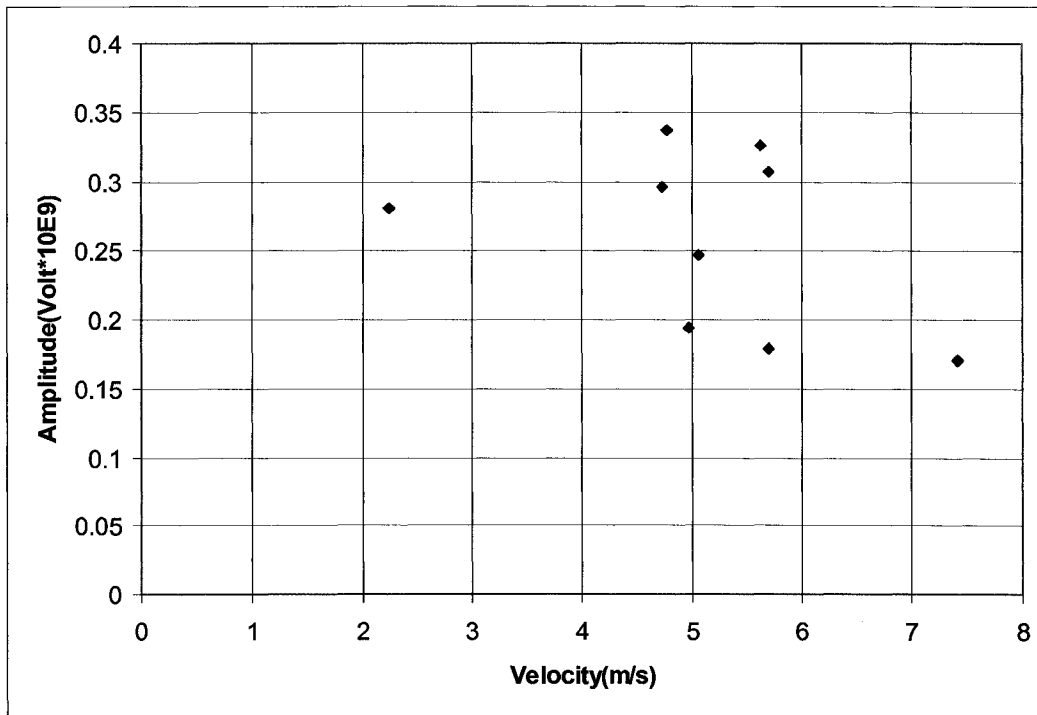


Figure 41: Unloaded truck velocity vs. sum of amplitude for day 2

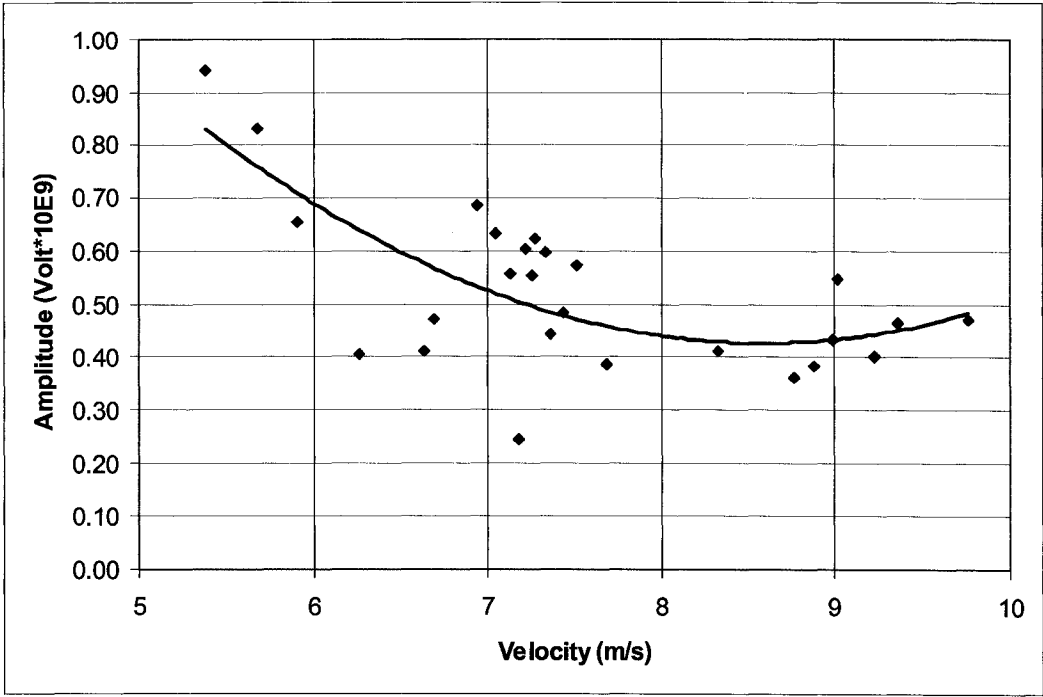


Figure 42: Unloaded truck velocity vs. sum of amplitude for day 3

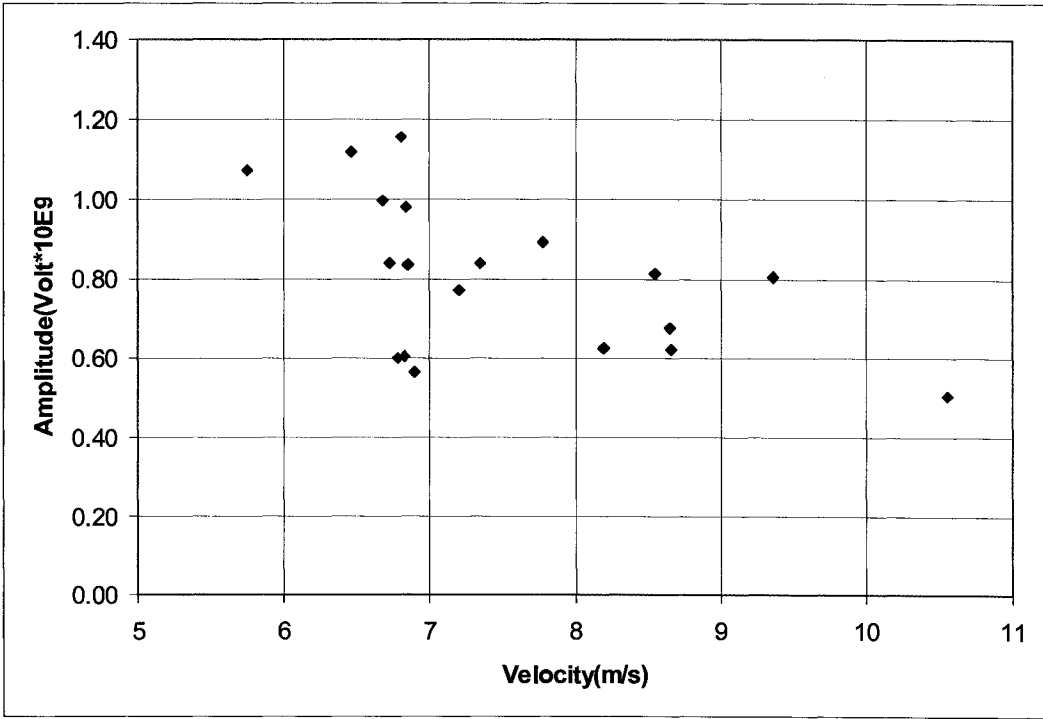


Figure 43: Loaded truck velocity vs. sum of geophones amplitude for day 3

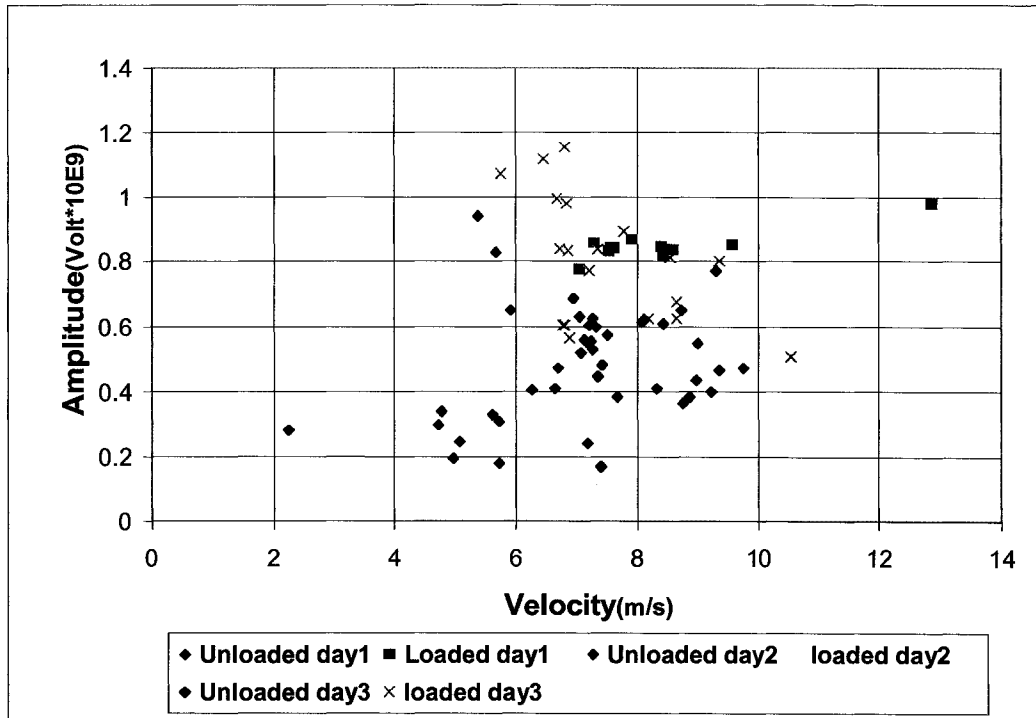


Figure 44: Loaded and unload trucks velocity vs. sum of amplitude for the 3 days

### 3.1.2 Determination of ground stiffness by using a geophysical technique

#### 3.1.2.1 Introduction

Characterizing the near subsurface via geophysical methods has been of great interest in recent years as these methods are cheaper and faster than other methods. Being able to determine a modulus-depth profile without the aid of boreholes via surface wave geophysics would be highly advantageous. The most powerful tools for evaluating the subsurface are the spectral analysis of surface waves, focusing on non-intrusive Rayleigh waves (Matthews et al. 1996, Haegeman 1999).

Knowing the properties of soil layers and having a profile are the key factors in analysing an overlying dynamic loading source. The spectral analysis of surface waves (SASW) is used primarily for the evaluation of subsurface wave velocity profiles. The results obtained via this method are representative of the average

properties of a relatively large mass of soil. This method can be very cost-effective for investigations (Haegeman 1999, Ganji et al. 1998).

An alternative technique for determining ground stiffness is continuous surface wave (CSW) analysis, which relies on the propagation properties of vertically polarised seismic surface waves, where the penetration depth by a surface wave is dependent on the wave length and frequency (Moxhay et al. 2001).

Shear wave velocity is a factor in identifying the shear strength of a given formation. Rayleigh wave dispersion has been used as a method for evaluating the shear modulus of near-surface materials. Using Rayleigh waves to obtain the shear wave velocity is difficult because two steps are involved: finding the dispersion relationship for the Rayleigh wave and applying the inverse procedure to convert the dispersion curve to the shear wave velocity versus the depth (Beaty & Schmitt 2003).

### **3.1.2.2 Body and surface waves**

Ground motions due to energy sources are called “seismic waves.” Identified close to the source, most ground motion is momentary. Waves can be divided into two categories: body waves and surface waves. P and S waves are known as “body waves.” Love and Rayleigh waves are known as “surface waves.”

- **Body waves:**

Body waves travel along a path through a continuum. P waves are compression waves involving volumetric changes like sound waves in a fluid. S waves or shear waves produce shearing deformation with no volumetric change. This type of wave cannot propagate in a fluid (fluids cannot bear shear waves). The motion of S waves can be in two directions: vertical or horizontal. Vertical and horizontal waves are known as SV and SH waves, respectively. The direction of the particle motion is relative to the propagation direction. Figure 45 shows the types of motion for P and S waves in media.

- **Surface waves:**

Raleigh waves involving wave motion are confined to and propagate along the surface of the ground. Love waves are formed in a bounded body with layered material properties. Both waves result from the interaction of P and S waves. Raleigh waves are produced by the combination of P and SV plane waves. For generating Raleigh waves, a free surface and P-SV waves are sufficient. The particle motion of surface waves is shown in Figure 45 (Lay 1995, Shearer 1999).

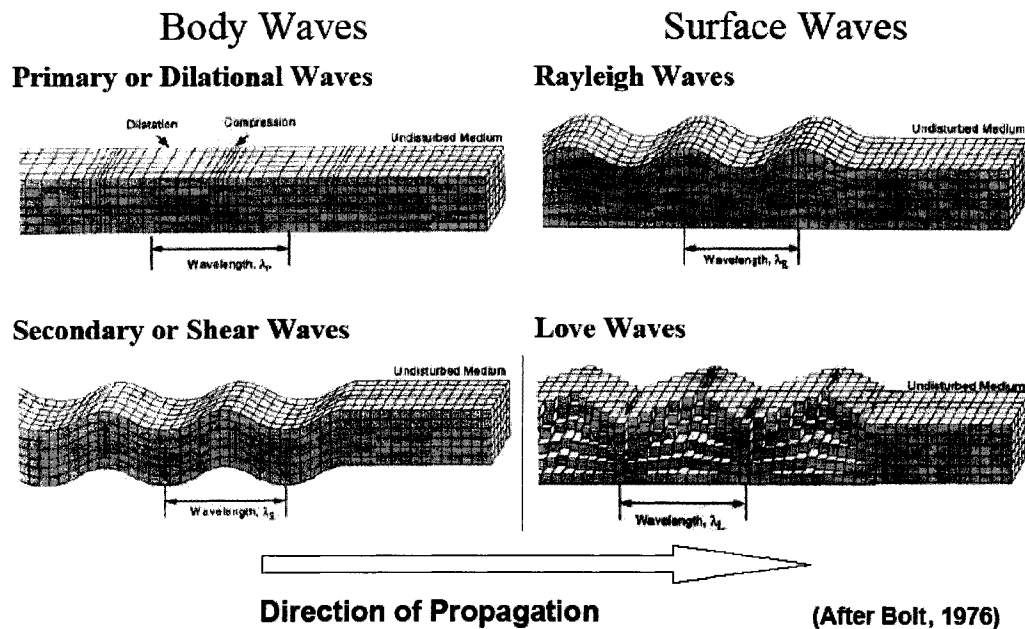


Figure 45: Particle motion of P, S, Love and Rayleigh waves (from Shearer 1999)

### 3.1.2.3 Dispersion

In an isotropic half-space, all surface waves show dispersion. Dispersion is an apparent velocity along a surface and is dependant on the frequency. The phase velocity of a wave is the rate at which the phase of the wave propagates in space. One particular phase of the wave could be selected (for example, the crest), and it would appear to be traveling at the phase velocity; however, the group velocity of a wave is the velocity at which the overall shape of the wave's amplitude (known as the "envelope of the wave") propagates through space. Figure 46 shows the difference between phase and group velocities (Shearer

1999). The phase velocity of the wave for each frequency is  $c(\omega) = \omega/k$ , and the group velocity or energy velocity is  $U(\omega) = d\omega/dk$ , where  $\omega$  is the angular frequency, and  $k$  is the wave number. The overall appearance of the surface wave dispersion changes as it propagates. Each frequency component has an amplitude  $A(\omega)$  and initial phase  $\Phi_0(\omega)$  determined by the excitation of the source and medium. Figure 47 shows the increase of the waveform dispersion as the wave propagates. Figure 47 was constructed from a simple shot gather, that distance in the vertical axis is the geophones position on the ground from shot point and the horizontal axis is the time of arriving waves at each geophone.

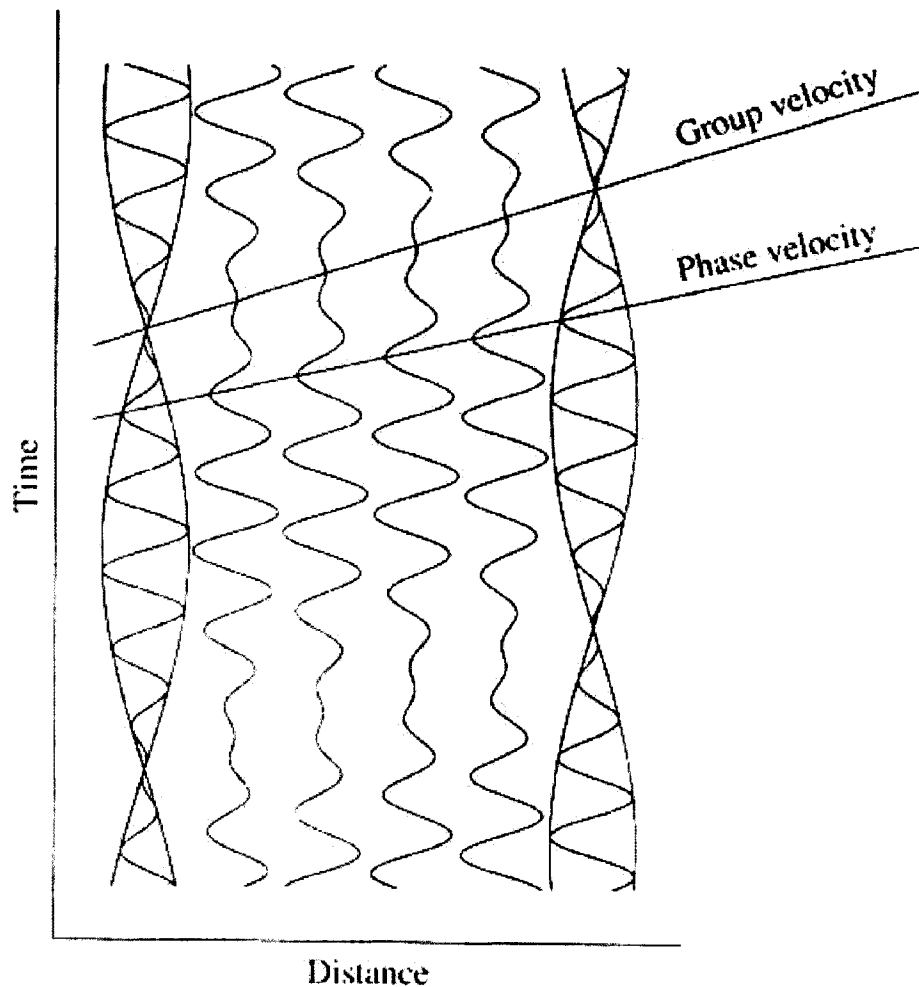


Figure 46: Phase and group velocity (from Shearer 1999)

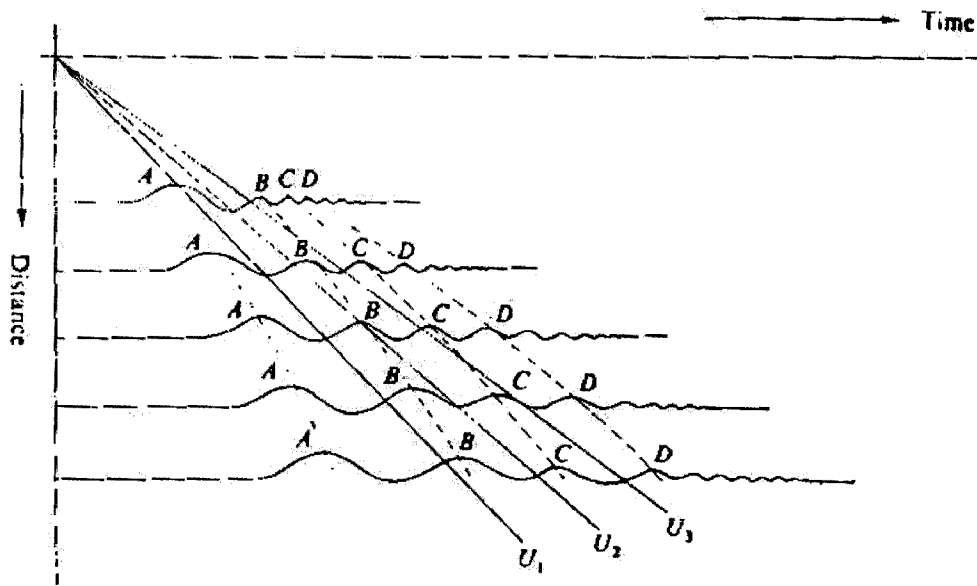


Figure 47: Dispersion of waveform (from Shearer 1999)

As the frequency is known, the wavelength is determined by dividing the velocity by the frequency. As most ground materials have Poisson's ratios in the range of 0.25 to 0.48, the approximation of Rayleigh wave velocities as shear-wave velocities causes less than a 10% error. The assumption that the depth of investigation is equal to one-half of the wavelength can be used to generate a velocity profile with depth. Consider a simple case: the vibrator is a surface wave source with known frequency  $f$ , and two geophones are positioned a distance  $d$  from each others. The phase difference  $\Phi$  in radians is measured, and then  $\lambda$  calculated:

$$\lambda = (2\pi d) / \Phi \quad \text{if } d \text{ is less than } \lambda$$

$$\lambda = (2\pi d) / (2\pi n + \Phi) \quad \text{if } d \text{ is greater than } \lambda \text{ and } n \text{ is an integer.}$$

The velocity of a Rayleigh wave is  $V_R = f\lambda$  (Matthews et al. 2000).

### 3.1.2.4 Determination of stiffness with Rayleigh waves

One technique uses the surface dispersion curve to determine the near-surface stiffness. Usually the dispersion curves for Rayleigh waves are used to examine the variability of near-surface properties up to 15 m depth. As was mentioned

previously, Rayleigh waves travel along the earth-air interface. Rayleigh waves usually contain more energy than body waves and also provide substantial information on shear wave velocity, identifying structures of the near-surface (Beaty 2000).

The dispersion nature of Rayleigh waves and the velocity depend on the frequency. Lower frequencies, or longer wavelengths, have deep penetration, which is appropriate for determining the depth stiffness (these phenomena contain information about the deep layers). On the other hand, high frequencies or lower wavelength Rayleigh waves are appropriate for determining the upper layer stiffness. A rule of thumb is that the depth of the relation of Rayleigh waves is one-half of the wavelength. Dispersion curves show the velocity of the wave at each wavelength or frequency. These can be inverted to obtain the shear wave velocity profiles of an area. One method to get dispersion curves from Rayleigh waves is to carry out  $\tau$ - $p$  transforms on the data, followed by a one-dimensional Fourier transformation along the  $\tau$  direction.  $\tau$ - $p$  transforms essentially carry the sum of the amplitudes along a line in the offset-time domain (seismic data) with intercept time  $\tau$  and slope  $p$  called the "slowness" (slowness is the inverse of velocity). This sum will map onto a point ( $\tau$ - $p$ ). After the dispersion curve has been attained, it must be inverted to a shear wave velocity profile. Figure 48 shows the sequence of obtaining the dispersion curve for the seismic data (Beaty 2000, Matthews et al. 2000).

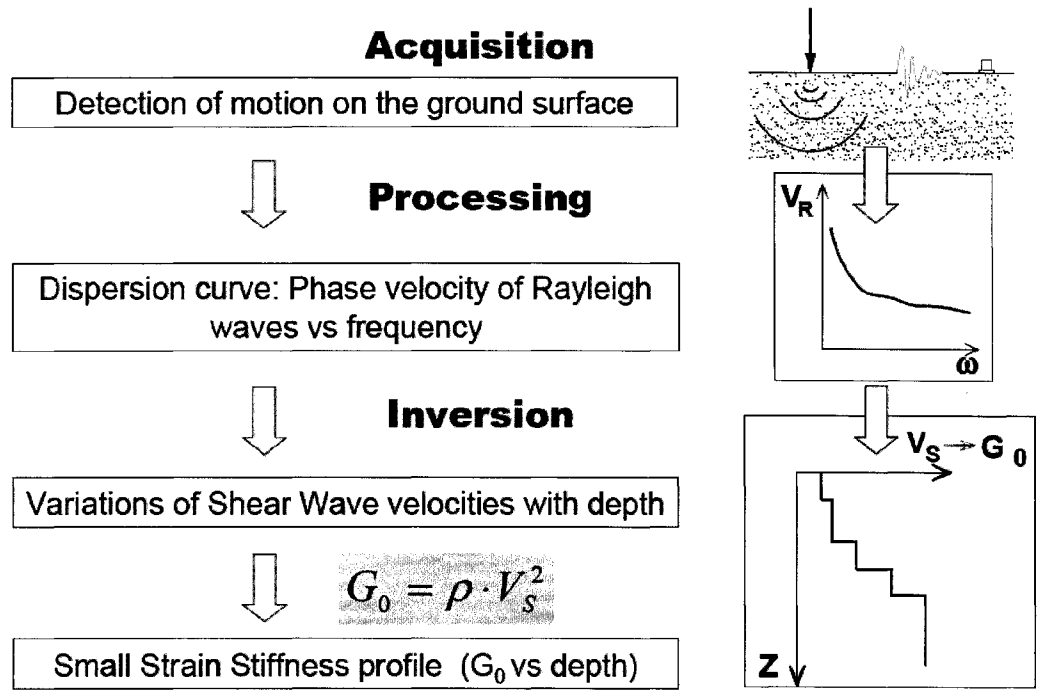


Figure 48: Sequence of obtaining Shear Wave velocities (from Matthews et al. 2000)

The Spectral Analysis of Surface Waves (SASW) is a technique developed by the engineering community for geotechnical purposes for the non-destructive testing of pavements. Figure 49 shows the different waves that can be found in a typical shot. For inversion, the P wave velocity and the thickness of the layer are needed.

Obtaining the phase velocity dispersion curve from Rayleigh waves requires two steps:

1. Isolate the Rayleigh wave from the other arrivals on the seismograph (this step can be performed by windowing the surface data in either the offset-time or frequency-wave number domain (f-k)).
2. Extract the dispersion curve. Different methods can be used:
  - Exploit the phase information of the Fourier transformation of the surface wave (used in earthquake seismology).
  - Use dispersion information to locate the f-k spectrum or frequency-slowness representing the data (used for an array of multiple geophones):

- Perform a  $\tau$ - $p$  transformation on the data followed by one-dimensional Fourier transformation along  $\tau$  direction.
- Pick the peaks associated with the surface wave energy in the  $f$ - $k$  domain.

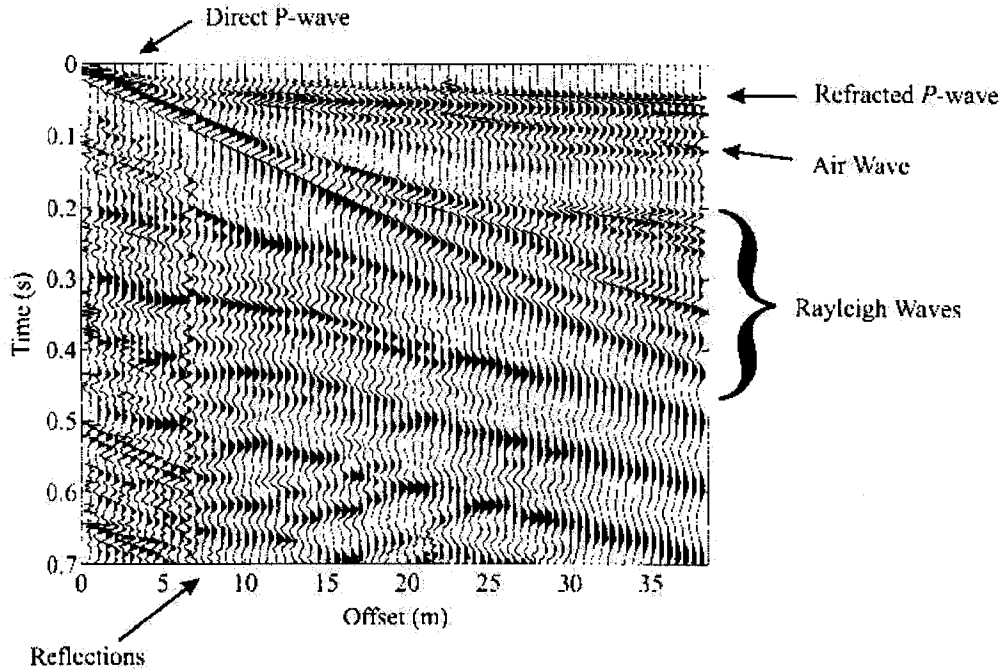


Figure 49: Typical waves in a shot gather (from Matthews et al. 2000)

### 3.1.2.5 $\tau$ - $p$ and $f$ - $p$ transformation for summer and winter data

Both  $\tau$ - $p$  and  $f$ - $p$  transformations were carried out on the winter and summer data. Figure 50 and Figure 51 show the results. Unfortunately, both sets of data were aliased due to the under-sampling time and the geophones offset. There are two different aliasing exist: aliased frequency and spatial aliasing. In order for all frequencies in the input to be correctly resolved, the sampling frequency must be greater than twice the highest frequency in the input waveform. If the sampling criterion holds, Fourier coefficients can be exactly reconstructed from the input waveform. For example: "If an input waveform is sampled at  $F_s$ , then the highest input frequency that can be resolved without aliasing, is  $F_s/2$ , called the Nyquist rate." Spatial aliasing is defined as insufficient sampling of the data along the space axis (distance between geophones). In Chapter 10 of this thesis, more study of this procedure is recommended.

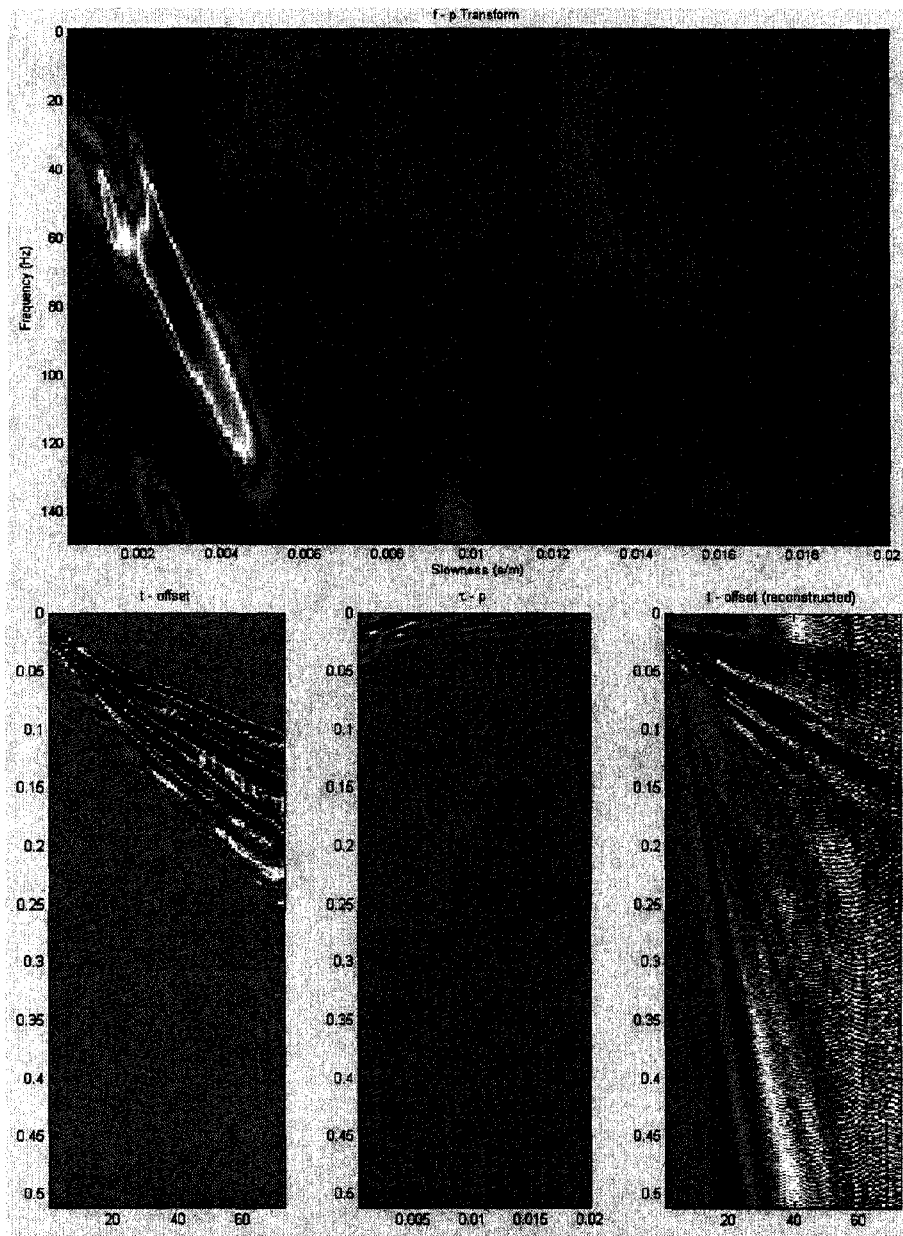


Figure 50: Summer data shot point 1st July 18 f-p and  $\tau$ -p graph

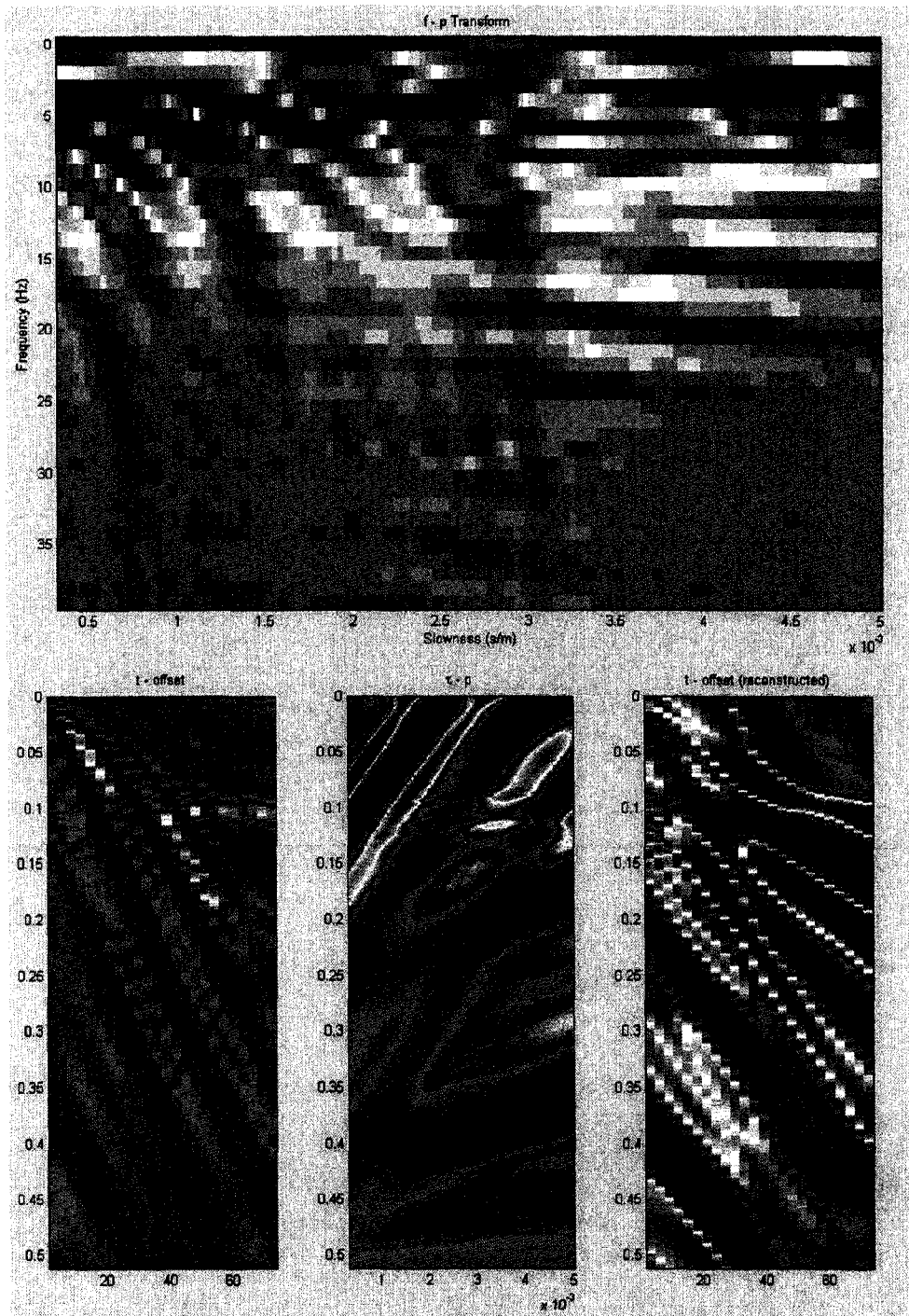


Figure 51: Winter data shot point 1st Jan 31 f-p and  $\tau$ -p graph

## **4 Literature Review**

### **4.1 Introduction**

Previous work on oil sand material behaviour over the past 25 years is reviewed and where appropriate, incorporated into this study's overall evaluation, enhancing the data acquired during the course of this investigation. Oil sand has a sensitive and complicated behaviour that changes according to the viscosity, bitumen content, temperature, and deformation rate. Also, the effect of cyclic loading on the other materials such as rock, soil, and asphalt is reviewed. A different theory for predicting plastic deformation, involving the surface bounding problem and damage mechanics, has been examined.

### **4.2 General soil parameters**

Some of the parameters used in the literature review must be explained (Craig 1996, Murthy 2003).

#### **4.2.1 Coefficient of volume compressibility**

The "coefficient of volume compressibility" is the compression of the soil per unit of original thickness, due to a unit increase of effective stress (effective stress is equal to difference of applied stress and pore pressure), in the load range exceeding the reconsolidation stress. This coefficient is expressed

by  $m_v = \frac{\Delta H}{H_o \times \Delta \sigma'_v}$ , as shown in Figure 52 (Craig 1996). This is a confined

measurement and drained test.

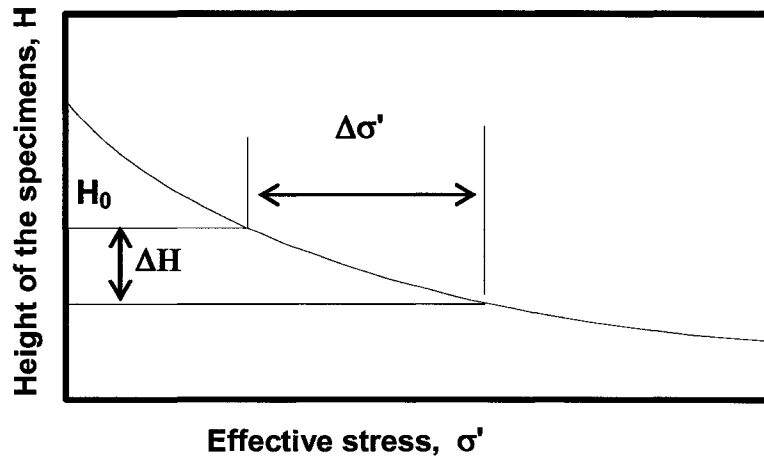


Figure 52: The coefficient of volume compressibility (after Craig 1996)

#### 4.2.2 Coefficient of compressibility

“Compressibility” is the ability of the soil to be deformed and is expressed by means of a coefficient, which is the ratio between a void ratio (void ratio is defined as the ratio of the volume of voids to the volume of solids) decrease from  $e_0$  to  $e$  and an increase in the effective stress. The value  $a_v = \frac{\Delta e}{\Delta \sigma'} = m_v(1 + e_0)$  represents the coefficient of compressibility for the range  $\Delta \sigma'$ , as shown in Figure 53 (Craig 1996, Murthy 2003). This is a confined measurement and drained test.

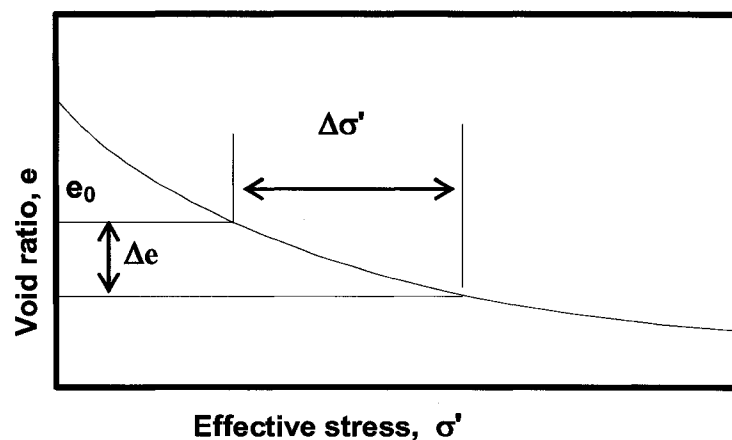


Figure 53: The coefficient of compressibility (after Craig 1996)

### 4.2.3 Compaction

“Compaction” is defined as the decrease in the thickness of a deposit ( $\Delta p = H-h$ ), as a result of an increase in the vertical compressive stress, and is synonymous with the expression "one-dimensional consolidation," as used by engineers.

### 4.2.4 Modulus of deformation or Young's modulus

The modulus of deformation is referred to as the “modulus of elasticity” and is an extremely important characteristic of a material. The modulus is the ratio of stress to vertical strain  $E = \Delta\sigma / \Delta e$ , as shown in Figure 54 (the measure of resistance to elastic deformation). This modulus can also be calculated as the slope of the straight-line portion of the stress-strain curve (Craig 1996, Murthy 2003).

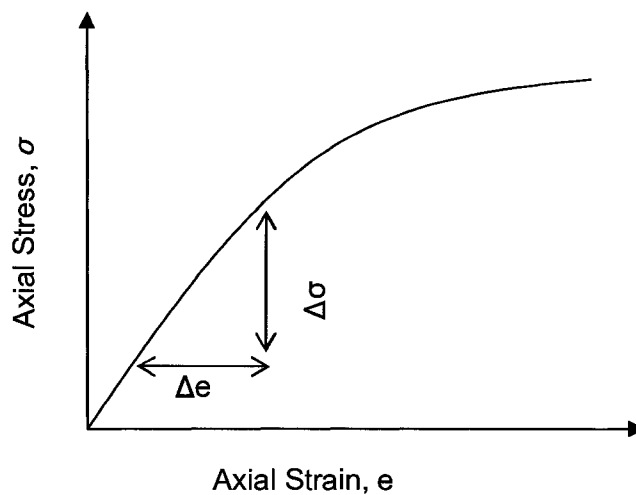


Figure 54: Modulus of deformation (after Craig 1996)

### 4.2.5 Pre-consolidation Ratio

Soils can be classified as

#### a) Normally consolidated (NC):

Never subjected to a stress greater than the present overburden stress (“virgin compression”).

#### b) Pre-consolidated (OC):

The Pre-consolidation Ratio or Over Consolidation Ratio (OCR) is defined as

$$\text{OCR} = \frac{\text{maximum past stress}}{\text{present stress}} \quad [7]$$

A soil is over-consolidated if the OCR is greater than 1. The deformations due to changes in the stress acting on a soil mass depend on the past history of the loading of the soil. The higher the value of the OCR for the new stresses, the stiffer the soil response is. As was mentioned previously, the in situ oil sand has a unique interlocking soil structure, due to high stress and pressure at the creation time. However near-surface oil sand, losing its interlocking structure, is due to the gas exsolved and moving mobile mining equipment. Therefore, near-surface oil sand behaves like normally consolidated soil (Craig 1996, Murthy 2003).

#### 4.3 Physical properties of oil sands

Kosar (1989), Dusseault (1977) and Plewes (1987) performed triaxial tests in a laboratory setting, using the Mohr-Coulomb approach. Dusseault (1977) conducted drained and undrained triaxial tests on recompacted rich oil sand with 13.5% (volume) bitumen content. The triaxial tests were run at around 4°C. The results showed a Mohr-Coulomb failure envelope for undrained rich oil sand of  $\tau_f = 1.13\sigma_n^{0.83}$  and for drained oil sand of  $\tau_f = 2.80\sigma_n^{0.84}$ . Figure 55 shows one failure envelope for rich oil sand, obtained via unsaturated triaxial tests.

Dusseault (1977) also conducted shear box tests on oil sand. He observed a shear box failure envelope of the form  $\tau_f = A\sigma_n^B$  where A varied from 0.4 to 2.37, and B varied from 0.714 to 0.899, yielding corresponding residual strengths of 0.325 to 0.7 MPa. He also showed that

1. In shear, the strength of oil sand is not directly a function of material density.
2. Strength is lost with the gross texture disturbance caused by sample expansion during sampling due to gas exclusion from sample.

TEST NO.	n	BD	T	OIL		$\sigma_c$	$\sigma_3$	$u_i$	$\left(\frac{\sigma_1 - \sigma_3}{2}\right)_f$	$\left(\frac{\sigma_1 + \sigma_3}{2}\right)_f$	$\phi_f$	$\frac{\sigma_1}{\sigma_3}$	$e_f$	k	COMMENTS	
				H <sub>2</sub> O												
T-50	32.7	2.11	3°	13.5	2.5	7.12	14.06	7.04	19.15	32.76	35.8	3.81	8.17	5.6	Shear failure 65°	
T-51	35.8	2.06	3°	13.3	3.3	10.5	10.70	5.50	13.95	23.9	35.7	3.80	6.19	1.4	Bulge failure	
T-52	36.1	2.05	3°	13.5	3.3	---	ELECTRONICS BREAK DOWN		---	---	---	---	---	---	Bulge failure	
T-53	35.9	2.06	4°	13.4	3.9	5.3	7.05	3.52	9.68	16.4	36.2	3.99	7.7	4.4	36.7	Bulge failure
T-54	35.9	2.06	4°	13.4	3.7	3.50	3.50	1.73	6.46	9.98	40.3	4.74	7.0	4.8	13.5	Bulge failure
T-55	34.7	2.08	7°	13.4	3.4	5.3	7.03	3.46	12.16	19.14	39.4	4.51	7.0	4.9	7.6	Bulge and Shea failure

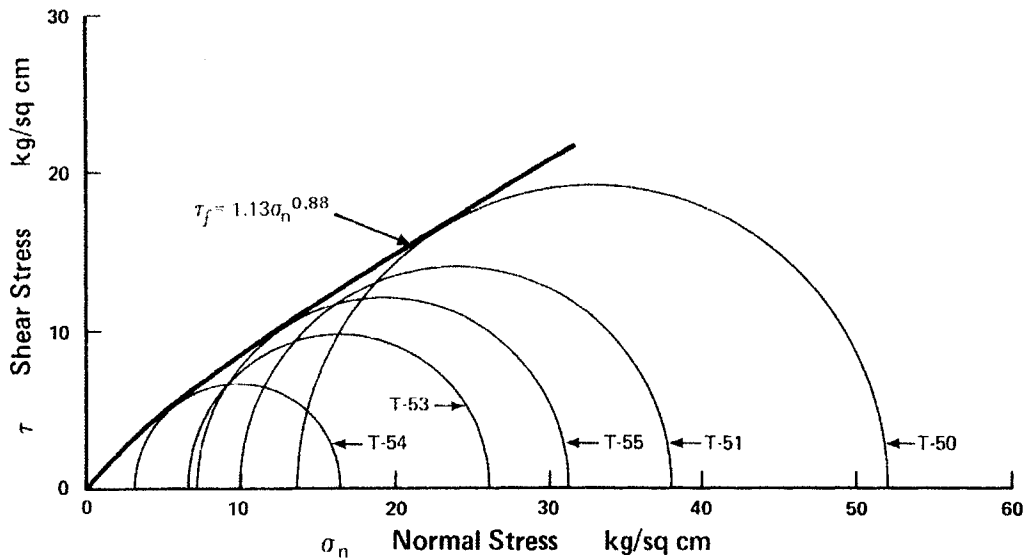


Figure 55: Failure envelope of re-compacted rich oil sand undrained triaxial tests (from Dusseault 1977)

It was observed that complete undrained behaviour occurred under rapid or transient stress, when insufficient time was available for significant drainage to take place. A partially drained condition occurred when the stress rate allowed the dissipation of pore fluid pressures. Under field conditions where equipment is loading the near-surface oil sand, undrained conditions predominate. During the underfoot shovel test that will be explained later the pore pressure does not change during test. Pore-pressure dissipation is a time-dependent function. If the physical properties of the oil sand structure are altered, this dissipation can increase by up to 10 times compared to largely unaltered situation (Plewes 1987).

Plewes (1987) found that the bulk density of uniformly graded rich oil sand ranged from 2.05 to 2.18 Mg/m<sup>3</sup>, the porosity ranged from 28% to 36%, and the water content ranged from 2% to 18% (volume). He also reported drained strengths for oil sand with high angles of friction approaching 60° at low stress. Two typical curves for samples under drained triaxial compression are shown in Figure 56. The failure strain for dense sand is usually less than 3 % (between 1 to 2 %).

Low stress failure modes are strain-softening in the post-peak region, and are the material behaviour that we are most likely to encounter. Peak and ultimate strength differences decrease with higher confining pressure. A relationship between the modulus of deformation (E) and the confining pressure ( $\sigma_3$ ) is shown in Figure 57.

The relationship between the tangent modulus of elasticity (E) and the effective confining stress ( $\sigma_3$ ) reported by Plewes (1987) is based on earlier work at higher values of  $\sigma_3$ ; in this case, we looked at low  $\sigma_3$  and loading-induced increments of  $\sigma_3$  at orders of magnitude less those that reported by Plewes (1987) and Samieh and Wong (1998). Plewes (1987) found that the effective angle of shearing resistance in undrained triaxial tests for a maximum principal stress at low confinements of 1.5 MPa was 59°. However, at ultimate shear strength, this value decreased to 53°. The effective angle of shearing resistance was between 50 and 60°. Figure 58 presents Plewes' (1987) p-q plot (p is  $\left(\frac{\sigma_1 + \sigma_3}{2}\right)$ , q is  $\left(\frac{\sigma_1 - \sigma_3}{2}\right)$ ) and the effective angle of shearing resistance for undrained Athabasca oil sand.

Plewes (1987) also studied the effect of the strain rate on the ultimate shear strength. He found that an increasing undrained strength was apparent at strain rates greater than 10<sup>-2</sup> s<sup>-1</sup>. The initial tangent modulus remained constant with the strain rate 10<sup>-2</sup> s<sup>-1</sup> and slightly increased with an increasing strain rate, as shown in Figure 59. At the very shallow depth, that is the depth of influenced mobile mining equipment, the confining pressure is very low and less 1MPa.

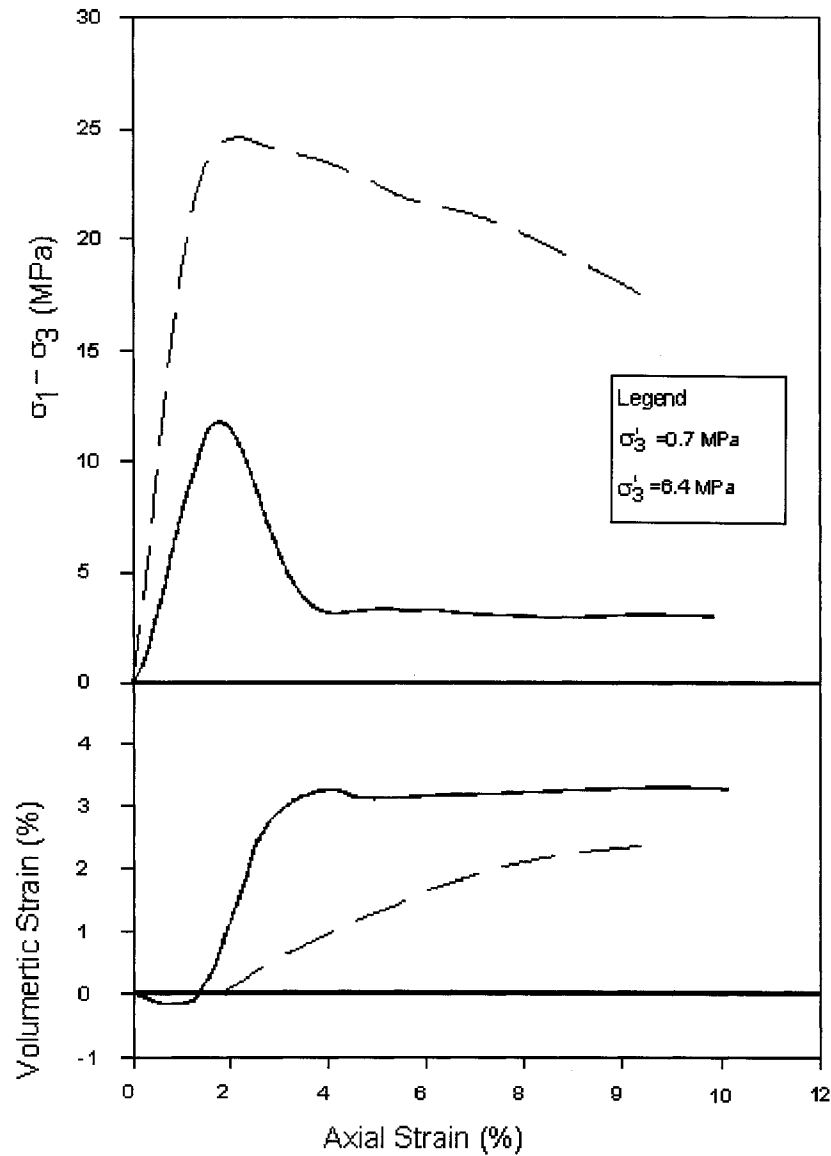


Figure 56: Typical drained stress strain curve for oil sand (from Plewes 1987)

The strength of the Athabasca oil sands (McMurray formation) somewhat decreases with increasing temperature. Also, temperatures up to 300°C do, not significantly affect the compressibility and absolute permeability of the McMurray formation. (Kosar 1989)

Chalaturnyk et al. (2003) plotted stress-strain curves at +30°C showing little variation with changing strain rate, which maximum varied from 0.1 to 10%/Min. However, at temperatures to -30°C, by increasing the strain rates, the maximum

deviator stress was increased by 40%. The shear strength of oil sand is sensitive to the strain rate at a temperature of  $-30^{\circ}\text{C}$ . Also, Chalaturnyk et al. found that the temperature had the greatest influence at the stress-strain curve. At a constant confining cell pressure (400 kPa), the maximum shear stress differed by 30%.

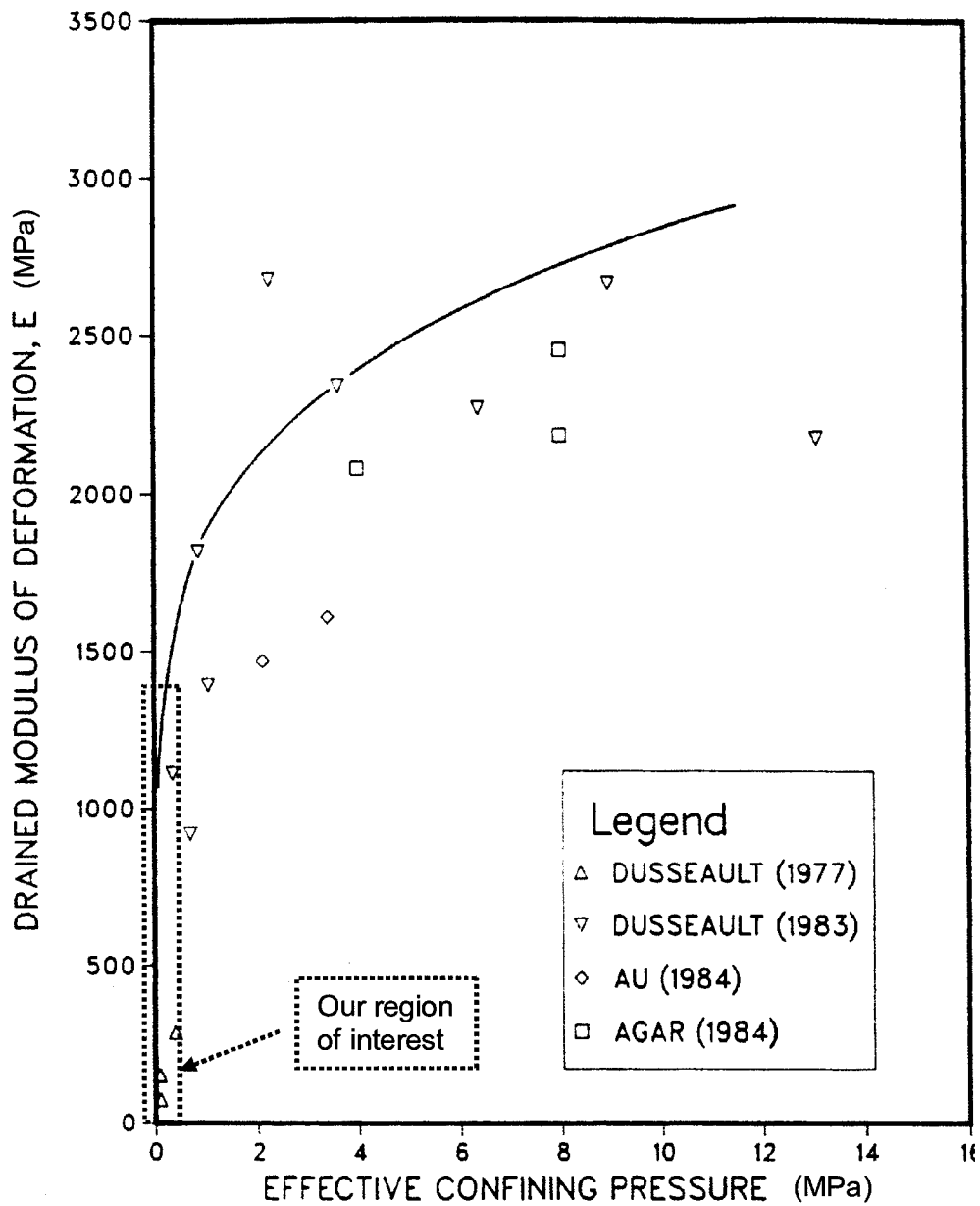


Figure 57: Deformation modulus for oil sand in drained triaxial testing (after Plewes 1987)

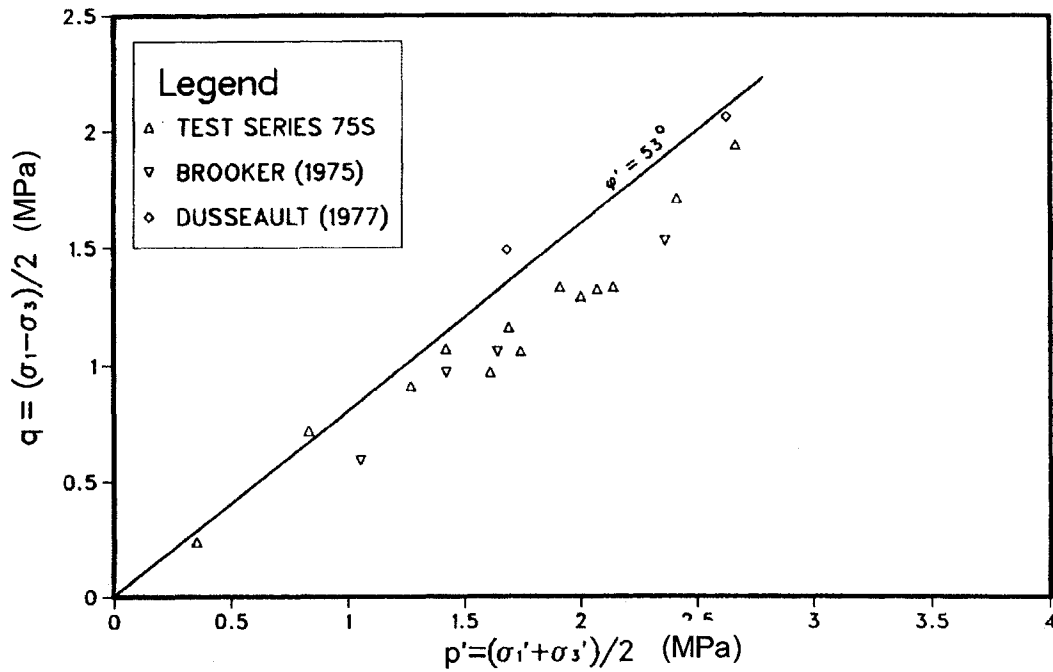


Figure 58: Ultimate shear strength of oil sand in undrained triaxial (after Plewes 1987)

Strength, deformation and permeability are related to the volume change and compressibility of the soil structure. Kosar (1989) obtained compressibility results for  $\sigma_3$  values greater than 2 MPa, but in his work, the  $\sigma_3$  associated with near-surface loading, was less than 1 MPa and often less than 300 kPa. Kosar (1989) found that the compressibility of oil sand was initially high on loading and then approached a lower constant value after the unload - reload cycles. In general, oil sand compressibility depends on the frictional resistance among the grains and the particle strength, void ratio, size, shape and gradation of the minerals. High-grade McMurray formation oil sand exhibits high dilatancy and post-peak strain softening behaviour under triaxial compression at low confining pressure. Table 3 summarizes the results from the different researchers' compressibility tests on oil sand.

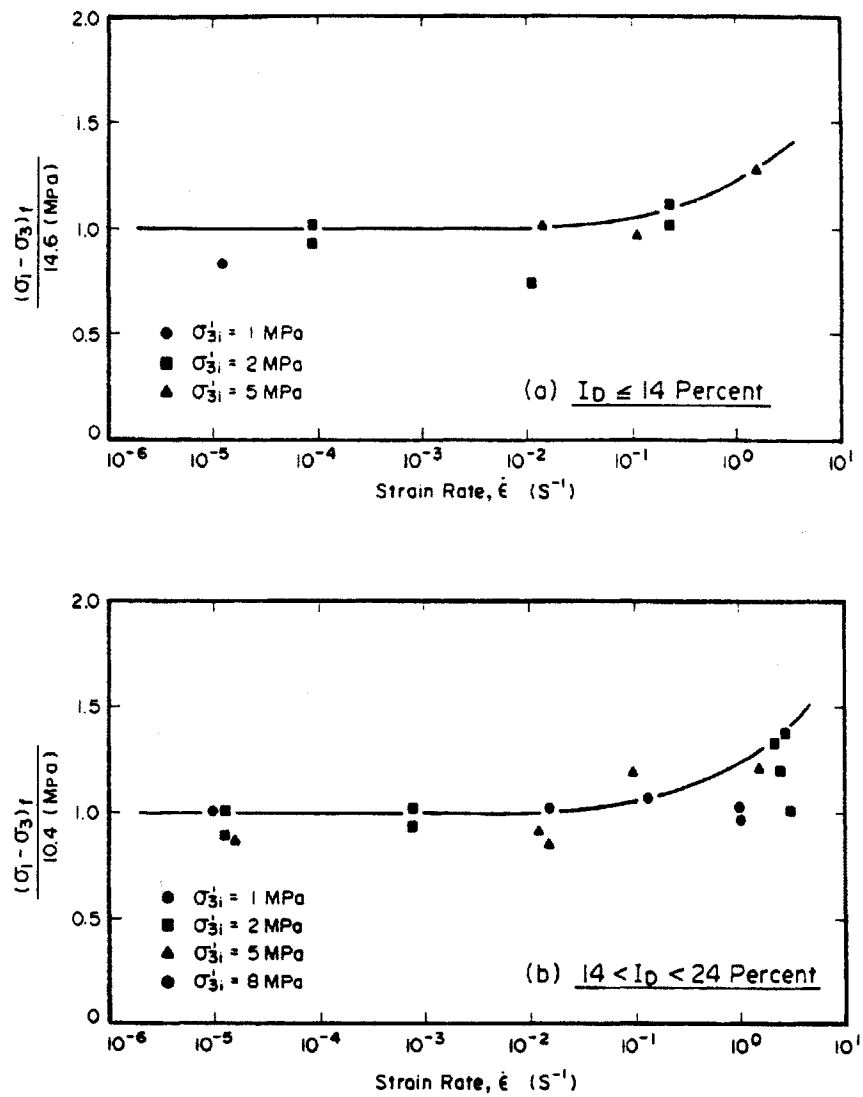


Figure 59: Effect of strain rate on ultimate strain undrained (after Plewes 1987)

Table 3: Results of compressibility tests

Compressibility (MPa)	Stress Range (MPa)	Note	Researcher
225-4000	---	Rich oil sand >12%	Au 1984
425-1140	2-4	Oil sand <12%	Plewes 1987
1250-4000	2.8-13.3	Oil sand <12%	Dusseault 1981
	4-25	Oil sand <12%	Agar 1984

Kosar (1989) also found that Poisson's ratio changed with the effective confining pressure (see Figure 60). At low confining pressures (less than 1MPa), Poisson's ratio converged on ~ 0.25.

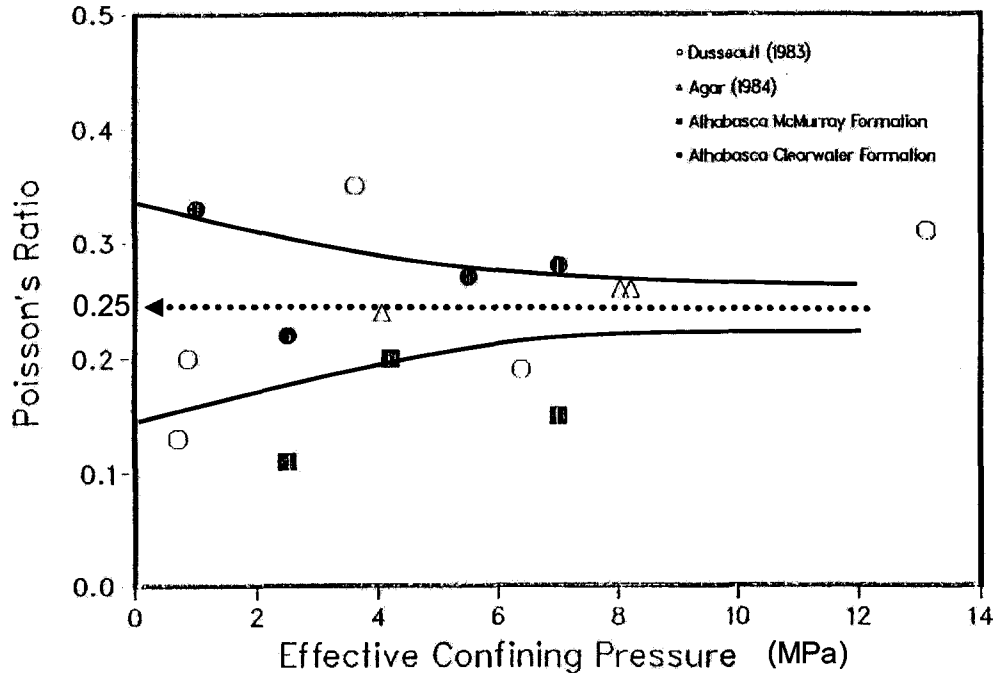


Figure 60: Change of Poisson's ratio with confining pressure (after Kosar 1989)

Kosar (1989) studied the undrained shear strength of McMurray formation oil sands over a range of initially effective confining stresses. The relationship between the elastic undrained modulus of deformation and confining pressure, as well as and the undrained failure envelope, in terms of effective stress at maximum stress is shown in Figure 61.

In situ or undisturbed oil sand contains three phases: solid, liquid mixture of water and oil, and gas dissolved in liquid. The sands are bonded firmly together by grain-to-grain contact that is called lock sand. The gas exsolution of oil sand results from its expansion and disturbs the locked nature of in situ oil sand. The gases come out of the solution to maintain the original pore pressure and allow stress relief, which is called gas exsolution. This process can occur during the sampling or removing of the overburden due to the reduced confining pressure and pre-pressure. Therefore, the characteristics of the soil skeleton, or the

disturbance of the oil sand, are influenced by the magnitude of the change in the effective stress, the rate of unloading, and the relative permeability. The existing models for predicting oil sand heave and settlement are categorized as “time-dependent” or “time-independent” models. In a time-dependent model, the response of the soil is free from the rate of unloading, and this rate is faster than the rate of the gas exsolution (Griffin 1986).

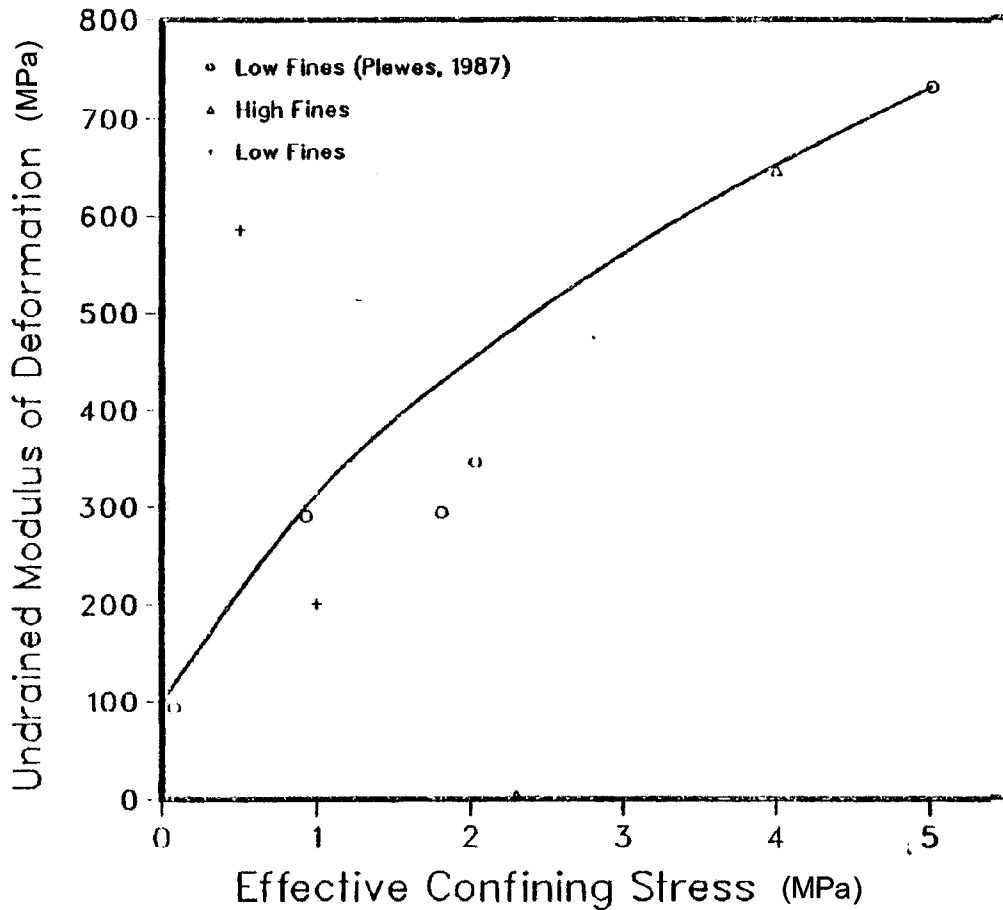


Figure 61: Tangent modulus of elasticity for undrained triaxial compression on oil sand (after Kosar 1989)

Griffin (1986) explored time-dependent models, in which the rate of unloading is faster than the rate of gas ex-solution, and found via the SPT (Standard Penetration Test) that the surface of oil sand is noticeably softer over time. After observing equipment operating on an in-pit oil sand surface, Griffin concluded that the ground was most likely fully exsolved of all gases. Therefore, the oil sand at the surface was noticeably softer than the oil sand below. Knowing the

stress change can simulate the effect of ground surface movement during excavation. Therefore, Griffin, through three case studies, showed that by using Boussinesq's method (Timoshenko 1934), the stress change can be calculated by

$$\Delta q = \frac{\Delta \sigma \times B \times L}{(B + Z)(L + Z)} \quad , \quad [8]$$

where;

$\Delta q$  is the change vertical stress at a depth Z

B & L are the foundation dimensions.

Three case studies at oil sands in northern Alberta, located at the foundation of a stack, a boiler house, and a dump pocket. It was found that soil disturbance occurred in the upper 10 to 40 metres and that a noticeable disturbance occurred in the upper 5 m. All three structures were on lean oil sand (oil sand with less than 5% bitumen) at a depth of 5 to 10 metres, followed by rich oil sand (oil sand with more than 10% bitumen). Figure 62 shows a disturbance coefficient of the volume compressibility below the final excavation level. Griffin found that the near surface oil sand was disturbed due to the gas exsolved. In the mining area, the oil sand was disturbed due to the moving mobile equipment and the gas exsolved.

The typical values of oil sand water permeability are  $10^{-8}$  to  $10^{-10}$   $\text{cm}^2 \text{s}^{-1}$ . The volumetric change of oil sand is highly stress-dependent. The compressibility of bitumen is  $30 \times 10^{-7} \text{ kPa}^{-1}$ , and the soil skeleton is around  $10 \times 10^{-7} \text{ kPa}^{-1}$  under one-dimensional (oedometer) compression test. Figure 63 shows the compressibility of oil sand at different stress levels.

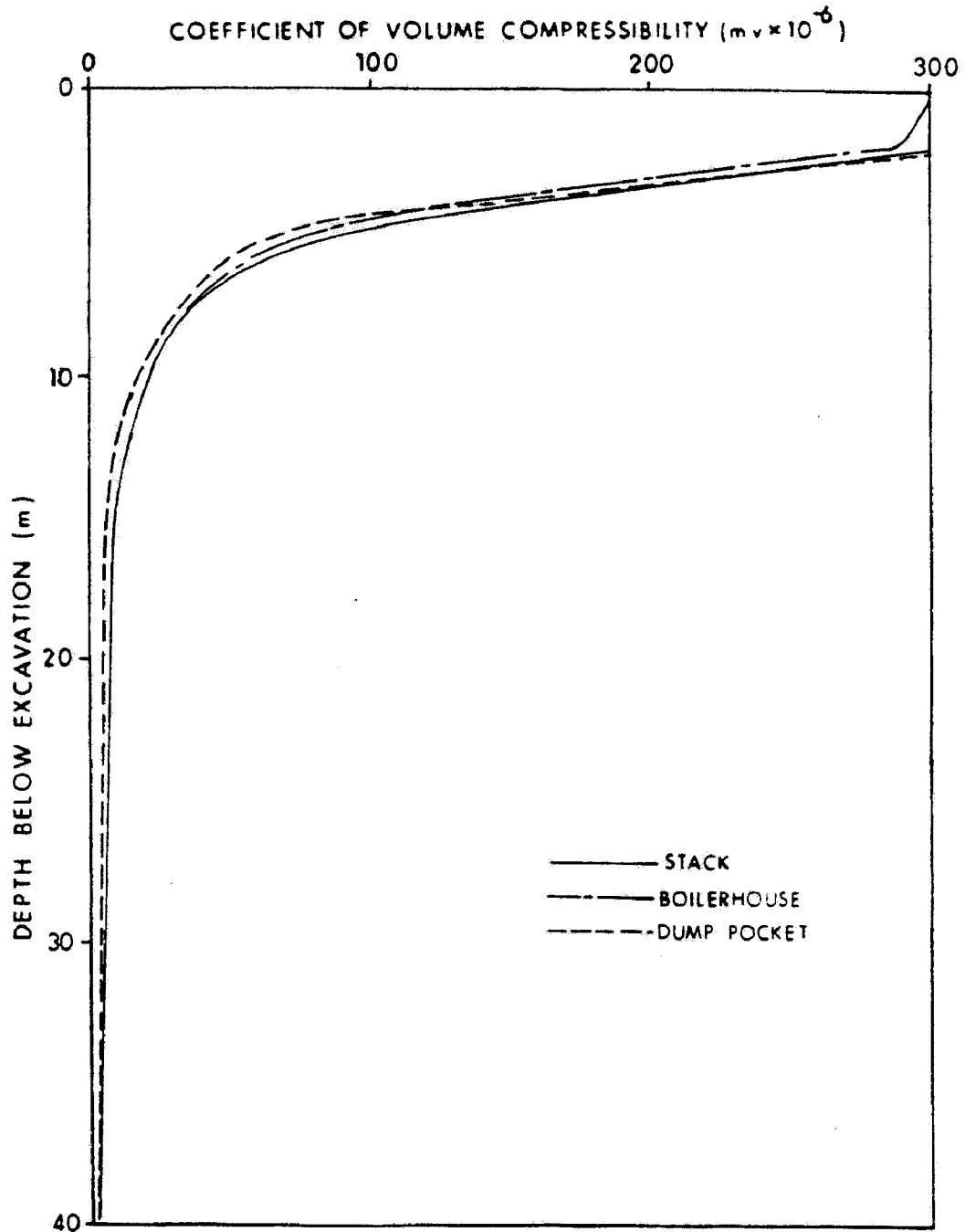


Figure 62: Disturbance of  $m_v$  with depth (after Griffin 1986)

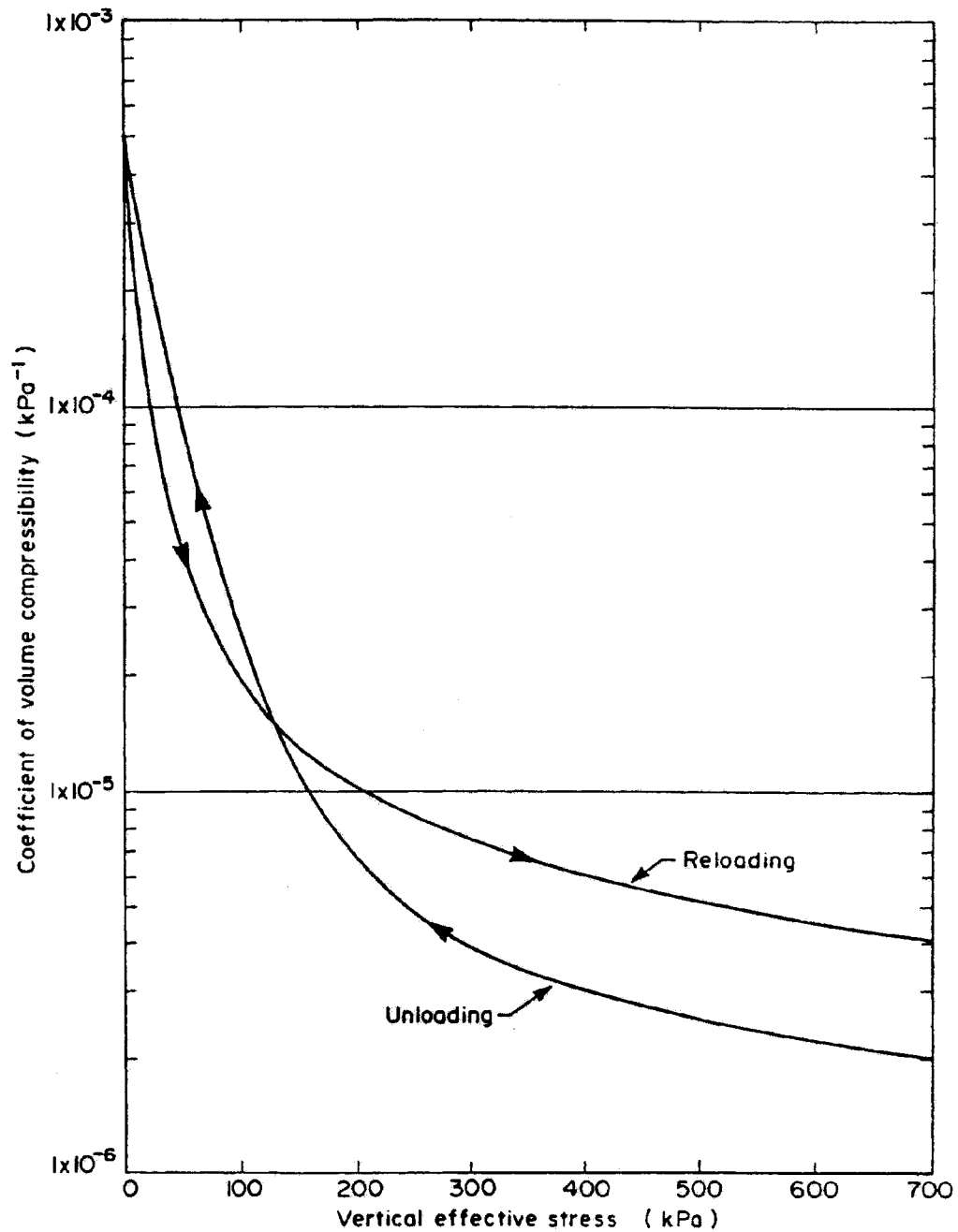


Figure 63: Compressibility of oil sand at different vertical effective stress (after Griffin 1986)

#### 4.4 Cyclic loading of materials

The response of materials to cyclic loading is complicated and very different from the response to static loading. Most structures and equipment are subject to cyclic loading. Source phenomena include wind loading upon a building, live

loading within a building, wave loading on an offshore structure, groundwater level change, heat, vibration, seismic loading due to traffic loading on pavements and heavy machine foundations, and the motion or vibration of equipment and the under-carriages of shovels during a loading cycle. Common cyclic loading situations that play an important role are wind loads on tall buildings, structures that support travelling machinery such as cranes, large telescopes and radar antennae, viaducts and train tracks, storage facilities for grains, and oil tanks which have a wide range of cyclic loading amplitude. The strain rate is highly variable in cyclic loading. However, the main parameters in cyclic loading cases are the loading amplitude, number of cycles, time of loading, and the materials' properties.

In mining, cyclic loading and rock fatigue are important in pillar design, underground opening design, assessment of drilling and blasting conditions, road and ramp construction and rock excavation, etc. Due to cyclic loading, many parameters such as loading amplitude, frequency, and loading wave shape (sinuosity, triangle or rectangular) affect the strength and the analysis of material.

According to cyclic-loading research on different materials, almost all materials lose their stiffness or soften with an increasing number of cycles. However, some parameters affect the degree of softening during cyclic loading, such as the load level, the material structure, and the temperature. The mechanism of cyclic loading and the response of highly variable materials like soil and metal appear similar. This similarity leads us to conceptualize potential cyclic tests for soil that may also be applicable to other materials.

This thesis does not deal with rock, wood, metal or even asphalt; however, this chapter shows that the parameters for these materials could be important in this present study and influence its results. This literature review on cyclic loading shows that cyclic loading is a very complicated phenomenon its results could be very different even for the same material. Although for the ultra-class mining equipment such as trucks and shovels, the loading can be very complicated, for the sake of simplicity and to provide some boundaries for this study, it will be assumed that for an ultra-class truck under static conditions and with a 1.3 m<sup>2</sup> tire

contact area,  $\sigma_1$  is roughly 780 kPa, and that for a large-capacity cable shovel with a contact area of 62.55 m<sup>2</sup> (3.5m×9m),  $\sigma_1$  ranges from 200 kPa, as shown in Table 4. However, according to section 1.2, the cable-shovel pressure could reach 500 kPa. The wheel base of a 797B truck is 7.2 m. The frequency of loading depends on the truck velocity. Therefore, the range of the loading frequency in the most situations will be from 0.2 to 0.57 s<sup>-1</sup> (5/3.6×7.2, 15/3.6×7.2), for 5 to 15 km/h respectively. A shovel's loading rate depends on the loading cycles; the average shovel loading cycle is approximately 30 to 45 seconds. Therefore, the loading rate due to the racking motion of shovel activity is 0.03 to 0.022 s<sup>-1</sup>, respectively (1/30, 1/45).

Table 4: Equipment ground pressure

Equipment	Gross Machine Operating Weight (kg)	Static ground pressure (kPa)
Truck (797 B)	623,690	(624×9.8/1.3×6)=780
Shovel (4100 BOSS )	1,210,411	(1210×9.8/3.5×9×2)=200

#### 4.4.1 Rock

Under cyclic loads, rock strength versus the fatigue and strain rate is important in mine design. Fatigue in rock causes the deterioration of rock strength and failure at stresses lower than the static compressive strength. The important parameters of rock fatigue are rock type, water content, confining pressure, discontinuities, frequency of loading, strain rate, type and amplitude of loading (Ishizuka et al., 1990).

Ishizuka et al. (1990) investigated the fatigue behaviour of a granite with a strength of  $\sigma_1$  (kPa) = 200.9 + 2.08 $\sigma_3$  (kPa) at a strain rate  $\dot{\epsilon}$  = 8.33e<sup>-6</sup> s<sup>-1</sup> under sinusoidal loading at a frequency of 0.00025 to 0.5 Hz and amplitude at 80% static strength. With an increasing strain rate, the strength increased by 15 to 25% in dry samples and decreased by 5 to 8% in wet samples. Dry samples are frequency-dependent, but wet samples are not. Fatigue failure occurred at 10 to 60 cycles under uniaxial compression, and at 30 to 600 cycles under triaxial

compression at  $\sigma_3 = 3.92$  MPa. Figure 64 shows the number of cycles to failure versus the frequency for this case.

Marble and sandstone samples were tested by Zhenyu and Haihong (1990) under stress-controlled cyclic fatigue conditions. The number of cycles to failure was found to be inversely proportional to the peak stress. The loading type thus greatly influenced the number of cycles to fatigue. Haimson (1974) also found that with triaxial compression, the fatigue strength increased as the confining pressure increased.

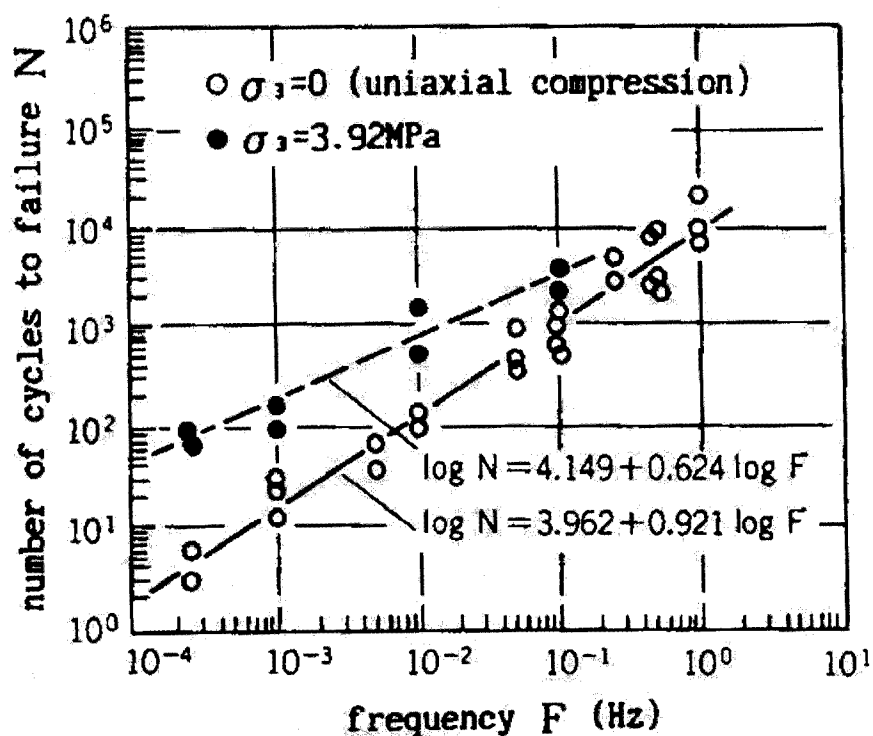


Figure 64: Number of cycles to failure  $N$  versus frequency  $F$ , at constant applied stress (after Ishizuka 1990)

Singh (1989) reported that Young's modulus, Poisson's ratio and uniaxial compressive strength are noticeably strain rate-dependent. Ray et al. (1999) found that for sandstone, an increase in the stress amplitude caused the uniaxial compressive strength (UCS) to decrease, varying from 6% to 11% of the applied

stress, as a linear relationship. The effect of increasing strain rate causes a noticeable increase on static, UCS samples. However, in a fatigue test with an increasing strain rate due to cyclic loading, the number of cycles to failure decreased. Young's modulus was also found to be strain-rate-dependent.

Biswas et al. (2001), studying basalt samples, found that the strain energy during loading and unloading could be calculated from the area under the stress-strain curve. The amount of strain energy is calculated from the strain retained in the sample when it is completely unloaded. The residual strain energy fixed in a sample at each cyclic stage needs substantially less energy to reach the same stress level in later stages. Rocks with lower residual strain energy need less energy for subsequent cycles if the lag time between the subsequent loading cycles is minimized. Therefore, the magnitude of energy saving is directly related to the time of relaxation for the rock sample. When the load increases, the capacity of the rock for storing residual energy increases, and the plastic deformation of the rock sample also increases.

#### **4.4.2 Clay**

Anderson (1988) researched the static, cyclic and combined loading properties of soil, including the cyclic shear strength, deformation and pore pressure, post-cyclic static and cyclic shear strength, and post-peak behaviour. Direct simple shear and triaxial tests were carried out on plastic Drammen clay overconsolidated to a ratio of 1 to 4. The research on offshore gravity foundation platforms showed that the cyclic shear stress, was caused by the cyclic wave loads.

Figure 65 illustrates shear stress - shear strain behaviour during cyclic loading. Static tests were run under strain control at a rate of 3% per hour for triaxial tests and 4.5% per hour for direct simple shear tests. The cycles were applied as stress-control sinusoidal loading for 10-second load periods. Figure 66 shows the results of the shear stress, strain, and pore pressures during cyclic loading. The cyclic shear stresses caused shear strain development according to the number

of cycles, so that the average values increased with an increasing number of cycles. According to Anderson (1988), the results showed that the combination of the average and cyclic shear stress, not the maximum shear stress, was important at failure. The cyclic behaviour of clay depends heavily on the over-consolidation ratio (OCR), which is defined as the ratio of the maximum pressure that a soil particle experiences to the present effective vertical pressure.

Butterfield and Georgiadis (1980) conducted circular and square plate bearing tests on remoulded London clay at a constant penetration rate of 7 mm/min with 9kN loads on a 1.5×1.5×1.4 m clay bed. Five circular plate diameters were used, in sizes ranging from 12.5 to 76 mm, and the square plates' side lengths ranged from 50 to 100mm. An empirical equation was produced:

$$\frac{q_1}{q_u} = \frac{Q}{Q_u} = 1 - e^{-(K_0 - K_f) \frac{W}{D}} + K_f \frac{W}{D}, \quad [9]$$

where;

$k_0$ ,  $k_f$  are the experimentally determined stiffnesses, and  $K_0$ ,  $K_f$  are the dimensionless parameters

$$K_0 = \frac{k_0 D}{q_u} \quad [10]$$

$$K_f = \frac{k_f D}{q_u} \quad [11]$$

$Q_u$  is the load axis intercept plotted against displacement,  $Q$  is the applied load, and  $W$  is the displacement and  $D$  is either the plate diameter or the square side length

$$q_1 = \frac{Q}{A}, \quad q_u = \frac{Q_u}{A} \quad [12]$$

$A$  is the area of the plate.

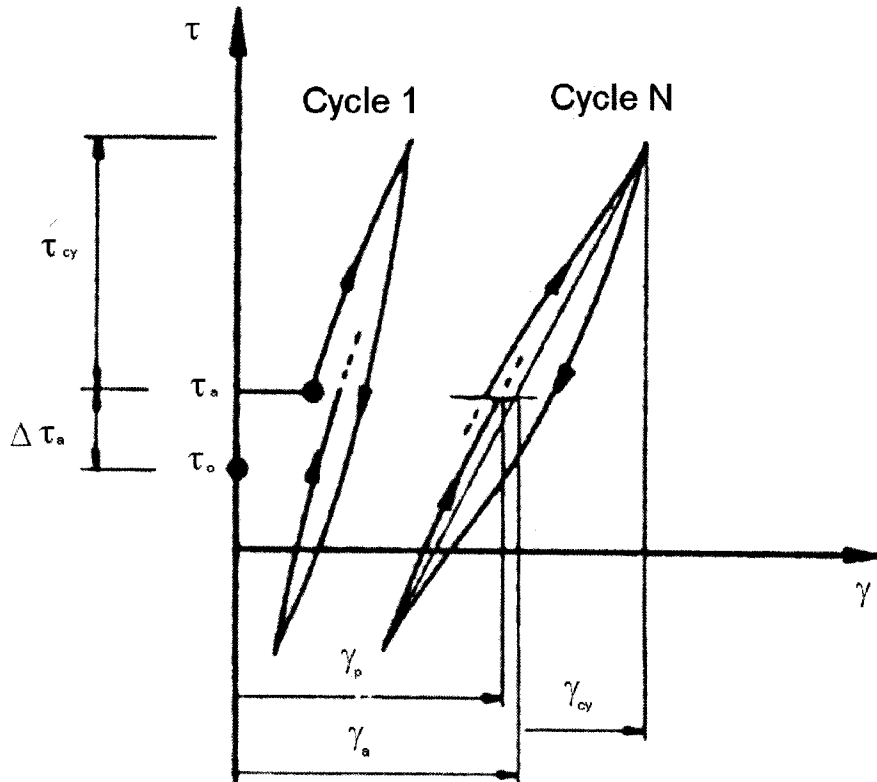


Figure 65: Shear stress and strain behaviour during cyclic loading (after Anderson, 1988)

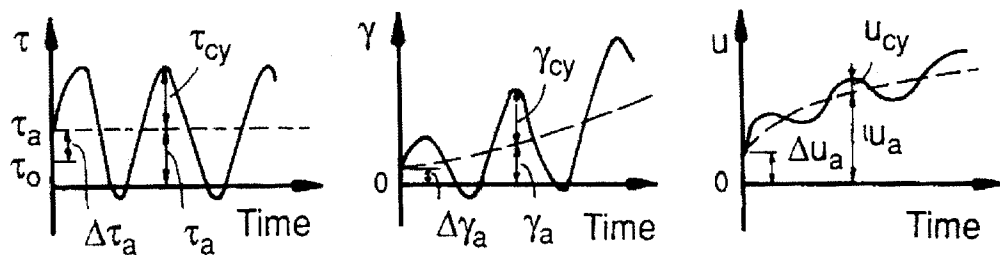


Figure 66: Shear stress, shear strain and pore pressure during cyclic loading (after Anderson, 1988)

Figure 67 shows the change of stiffness during cyclic loading. It was found that the slope of the reloading line remained approximately constant regardless of the number of previous load cycles, but that this slope decreased with an increasing load level. The slope of the unloading line, connecting the maximum load of the

previous cycle with the subsequent zero load point, decreased with an increasing load level and the number of load cycles. Figure 68 illustrates a cyclic plate (50mm) bearing test.

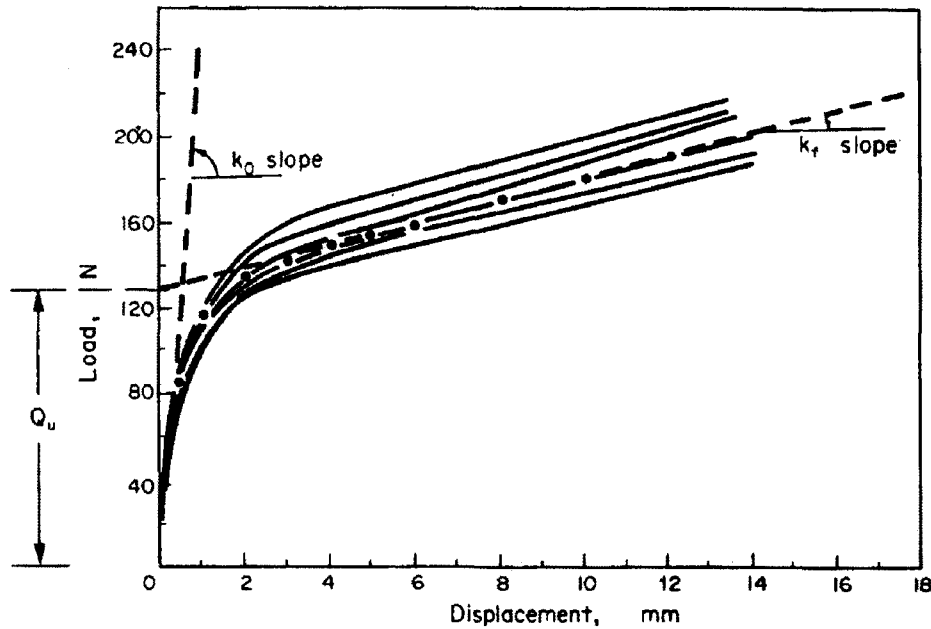


Figure 67: Change of the stiffness during cyclic loading (after Butterfield and Georgiadis 1980)

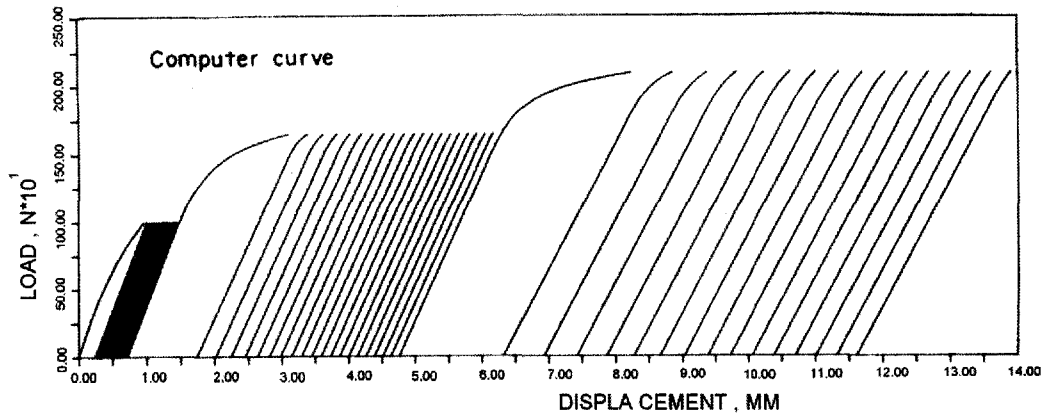


Figure 68: Cyclic plate 50mm bearing test (after Butterfield 1980)

Madshus & Kaynia (1999) found that dynamic triaxial loading on organic and soft marine clays yielded a modulus reduction as a function of the strain level.

Anderson (1988) found that in clay, the slope of the loading versus displacement decreased with an increasing number of cycles, but Butterfield and Georgiadis (1980) found the opposite.

#### **4.4.3 Sand**

A phenomenon peculiar to sand under cyclic loading is cyclic liquefaction, defined as the rapid loss of shearing resistance or the development of excess strain as a result of transient or repeated disturbance, as shown in Figure 69 (Grozic, 1999).

Liquefaction can be categorized based on different mechanisms:

- Flow liquefaction
  1. The soil must have a strain-softening response to undrained loading.
  2. The in situ shear stress must be greater than the undrained or steady state strength.
  3. Can happen via either monotonic or cyclic loading.
  4. Can occur in very loose granular materials such as very sensitive clays or loose deposits.
- Cyclic liquefaction
  1. Due to undrained cyclic loading (e.g., an earthquake), illustrated in Figure 69.
  2. Sufficient loading to cause shear stress reversal and an effective confining pressure to essentially reach zero.

Grozic (1999), studying gassy Ottawa sands, found that the soil resistance to cyclic loading was influenced by the applied shear stress as well as the soil state, which is described by terms like void ratio, effective confining pressure, soil structure or grain properties. The influence of cyclic loading through loading intensity, duration, and frequency can cause major differences. Moreover, in gassy sands, the initial degree of saturation, the gas characteristics, and the sample preparation greatly influence the results. For dense sand, the cyclic resistance decreased with increasing confining pressure, increasing fines content, and the presence of gas (Grozic, 1999).

Sand behaviour is similar to that of oil sand but in the case of liquefaction, the frequency range, duration of cycles, and fluid pressure are necessary to induce a response.

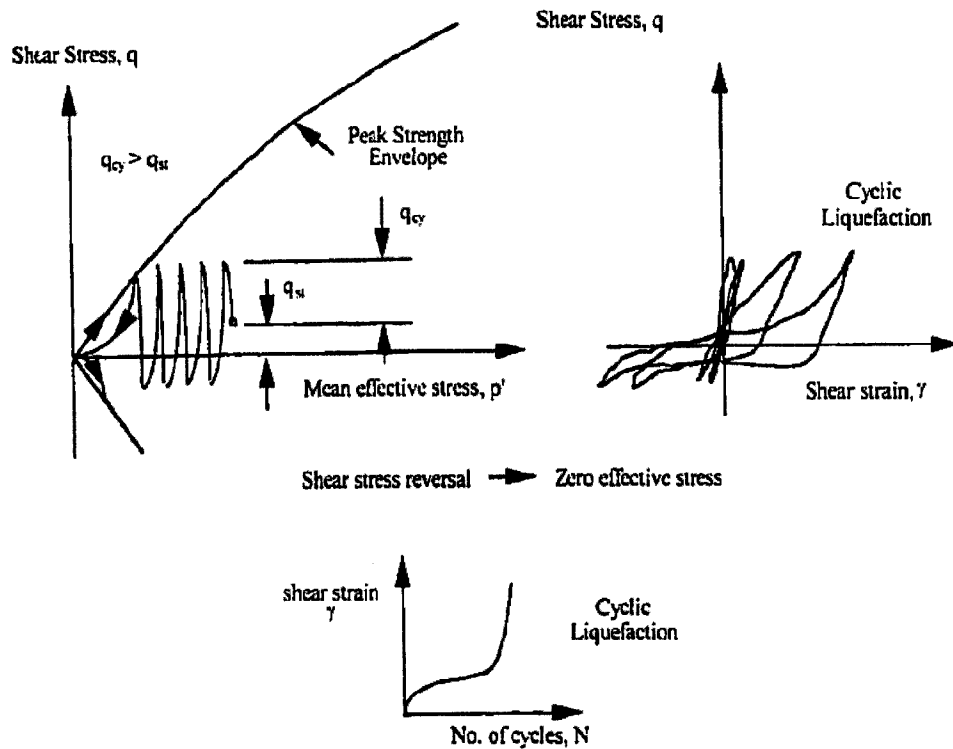


Figure 69: Schematic illustration of cyclic liquefaction (after Grozic, 1999)

#### 4.4.4 Asphalt

Fatigue failure is a common failure mechanism in asphalt pavement. During the spring thaw in cold regions, the sub-grade gravel may be softened by higher than normal water content. Other parameters that may be important are the frequency of the load, the temperature, the binder grade and content, and the void ratio or grid reinforcement (polygrid). Research has shown that determining the stiffness, such as the flexural stiffness of a beam specimen or the dynamic stiffness, by using cylindrical specimens or a dynamic indirect tensile test provides variable results. The initial flexural stiffness is stress-dependent, and the dynamic stiffness is about 1.5 times the flexural stiffness. Also, flexural stiffness is stress-dependent, with the stress dependency increasing with the temperature and void ratio. The fatigue curve for asphalt shows that its life cycle depends greatly on

the constant stress or the strain modes of loading. Tests revealed that the fatigue life increased with the temperature for constant strain and decreased under constant stress loading. A stiffer mix of material had a longer fatigue life under constant stress. On the other hand, in the constant strain mode, lower stiffness yielded a higher fatigue life (Myre 1990).

Khalid (2000) found that for a stiffer mix, the fatigue life was greater than expected under a stress-control test. A thick asphalt layer is good for stress control, but a thin asphalt layer is more suitable for strain control.

Ling and Liu (2001) found that geo-synthetic reinforcement increased the stiffness and bearing capacity of asphalt. The stiffness of reinforced asphalt was around 60% higher than that of unreinforced asphalt. In addition, it was observed that the stiffness decreased when the load level was increased, while the stiffness increased with the number of cycles within each load level.

Asphalt is usually a combination of crushed stone and some sand, with bituminous as a binder. In winter, asphalt could be a firmer version of oil sand, which is a combination of bitumen and sand. Because of freezing near surface of oil sand, a firm layer is overlying a soft layer. The thickness of the firm layer is around 2 to 4 metres, depending on the weather and the duration of ambient conditions, making this layer suitable for a stress-control test, according to Khalid's (2000) study.

#### **4.4.5 Other materials**

##### **4.4.5.1 Concrete**

Lahlou et al. (1999) studied the behaviour of high- and very high-strength concrete inside circular steel tubes during rapid cycles of compressive loading. The tubes' (total system) behaviour was very similar to that of elasto-plastic materials such as steel. Elastoplastic material subject to unloading and reloading remains linear and parallel; moreover, degradation is obvious in plastic strain. Lahlou et al. (1999) reported that in conventional concrete, when the strain rate increased, so did the ultimate stress, elastic modulus and peak strain. However,

Poisson's ratio post-peak slope decreased. Very high-strength concrete is less sensitive than normal to the loading rate and also has an unstable post-peak response. The first and second load-unload cycles always differ from subsequent cycles. A low stiffness with a large residual effect occurs after unloading. The envelope of rapid cyclic loading can be found by multiplying an amplitude factor that is related to the strain rate, the compressive strength, and, perhaps the confinement level (Lahlou et al.1999).

#### **4.4.5.2 Wood**

Wood is a unique natural fibre-composite material. During compression, it has an uncoupled behaviour that allows the evolution of plastic deformation and yielding in two directions. On loading beyond the residual plateau, wood noticeably strain hardens. Adalian and Moriler (1974) found that for wood with specific gravity between 0.35 and 0.53, behaviour was controlled only by the strain rate. During a variable load, the strain rate had no influence on the wood's behaviour.

Gong and Smith (2003) studied the effects of the waveform and loading sequence on low cycle fatigue life, and found it to be a function of the waveform, cycle, and load.

#### **4.4.5.3 Metals**

Machine-component elements or structures subjected to either cyclic stress or strain are highly susceptible to fatigue. "Classic fatigue" is defined as failure of an object due to fluctuating loads (Mater, 1988).

The factors strongly influencing fatigue life are the microstructure (grain size, texture), load range (sign, magnitude, rate and history), geometry of the component, thickness, environment (temperature, corrosive medium), and processing (deformation history, manufacturing). Fatigue damage changes the mechanical properties (axial stiffness, residual tensile strength and shear strength) (Ellyin 1997).

#### 4.5 Damage mechanics and surface bounding modelling

Almost all materials subjected to adverse environmental and mechanical conditions experience microstructural changes which decrease their strength. Examples of material damage are creep, ductile plasticity, fatigue damage, embrittlement, chemical and mechanical damage, environmental degradation, and concrete damage. Material damage changes material structures irreversibly which is the consequence of changing the property of the material. Damage can take place under elastic (high cycle fatigue), elastic-plastic (ductile plastic and low cycle fatigue) deformation or under creep conditions and damage (Kachanov 1986).

Damage variables can be calculated as the surface density of the intersections of cracks and cavities.  $\omega$  describes the damage parameters, and  $\omega=0$  describes the undamaged material. In the case of isotropic damage,  $\omega$  is defined as

$$\omega = \frac{A'}{A_0} \quad 0 \leq \omega \leq 1 \quad \text{or} \quad \psi = 1 - \omega \quad 0 \geq \psi \geq -1 \quad , \quad [13]$$

where;

$A'$ =damage area

$A_0$ =initial area

$\omega$  is unit less parameter; therefore,  $A_0$  and  $A'$  have the same surface unit area (see Figure 70).

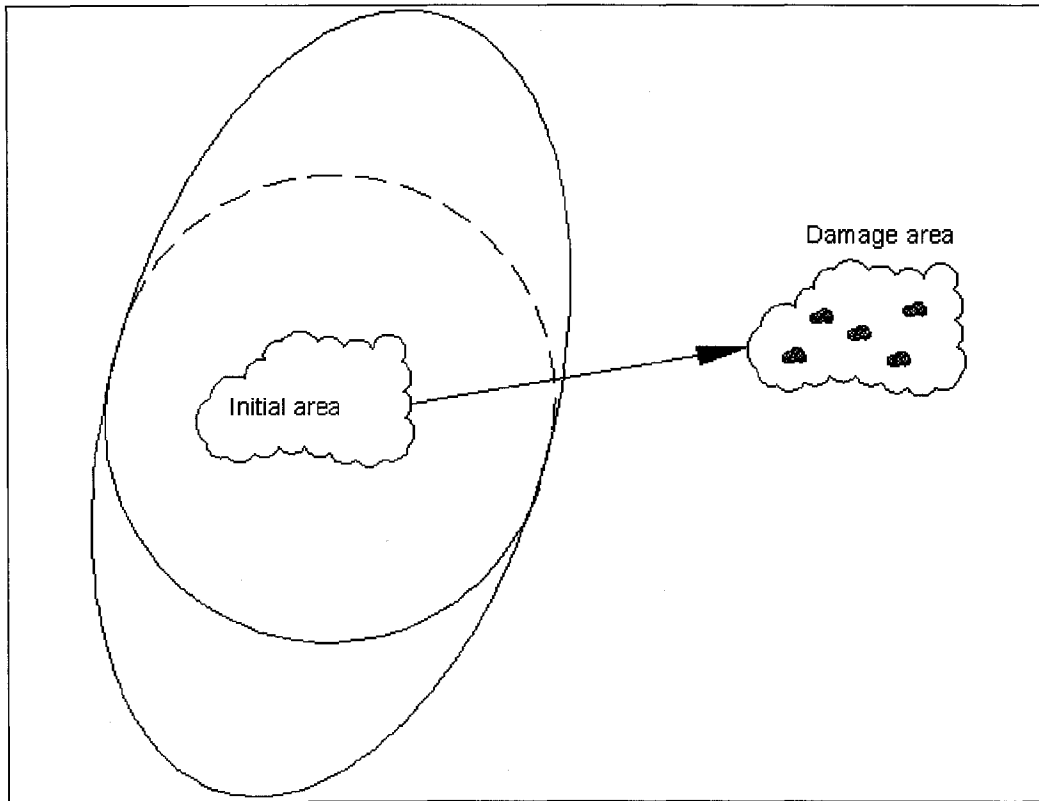


Figure 70: Damage mechanic parameters

According to the above, the stress-strain behaviour equation of the damaged material can be represented by the constitutive equation of the initial material.  $E'$  can be identified with the unloading modulus (Kachanov 1986):

$$E' = E \psi \quad [14]$$

$E$  = Young's modulus of initial or undamaged material

$E'$  = Young's modulus of damaged material.

Damage under creep conditions is expressed by

$$\dot{S} = \dot{\varepsilon}_{ij} \sigma_{ij} + Q \dot{\psi} \quad [15]$$

where;

$\dot{S}$  is the component of the rate of stress deviator (tensor), and  $Q_t$  is the thermodynamic force (force in macroscopic scale during motion of particles)

associated with the rate  $\dot{\psi}$ . Creep curves under a constant load have three regions. The instantaneous elastic region at the moment of loading (AB), the elastic-plastic region (BC), and the acceleration region usually depend on the material's properties and the temperature (CD) (see Figure 71). Fracture can happen in any of the three regions, depending on parameters such as the stress level, temperature, and material properties. In plastic creep, the strain rate is a function of mainly the stress rate (Kachanov 1986):

$$\dot{\epsilon}_{ij} = \dot{\epsilon}_{ij}^p + \dot{\epsilon}_{ij}^e \quad [16]$$

$$\dot{\epsilon}^p = \phi(\sigma) \frac{d\sigma}{dt}, \quad [17]$$

where;

$\dot{\epsilon}^p$  = plastic strain rate,

$\dot{\epsilon}^e$  = elastic strain rate, and

$\phi(\sigma)$  = non-negative monotonically increasing function.

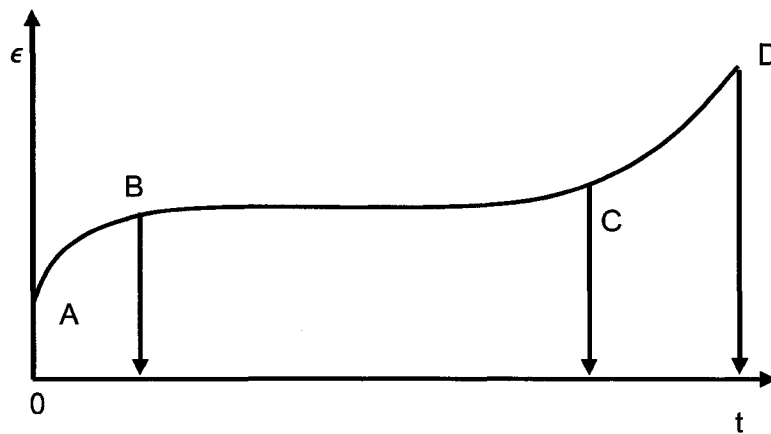


Figure 71: Creep Curve (after Kachanov 1986)

Voyiadjis (1993) proposed a continuum damage mechanics model for the monotonic and cyclic behaviour of concrete. Damage growth occurred when the loading surface was outside the initial fracture surface that is usually represented a surface of all possible stress points in stress surface. The damage bounding surface is a function of the stress invariant and damage parameters. Voyiadjis (1995) found that the damage modulus decreased as the distance to the loading surface and bounding surface decreased, and that this decrease was manifested in increasing damage. An asphalt model based on continuum damage mechanics, and elastic-viscoelastic models, was designed by Lee et al. (2000). They modeled the changing pseudo-stiffness during the cyclic loading and rest period. The pseudo-strain accounts for the linear viscoelastic hereditary effect of the material. The pseudo-stiffness is defined as

$$S^R = \frac{\sigma_m}{\varepsilon_m^R} \quad , \quad [18]$$

where;

$\sigma_m$  = stress corresponding to  $\varepsilon_m^R$  , and

$\varepsilon_m^R$  = peak pseudo-strain in each stress-pseudo-strain cycle.

The general form of the model is  $\sigma = k(\varepsilon_e^R)[F+G+H]$ . [19]

where;

$k(\varepsilon_e^R)$  = the initial pseudo-stiffness function of the effective pseudo-strain, and F and H are functions characterizing pseudo-stiffness changes due to damage growth and microdamage healing. The G function accounts for the different values of the stress between the loading and unloading paths. Function F has two component correction factors and changes in  $S^R$  under a continuous cyclic loading without rest in the controlled-strain mode. H is the function representing the change in  $S^R$  due to rest periods. G is the hysteresis function, which accurately describes the stress-strain of both the loading and unloading paths.

The bounding surface formulation for soil plasticity, proposed by Dafalias and Hermann (1982), is a two-surface model consisting of a bounding surface, and a loading surface in 2-dimensional space. The bounding surface in the stress space of this model, always encloses the second surface-which is the loading surface, representing the elastic behaviour. The loading surface, (yield surface) is constrained to always move inside this spatial dynamic. In general terms, in any bounding surface model, the variation of the state of stress and plastic modulus are defined on the basis of a very simple radial mapping rule. For each actual stress point within, (or on) the bounding surface, a corresponding "image" point on the surface is specified at the intersection of the surface, with the straight line connecting the origin with the current stress point. The actual plastic contribution to the total deformation, is then assumed to be a function of the plastic modulus on the bounding surface, at the "image" point. This is the distance between the actual stress point and its "image". By allowing the plastic modulus to be a decreasing function of the distance of the stress state from a corresponding point on the bounding surface, this feature enables the plastic deformation to occur when the stress state lies on, or within the bounding surface. The bounding surface formulation closely follows classical plasticity, requiring a similar definition of the elastic response, loading (bounding) surface, flow rule, and hardening rule. In addition, it is necessary to define the direction and magnitude of plastic deformation occurring within the bounding surface (see Figure 72).

The bounding surface is determined as  $F(\sigma_{ij}^-, q_n) = 0$ , where  $\sigma_{ij}^-$  is the image of the actual stress point when  $\sigma_{ij}^+$  lies on  $F=0$ , and  $q_n$  is the previous loading history. Figure 72 illustrates the bounding surface in general stress space. Some soil behaviour under cyclic loading cannot adequately be described by the classical mathematical theory of plasticity. This theory does not provide enough flexibility for defining the plastic modulus change with the loading direction. The concept of the bounding surface was originally introduced by Dafalias (1982). The bounding surface and conjunction with the yield surface of metal plasticity can be expressed by stress-strain curves that converge with specific bounds at a rate depending on the distance of the stress point from a



The above equation is very general and can apply to any material. However, for isotropic soil, the bounding plastic modulus is as follows:

$$\bar{K}_p = 3(1 + e_0) \frac{\partial F}{\partial e''} \frac{\partial F}{\partial I'} \quad [21]$$

where;

$I'$ =first effective stress invariant

$e_0$ =initial void ratio

$e''$ =plastic void ratio.

Dafalias (1982) proposed a surface-bounding model for cohesive material with elastic-viscoplastic behaviour. This model's general formulations are as follows:

$$\dot{\varepsilon}_{ij} = \dot{\varepsilon}_{ij}^e + \dot{\varepsilon}_{ij}^v + \dot{\varepsilon}_{ij}^p \quad [22]$$

$$\dot{q}_n = \dot{q}_n^v + \dot{q}_n^p \quad [23]$$

where subscripts e, v, and p represent the elastic, inelastic viscoplastic, and plastic component, respectively.

Crouch et al. (1994) proposed a critical state bounding surface plasticity model for sand. This model used volumetric strain softening and hardening with a single set of material constants. At the same initial void ratio, the higher strength of normally consolidated sand for an undrained test was observed and compared to the results from a drained test and vice versa for overconsolidated sand. This model, however, did not consider the time-dependent phenomenon and fourteen material constants for sand need to be determined in order to use critical bounding surface plasticity modeling for sand. The elastic response affects the normal consolidation line, critical-state line, bounding surface, plastic potential surface and additive plastic modulus.

Papadimitriou et al. (2001) developed a plasticity model for sand under small and large cyclic strain. This model combined the large strain of the bounding surface with a Ramberg-Osgood-type hysteretic formulation for the small strain. Previous accurate simulations had demonstrated the degradation of the shear modulus and the increase of hysteretic damping with cyclic shear strain amplitude. The plastic modulus was considered as a plastic volumetric strain function.

Pender (1982) illustrated cyclic creep, or the ratchetting effect common to many materials' responses. Cyclic creep is not a time-dependent phenomenon; however, it increases due to loading-unloading cycles.

A constitutive stress-strain model for soil based on plastic damage, was proposed by Al-Shayea et al. (2003). This model is suitable for soil with post-peak strain softening, such as dense sand and stiff clay. The total strain was a combination of the elasto-damage formulation and the plastic strain, which was a time factor of the damage strain. The perfect elasto-plastic materials represented the unload at the same modulus as the initial modulus. Figure 73 shows the various strain components. The damage strain is due to the degradation on the initial modulus of elasticity, and the plastic strain is due to the dislocation and permanent readjustment of the soil particles. Therefore, the total strain is:

$$d\varepsilon = d\varepsilon^e + d\varepsilon^d + d\varepsilon^p \quad [24]$$

$d\varepsilon^e$  = Elastic strain

$d\varepsilon^d$  = Damage strain

$d\varepsilon^p$  = Plastic strain .

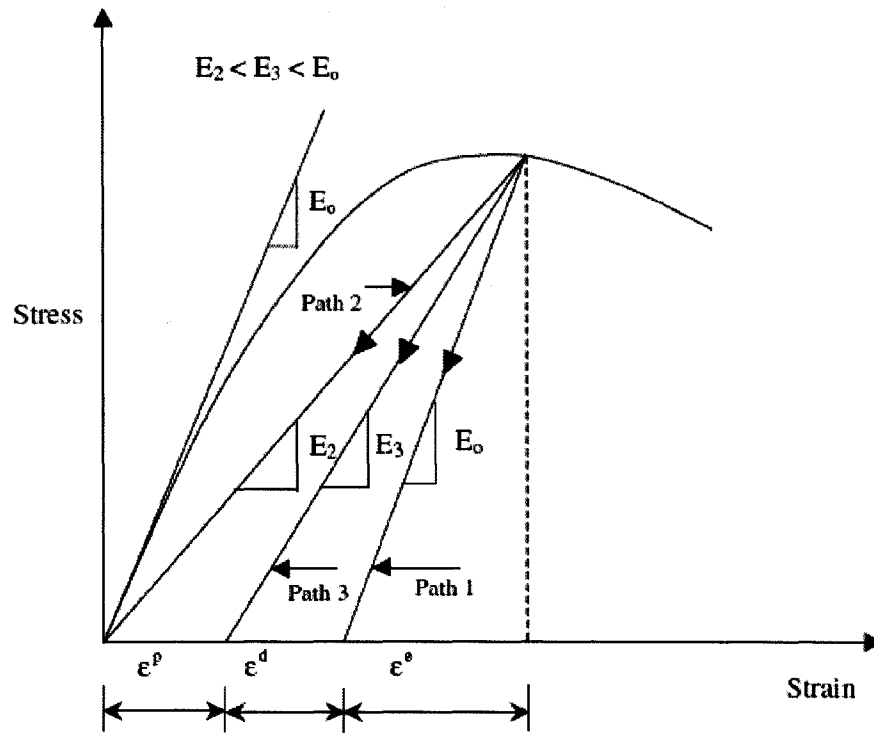


Figure 73: Path 1 ideal plastic deformation, path 2 perfectly brittle material and path 3 combination of plasticity and damage (after Al-Shayea 2003)

## **5 Initial Field and Laboratory Tests**

### **5.1 Introduction**

Laboratory and field tests can increase our understanding of oil sand behaviour. For this purpose, several triaxial tests using oil sand with 8 and 11% bitumen content (volume) were performed. Also, a simple and quick plate load test was proposed and developed. It was designed as a quick field test for the interaction between the ground and ultra-mining mobile equipment. This test is cheaper than the traditional plate load test. Also, the stress-deformation curve can be used to predict the ground deformation for mobile mining equipment.

### **5.2 Hypothesis and Assumptions**

1. Oil sand in the underfoot beneath operating mobile equipment is already broken and is defined as mobile and unlocked sand; however, because of the coarse shapes of the sand particles, considerable friction exists among them.
2. As the material is already broken and mobile, no peak value is easily discernable with increasing strain, and the material expresses post-peak behaviour converging on a residual value.
3. The bitumen and the water content comprising the fluid content remain relatively constant within the active in-pit mining unit.
4. In the vicinity of equipment activities that define as mining block, oil sand is homogenous and uniform, allowing the use of a pseudo-elastic approach to analyze this material despite its highly fragmented and elasto-plastic nature. Mining block is defined as a block of material that has constant grade.
5. In the near surface, pore pressures dissipate rapidly, and the oil sand is not saturated. Therefore, due to its unsaturated condition, pore pressures are not a major concern in calculating the effective stress beneath the equipment.
6. As the near-surface material is broken, any exsoluting gas has already left the material, with a negligible affect on the bearing capacity of the ground material.

Figure 74 illustrates the pseudo-elastic stiffness of the post-peak region, which decreases with an increasing number of cycles.

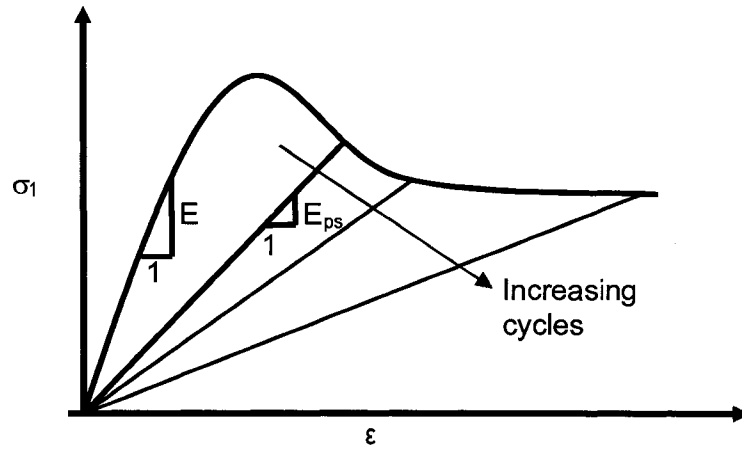


Figure 74: Changing stiffness with number of cycles

Figure 75 illustrates the principle that total deformation may be described as elastic and plastic deformation:  $\delta_t = \delta_p + \delta_e$ , [25]

where;

$\delta_t$  is the total deformation

$\delta_p$  is the plastic deformation

$\delta_e$  is the elastic deformation.

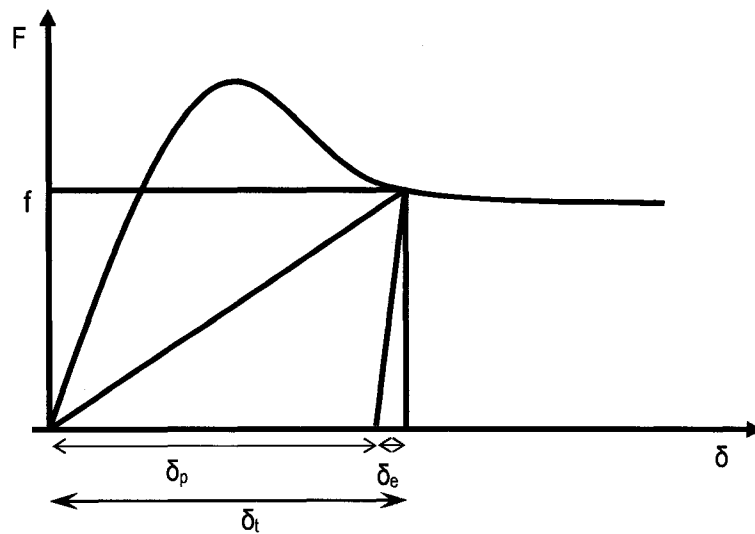


Figure 75: Total deformation in load-deformation curve

## 5.3 Laboratory triaxial tests

### 5.3.1 Conventional and cyclic triaxial tests

The ASTM 2850-95 conventional triaxial test procedure was used as the guidelines for both the conventional and cyclic laboratory triaxial tests. The conventional triaxial test determines, with respect to the given confinements, the stress-strain relationships for standardized cylindrical specimens. The specimen in the cell is subjected to the confining pressure of a fluid, usually water. For unconsolidated-undrained triaxial tests, no drainage from the specimen was permitted.

The apparatus for the conventional triaxial test consisted of the following:

- An axial loading device: A loading device in this case was represented by a screw jack driven by an electrical motor through a geared transmission.
- An axial load-measuring instrument: Electronic and hydraulic load cell devices can measure to an accuracy of 1% of the axial load at failure.
- A triaxial compression chamber, which consists of a top plate and base plate separated by a cylinder. The top plate must have a vent so that air can be forced out of the chamber as it is filled. The base plate has an inlet through which the pressurized liquid (water) is supplied to the chamber.
- An axial load piston, which passes through the top of the chamber to transfer the load to the specimen cap.
- A pressure control device capable of applying and controlling pressures to within  $\pm 2$  kPa for confining pressures less than 200 kPa and to within  $\pm 1\%$  for those pressures greater than 200 kPa.
- A specimen cap and base, which are impermeable rigid units that prevent drainage of the specimen through the circular plane surface of the contact with the specimen.
- A deformation indicator, such as a linear variable differential transformer (LVDT) device, is required for specimen-deformation measurement.
- A rubber membrane was used to encase the specimen to provide reliable protection against leakage in both directions.

- A specimen-size measurement device such as a caliper was used to measure the specimen's height and diameter.
- A data-acquisition system (Data Dolphin) was used to collect and monitor data from the load cell and LVDT by using a set time base.

### 5.3.2 Set-up and procedure

For the conventional triaxial test, the membrane was first placed on a membrane expander, and the specimen was placed on top of the triaxial cell base. The membrane expander was used to assist covering the specimen with the membrane. Next, the cap and the base of the specimen were sealed with O-rings. The triaxial chamber was then assembled, and the load piston brought into contact with the specimen cap. The pressure-maintaining and measurement devices were attached, and the chamber was filled with water manually. The pressure-maintaining and measurement devices were adjusted to the desired chamber pressure, with increasing application of pressure to the chamber fluid. The axial load-measuring device was located outside of the triaxial chamber, while the applied load was transferred via the piston to the specimen. During the test, LVDT and load cell data were collected by using the data-acquisition system as shown in Figure 76. It has been recommended that the axial load should be 1% for plastic material and 0.3% for brittle material (ASTM D2850-95). **The axial load rate for both static and cyclic load were kept at 0.076 mm/Min approximately 0.1%/min.**

For the cyclic triaxial test, the set-up procedure was exactly the same as for the conventional test. However, after the load approached approximately 75% of the peak value indicated in the earlier triaxial tests, the direction of the axial load was reversed (down to up) until the load cell showed no applied load to the specimen. The loading direction was again reversed (up to down) to increase the axial load on the specimen manually. Each cycle took around 2 ½ to 3 hours with axial load rate of 0.076 mm/min or approximately 0.1%/min. This process was repeated several times.

### 5.3.3 Laboratory tests

A triaxial compression test (ASTM D2850-95) was used to determine the stress-strain properties of remoulded oil sand samples. The remoulded samples' diameter was 4.8 cm, and the ratio of the length to the diameter was approximately 2. The standard triaxial test calls for a cylindrical specimen sealed in a rubber membrane to be placed in a cell and subjected to a uniform fluid pressure. The fluid pressure is defined as force acting normal to every unit surface area in the triaxial cell, in the horizontal and vertical directions. Then a vertical load is applied axially to the specimen, increasing the axial stress until the specimen fails. Under these conditions, the axial stress is the major principal stress  $\sigma_1$ , and the minor principal stress  $\sigma_3$  is equal to the cell pressure kept constant during the test. In this research, all the triaxial tests were performed as unconsolidated-undrained (UU), meaning that no drainage was allowed during the application of the cell pressure or confining stress during the triaxial test. Figure 76 illustrates the standard triaxial test and the principal stresses.

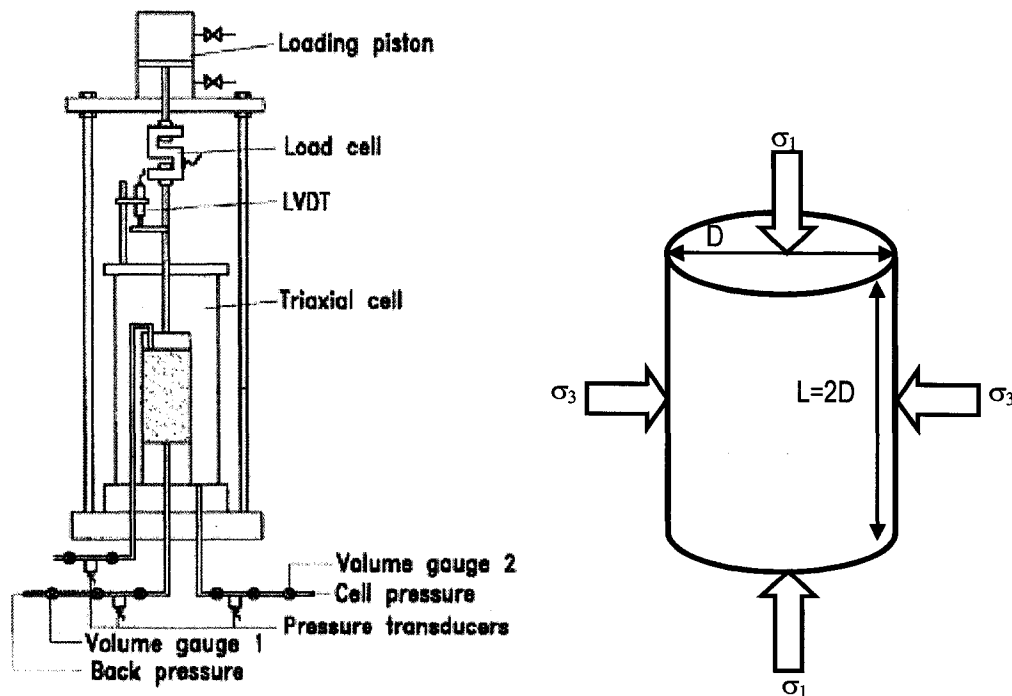


Figure 76: Schematic of triaxial test and principal stresses

To compact 8% oil sand, the disturbed in-pit oil sand was compacted in a kneading compactor by using a two-piece 10.16×20.3 cm cylindrical stainless steel mould. Three layers of oil sand were poured, and for each layer, twenty to twenty-five lifts were used during the sample compaction with the ram pressure at 250 kPa. As the rich oil sand tended to extrude from under the ram foot at high pressure, a flat metal circle, the same size as the cylindrical mould, was added. The initial 4 cm lift, followed by a series of 1.5 cm lifts to the full height, was used during each layer's compaction. The triaxial samples were extruded by using a metal pipe.

Several triaxial tests (ASTM D2850-95) were performed on 8% bitumen samples at a strain rate of  $35 \times 10^{-4}$  per minute and a material density of 2 to  $2.1 \text{ Mg/m}^3$ . This density was chosen according to the literature review. In previous laboratory and field tests, the material density was varied between a density of 1.8 to  $2.1 \text{ Mg/m}^3$ . As the material was broken and loose, the samples required compaction to approach field density for use in a triaxial cell. Figure 77 shows the stress-strain results at varying confining pressures.

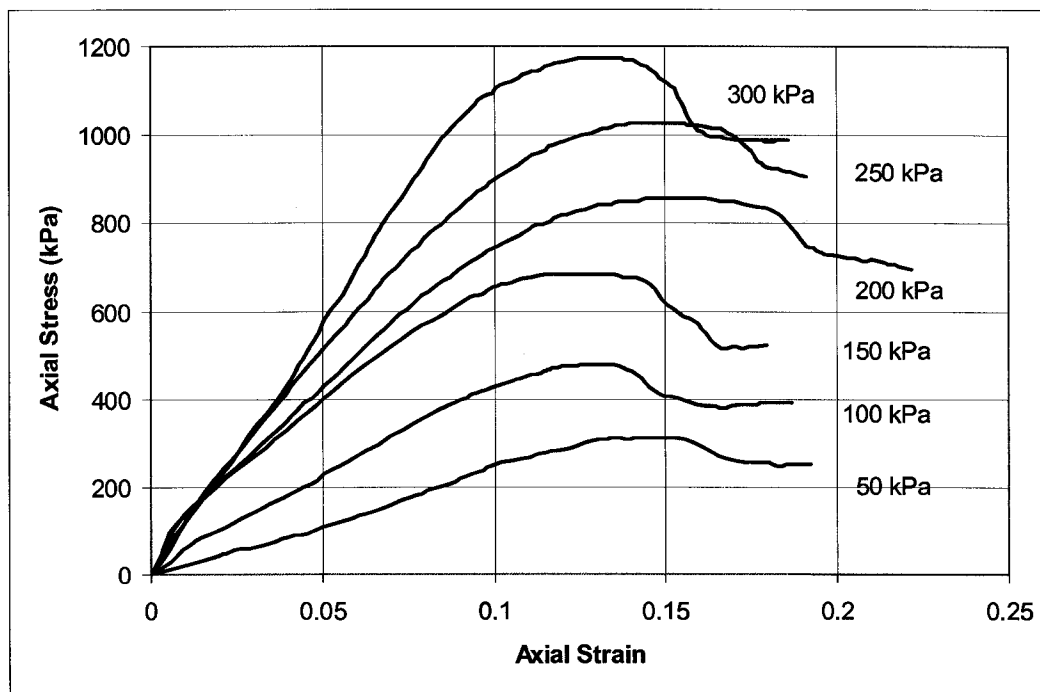


Figure 77: Stress- strain curve for 8% bitumen at room temperature

The peak strain was fairly consistent at around 0.12-0.15, due to the low range of the confining pressures applied, revealing a linear relationship between  $\sigma_1$  and  $\sigma_3$  (see Figure 78):

$$\sigma_1 = 3.65\sigma_3 + 122.5 \quad (\text{kPa}). \quad [26]$$

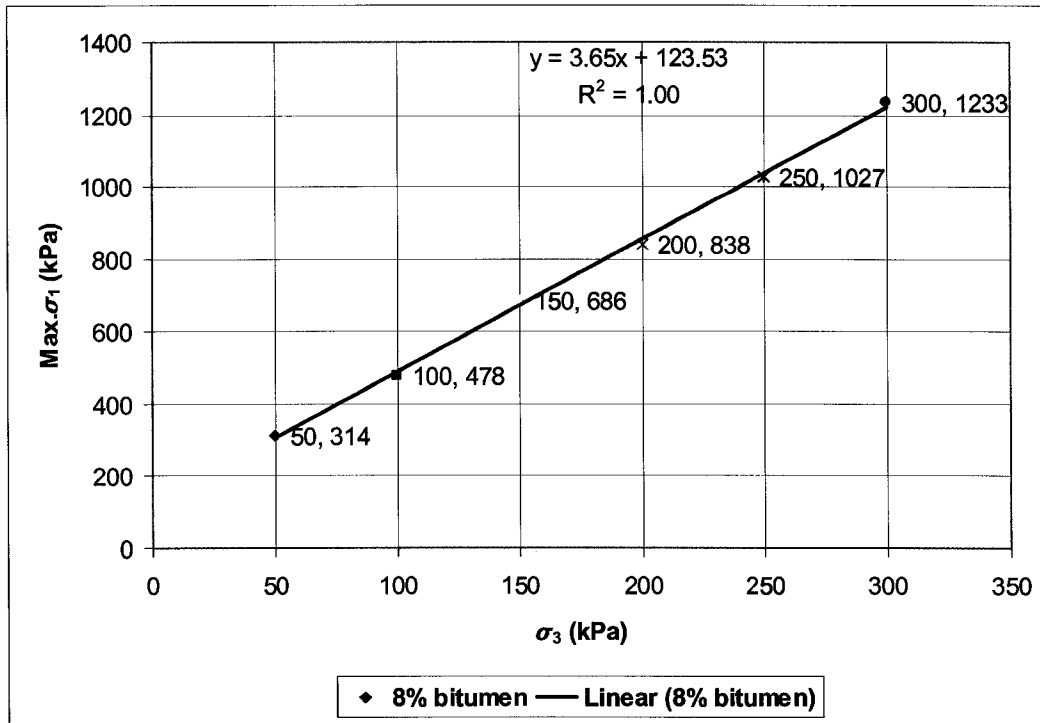


Figure 78: Linear relationship between  $\sigma_1$  and  $\sigma_3$

Further triaxial tests (twenty one) were performed on samples with 11% bitumen content (see Figure 79 and Appendix 1). The strain rate was kept the same, the only difference being the use of a hydraulic jack to compact the sample in a metal cylinder to reach the field density.

In addition to the conventional triaxial tests, three tests were done under cyclic loading at 100, 300, and 500 kPa confining pressures. Figure 79 shows the stress-strain curves resulting from the conventional tests, which are similar to the 8% bitumen, which is a linear relationship that was found between  $\sigma_1$  and  $\sigma_3$  (see Figure 80). Also, Figure 82 shows the cyclic loading and conventional loading comparison for a 300 kPa-confined sample. Three different cyclic loading tests at

different confining pressure were performed. The peak strain was fairly consistent at around 0.04-0.07 for the 11% oil sand triaxial test. The peak strain for the 8% oil sand was around 2.5-3 times greater than that for the 11% oil sand, due to the finer grain of richer oil sand and a tendency towards a better arrangement of the particles during compaction. In addition, the richer oil sand had less clay and silt clasts in the sample and caused less deformation.

The pore pressure can be calculated by:

$$\Delta u = B (\Delta \sigma_3 + A(\Delta \sigma_1 - \Delta \sigma_3)) , \quad [27]$$

where A and B are called the “pore-pressure parameters.” The B parameter, which is known as skempton’s coefficient, has a relationship with the sample’s degree of saturation. If the sample is fully saturated, then the B parameter is equal to one. The A parameter depends on the degree of consolidation and material type. The average rich oil sand’s fluid content (water and oil) is around 15% of the volume, and from literature review, the average void ratio for in situ oil sand is approximately 30 to 35% (volume). Therefore, the degree of saturation, is defined by the volume of water in a soil divided by the volume of voids, for near surface oil sand is 40 to 50% ( $\frac{15\%}{35\%} = 42\%$ ), and the B parameter for this saturation is very small and close to zero. Thus, from equation 27, the pore pressure is negligible compared to the applied load. The effective stress is calculated by

$$\sigma'_1 = \sigma_1 - u, \quad [28]$$

where;

$\sigma'_1$  is effective stress

$\sigma_1$  is applied stress

u is pore pressure.

Therefore, when the pore pressure is negligible, the effective stress is the same as the applied stress.

The cyclic loading tests were performed with the same set-up used as the undrained unconsolidated (UU) triaxial test, and the cycles were mimicked by changing the loading direction during compression shearing. The aim of the cyclic loading test was to understand the behaviour of oil sand under constant confining pressure and very low cyclic loading. As well, this researcher wanted to observe how large mobile mining equipment can induce early failure in underfoot materials and lead to premature residual values. Figure 82 illustrates the softening of the ground via cyclic loading is the mechanism by which mobile mining equipment loads the ground. Appendix 1 presents the series of laboratory cyclic and conventional tests. Table 5 summarizes the laboratory sample properties. The strain rate for the laboratory tests was chosen as 0.1%/min or 0.076 mm/min to get the test duration to around 3 to 4 hours as ASTM recommended.

Table 5: Summary of laboratory sample properties

<b>Oil Sand % (volume)</b>	<b>Density</b>	<b>Diameter sample (mm)</b>	<b>Length / Diameter</b>	<b>No. of tests</b>	<b>Average strain at peak strength</b>
8%	1.99	49.06	2.18	6	0.12-0.14%
11%	1.99	52.24	2.03	19	0.05-0.07%
11% Cyclic	2.02	51.86	2.04	3	----

The undrained triaxial tests conducted by this researcher on 8% and 11 % bitumen gave different results, so it can be concluded that oil-sand behaviour is highly variable depending on the grade and degree of disturbance. When large mining mobile equipment is used, the ground is highly disturbed, with a trend towards residual behaviour. Hence, the material properties for this investigation will veer towards those of broken material and residual behaviour. Joseph (2000) studied the post-peak behaviour of broken material. Figure 81 through Figure 83 compares the cyclic loading test versus conventional triaxial test at constant confining pressures at 100, 300 and 500 kPa. Figure 81 through Figure 83 show that the cyclic loading from mobile mining activity can trigger the stress-strain curve. However, these graphs do not show any effect on the peak values due to cyclic loading at constant confining pressure.

Figure 84 illustrates time strain curve for the three triaxial cyclic loading, performed at a constant confining pressure of 100, 300 and 500 kPa. Little similarity can be found from this when comparing results with the field cyclic plate loading testing (see Figure 93).

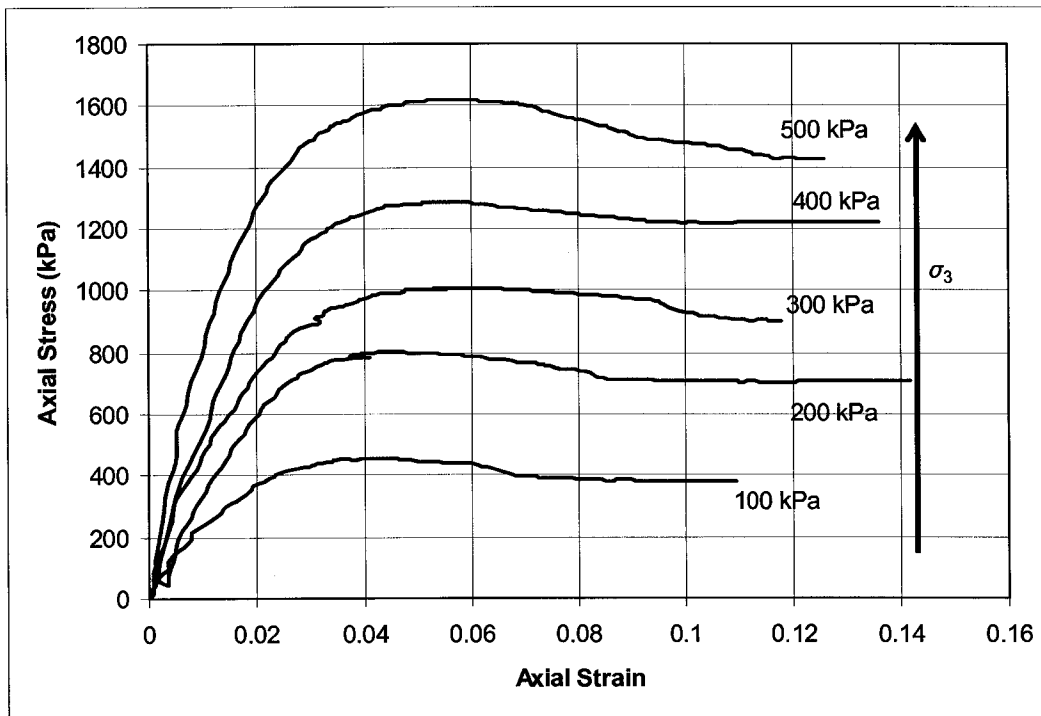


Figure 79: Stress-strain curve for 11% bitumen

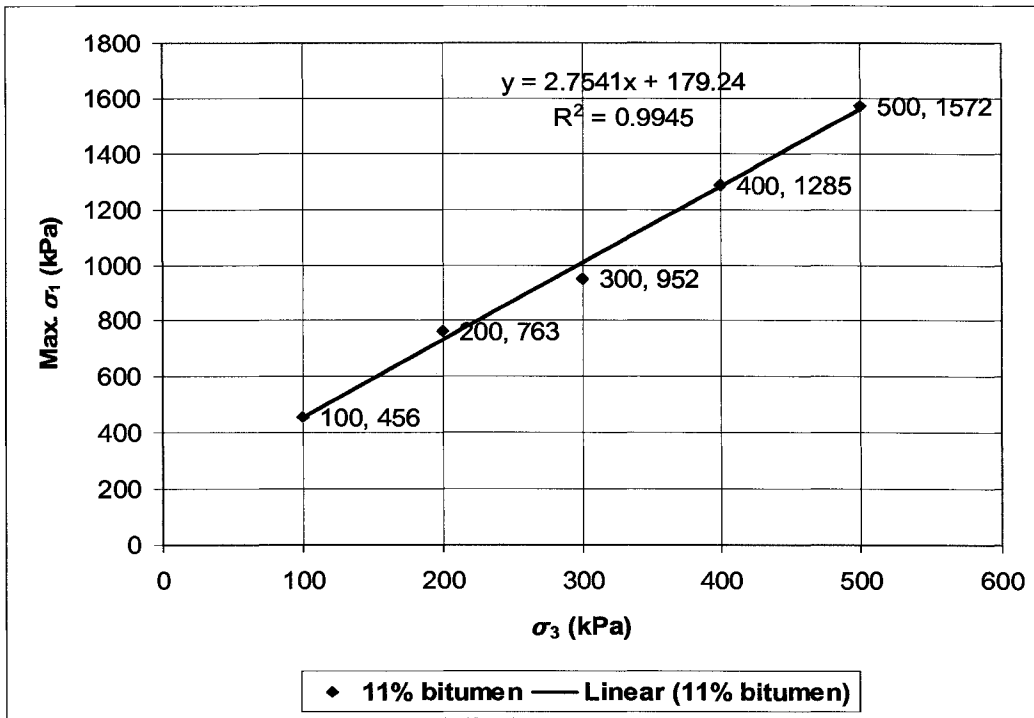


Figure 80: Linear relationship for 11 % bitumen between  $\sigma_1$  and  $\sigma_3$

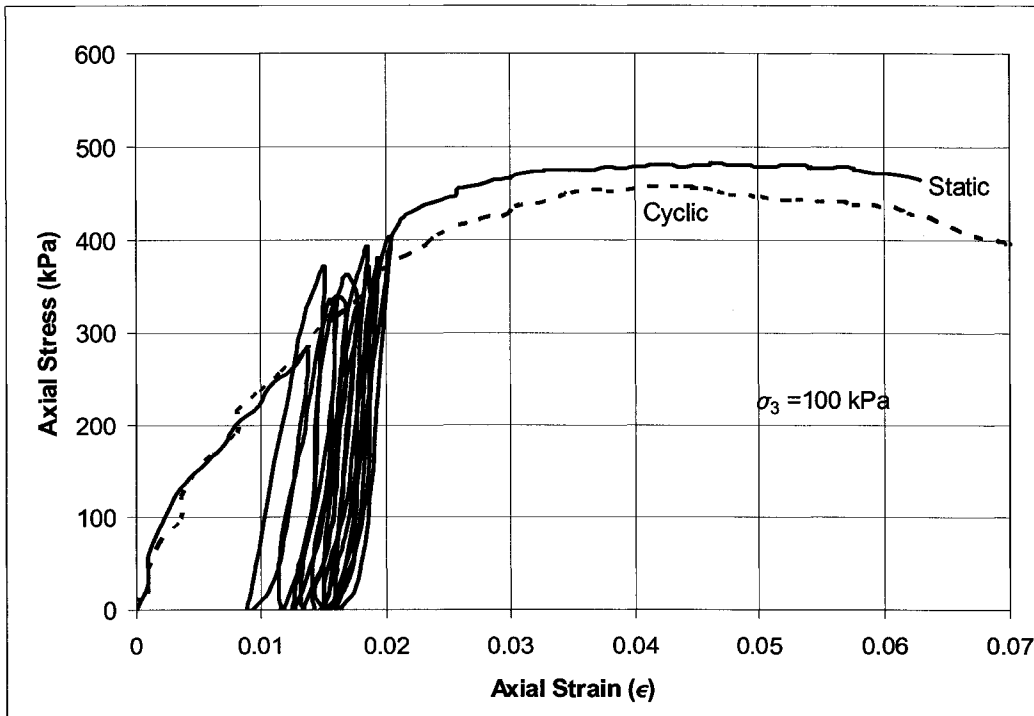


Figure 81: Cyclic and conventional stress-strain curve comparison for 100 kPa confining pressure

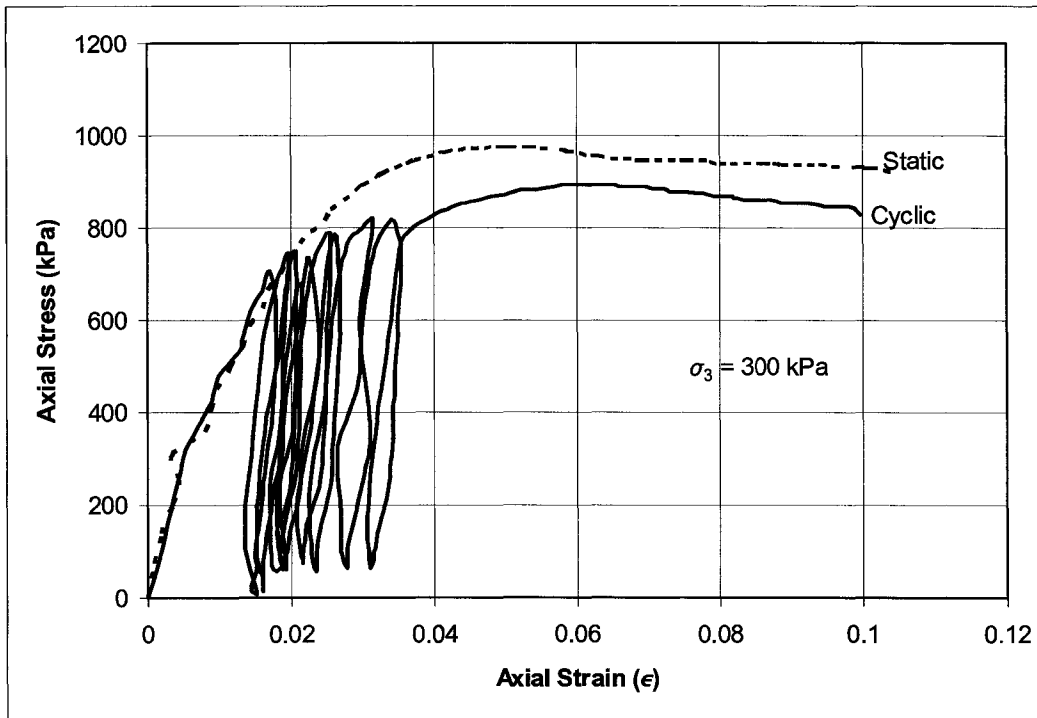


Figure 82: Cyclic and conventional stress-strain curve comparison for 300 kPa confining pressure

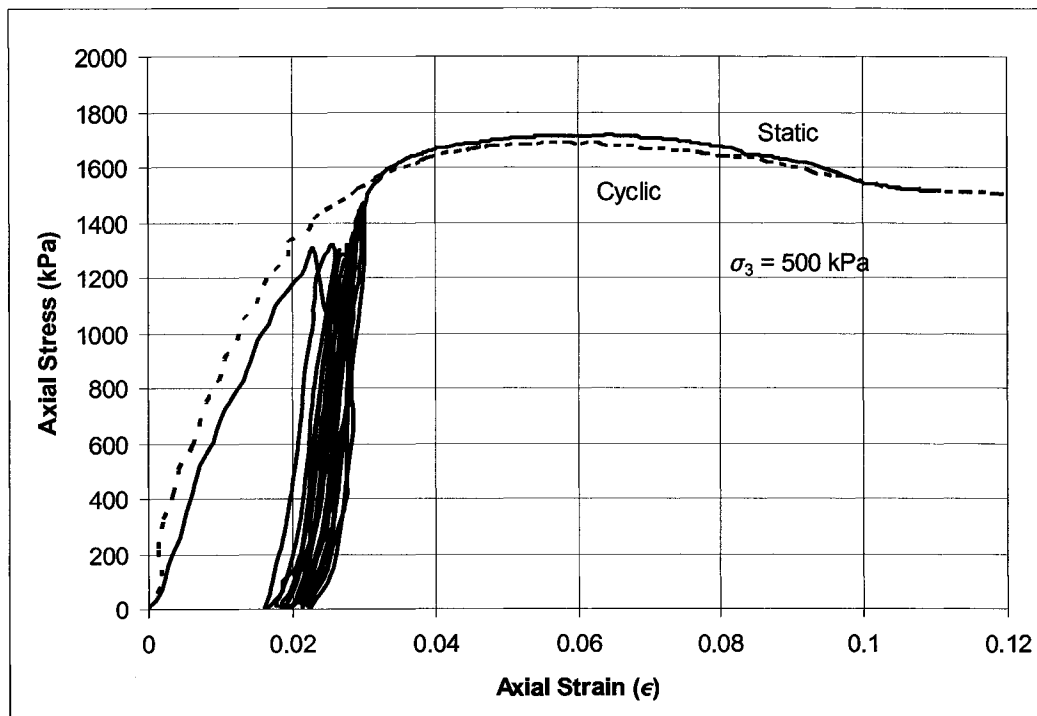


Figure 83: Cyclic and conventional stress-strain curve comparison for 500 kPa confining pressure

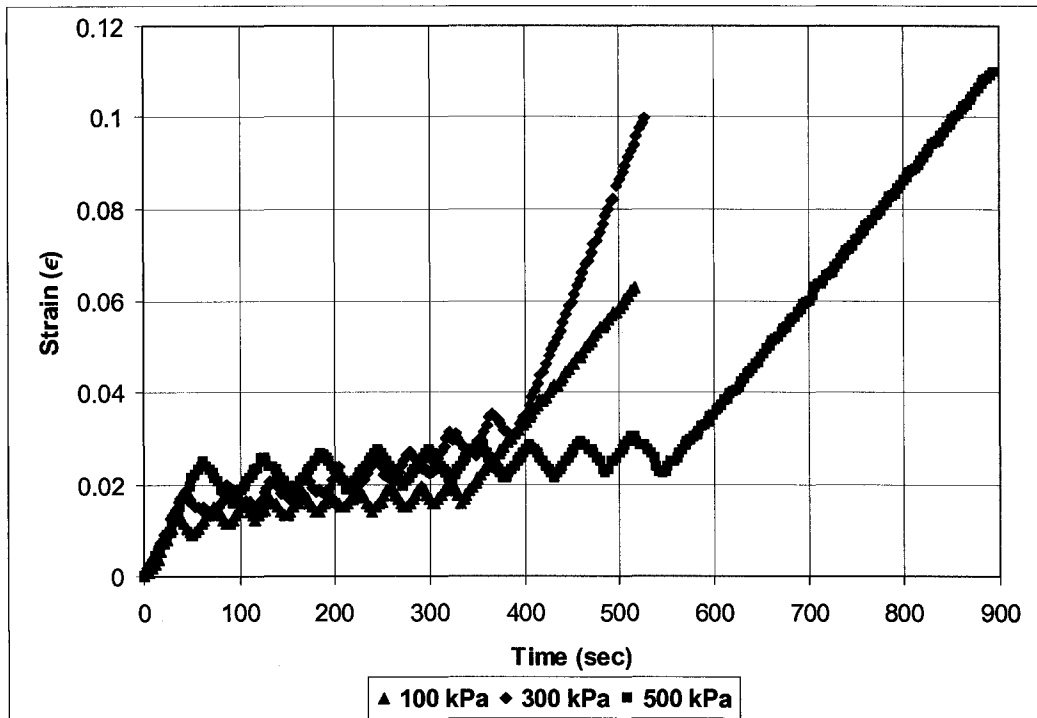


Figure 84: Time - Strain curve for triaxial cyclic loading

### 5.3.3.1 Material properties of tested Oil sand

The fundamental shear strength of soil is through an equation proposed by the French engineer Coulomb (1776):

$$\tau_f = c + \sigma_n \tan \phi$$

$\phi$  is the angle of friction in degree

$c$  is the 'cohesion' intercept in kPa

The shearing strength at zero normal pressure on the plane of rupture, defined the cohesion of a soil, with  $c$  and  $\phi$  as empirical parameters in the mechanics of Coulomb's equation. The Mohr-Coulomb envelope was drawn for 8 and 11% oil sand. Illustrated in Figure 85, the Mohr-Coulomb equation for 8% oil sand is " $c$  is equal to 33.5 kPa", and " $\phi$  or friction angle is equal to 35 degrees". In the Mohr-Coulomb for 11% oil sand, Figure 86 illustrates " $c$  as equal to 28 kPa", and " $\phi$  or friction angle, as equal to 28 degrees". As past researchers indicated, remoulded oil sand has a lower friction angle, compared to the in situ oil sand because of the disturbance of interlocking oil sand. It was discovered that the 11% oil sand had a

slightly lower friction angle, compared to 8% oil sand. This finding may be due to the accumulation of finer material, which occurs with the increase of oil sand content.

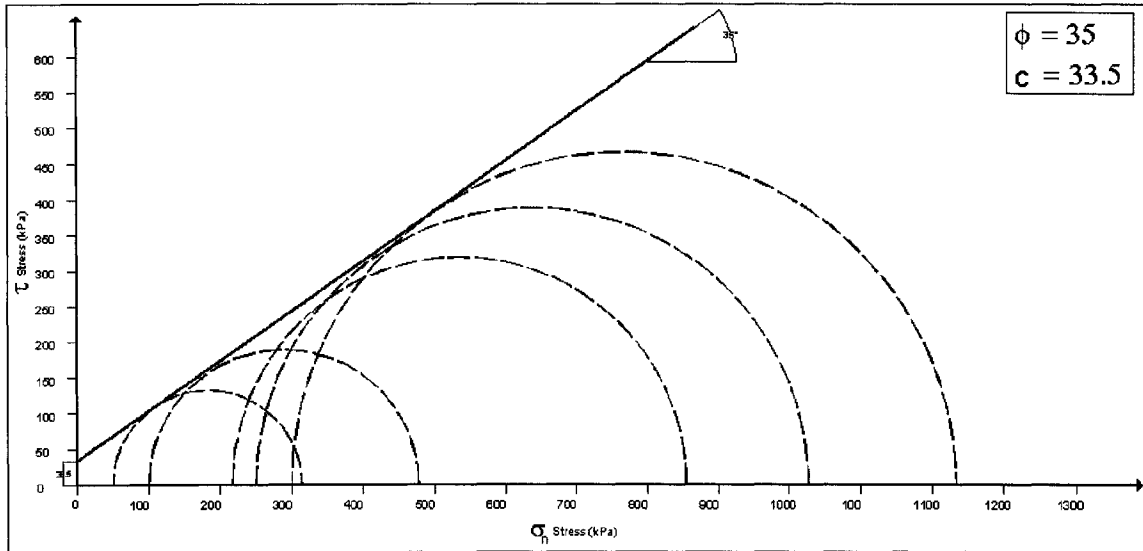


Figure 85: Mohr-Coulomb envelope for 8% oil sand

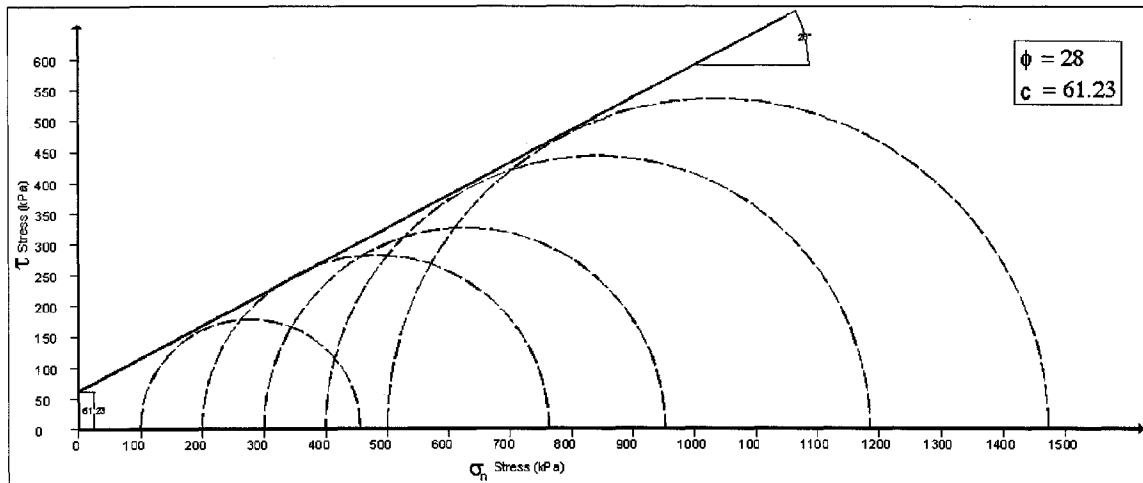


Figure 86: Mohr-Coulomb envelope for 11% oil sand

#### 5.4 Field tests

The conventional plate load test is expensive and slow, as well as difficult to use to mimic mobile mining equipment cyclic loading. Plate bearing (plate-load) tests,

used to determine sub-grade modulus and occasionally to determine strength, are easily conducted on soil or soft rock. The usual procedure is to jack-load a 30- or 76-cm (12- or 30-in.) diameter plate, against a reaction twice the design load, measuring the deflection under each loading increment. The applied load is measured using calibrated electronic load cell. With an error not exceeding  $\pm 2\%$  of the load increment used, or 1% of maximum load, whichever is lesser, the force measuring devices should be capable of recording the load. The sub-grade modulus is the ratio of unit pressure, to unit deflection. The settlement-recording devices, such as dial gauges, should be able to measure to an accuracy of at least 0.25mm. For correction of dial gauge readings, precise levelling optical survey (to accuracy of 0.01mm) with respect to fixed datum, will be carried out to measure plate settlement and movements of the reference beam. To minimize errors of measurement, which can easily arise, the reference beam and measuring devices will be protected from the direct rays of the sun and wind, with the use of tarpaulins, or other forms of shelter. Because of cost, such tests are normally performed during advanced design studies or during construction.

The simple cyclic plate load test uses a 10 tonne hydraulic cylinder mounted on the back of a half-ton truck to generate the load, a load cell to measure the load, and a plate to transfer the constant pressure to the ground. The deformation was measured by using a spring extensometer. Also, a hand pump was used to pump hydraulic oil and to create the cyclic loads. The data from the load cell and extensometer were collected by using a 0.33 Hz data acquisition system.

#### **5.4.1 The plate load cyclic field test**

The cyclic plate load test was a modification of the ASTM standard test method for the bearing capacity of soil for a static load and spread footings D 1194-94. This modification was made to facilitate the use of the tests for the scaled estimating of the cyclic footprint loading and the deformation prediction due to ultra-class mobile mining equipment's motion. The apparatuses used for the cyclic plate load test were the following (see Figure 87):

- A hydraulic jack and manual pump assembly to effect loading to a circular plate at the ground contact, providing loads akin to those of the cyclic triaxial test.
- An electronic load cell to measure the loads during the test.
- An S-shaped bearing frame to bear the applied load, fixed to the hitch of a light vehicle for easy field use.
- A ground deformation measurement device, in this case a spring extensometer, to measure ground deformations and rebounds during cyclic loading.
- Bearing plates of different diameters to transfer the load to the ground.
- A data-acquisition system to collect data from the load cell and extensometer.

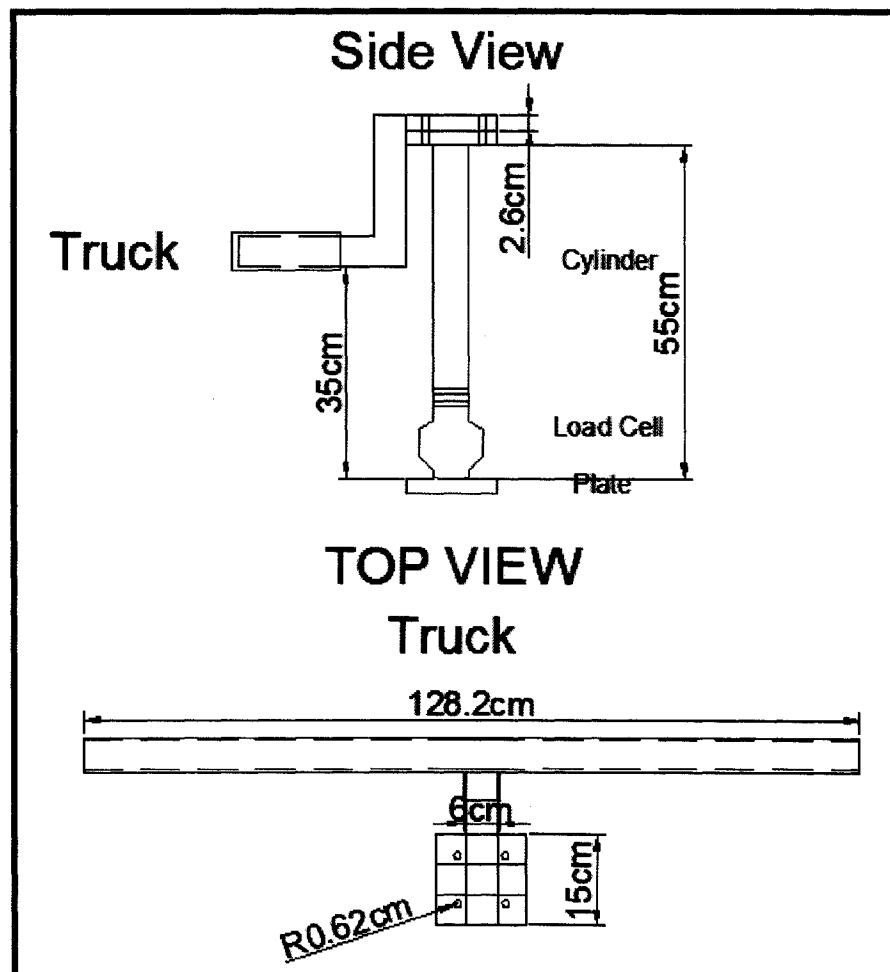


Figure 87: Cyclic plate load apparatus

#### 5.4.2 Set-up and procedure

After selecting in-pit ground that was approximately flat, the frame was mounted to the rear hitch of a half-ton truck. The hydraulic jack was connected to the square plate on the underside of the bearing frame. The load cell was placed between the hydraulic jack and the foot circular plate. The load on the plate was applied by manual application of the hydraulic jack. The corresponding plate settlement was measured via the spring extensometer installed on an independent frame outside the range of the loading action. Therefore, during the test, truck motion fluctuation had no influence on settlement readings. A small hook on the top of the plate connecting the extensometer to the plate allowed both the deformation and rebound to be measured. Data were collected by using a "Data Dolphin" acquisition system every 3 seconds. Test duration was completed for each plate size by loading and unloading. To mimic the cycles, the time was logged for the loading, the unloading, and the intervals between the loading and unloading activities (see Figure 88).

A variation on the conventional plate load test was designed to provide a better understanding of the behaviour of oil sand under mobile mining equipment loading. Inferring ground behaviour from laboratory tests is difficult, especially for near-surface material, due to the many factors affecting the behaviour of soil under equipment. The cyclic plate load test device was made to be simple, fast and easy to use and comparable to the traditional plate load test.

The cyclic plate load test was conducted in a newly opened oil sand bench. Thirteen cyclic and static tests were conducted at three different locations. The average grade of the bench varied from 8%-10% bitumen content. The grade was printed on the mine section bench plan that the mine had prepared. The temperature was 0°C, and ground was still soft (unfrozen). The average density was approximately 1800 kg/m<sup>3</sup> for most of the bench area. However, for the pre-compacted area (old shovel track) the density was around 1900 1800 kg/m<sup>3</sup>. However, the old shovel track path had harder ground or higher density due to pre-compaction. Two tests conducted in the old shovel track path that showed higher initial stiffness. For the short-duration tests, punching failure was

observed. However, for tests greater than 5 minutes, the failure changed from punching to local shear failure, with circular bulging diameters of 1.5-1.75 times the plate size. The ground rebounded approximately 5mm after removing the plate after a one-hour period. In relation, the empty weight (curb weight) of the truck was 1.6 tonnes (3756 lbs). The distribution of curb weight of vehicle, according to the manufacturer, is 55% in the front, and 45% in the rear. As shown in table 6, during the jacking up of a truck, a maximum truck slope of 35 degrees will result in maximum pressure being placed on different plate sizes.

Table 6: Maximum pressure according to truck weight

Plate Size	Maximum Pressure (kPa)	Calculation
Large	336	$\text{Cos}(35^\circ) \times 45\% \times 1.6 \times 9.8 / 0.017437$
Medium	571	$\text{Cos}(35^\circ) \times 45\% \times 1.6 \times 9.8 / 0.010261$
Small	1285	$\text{Cos}(35^\circ) \times 45\% \times 1.6 \times 9.8 / 0.00456$



Figure 88: Cyclic plate load test in the field

Tests were carried out with three different plate sizes. Table 7 shows the plate sizes and maximum stresses reached during the tests, a function of the reaction weight of the light vehicle. The summary of all tests is reported on Appendix 2.

Table 7: Plate size and test information

<b>Plate size cm (inch)</b>	<b>Max stress (kPa)</b>	<b>Max duration of test (min)</b>
large 14.9 (5.87")	300	9:39
medium 11.43 (4.5")	420	1:21
small 7.62 (3")	961	2:00

To be illustrated later by modeling the field plate load test, it has been shown that induced pressure is a function of the initial loading. It has also been found, that maximum stress is dependent on the plate size, and the weight of the vehicle, with the magnitude of confining pressures occurring during the test a natural function of the plate size. As shown in Figure 89 and Figure 93, plastic deformation is a function of the induced, confining pressure or the initial loading, as well as time required and number of cycles performed in the loading. The rebound of the material after removing the load is time-dependent, and related to the relaxation of the induced confining pressure. The response of the ground to impact, corresponded to 3 different stages: a loading stage incremental to a maximum value; a post-peak decreasing load stage, where active loading was stopped, allowing the ground to exhibit pressure relief by deformation; and finally, an unloading stage on complete load removal. The different stages of the test are shown in Figure 89. The loading stage time for different tests was varied from 12 seconds to 579 seconds (9 minutes and 39 seconds).

By normalizing the load by plate size using pressure instead of force, the effect of the plate size was eliminated. To understand how the slope of the pressure-deformation graph changed during different stages of the test, the slope (pressure stiffness) of a point on the pressure-deformation graph was evaluated. The pressure stiffness (deformation divided by pressure) has advantages compared to stiffness (deformation divided by force), because of normalization of the stiffness by the contact area (plate size). It was revealed that the pressure stiffness reached a constant value with the increasing deformation. Moreover, the

pressure stiffness during a decreasing load subsided with elevation of deformation (see Figure 90).

Figure 90 illustrates the pressure stiffness (kPa/mm), versus deformation of the loading portion of Figure 89. The benefit of the pressure stiffness instead of stiffness (N/mm) does not depend on the plate size. On the initial attempt, with the pressure stiffness approach and modified plate load test, these results were obtained to predict deformation for mobile mining equipment. The dash box in Figure 90 shows that the pressure stiffness reaches the constant value, regardless of the plate size and test duration.

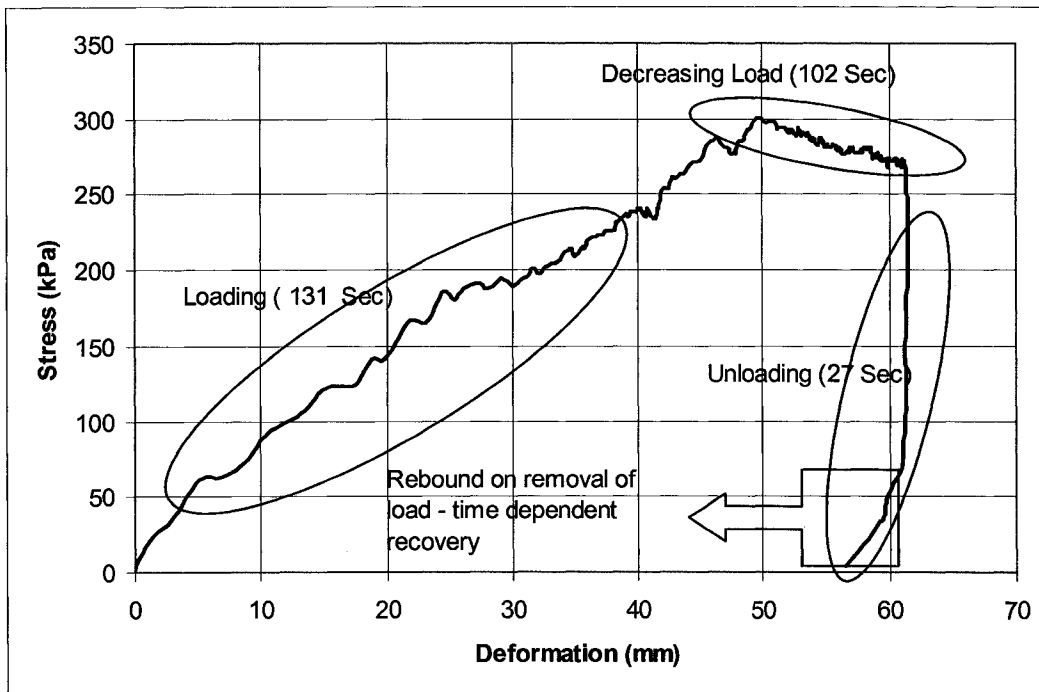


Figure 89: Stages of a cyclic plate load test

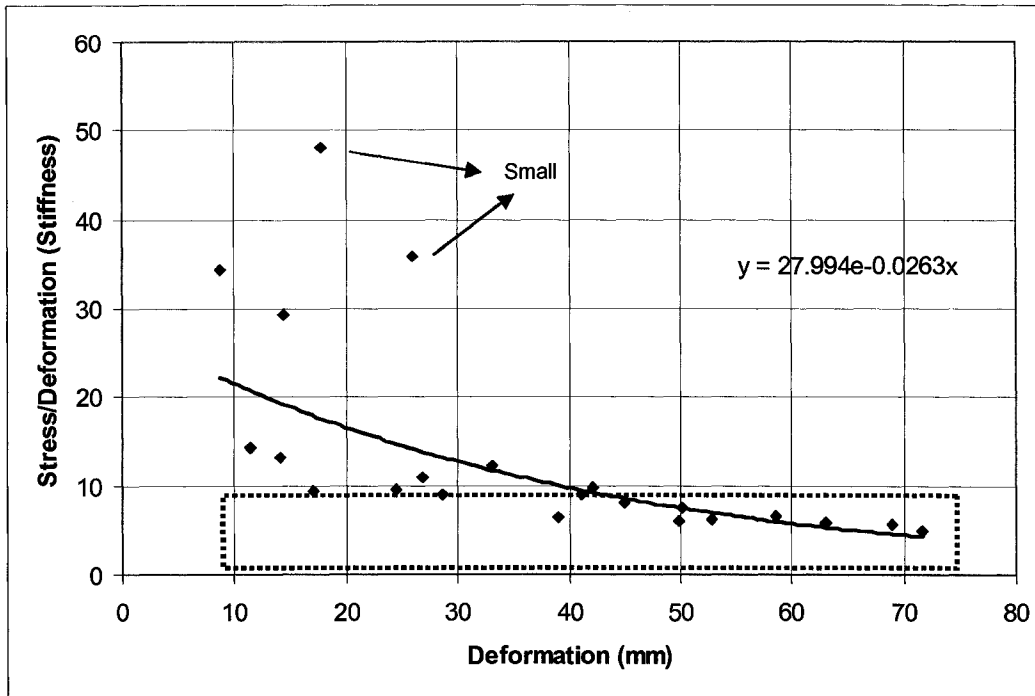


Figure 90: Changing stiffness during loading for oil sand

Appendix 3 presents the entire cyclic plate load test results. Thirteen plate load tests were conducted. By plotting the total test results, two groups of curves were recognized. The majority of the tests were consistent in terms of stress-strain that was named as group two (see Figure 91). Only two tests were run, and the pre-compacted field zone exhibited a higher stiffness that was named as group one.

Figure 92 illustrates the stress-deformation relationship for oil sand for a cyclic test of around 46 minutes duration and containing 7 cycles. The average time for each cycle was approximately 7.5 minutes. The unloading and loading slopes are relatively consistent. The unloading slope is 0.095 kPa per millimetre. As oil sand has a viscous behaviour, the rebound cycle is time-dependent. Therefore, deformation should be a function of time and stress. Moreover, by plotting the deformation versus the time, it can be shown that the plastic deformation increased with test duration and that the elastic deformation reached a constant value (see Figure 93). Table 8 shows the time for each stage of the cyclic plate load test.

To be able to separate the plastic and elastic deformation during the test, the deformation versus the time was plotted. Figure 93 shows the plastic and elastic deformation components of the cyclic test with respect to time when the elastic deformation (bounded) converges to a constant value. As the graph shows, the plastic deformation increased with increasing time, with the total deformation being the elastic plus the plastic or the permanent deformation. The upper bound deformation shows the total deformation for a constant loading over a given time. The elastic value reaches a constant value after that time, with any cycles converging on a residual value.

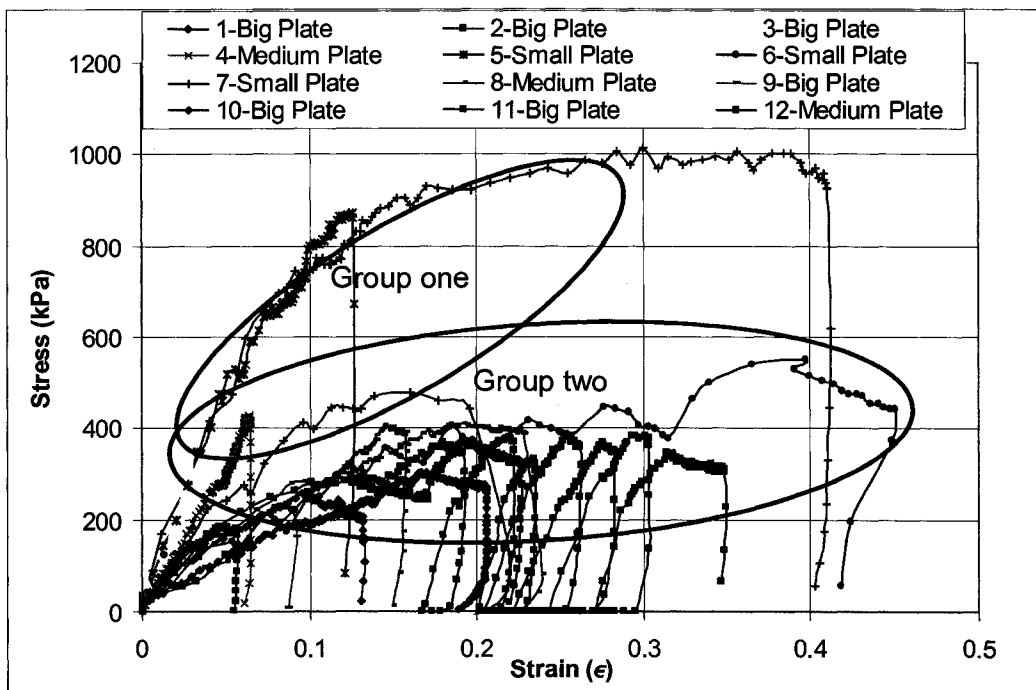


Figure 91: All cyclic plate load test

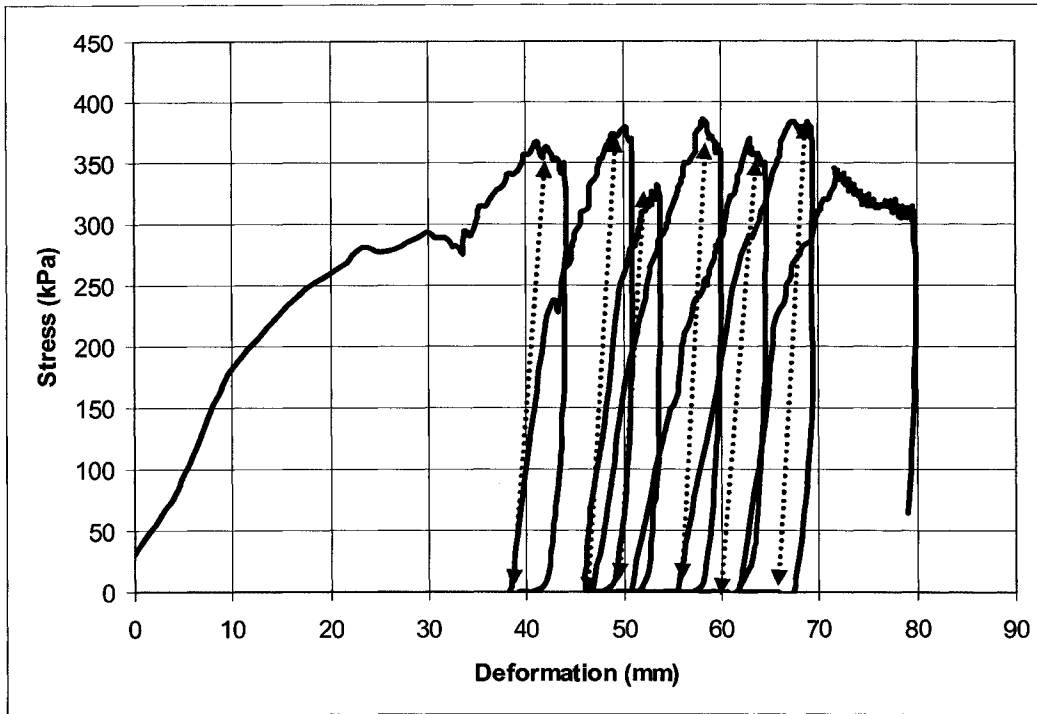


Figure 92: Stress-deformation curve for a cyclic test, showing unload-reload cycles

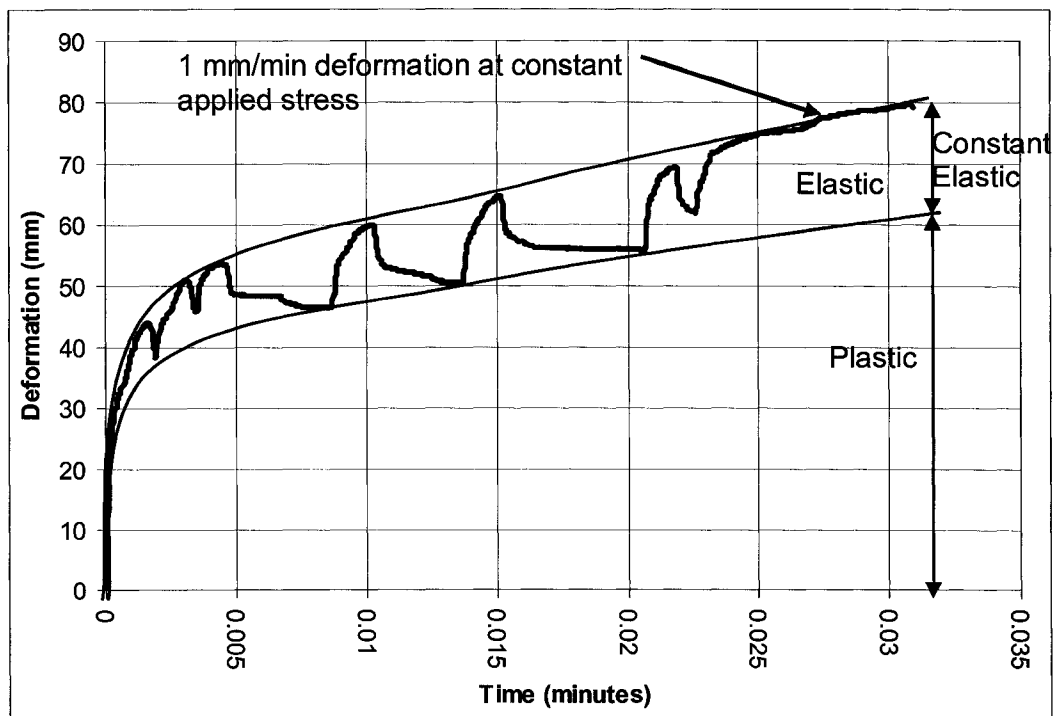


Figure 93: Plastic and elastic deformation components

Table 8: Time line for cyclic plate load test

<b>Test Stage</b>	<b>Hour; Min : Sec</b>
Loading 1	0:01:39
Decreasing load	0:00:36
Unloading 1	0:00:21
Holding unload 1	0:00:09
Loading 2	0:01:24
Unloading 2	0:00:36
Holding unload 2	0:00:12
Loading 3	0:00:45
Unloading 3	0:01:03
Holding unload 2	0:05:45
Loading 4	0:01:21
Decreasing load	0:00:45
Unload 4	0:00:18
Holding unload 3	0:04:48
Loading 5	0:01:15
Decreasing load	0:00:45
Unloading 5	0:00:12
Holding unload 4	0:07:51
Loading 6	0:01:21
Unloading 6	0:00:27
Holding unload 5	0:01:03
Loading 7	0:00:57
Decreasing load	0:10:51

## **5.5 Modeling of a plate load test with FLAC**

### **5.5.1 Background of FLAC software**

FLAC, or Fast Lagrangian Analysis of Continua, is used for modeling the static mechanical analysis for geotechnical engineering application. FLAC uses the finite difference equation for each element, relating the forces at the nodes to the displacement at the nodes. For the elastic material, the resulting elements are identical to those obtained by using the finite element method for the constant triangle elements.

FLAC is two-dimensional explicit finite difference method software. Several materials can be used when modeling with FLAC, which also has the ability to customize calculations.

- Elastic
  - Elastic, isotropic model
  - Elastic, transversely isotropic model
- Plastic
  - Drucker-Prager model
  - Mohr-Coulomb model
- Ubiquitous-joint model
- Strain-hardening/softening model
- Bilinear strain-hardening/softening ubiquitous-joint model
- Double-yield model
- Modified Cam-clay model
- Creep model

FLAC works based on the finite difference method, which is perhaps the oldest numerical technique used for the solution of the sets of differential equations, given the initial values and/or the boundary values. In the finite difference method, every derivative in the set of governing equations is replaced directly by an algebraic expression written in terms of the field variables (e.g., stress or displacement) at discrete points in space; these variables are undefined within

elements. In contrast, the finite element method's central requirement is that the field quantities (stress, displacement) be varied throughout each element in a prescribed fashion, by using specific functions controlled by the parameters. The formulation involves the adjustment of these parameters to minimize error terms or energy terms. The general calculation sequence embodied in FLAC is illustrated in Figure 94 (FLAC 2002).

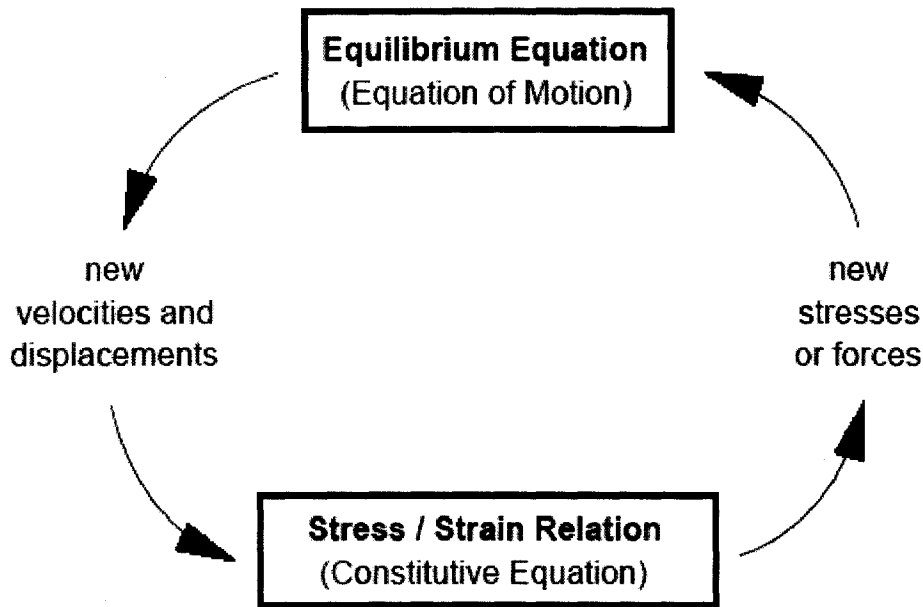


Figure 94: General calculation sequence in FLAC (after FLAC 2002)

### 5.5.2 Modeling

Numerical modeling of a plate load test allows a simple field elastic approach to be used to predict the ground deformation during the loading of oil sand. Here, the basic assumption is that oil sand is uniform and that homogenous load deformation behaviour is like elastic deformation behaviour, although permanent deformation occurs. FLAC 2-D was used to model the cyclic plate load field test and ground deformation, as the software provides the user with defined constitutive modeling or even empirical equation. As shown in Figure 95, the circular plate is symmetric and can be modeled by using only one-quarter of the circle. Also, it was assumed that the soil particles exactly beneath the center of the circular plate could move only in a vertical direction and that no horizontal

movement occurred. The boundary dimension for the bottom and right side of the model was 3 times the dimension of the plate diameter so that the plate would have minimal effect on the boundaries. Three different plate sizes were modeled. Figure 96 illustrates the boundary conditions and the applied loads used. By modeling the 2-D motions of soil particles beneath a plate, the particles were located exactly at the center of the plate, assumed to move only in a vertical direction, as a constant pressure was applied to the circular plate. The elastic modulus was defined as the slope of the stress-strain curve for each point. The load was applied on the 3 grids on the top left side of the mesh. Table 7 was used for applied load input for FLAC modeling. Unfortunately, FLAC can not handle the time dependency during applying of the load. Therefore, for field plate load test only the first portion of the graph or initial loading was modeled. To avoid causing instability from a high-applied load (for small- and medium-sized plates), the load was applied in different stages. From the triaxial laboratory tests, the elastic modulus for the material  $E \text{ (kPa)} = 25\sigma_3 \text{ (kPa)} + 1465$  is the pre-peak elastic modulus for the 8% and for 11% bitumen content is  $E \text{ (kPa)} = 148 \sigma_3 \text{ (kPa)} + 2574$  (see Figure 97).

By holding Poisson's ratio constant, and varying the elastic modulus with induced confining stress changes such that  $E \text{ (kPa)} = 25\sigma_3 \text{ (kPa)} + 1465$  (Figure 97), the following results were found. The small plate modeling results showed that for an induced confining pressure of 50 kPa, the resulting deformation increased until the load reached a constant value, accurate to  $\pm 15\%$  of the actual field values. Figure 98 through Figure 101 illustrate the vertical stress, horizontal stress, vertical deformation and  $\sigma_3$  for the large plate configuration. The boundary of modeling was around 3 times of the plate size. Modeling results of stress and deformation showed that the boundary was big enough to give a modeled result approaching to zero around 0.2 metres from the center point of the plate. The induced confining pressure from FLAC modeling for different plate size is shown in Figure 104. The vertical deformation was shown to have an error of -15% of the actual values from the field tests. As was mentioned previously, oil sand has a viscous behaviour; therefore, the 15% error may come from the time a load takes to reach a maximum value. In the modeling, however, this process is instantaneous. Appendix 4 presents the FLAC results for the medium and small

plates. Figure 102 shows the unbalanced force for the large-sized plates. This force reached the steady state or equilibrium after 5000 steps. The equilibrium force shows the steady state of the model's results. Figure 103 illustrates the summary of the maximum deformation and stresses beneath the plate, as obtained from the FLAC modeling. These values are the maximum values that occurred exactly beneath the circular plate.

The horizontal stress from the FLAC modeling shows in Figure 104. The induced confining pressure for different plate sizes were around 0.27 times of the applied vertical load. The horizontal stress value of the modeling was taken from the maximum stress that was at the edge of the plates.

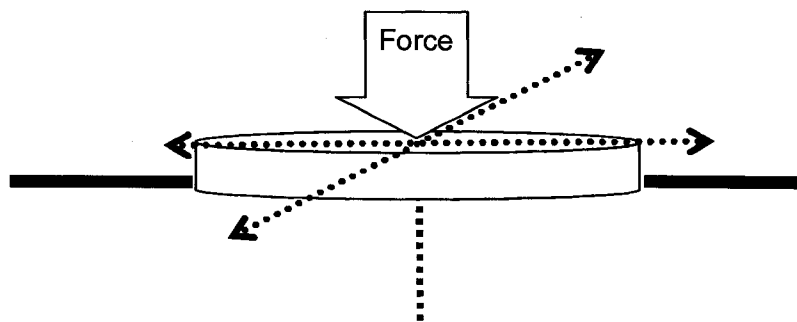


Figure 95: Modeling of circular plate

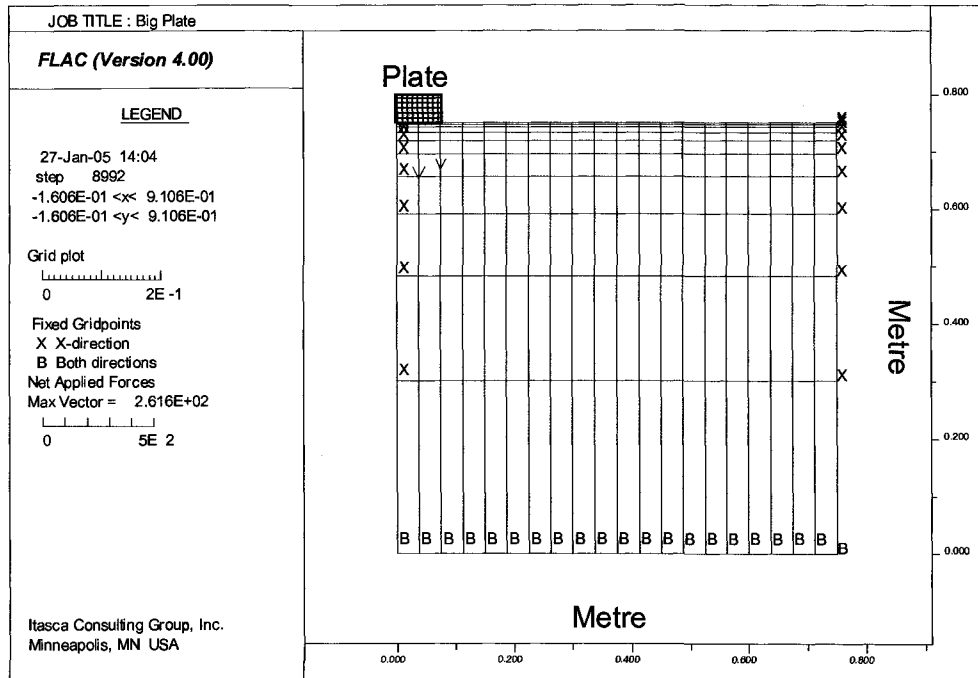


Figure 96: Boundary condition and applied load

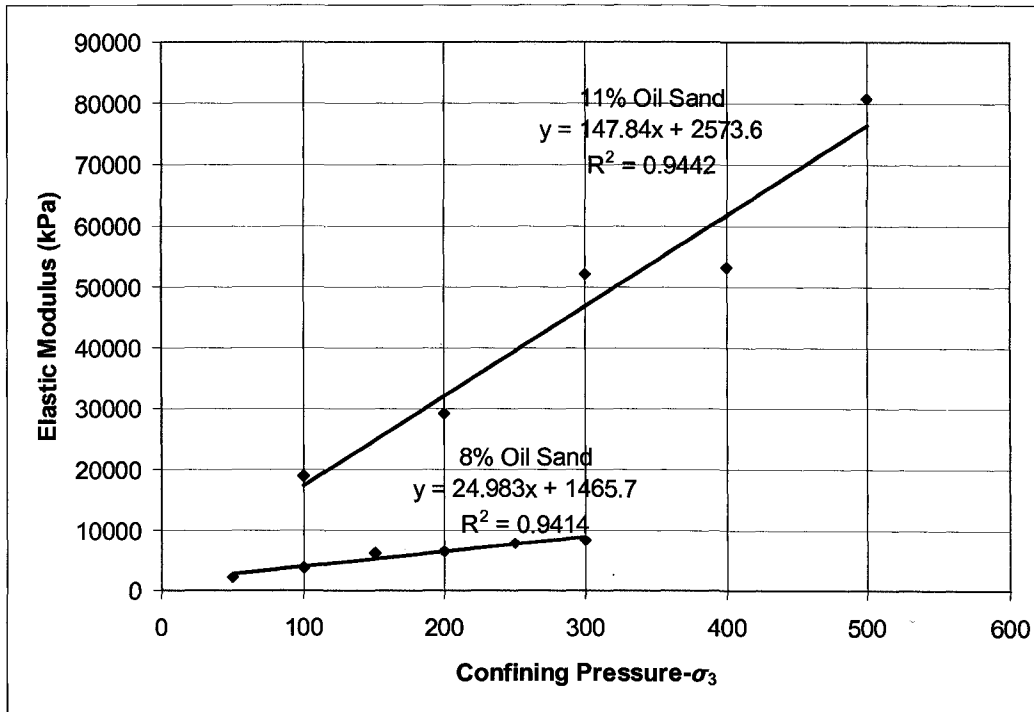


Figure 97: Elastic modulus change with confining pressure for 8 and 11% oil sand

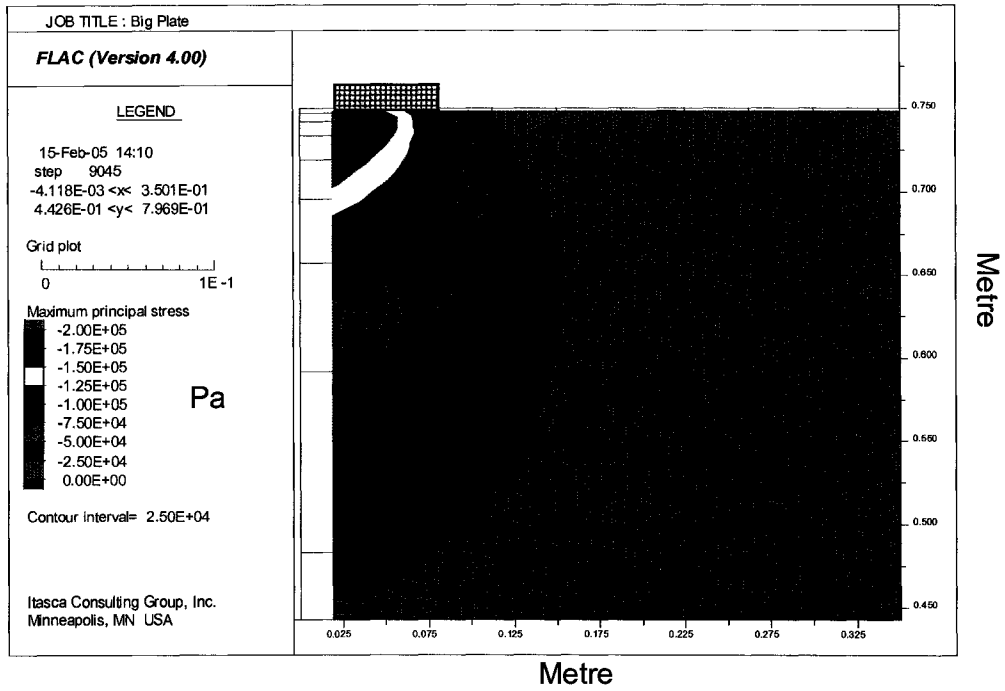


Figure 98: Vertical stress under large plate

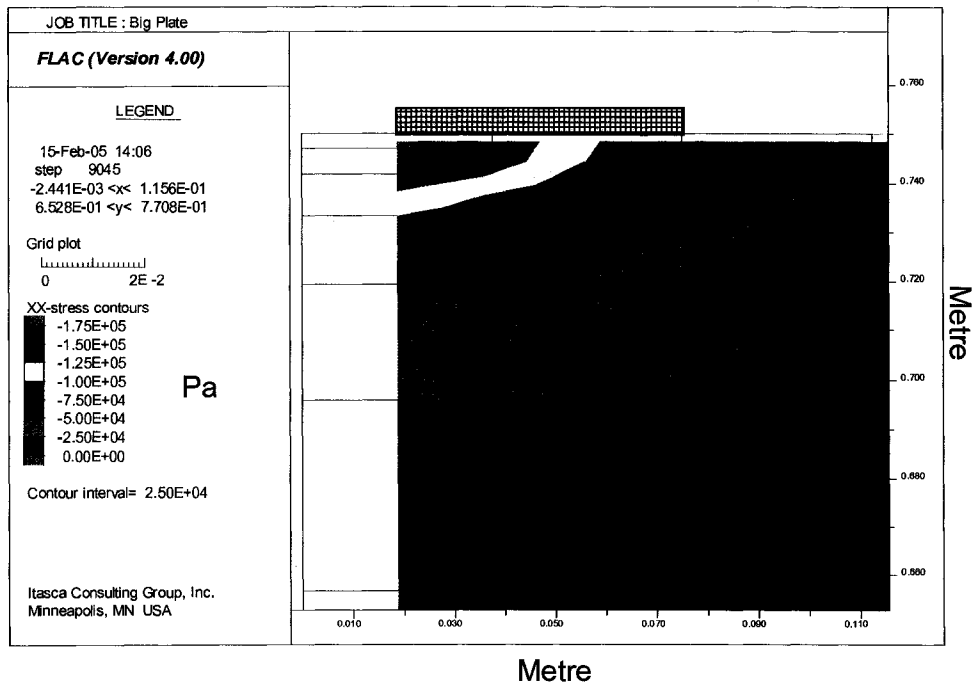


Figure 99: Horizontal stress under large plate

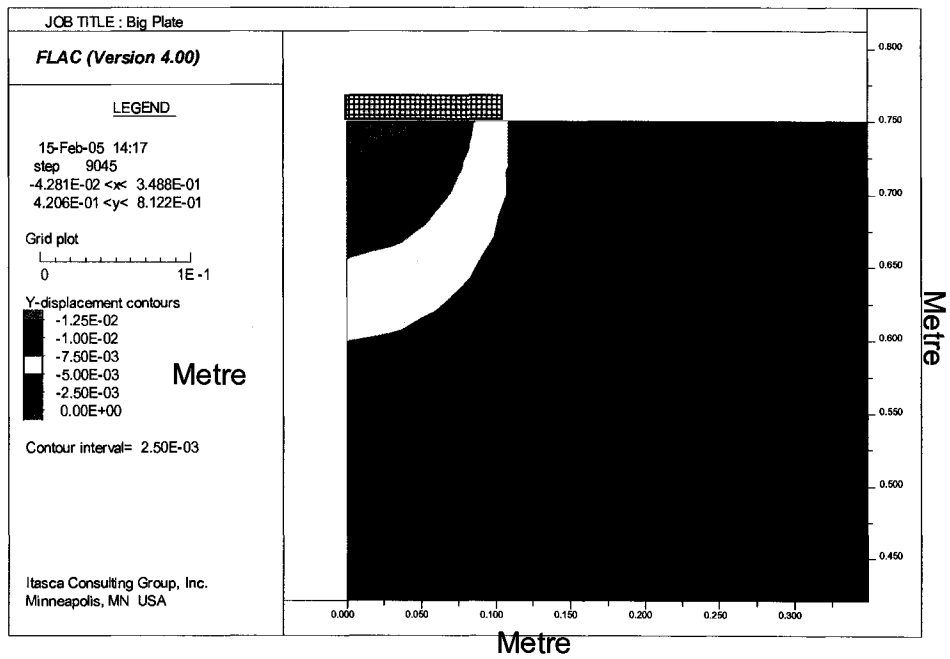


Figure 100: Vertical deformation under large plate

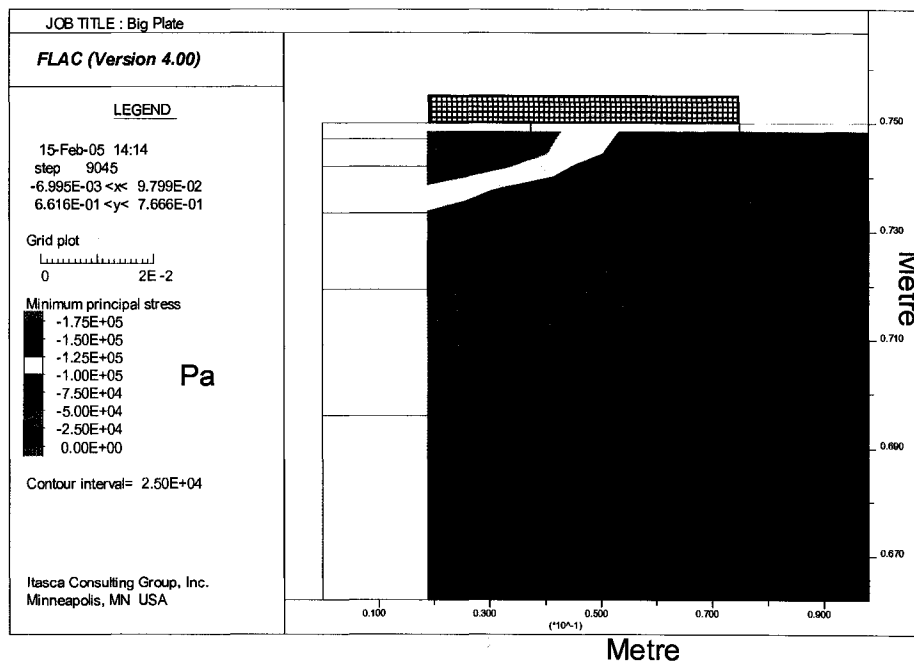


Figure 101: Confining pressure  $\sigma_3$  under large plate

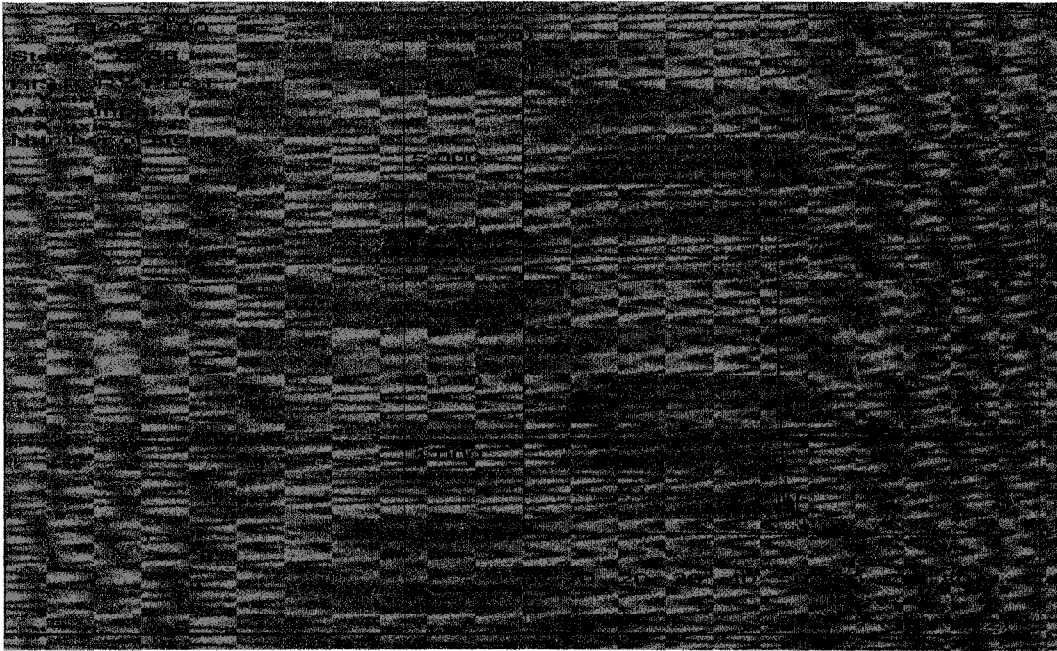


Figure 102: Unbalanced force for large plate

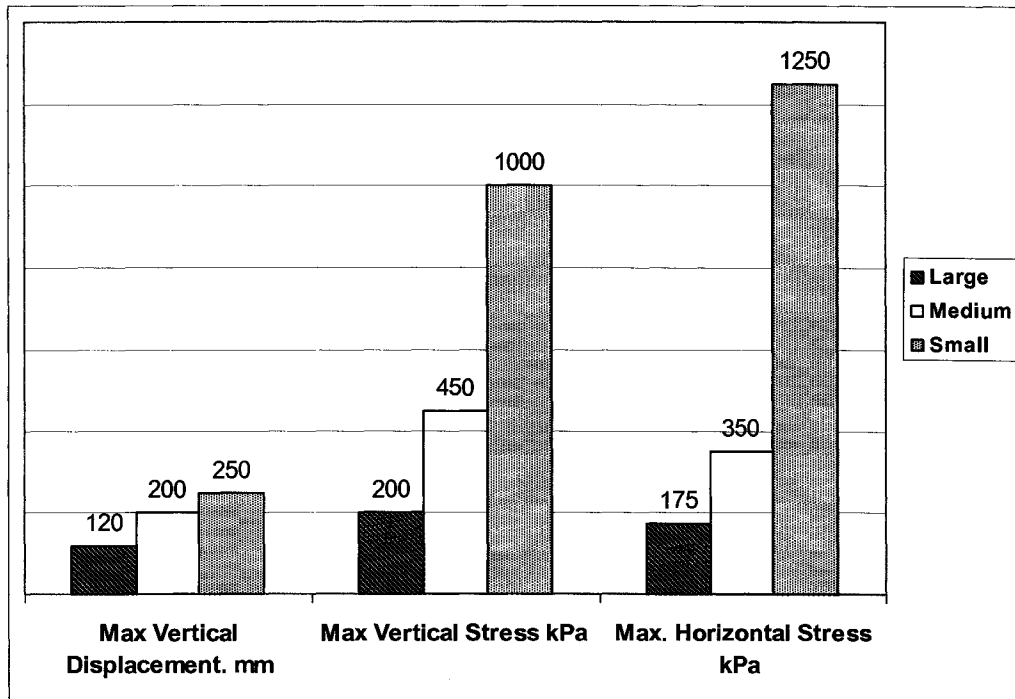


Figure 103: Summary of FLAC modeling for deformation and stresses

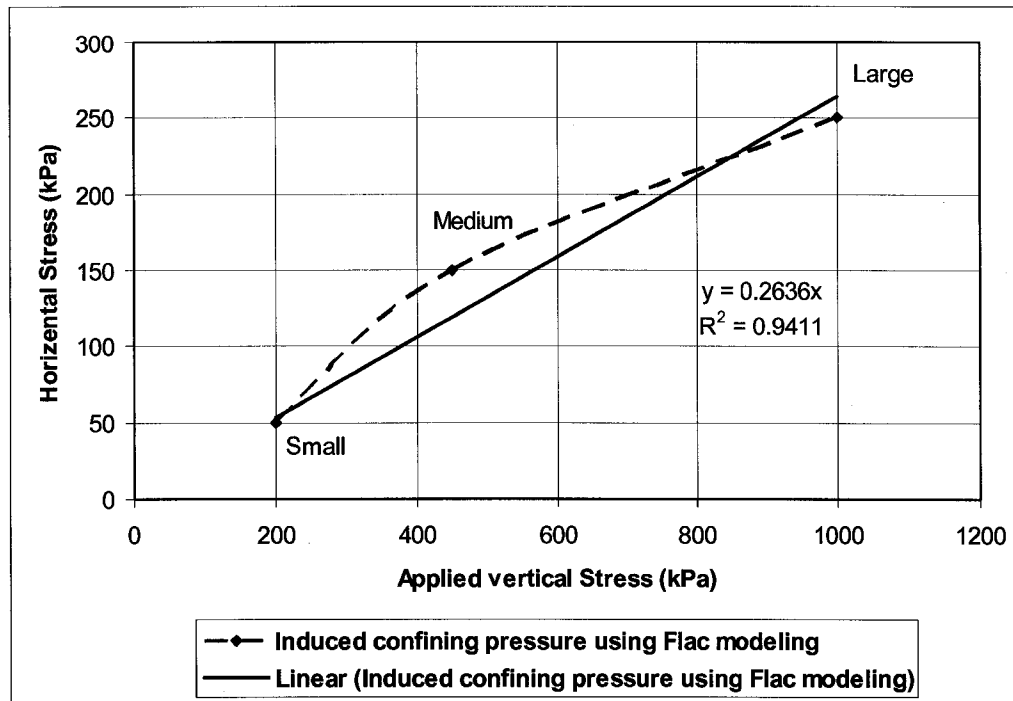


Figure 104: Induced confining pressure by FLAC modeling for different plate size

### 5.6 Vertical and horizontal stress modeling beneath for field plate load test via Boussinesq's approach

The Boussinesq analysis method calculates the stresses in strata due to applied loads. The method uses the integrated forms of well-known equations derived by Boussinesq (1885). The accuracy of the prediction is influenced by the spacing of the force-evaluation points. Decreasing the horizontal distance between the points increases the accuracy of the prediction. The stress-evaluation points should, therefore, also be closely spaced beneath and around the localized loads and where the variation of stiffness with depth is large.

The objective here was to estimate the induced stress in oil sand due to the action of a shovel. Boussinesq's assumptions are appropriate for use with a space assumed to be a homogeneous, isotropic, elastic half-space with vertical concentrated loads. The ground material was treated as pseudo-elastic, allowing an estimation to be made by using this approach.

In a two-dimensional r-z rectangular coordinate system  $\sigma_z$ ,  $\sigma_r$  and  $\tau_{rz}$  were defined as the vertical, horizontal and shear stress components, as shown in Figure 105. The shear stress was considered to be on a normal plane to the r axis and along the z direction. The standard equations are given as 26, 27 and 28 (Craig 1996):

Vertical stress:

$$\sigma_z = \frac{3Q}{2\pi z^2} \left\{ \frac{1}{1 + \left(\frac{r}{z}\right)^2} \right\}^{\frac{5}{2}} \quad [31]$$

Horizontal stress:

$$\sigma_r = \frac{Q}{2\pi} \left\{ \frac{3r^2 z}{(r^2 + z^2)^{\frac{5}{2}}} - \frac{1 - 2\nu}{r^2 + z^2 + z(r^2 + z^2)^{\frac{1}{2}}} \right\} \quad [32]$$

Shear stress:

$$\tau_{rz} = \frac{3Q}{2\pi} \left\{ \frac{rz^2}{(r^2 + z^2)^{\frac{5}{2}}} \right\} \quad [33]$$

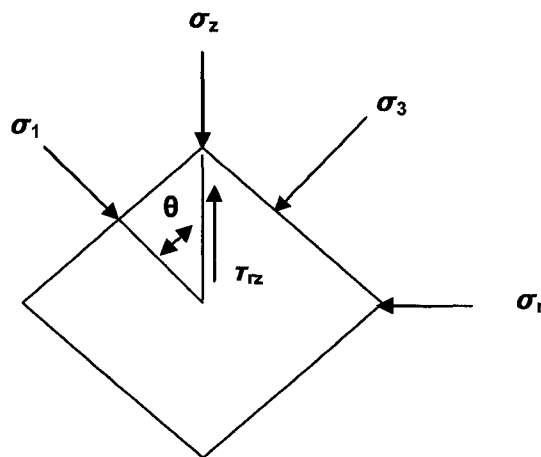


Figure 105: Principal, horizontal and vertical stresses on an element

When Q is the load (kN), and r and z are the distances from the load (m), the resulting stresses will be in kPa, as shown in Figure 106.

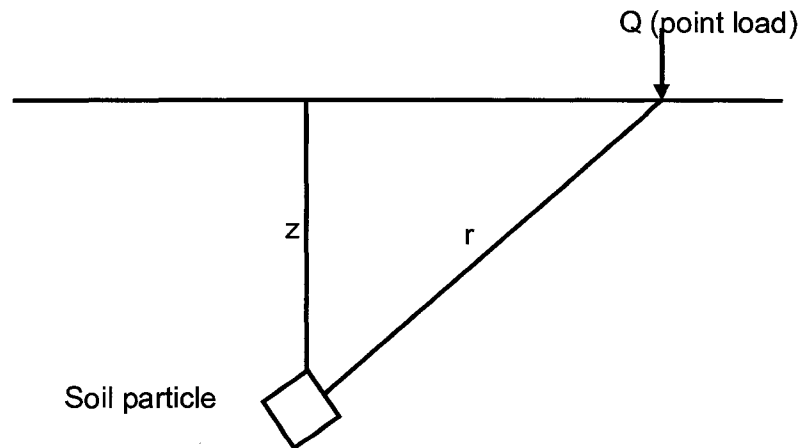


Figure 106: Load and distances from surface to soil particles

MATLAB was used to write a program using this approach. (Appendix 5 provides the programs for the field plate load test). The model design was applied to different plate sizes of field cyclic plate load tests. For the plate size, the constant area for different plate diameters, were as follows: small plate 45 cm<sup>2</sup>, medium plate 101 cm<sup>2</sup>, and 172 cm<sup>2</sup> for the large plate. The constant force was 5KN, was approximately the maximum force achieved during field cyclic plate load tests. This study evaluated only a very simple case, with the load being held at the maximum value.

Figure 107 through Figure 109 illustrate the horizontal and vertical stresses for different plate sizes. The maximum vertical and horizontal stresses are summarized in Table 9.

The horizontal stress from the Boussinesq's equation provides a reasonable match between the FLAC modeling field plate load tests. Only a static situation was considered for the Boussinesq approach because of the complexity of programming required in MATLAB. The Boussinesq approach is often used in geotechnical engineering for shallow foundations; and in this case, because of the shallow depth, the virtual simulation using the Boussinesq approach should mirror very closely the results of the real horizontal and vertical stress.

Table 9: Result of vertical and horizontal stress using Boussinesq approach

Plate size	Maximum vertical stress (kPa)	Maximum horizontal stress (kPa)
Small	300	250
Medium	450	350
Large	950	450

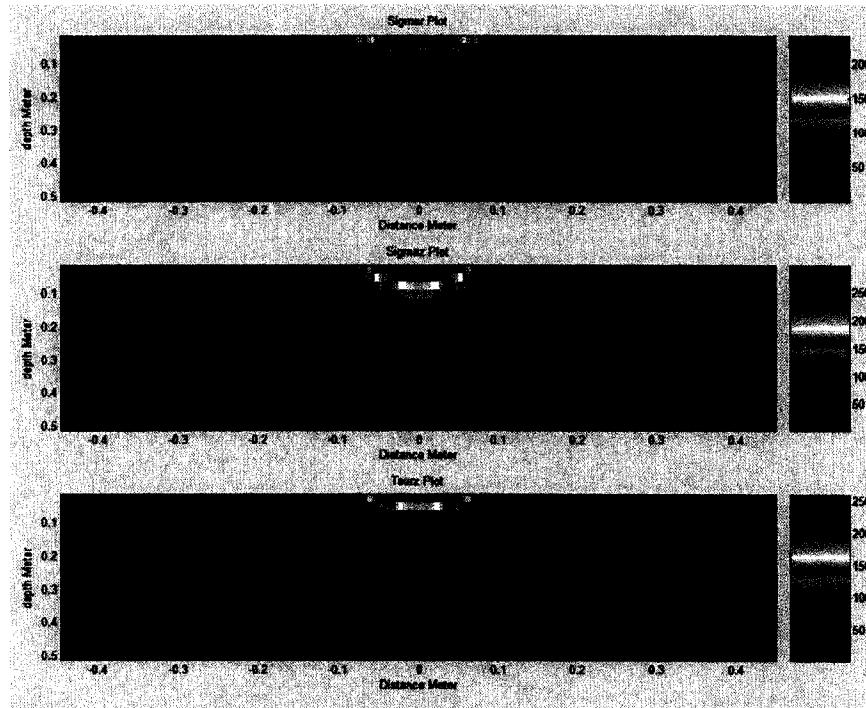


Figure 107: Vertical and horizontal stresses for large plate

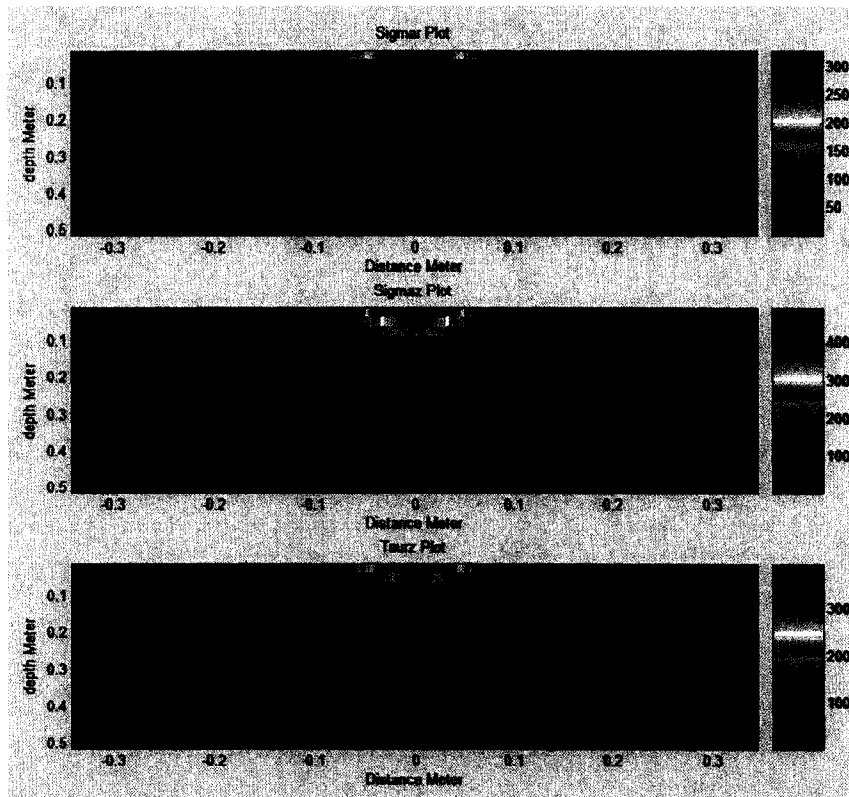


Figure 108: Vertical and horizontal stresses for medium plate

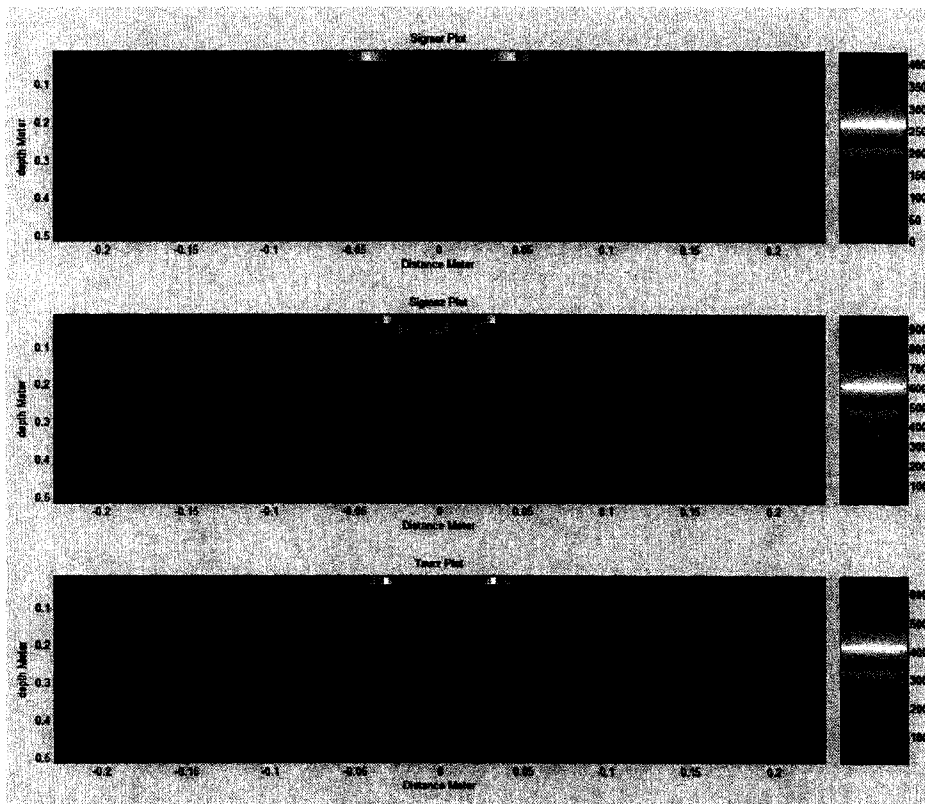


Figure 109: Vertical and horizontal stresses for small plate

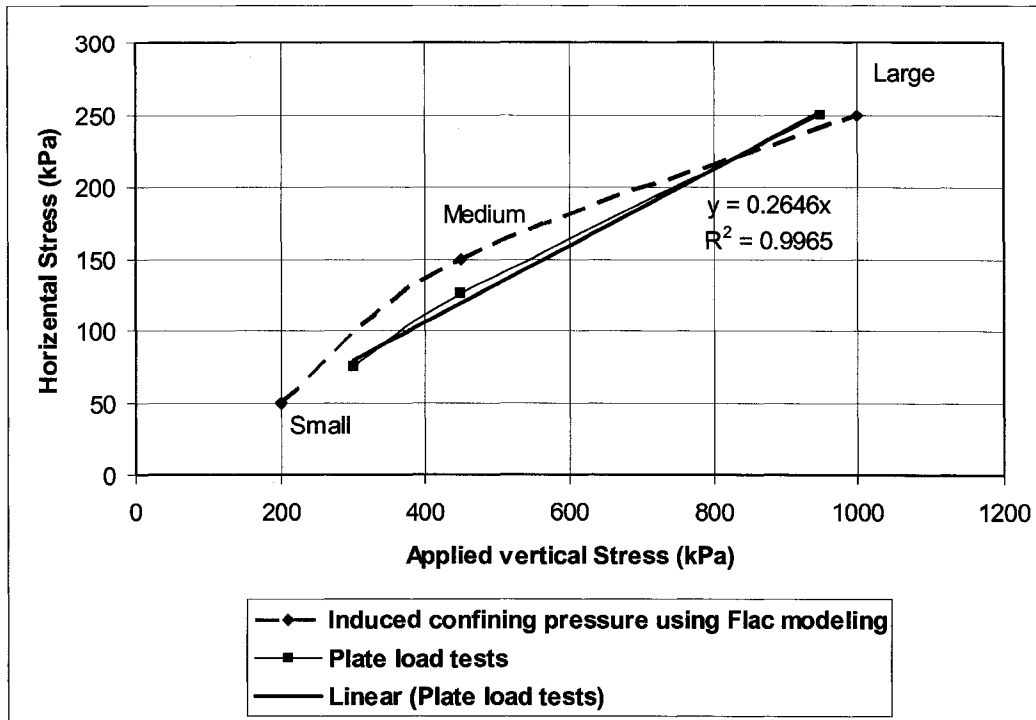


Figure 110: Comparing Boussinesq and FLAC results

### 5.7 Remarks

The induced confining pressure occurring during mobile mining activity, can be predicted by FLAC modeling procedure, that was increased to approximately 0.27 times of applied vertical load. The induced confining pressure rose with increasing applied load. A Poisson ratio of 0.25 can be used for the near-surface 8 and 11% bitumen content, to predict the ground stress during mining activities. Also, the bitumen content has great influence at the strain, hitting the peak point.

For the cyclic loading of oil sand in the field, the load-deformation and deformation-time graphs, show that the slope of the loading reached a constant value after a given time. The Boussinesq approach was used to predict induced confining pressure during applied load. Very close results were obtained using numerical modeling from the FLAC and Boussinesq approach. Also, both methods indicated that the approximate horizontal stress is equal to 0.26 of the vertical stresses.

The time-strain curve for laboratory cyclic triaxial tests under constant confining pressure, was different compared to cyclic plate load tests at field. The differences resulting from constant confining pressure in laboratory tests, compare well to the increasing confining pressure that happens with increasing load, during field tests.

## **6 Large-scale laboratory tests**

### **6.1 Introduction**

To increase our understanding of oil sand behaviour under cyclic loading, a large-scale laboratory test was designed based on the cyclic field test and aimed at investigating controlled equipment-ground interactions. This laboratory test was one of the largest laboratory-scale tests for oil sand ever performed at the University of Alberta. The large-scale laboratory tests have been performed on the re-compacted oil sand, in order to have comparable field and laboratory tests. Prior to commencing, a standard compaction (the standard proctor compaction ASTM D698-70) procedure was conducted to establish the compaction characteristics of the sample taken from one of the open-pit mines in northern Alberta, from in-pit oil sand with a bitumen content of 11%, compared with the characteristics established by the previous study.

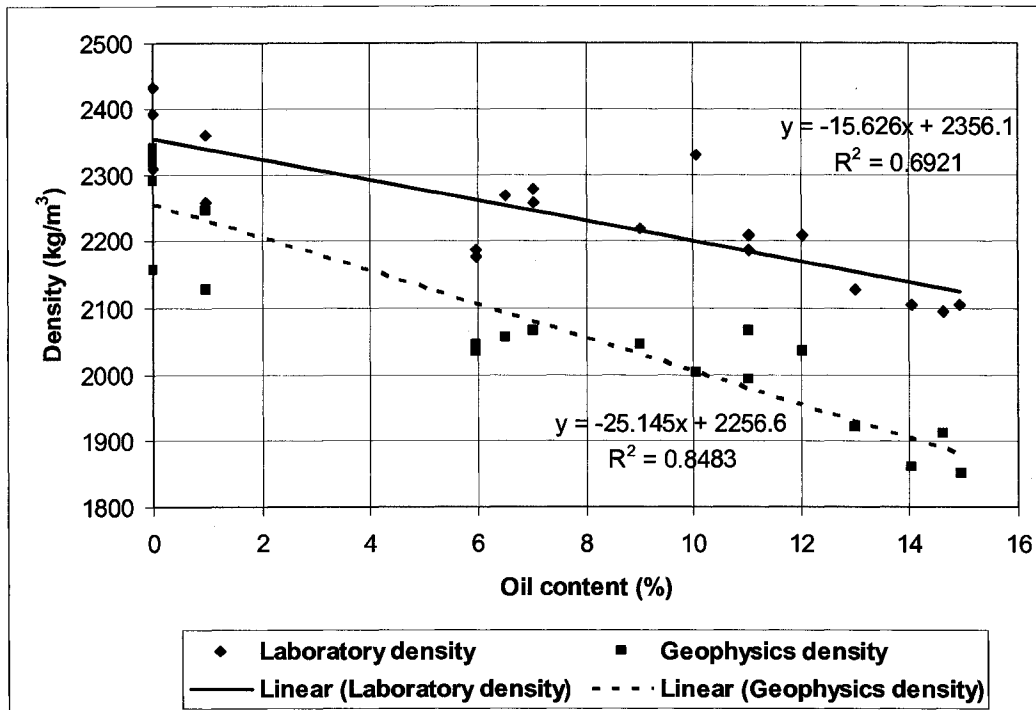
A standard compaction test was performed to

1. Predict the maximum density that can be reached by compaction
2. Achieve a density benchmark to measure the density changes before and after each plate load test, compared to the initial standard compaction
3. Learn any deficiencies of the standard compaction test when used for oil sand material
4. Understand the compaction characteristics of oil sand prior to compacting oil sand in a large-scale box

The final goal of the large-scale laboratory tests was to investigate the total deformation as a function of the number of cycles, load level, duration and density for 11%-bitumen-content oil sand samples at room temperature. This investigation would then allow a standard, quick method to model the results of the cyclic plate load tests to be proposed.

## 6.2 Density and compaction

Figure 111 presents Dusseault's (1977) data for oil sand composition at 1m horizons over a 40 m depth. The wet and dry densities have an average difference of approximately  $300 \text{ kg/m}^3$ . This difference increases with increased oil content. As the fluid content increases, the densities of both the wet and dry samples decrease. This result is not unusual since the density of the sand is far greater than that of the water and oil.

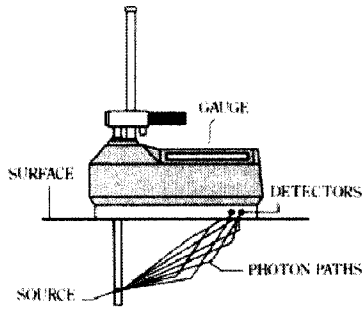


ground is already disturbed. However, the density measurement by Troxler provides the bulk or average density of the volume beneath Troxler.

The Troxler MC-1 or nuclear densometer is operated in either drilled holes or from the surface. The usual radioactive source employed is Cesium-137 ( $\text{Cs}^{137}$ ). The source is permanently housed within the gauge or, on many models, is located at the end of an extendable source rod. When the source is placed in the rod, the  $^{137}\text{Cs}$  has two positions, retracted (in the housing) or extended to one or more preset depth positions. When extended, the  $^{137}\text{Cs}$  is placed in a hole in the material to be measured (usually soil) directly below the gauge. The extended source and the retracted source both rely on photons traveling from the source, interacting with the surrounding material, and being detected by a Geiger Muller (GM) detector located within the body of the gauge. The extended source creates a zone in which the photons travel, through the media to be measured, to the detector. This process is referred to as "direct transmission." When the source is within the body of the gauge, the set-up is called a "backscatter." In both configurations, photons leave the source in all directions. The density measurement is dependent on the water content and, hence, must be corrected for it. The density measurement may also be affected by the chemical composition of the medium. The instrument measures the weight of wet soil per unit volume and also the weight of the water present in a unit volume of soil. The dry unit weight of the compacted soil can be determined by subtracting the weight of water from the moist unit of soil. Figure 112 illustrates the two different measurement arrangements (Evet 2000).

The MC-1 "Troxler" moisture and density gauge was used in the laboratory tests. The final density or moisture count was obtained by dividing the field or laboratory count, by the standard count or calibration. Figure 113 and Figure 114 present the calibration curve used to convert obtained ratio into equivalent density (MC-1 Manual 1980). The legend in Figure 113 refers to the position of the handle on the densometer (as shown in Figure 112). Therefore, based on the handle position and the calculated ratio (field or laboratory count divided by calibration count), the density or moisture can be found from Figure 113 and Figure 114.

Example of Direct Transmission



Example of Backscatter Geometry

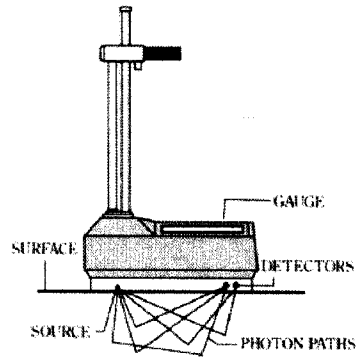


Figure 112: Two different methods for measuring density with a Troxler (after Evett 2000)

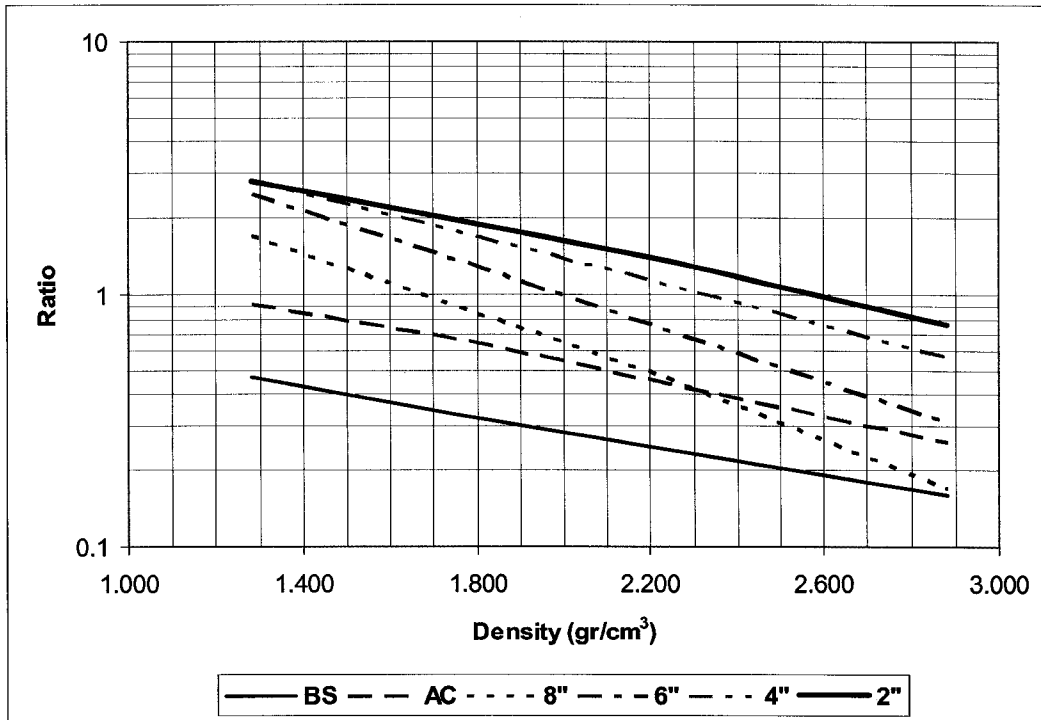


Figure 113: Density calibration curve for MC-1 densitometer

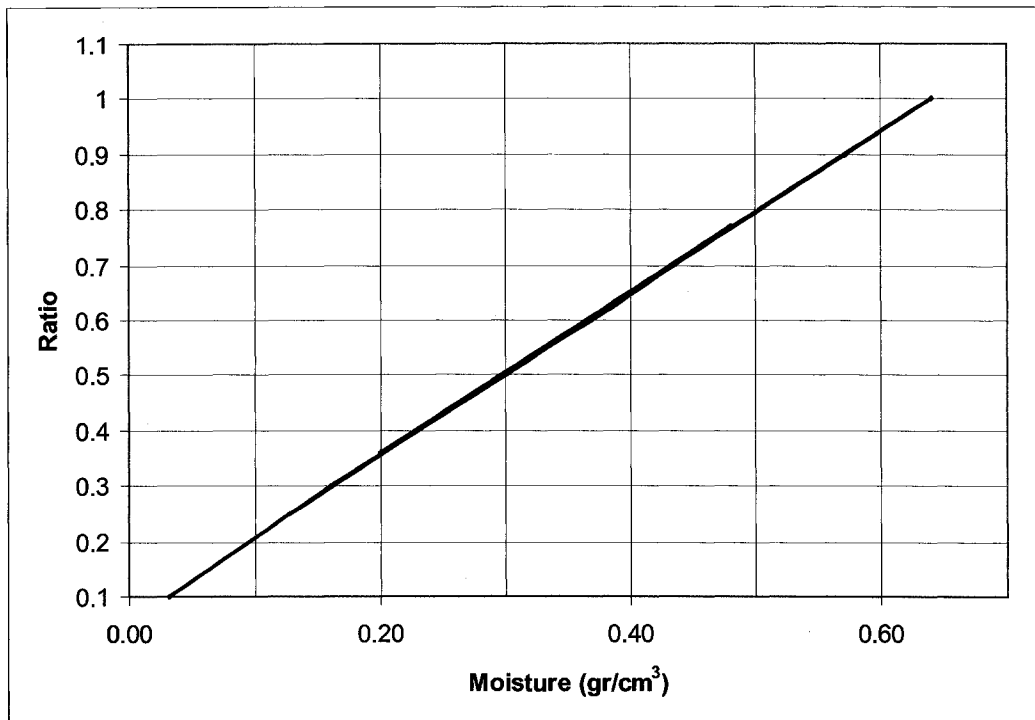


Figure 114: Moisture calibration curve for MC-1 densometer

Also, the data collected from the standard penetration test (SPT) on the oil sand showed that a blow count of 100 – 150 is typical for oil sand. The SPT test involves driving a standard cylindrical sampler into the bottom of a borehole. The total blows required from a hammer, over the interval of 150 to 450 mm (6 to 18 inches) are summed up to give the blow count N, in blows per foot. The closer the count approaches 100, the higher the oil content regardless of the overall fluid content (oil + water). The average SPT blow count was 112, as shown in Figure 115. However increasing the fluid content density decreases the density, and the blow count increase may be caused by a fluid-pressure increase and the low mobility of oil during a SPT.

Lord and Cameron (1985) conducted a compaction oil sand test, using varying bitumen contents in order to use the results in construction work. This study included the standard proctor compaction test “ASTM D698-70.” The summary of their results (see Figure 116) reveals the relationship between the dry density and the bitumen content:

$$\text{Dry density} = 1800 - 13 (\% \text{bitumen}) \text{ kg/m}^3,$$

[34]

where the upper limit is  $1800 \text{ kg/m}^3$ . However, the analysis of the data collected from the field during this current investigation found an alternative relation of dry density =  $2150 - 37(\% \text{ bitumen})$  that yields an upper limit of  $2150 \text{ kg/m}^3$  (see Figure 116). In general, the recent data set follows the same trend as that reported by Lord and Cameron (1985), regardless of the richer material encountered. Lord and Cameron were doing research for construction purposes; therefore, it is not surprising to find that the richer grades of the latter data set provide an alternate relation which is closer to the conditions experienced in-pit for mining-grade oil sand rather than for construction grades.

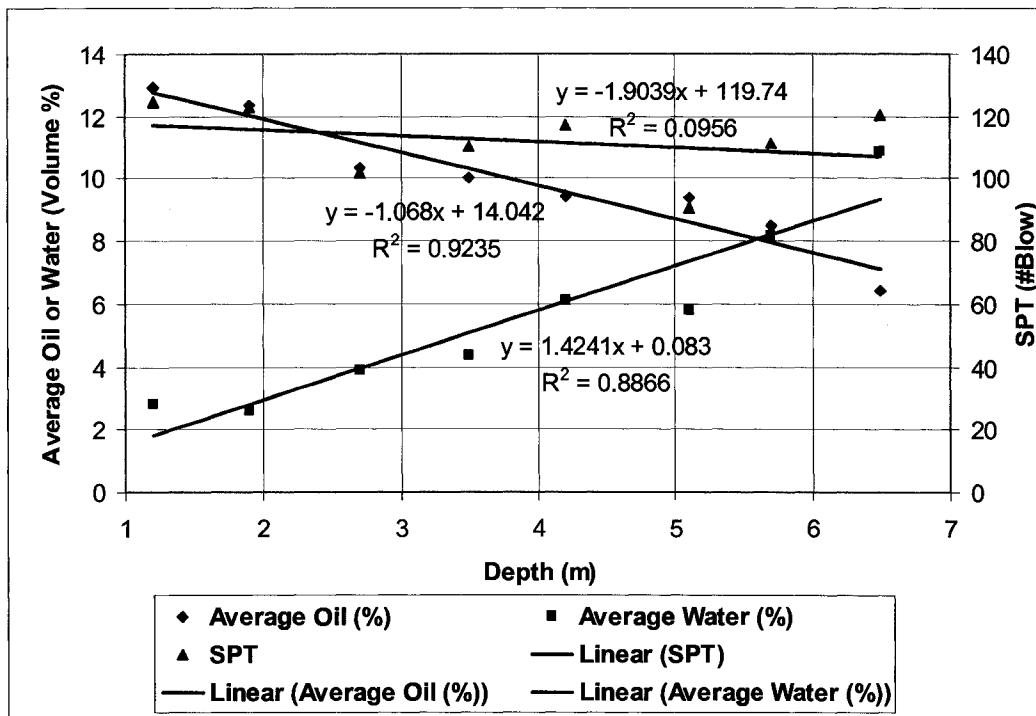


Figure 115: Data from a 7 m profile measuring SPT blow count and fluid content (Joseph, 2001)

Wet density Troxler measurements were made from the surface over a number of pit areas in oil sand of varying oil and water content. Wet density is defined as total weight of solid and water divided by total volume. Figure 117 shows that no correlation was found between the wet density and the fluid content, likely due to the different compaction characteristics in pit areas because of the equipment

operating in those areas. However, the dry density and fluid content for the same data provide some sense of a trend (see Figure 118).

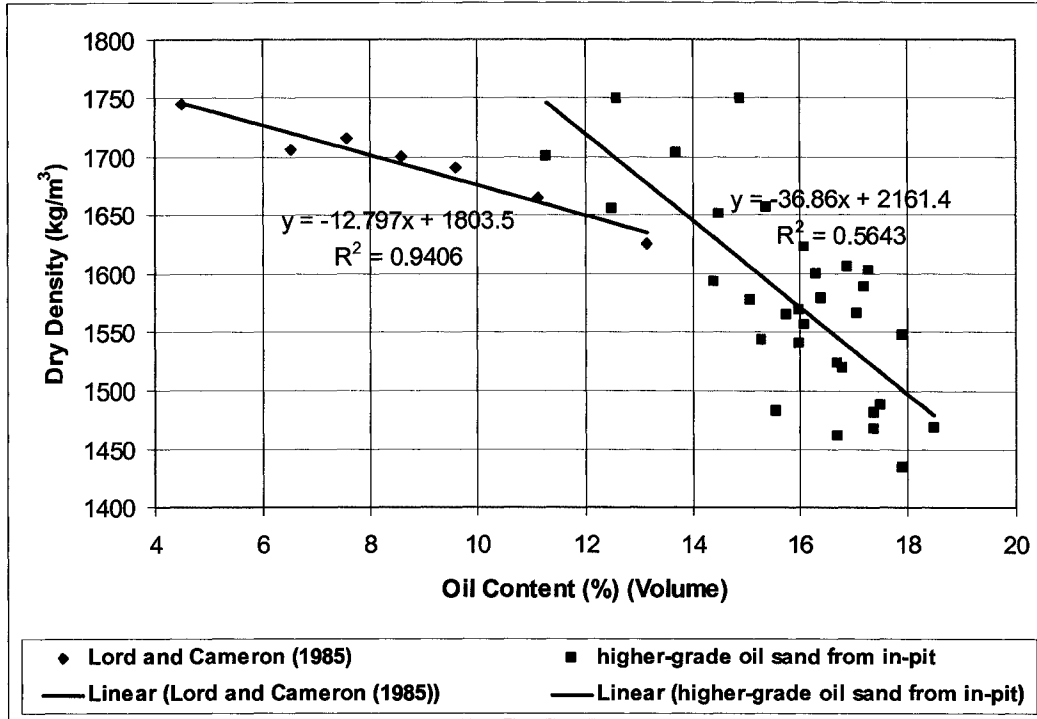


Figure 116: Analysis of compaction data by using results reported by Lord and Cameron (1985) and higher-grade oil sand from in-pit

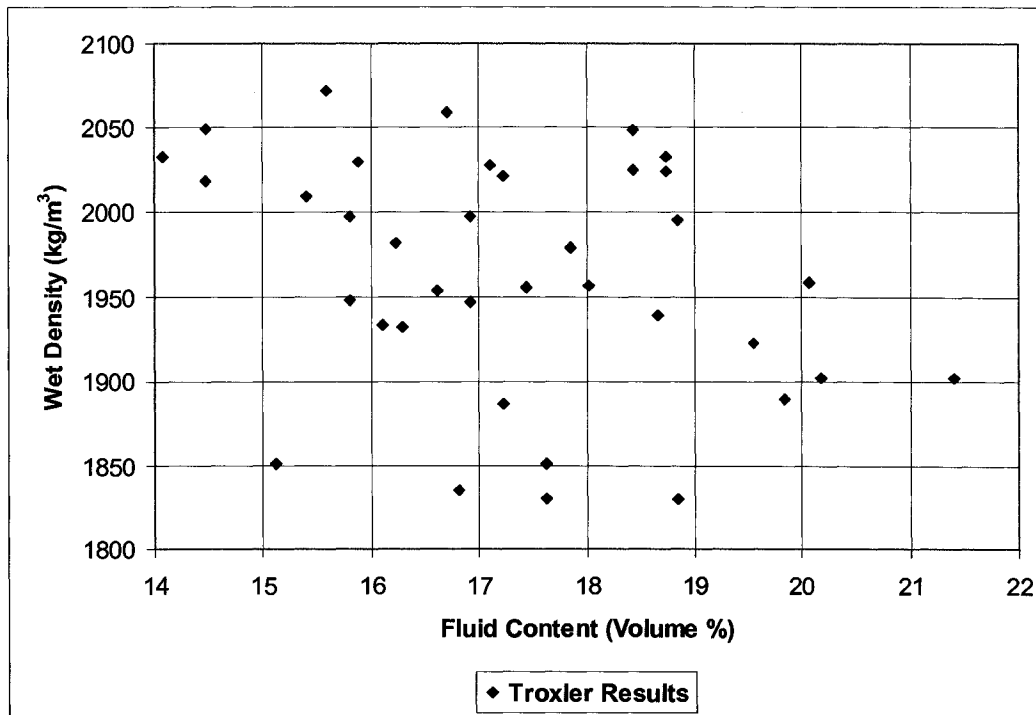


Figure 117: Troxler wet bulk density results vs. fluid content

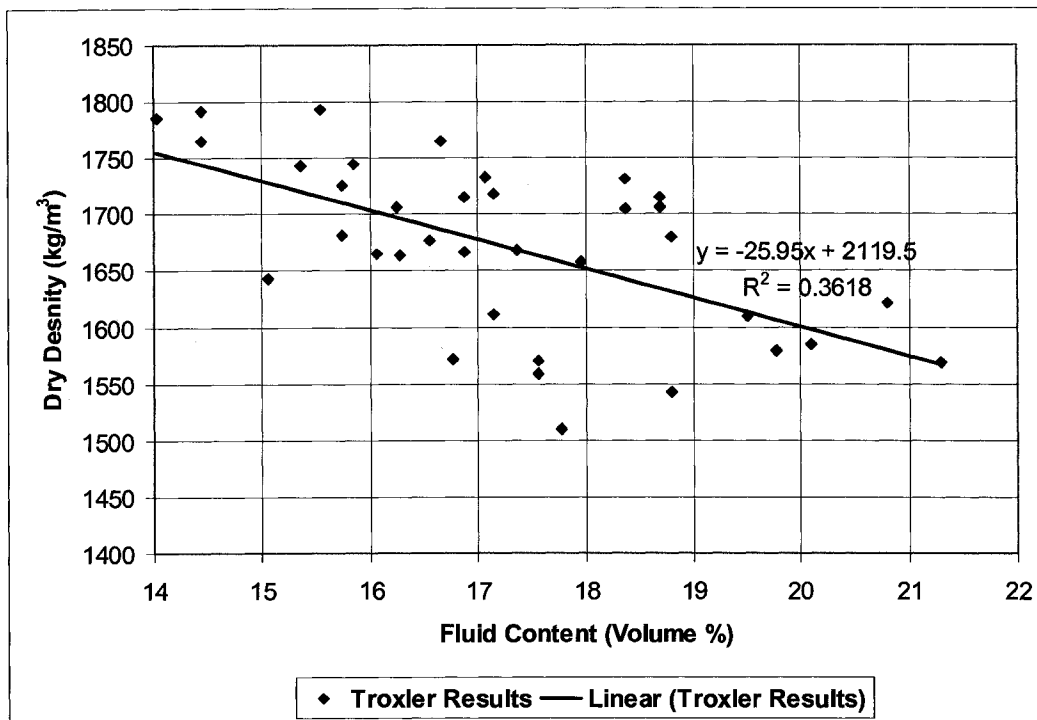


Figure 118: Troxler dry bulk density results vs. fluid content

Compared to the results reported above, the results provide a reasonable agreement with the results from the laboratory compaction test samples taken from various in-pit locations. However, the result is difference between the laboratory and the geophysical findings reported by Dusseault and Morgenstern (1978) and mentioned earlier.

### 6.3 Oil sand water content

Samples acquired from several boreholes over a bench area from depths to ~7 m provided sufficient data to allow a reasonable correlation between oil and water content (see Figure 119). The relation in this case was estimated by using a linear regression result of water content % = 18.5 – 1.3 (% oil content).

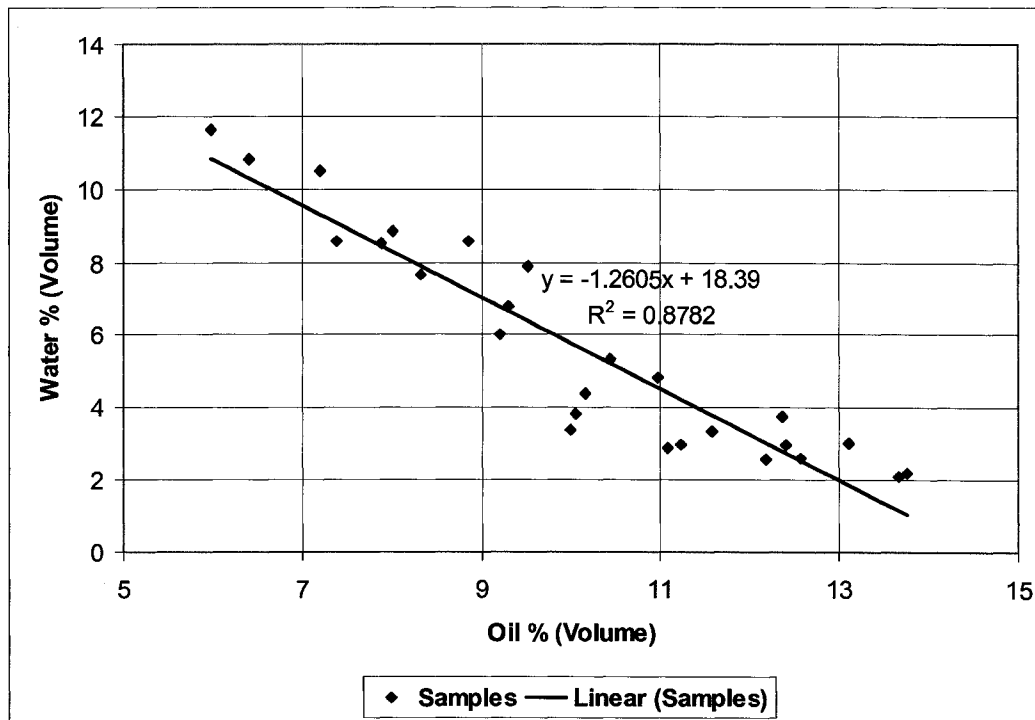


Figure 119: Relationship between oil and water content in oil sand pit

#### 6.4 Confining stresses

The confining stress for near-surface oil sand appears to be very low and approaching to zero. The vertical stress can be calculated from  $\sigma_1 = \rho g z$ , where  $\rho$  is approximately  $2000 \text{ kg/m}^3$ ,  $g$  is  $9.81 \text{ m/s}^2$  and  $z$  is the depth in metres of interest below the surface. The horizontal stress  $\sigma_3$  can be found from the vertical stress by using the plain strain approach:

$$\sigma_1 = \sigma_3(1-\nu)/\nu \quad [35]$$

$$\sigma_1 = \rho g h,$$

where  $\nu$  is the Poisson's ratio earlier defined for oil sand at approximately 0.25 that  $(1-\nu)/\nu$  become  $1/3$ . For depths from 3 to 5 metres,  $\sigma_3$  is 19.6 kPa ( $3 \text{ m} \times 9.8 \text{ m/s}^2 \times 2000 \text{ tonne/m}^3 / 3$ ) and 32.7 kPa ( $5 \text{ m} \times 9.8 \text{ m/s}^2 \times 2000 \text{ tonne/m}^3 / 3$ ), respectively. These confining pressures, compared to the pressure caused by equipment which loads the ground, are very low. However, the confining pressure generated by running equipment on the surface introduces the major

confining pressure component, which contributes to floating equipment on the surface. The influence depth of the induced confining pressure, is caused by the equipment, may be controlled by the size of the equipment footprint, and the degree and rate of the ground deformation possibly are controlled by the induced confining pressure dissipation.

In the case of a truck tire, where the footprint and the area of contact change due to the flexure of the tire and the ground stiffness, the depth of influence must change compare to static tire footprint. For example, if a static footprint were as much as  $\sim 1.3 \text{ m}^2$ , then the depth of influence would be  $\sim 3.4 \text{ m}$  ( $\sqrt{1.3 \text{ m}^2} \times 3$ ), it is two to three times of the tire dimension. If the tire footprint increased to  $2.0 \text{ m}^2$  due to rack, pitch and roll, the depth of influence might approach  $\sim 4.3 \text{ m}$  ( $\sqrt{2 \text{ m}^2} \times 3$ ) which is two to three times of the tire dimension. Therefore the zone of influence for the static and dynamic loading for truck could be different. In the case of a shovel track, the same analogy can be applied. The area of the shovel track is close to a rigid area. The static shovel footprint is as much as  $\sim 31.2 \text{ m}^2$ , the smallest lateral truck dimension controls the depth of influence, akin to the strip foundation, in this case,  $2.7 \text{ m}$  is the smallest track dimension. Therefore, the depth of influence might approach  $\sim 8 \text{ m}$  ( $2.7\text{m} \times 3$ ) which is three times of the smallest track dimension.

## 6.5 Compressibility

Scott and Kosar (1984) studied the variation of the volumetric strain with the confining pressure by using oedometers with three unload-reload cycles. The results showed that any initial compressibility was higher than that of the following cycles. One-dimensional compression oedometer tests yielded a cyclic co-efficient of the compressibility volumes of  $0.3$  to  $0.6 \times 10^{-6} \text{ kPa}^{-1}$ . During one-dimensional loading and unloading, the horizontal effective stress  $\sigma'_h$  will change since the condition of zero horizontal strain ( $\varepsilon_h = 0$ ) is imposed. Kosar and Scott (1987) found the bulk modulus compressibility ( $K$ ) to be  $720 \text{ MPa}$  for Athabasca oil sand and determined its isotropic compression for a range of confinement from  $1$  to  $4.5 \text{ MPa}$ , which was much higher than the confinement expected in a

pit environment. Kosar and Scott (1987) concluded that the strength and compressibility characteristics of oil sand do not differ significantly from those of dense sand deposits.

By applying Kosar and Scott's (1987) work to the unload-reload cycle of a truck tire acting on the ground, and assuming that Poisson's ratio is  $\sim 0.25$  and the compressibility co-efficient is constant, the expected induced confining pressure for a 797B truck, as shown in Table 4, would approach 800 kPa. An extrapolation of Kosar and Scott's findings shows that 800 kPa approximately corresponds with  $7.2 \times 10^{-5} \text{ kPa}^{-1}$  volumetric strain. In the case of shovel loading, this strain would approach 200 kPa, as shown in Table 4, with a volumetric strain of  $1.82 \times 10^{-5} \text{ kPa}^{-1}$ . If we conservatively assume a constant footprint during the cyclic process, similar to the one-dimensional loading is applied in an oedometer, the vertical strain would be equivalent to the volumetric strain (vertical strain = volumetric strain  $\varepsilon_v = \Delta H / H_0 = \Delta\varepsilon / (1+e_0)$ ), which is very low. The higher-bitumen-content material, which is the target of this investigation, is expected to give a greater deformation on cyclic loading than that indicated by Kosar and Scott's work.

## 6.6 Compaction test in the large-scale laboratory test

A standard proctor compaction test (ASTM D698-70) was used to investigate the compaction characteristics of oil sand samples. The soil was compacted in a standard mold of  $943.3 \text{ cm}^3$  capacity and 101.6 mm diameter, which was attached to a base plate at the bottom and an extension at the top. Then soil was compacted in three equal layers by a hammer of 24.4 N weight, dropped at 304.8 mm for 25 blows. Compaction is basically the densification of soil by the removal of air, requiring mechanical energy. Simply put, compaction may be defined as the process in which soil particles are forced closer together through reduction in air voids. The unit of compaction,  $\gamma$ , can be calculated from (Das 2000):

$$\gamma = \frac{W}{943.3\text{cm}^3}, \quad [36]$$

where;  $W$  = weight of the compacted soil in the mold.

Compaction tests were performed four times, giving an average final density of  $1730 \text{ kg/cm}^3$  with upper and lower bounds of  $1740 \text{ kg/cm}^3$  and  $1710 \text{ kg/cm}^3$ , respectively, the compaction density closely compares to Lord and Cameron's (1985) results. However, during the compaction of the oil sand in the larger scale box test by using a hydraulic jack and metal bar, densities reached 1800 to 2000  $\text{kg/cm}^3$ . The lower range obtained from the earlier work, demonstrates that the standard compaction test is an inappropriate test for determining the maximum oil sand density during equipment activity. It was observed during the preparation of the plate load test that the best oil sand compaction was achieved by pressing the oil sand and not striking it.

This research does not deal with in situ oil sand that has interlocking structure. Also, in the equipment interactions investigation, oil sand is unlocked due to gas exolution and mining equipment activity as explained in the literature review, the compacted oil sand for large-scale laboratory test was accepted.

#### **6.7 Plate load cyclic laboratory test set-up**

To provide a better understanding of the behaviour of oil sand under mobile mining equipment, a simple plate load test was designed. This test was successfully conducted in the field to investigate the stress-deformation of oil sand under equipment loading. However, to investigate the oil sand deformation for a varying number of cycles, applied load, and relaxation time, a laboratory test was run under controlled conditions. Using the same instrumentation for the field and laboratory tests allowed the field and laboratory results to be compared. A frame was used to hold the active hydraulic cylinder in place on a  $1 \text{ m}^3$  oil sand box, and a 12 cm circular plate with a maximum pressure of  $\sim 800 \text{ kPa}$  was loaded.

#### **6.8 The equipment of laboratory cyclic plate load test**

The laboratory cyclic plate load test was similar to a field cyclic plate load test, which was made to facilitate the use of the tests for the scaled estimating of the cyclic footprint loading and the deformation prediction due to ultra-class mobile

mining equipment's motion, with reasonable control on load, duration of tests and cycles and deformation measurement. The apparatuses used for the cyclic plate load test were the following (see Figure 121):

- A hydraulic jack and high-pressure pump (AP-3000 Model) assembly to effect loading to a circular plate at the ground contact, providing cyclic loading.
- An electronic load cell to measure the loads during the test.
- A rigid steel frame to bear the applied load, the weight of oil sand box and frame (close to 2000 tonnes) were provide a force to get reaction of frame movement.
- A ground deformation measurement device, in this case a spring extensometer, to measure ground deformations and rebounds during cyclic loading.
- Bearing plates to transfer the load to the ground, the diameter of plate was one-third of the box width.
- A data-acquisition system (Data Dolphin) to collect data from the load cell and extensometer.
- A wooden box with width of 1.07m, 1.11m and height of 0.77 m was strength with wooden liner inside and metal strip outside.

## **6.9 Test Set-up and procedure**

A laboratory cyclic plate load set-up was designed similar to that of the plate load cyclic field test. Instead of a bearing S frame in the field, a rigid steel frame was used in order to take the reaction of the hydraulic jack. The hand pump for actuating the hydraulic jack was replaced by an air-oil pump (AP-3000 Model) to provide better control over load levels and load duration. A 1 m<sup>3</sup> oil sand box was placed on the steel bar connecting the bottom of the rigid steel frame. The weight of the box provided enough force to prevent the movement of the steel frame during loading (see Figure 120). Loading and unloading cycles were carried out, just as they had been for the cyclic triaxial and cyclic field plate load tests. Figure 121 shows the set-up for the large-scale laboratory plate load test.

The hydraulic cylinder was attached to the rigid steel frame with a couple of clamps. The load cell was connected to the bottom of the hydraulic cylinder between a circular plate and a hydraulic cylinder. The load cell was placed between the hydraulic jack and the foot circular plate. The load on the plate was applied by closing the valve of the hydraulic pump and application of the hydraulic jack. The corresponding plate settlement was measured via the spring extensometer installed on an independent frame outside the range of the loading action. Therefore, during the test, any unwanted fluctuation had no influence on settlement readings. A small hook on the top of the plate connecting the extensometer to the plate allowed both the deformation and rebound to be measured.

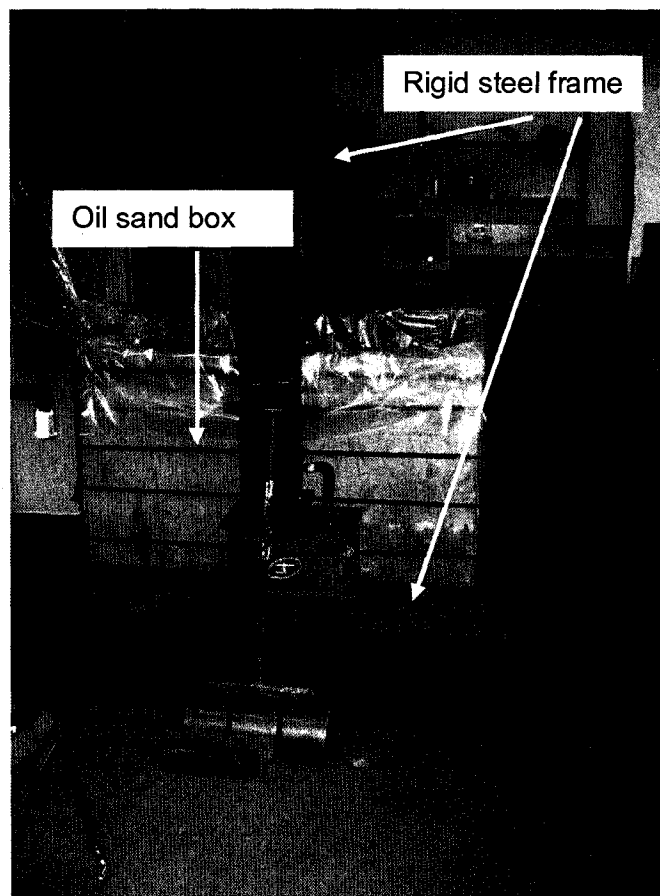


Figure 120: Rigid steel frame and oil sand box

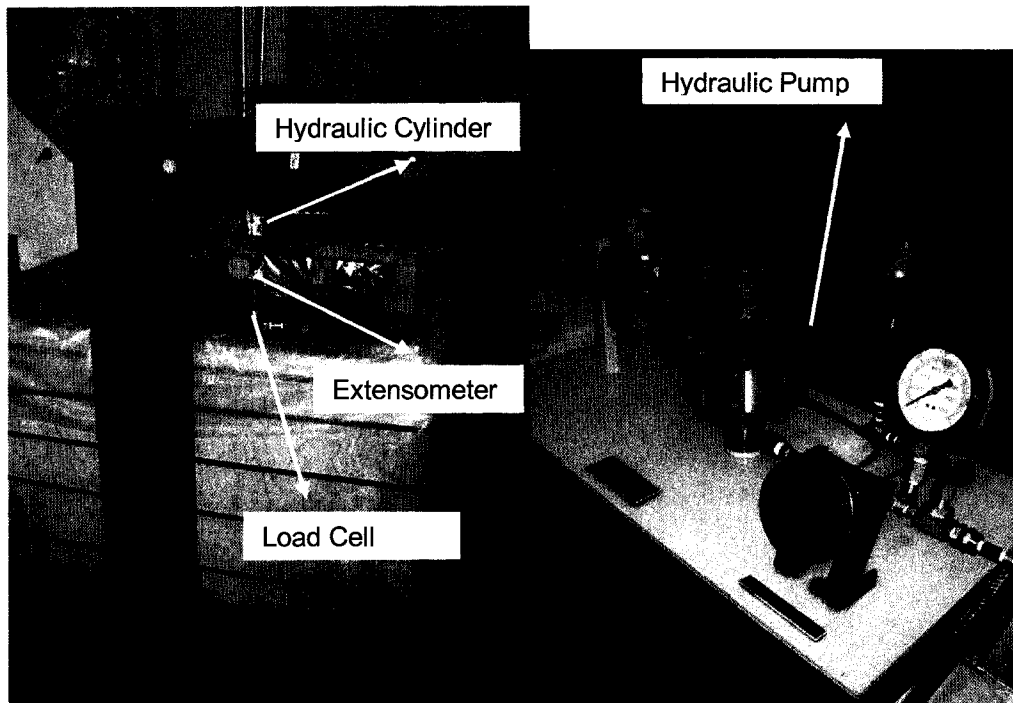


Figure 121: Plate load laboratory test set-up

The load was applied by using a hydraulic cylinder and a high-pressure pump (AP-3000 Model) in order to mimic the loading and unloading cycles. Also, the high-pressure pump provided the ability to keep the load constant throughout each test between cycles. The laboratory plate load test was conducted by using a circular plate with a diameter of 14.9 cm at different stress levels: 200, 400, 500 and 600 kPa. The plate load test was conducted for varying load maintenance and relaxation times of 0, 2, 5 and 10 minutes for each stress level applied. Each test was performed for 20 cycles with the same load maintenance time for both loading and unloading conditions.

A 38 cm cable extensometer (PT8420) was used to measure the deformation, and a load cell was used to measure the applied loads. An LP (Linear Potentiometer) that measures linear position or displacement by converting the output voltage to displacement, was chosen to monitor the longer time (~2 days) rebound. The data was gathered by using a data-acquisition system (Data Dolphin) with 22 channels, the DD-400 Model.

## 6.10 Compaction of oil sand (sample preparation)

Oil sand was compacted in a 1.07×1.11×0.77 m (width × width × height) box by using a vibratory plate compactor and a hand roller (see Figure 122). To compact the oil sand, the hand roller was used for every 5 centimetres of material, and the vibratory plate compactor for every 10 centimetres. The bulk density of the oil sand after compaction in the box that was determined by nuclear densometer was  $\sim 1.7 \text{ kg/m}^3$ , or 98% of that of a standard compaction test. Figure 123 illustrates the oil sand compaction in the laboratory. The wooden box was strengthened with the metal stripping outside and the wood plate inside. The width of the box was 3 times the diameter of the circular plate. The deflection of the box was not measured during the test because it did not have a major impact on the result of the test. The density of the oil sand was measured by Troxler before and after the test. Therefore, the deflection of the box does not influence the result of the cyclic plate load test.

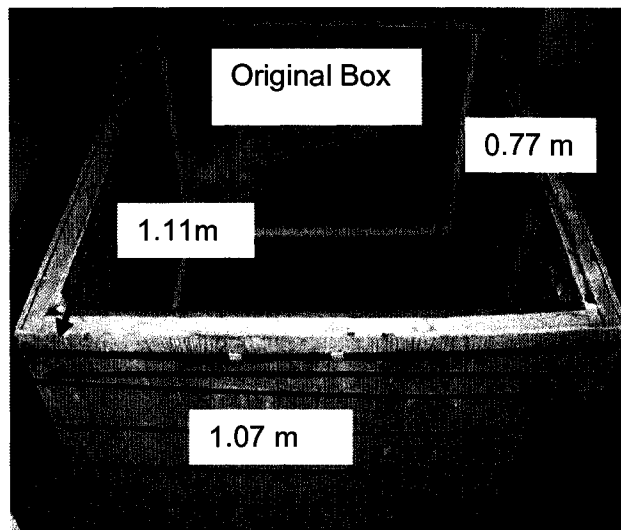


Figure 122: Original box for laboratory test

However, to reach a field density of 1.8 to 2  $\text{kg/m}^3$ , a hydraulic jack and a steel bar were used to compact the oil sand. The hydraulic cylinder was attached to the rigid steel frame with couple of clamps and then the rigid steel bar was placed beneath the hydraulic jack to transfer the load to the soil. The load on the plate was applied by closing the valve of the hydraulic pump and applying the hydraulic

jack (see Figure 124). Moreover, after each cyclic plate load test, the compacted oil sand under the plate was recompacted over an area twice the size of the plate to a depth of 10 cm from the surface to make an even surface for the subsequent tests. However, keeping the same density for all tests was nearly impossible, so after each compaction, the density was measured with a nuclear densometer (Troxlner) in an attempt to maintain similar densities. After each test and before running a new test, the density was measured with the nuclear densometer to keep track of the density change after completing each cyclic test. Figure 124 shows the compaction following each test and density measurement.



Figure 123: Compaction of oil sand by using vibratory plate and hand roller

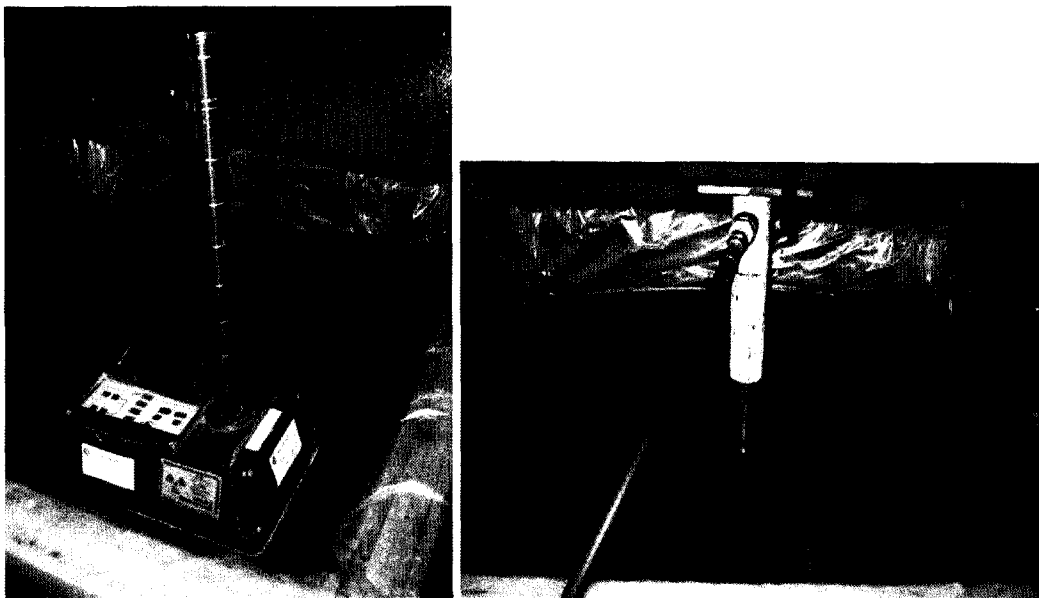


Figure 124: Compaction of oil sand by using steel bar and measuring density with nuclear densometer

### **6.11 Large-scale laboratory plate load test results**

The laboratory plate load test was conducted by using a circular plate with a diameter of 14.9 cm at different stress levels: 200, 400, 500 and 600 kPa. To study the slope of the cycles during cyclic loading and oil sand deformation under constant loading, the plate load test was conducted for varying load maintenance and relaxation times of 0, 2, 5 and 10 minutes for each stress level applied. Each test was performed for 20 cycles with the same load maintenance time for both loading and unloading conditions.

As was mentioned earlier, the density was kept constant for all tests and was monitored before and after each test. The Troxler MC-1 is able to measure the density and moisture content, without disturbing the soil, and this was explained at the beginning of this chapter. The density is measured at two depth ranges of 3 to 6 and 5 to 10 cm below the surface where 80% of the gamma radiation is reflected. To measure the density precisely, the surface must be flat with no holes or empty spaces between the surface and the instrument. However, after each test due to the penetration of the plate into the oil sand, density measurements beneath the plate footprint were impossible, so the edge of the Troxler was matched to the boundary of the circular footprint to provide a measurement that was as accurate as possible. Figure 125 illustrates the stress-deformation for different stress levels at 2-minute loading time tests. Also, Figure 126 shows the deformation versus time for 2-minute loading time tests at different stress levels. Appendix 6 presents the results of all the laboratory plate load test results.

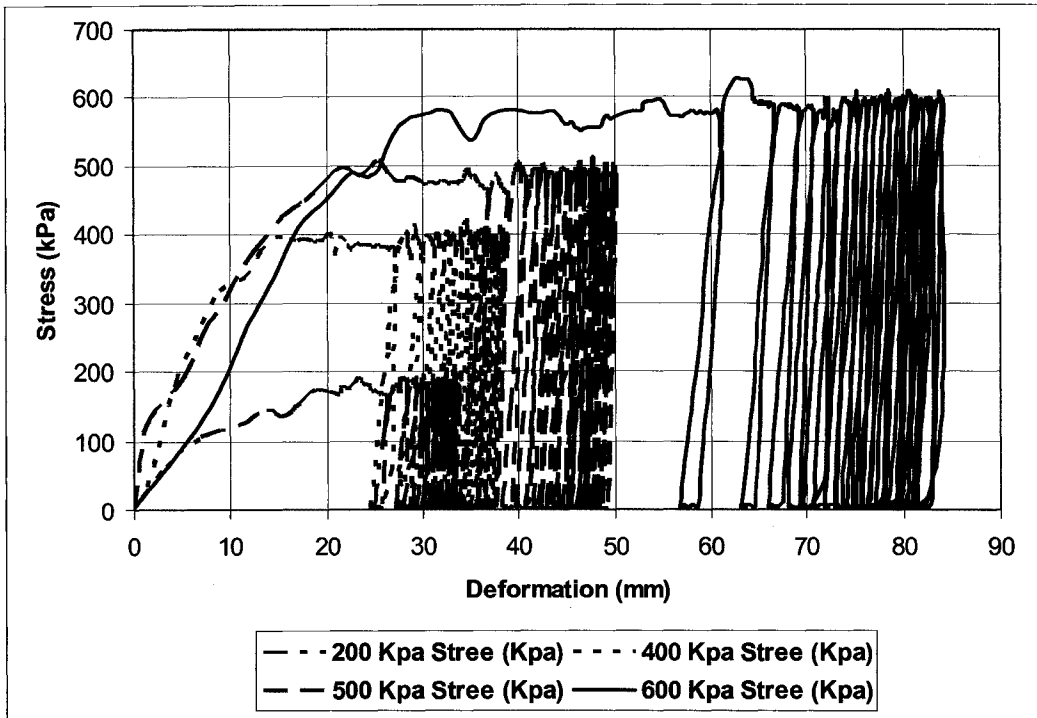


Figure 125: Plate load test results at different stresses for 2-min. loading time

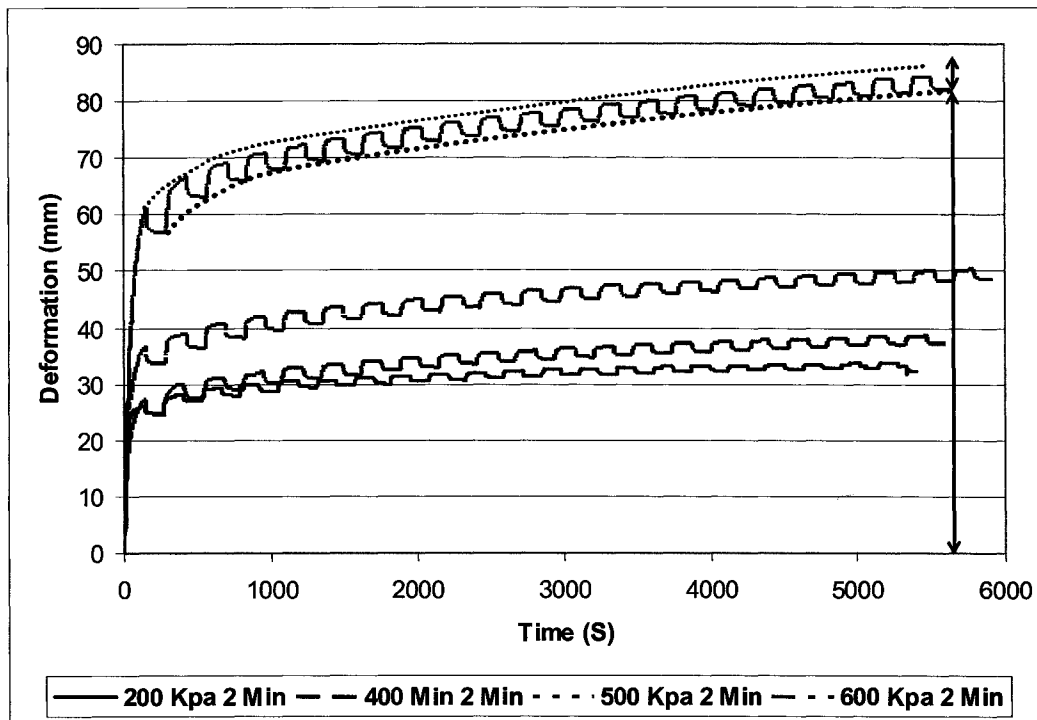


Figure 126: Time deformation results at different stresses for 2-min. duration

## **6.12 Bearing capacity failure types**

### **6.12.1 Background:**

After observing the behaviour of foundations subjected to a load in which bearing capacity failure usually occurs, Craig (1992) identified 3 principle modes of shear failure under a foundation:

#### 1- General shear failure

Failure is identified by a well-defined wedge beneath the foundation and slip surfaces extending diagonally from the side edges of the footing downward through the soil, then upward to the ground surface. The ground surface adjacent to the footing bulges upward. Soil displacement is accompanied by tilting of the foundation (unless the foundation is restrained). The load-settlement curve for the general shear case indicates that failure is abrupt.

#### 2- Local shear failure

Failure has elements of both general and punching shear failure. It has the well-defined slip surfaces that fade into the soil mass beyond the edges of the foundation and do not carry upward to the ground surface. Slight bulging of the ground surface adjacent to the foundation does occur. Significant vertical compression takes place beneath the foundation.

#### 3- Punching shear failure.

Failure involves significant compression of a wedge-shaped soil zone beneath the foundation and is accompanied by the occurrence of vertical shear beneath the edges of the foundation. The soil zones beyond the edges of the foundation are little affected, and no significant degree of bulging occurs. Aside from a large settlement, failure is not clearly recognized.

Type 2 and 3 failures are shown in Figure 127. During plate load tests with different loading times, it was observed that the punching-type failure occurred with instant loading and unloading. However, with increased loading time, the failure mode changed from a punching shear failure to local shear failure. Selig (1961) reported a punching effect in transient or dynamic loading. Figure 128 illustrates the soil's upward movement around the test plate.

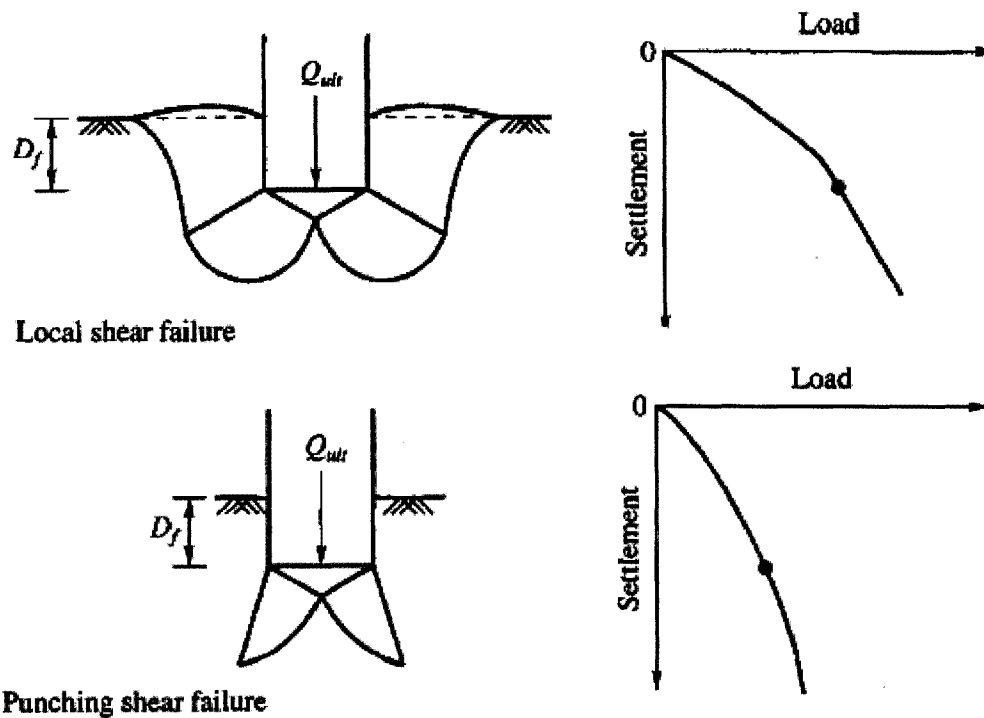


Figure 127: Bearing capacity failure (after Vesic 1963)

### 6.12.2 Failure type of cyclic plate load test:

The soil failure type beneath the circular plate, was changed from pushing shear failure to local shear failure. This failure change was observed with increasing duration between the cycles and increasing load magnitudes. For 10-minute loading time test, the failure or soil movement appeared as a swollen cylinder with a radius of 2.8 times the size of the plate radius. The punching shear failure was due to the instant compaction of the soil under the plate. The explanation for changing the soil failure could be that the soil particles were given enough time to move upwards and to push the material upwards into plate sides by increasing the test duration. In the case of instantaneous loading due to generated confining pressure caused by applied loads, no side movement of the material occurred.

### 6.13 Remarks

During the large-scale laboratory test, it was observed that oil sand can be compacted by a continuous load application as opposed to impacting. Also, the

failure mode of the oil sand under the constant footprint was time-dependent and changed from punching to local shear failure with increasing duration. Therefore, it can be inferred that during mobile mining equipment's operation, the oil sand beneath the equipment becomes more compacted. However, the ground stiffness decreases due to increasing deformation by increasing time and test duration. The compaction is a function of the applied load and the duration of loading.

The general stress-deformation curve from the laboratory tests (see Figure 126) illustrated that the plastic deformation increased and that the elastic deformation reached a constant value after a given duration and number of cycles. The general curve of the large-scale laboratory and field tests are similar, as might be expected.

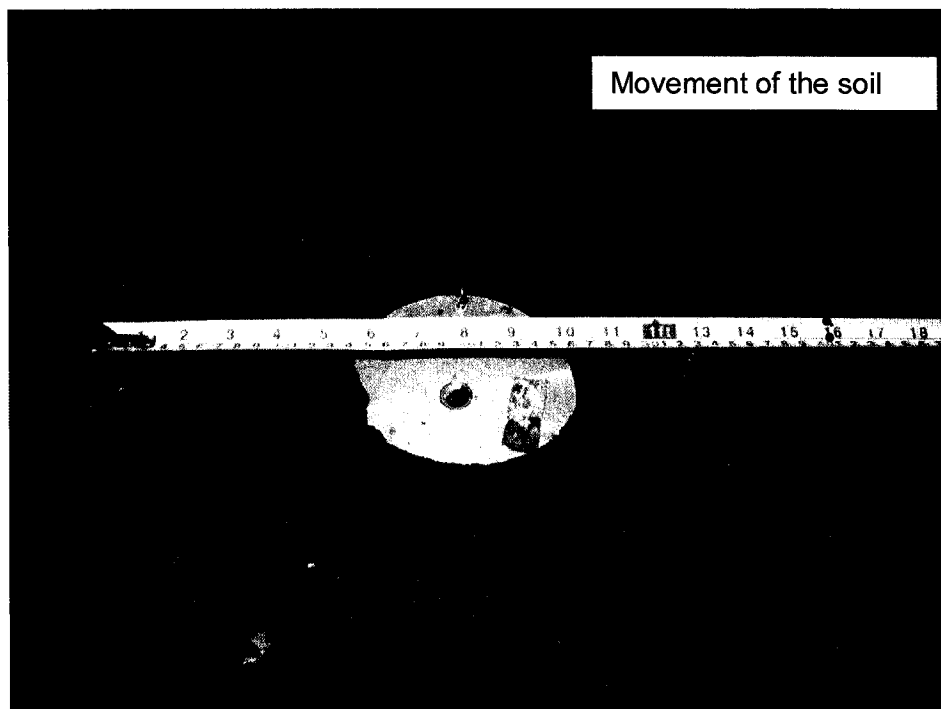


Figure 128: Local shearing failure at 10-min. loading time

## 7 Analysing the large-scale laboratory tests

### 7.1 Introduction

As was previously mentioned (previous chapter), plate load tests were performed at different stress levels and durations. The number of cycles was kept constant at 20 cycles for all tests. Analysis of stress-deformation curves for the plate load test was divided into two categories:

- Initial loading: The behaviour of the oil sand before applying cyclic loading; the initial properties of the stress-deformation graph.
- Cycling: The behaviour of the oil sand after the initial loading; the second portion of the stress-deformation graph

For large mobile mining equipment, initial loading occurs only when the equipment (like shovel) moves into a new area. For instance, when a shovel moves to a new face, the ground experiences initial loading. However, beyond that period, initial loading does not occur, but the ground deforms in a cyclic manner.

To normalize the effect of a variable footprint, it will be calculated the pressure stiffness (Pa/m) rather than the load stiffness (N/m). “Pressure stiffness” is defined as stress per unit deformation, explained as a normalized load for a footprint area. Pressure stiffness can be calculated in two ways:

- A global slope (pressure stiffness): The calculations include each point on a stress-deformation curve where the total pressure divided by the total deformation corresponds to the stiffness at that point termed  $\xi_g$  (see Figure 129).
- A local slope (local pressure stiffness): The calculations include every two points on the loading or unloading portion of a stress-deformation curve, where the stress difference per unit deformation calculated difference at those two points, termed  $\xi_l$  (see Figure 129).

The objective of this chapter is to find the relationships among the stress, loading time, deformation, number of cycles and relaxation time. Also, scaled laboratory tests for constant footprints will be used to predict the deformation for large-scale, field equipment.

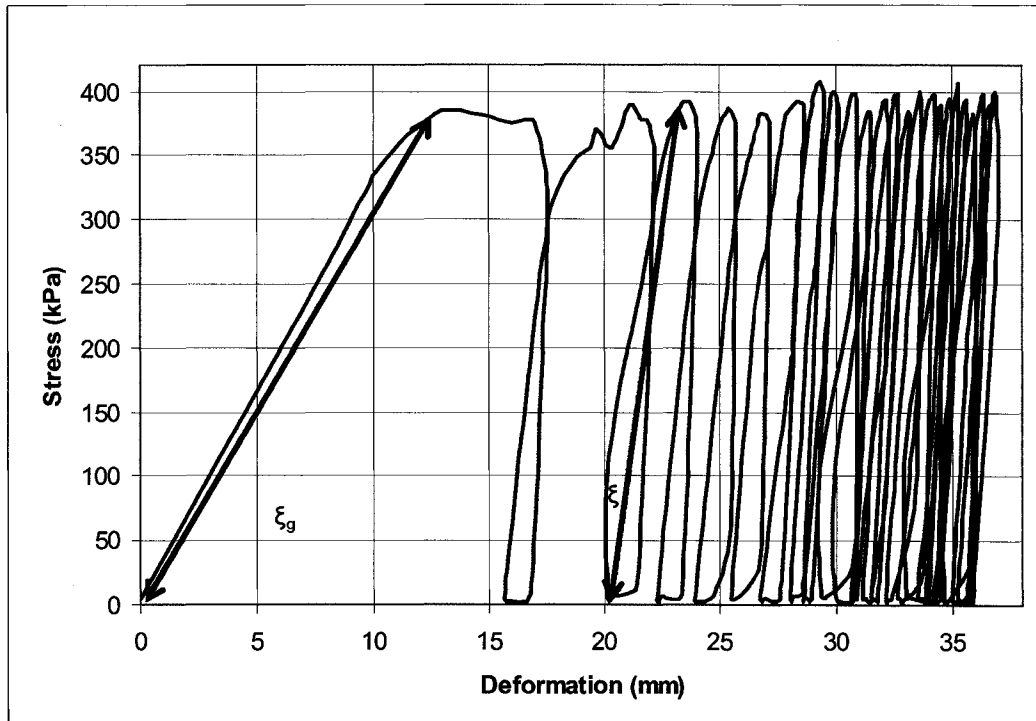


Figure 129: Global and local slope (stiffness)

## 7.2 General pressure-deformation overview

The stress-deformation plot for a plate load test contains three different stages as illustrated in Figure 130. The first stage involves the initial loading or initial loading to the desired pressure. During the second stage, the desired pressure remains constant followed by unloading. Minor fluctuations in the stress due to the soil movement under the plate and to the flow rates in the pressure pump during loading occur. The third stage involves cycling with loading, constant load, and unloading followed by relaxation stages. The density was measured before and after each test to investigate any relationship between the initial density and the deformation. The initial densities varied from 1.7 to 2 kg/m<sup>3</sup> and the final density from 1.7 to 1.9 kg/m<sup>3</sup>. Appendix 6 presents the complete results of the

laboratory plate load tests. Also, fourteen tests have been numbered as shown in Table 10.

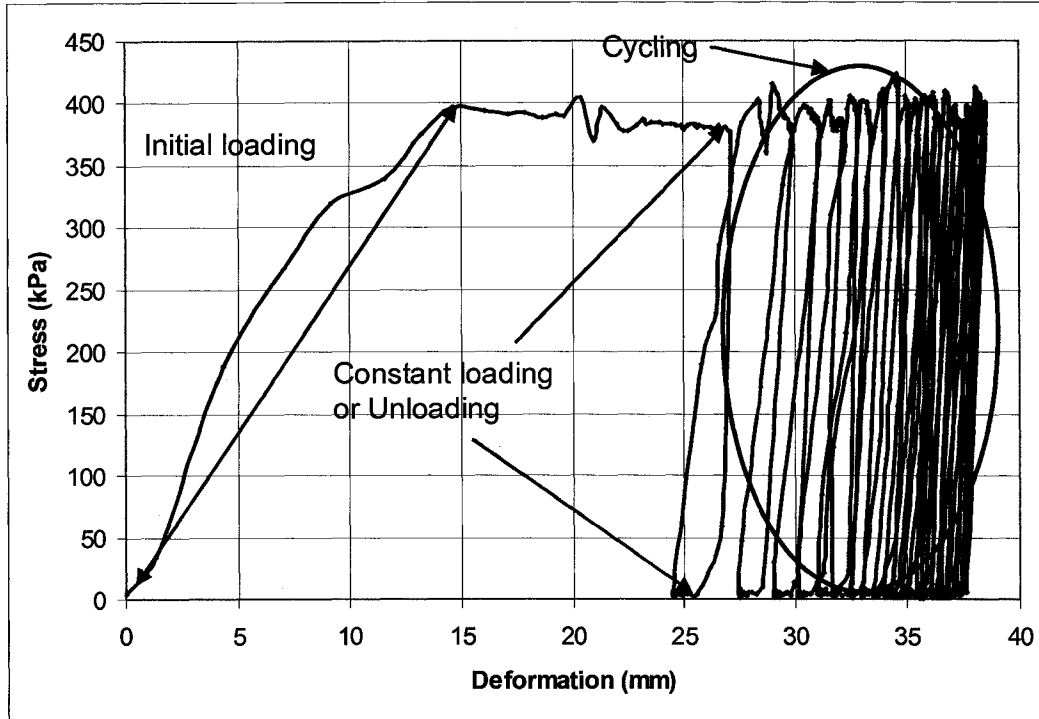


Figure 130: General stress-deformation curve for plate load test

### 7.3 Initial loading Analysis

To provide a better understanding of the stress-deformation curve and to improve the ability to predict oil sand deformation under cyclic loading, the pressure stiffness, deformation, loading rate and density were analysed to reveal any relationships among those parameters.

#### 7.3.1 Deformation

Plotting the deformation versus the pressure for initial loading revealed a very low correlation between increasing pressure and increased deformation. However, the initial starting material's density affected the initial loading deformation. No relationship was found between the deformation and the loading rate. The loading rate for the initial loading was calculated by dividing the maximum pressure at the stress-deformation graph by the time of initial loading that is the

time of pressure reached from zero to maximum. The loading rate was independent of the test duration and it was controlled by manually closing the speed of the pump valve. This result might have been due to the soil particles having insufficient time to rotate and reach an equilibrium position. This finding implies that for the deformation of mobile mining equipment, the loading rate is not an important factor in ground deformation. The main factor that influences deformation is the load and loading rate. If the loading rate was very slow due to viscous behaviour of the material, it will be deformed more compared to a very high loading rate. Also, load level is a very important parameter for deformation and by increasing the load level deformation it will be increased.

Table 10: Results of large-scale laboratory tests

No	Pressure (kPa)	Density Before	Density After	Loading Rate (kPa/sec)	Deformation (mm)
0 Minutes					
1	200	1.928	1.773	8.6	15.0
2	400	1.771	1.807	31.8	12.7
3	500	1.737	1.826	14.5	39.0
4	600	1.923	1.807	21.0	21.9
2 Minutes					
5	200	2.017	1.963	4.9	23.4
6	400	2.033	1.823	16.5	14.7
7	500	2.042	1.935	16.6	21.7
8	600	1.901	1.831	16.1	32.7
5 Minutes					
9	200	1.948	1.902	13.7	13.5
10	400	1.969	1.852	16.9	24.0
11	500	1.885	1.956	27.7	33.4
12	600	1.945	1.837	23.8	35.4
10 Minutes					
13	400	1.809	1.956	21.0	25.0
14	600	1.972	1.924	14.7	35.4

### 7.3.2 Pressure Stiffness

The global pressure stiffness for the 5-minute duration tests is illustrated in Figure 133. The curves for the different pressures are very similar and close to each other. Two different methods were used in averaging the data:

The first method averaged the data points. The data points during the unloading and relaxation procedures were removed for all stress levels, and then, the existing data points during the loading stage were averaged (see Figure 131).

The second method averaged the data points on the rebuild curve. First, a curve was fitted onto each data series for different stress levels, and by removing the points for the unloading and relaxation procedures, the data were averaged on the regenerated data points by using a curve-fitted equation (see Figure 132). The viscous material is usually expressed by a power or exponential equation. The power equation was fitted with a higher coefficient factor compared to the exponential equation. For both methods, the global pressure stiffness versus time data was plotted as

$$\xi_g = At^B. \quad [37]$$

Table 11 presents the coefficients A and B for two different methods, which are very consistent.

Table 11: Coefficient factor via each of the two analytical processes

Pressure(kPa)	Analytical Process	A	B
0 Min.	Curve Fit	29.25	-0.193
	Average Data	29.52	-0.194
2 Min.	Curve Fit	21.56	-0.118
	Average Data	21.83	-0.128
5 Min.	Curve Fit	15.39	-0.072
	Average Data	15.56	-0.074
10 Min.	Curve Fit	14.72	-0.061
	Average Data	14.61	-0.060

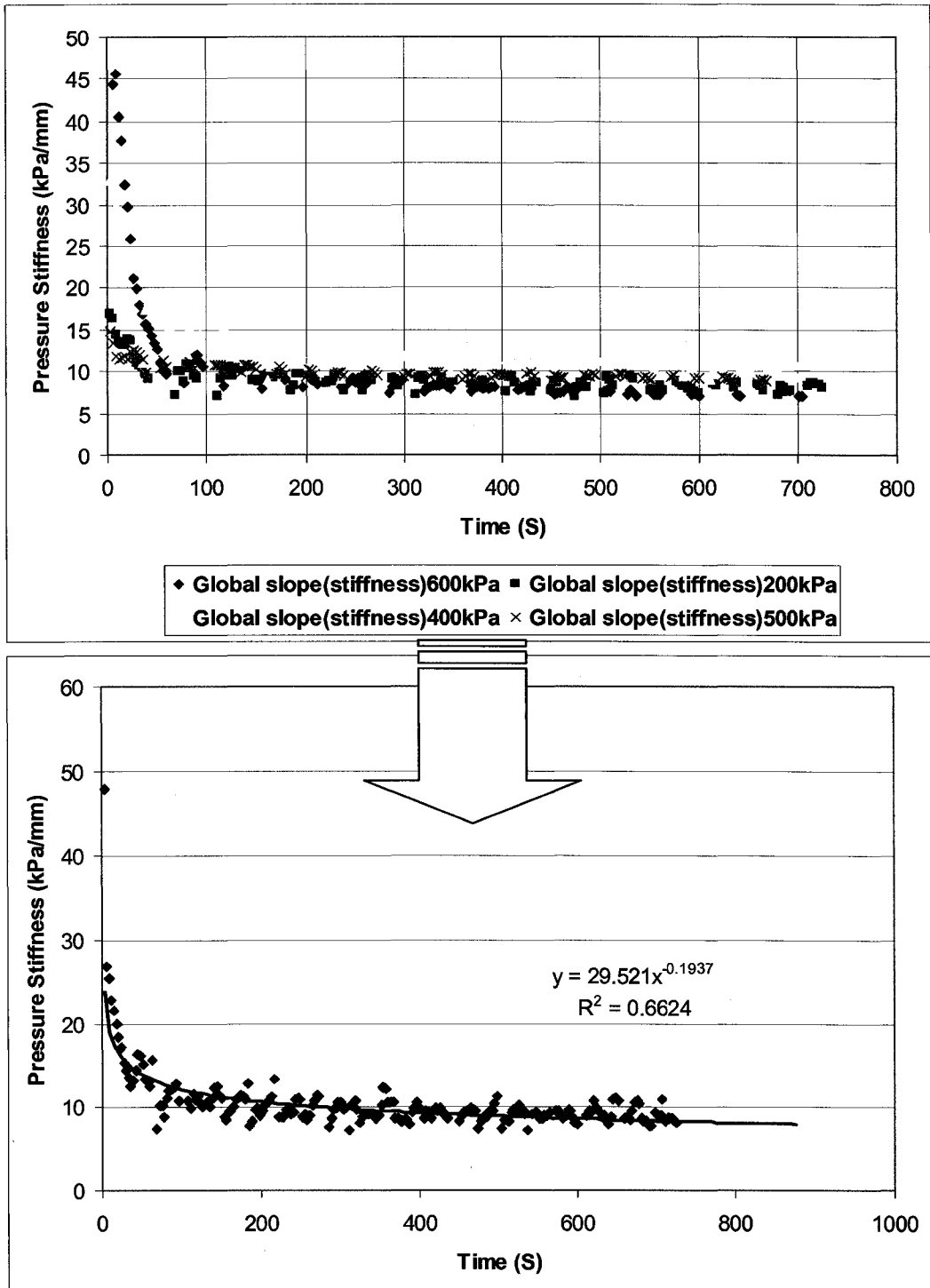


Figure 131: Average data method

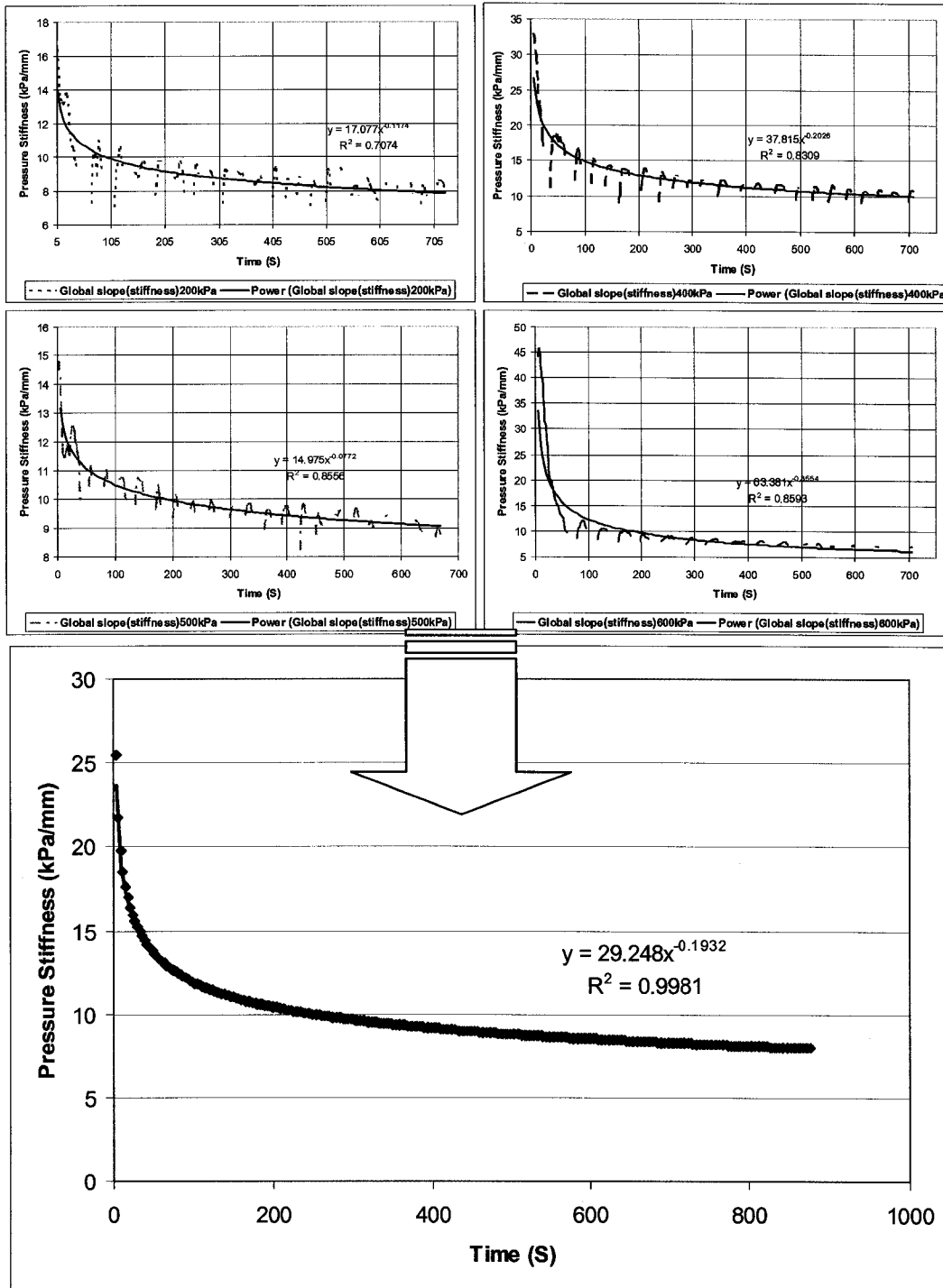


Figure 132: Curve fit method

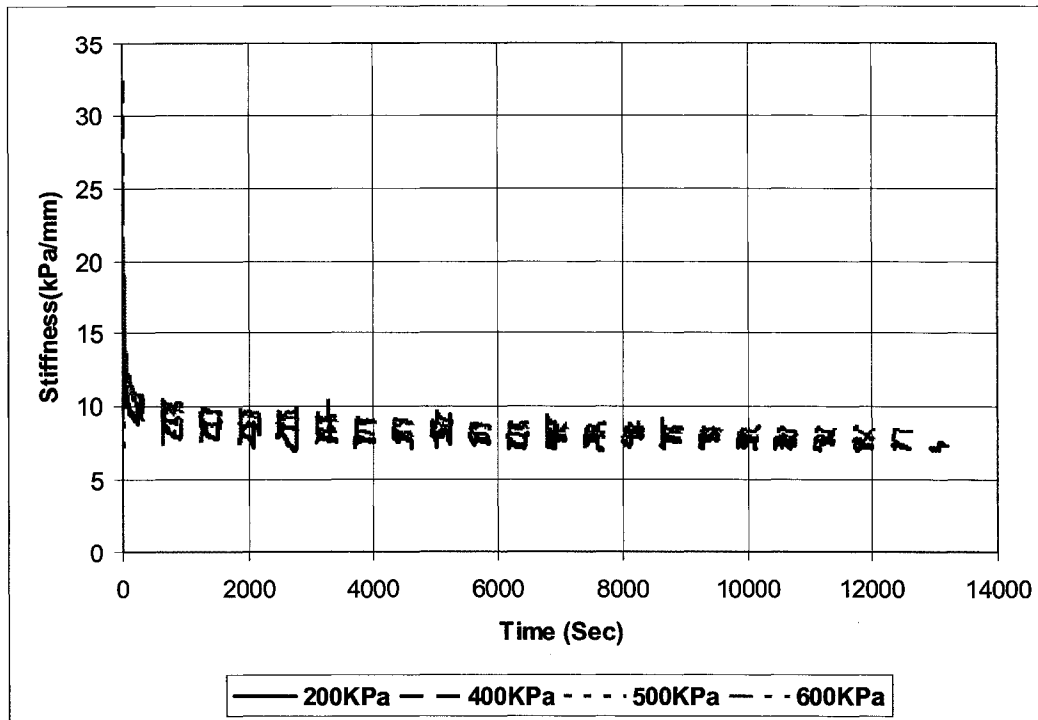


Figure 133: Pressure stiffness vs. time for 5-min. tests

Figure 134 and Figure 135 present the results of both analytical approaches for the first 100 seconds. Despite using the averaging method within the 100-second range, the 5- and 10-minute tests are identical. However, the 0-min test's resulting graph is different due to punching failure. The 0-minute test duration means that loading is followed instantly by unloading and vice versa. Punching failure occurs in the dense material, so this test may be considered as a compaction test for the material as there was no time for relaxation. The 2-minute test is a transitional or partial compaction equivalent. However, after running tests for 200 seconds, the 2-, 5-, and 10-minute tests converged on each other. For the 0-minute test, insufficient time was available for material rehearsal deformation to occur.

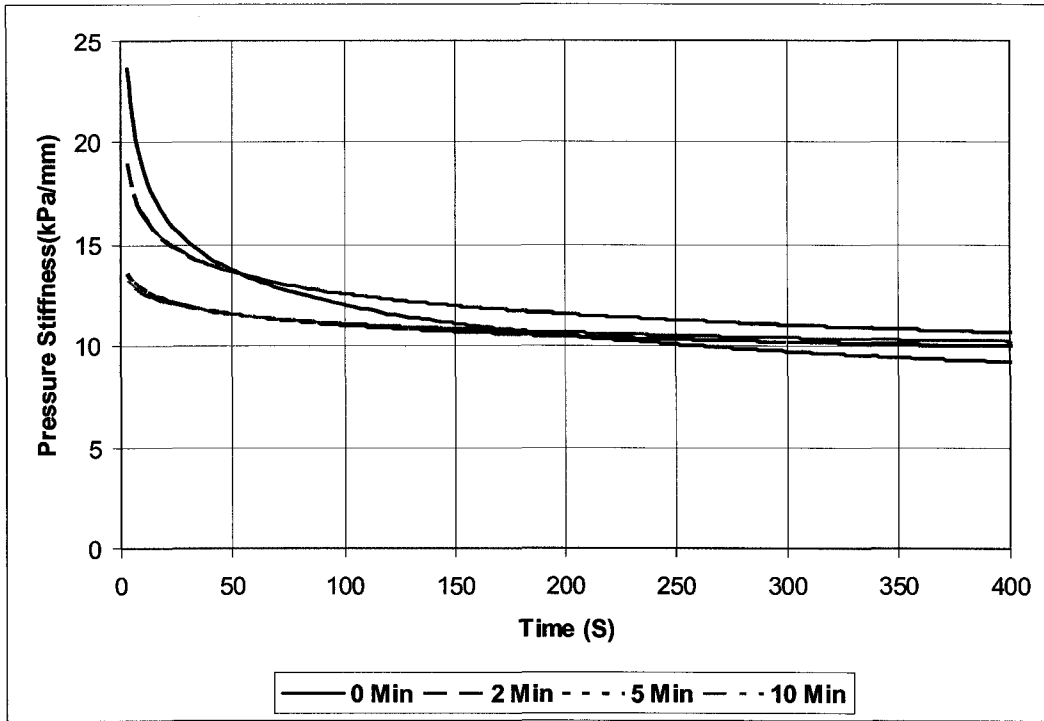


Figure 134: Final curves for different tests based on averaging curve fit

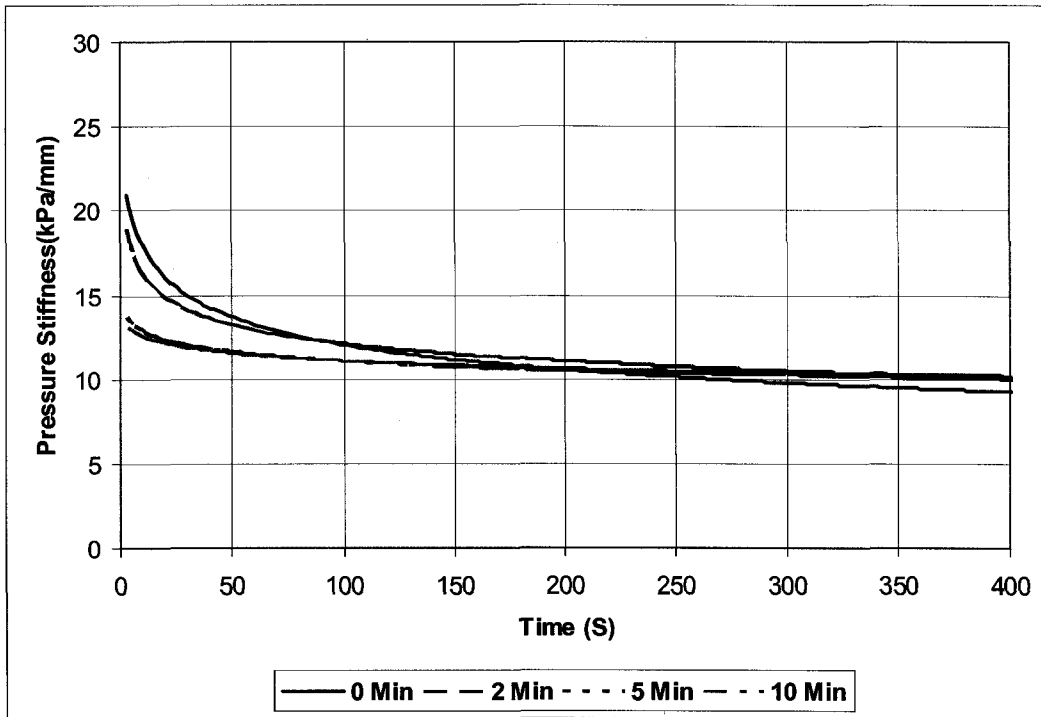


Figure 135: Final curves for different tests based on averaging data points

### 7.3.3 Loading rate

The loading rate for initial loading was calculated from time zero to the maximum load on initial loading. The load was actuated by an air-hydraulic pump, which gave good control of the loading condition. However, during initial loading, due to the slowness of the available data-acquisition system, which was 0.3 Hz slower than the cyclic test demand, it was difficult to keep the loading rate constant. The 0.3 Hz of data-acquisition system did not response when there was a sudden change in voltage at less than 0.3 Hz. This was caused by load or deformation, during the loading. The sudden load change caused a delay in response of the data-acquisition system. The loading rate should be considered as one of the key parameters in pre-cyclic deformation. However, no strong relationship was found between the loading rate and the deformation or pressure stiffness (see Figure 136). Figure 137 illustrates a very strong relationship between the loading rate and deformation rate for 5 min test.

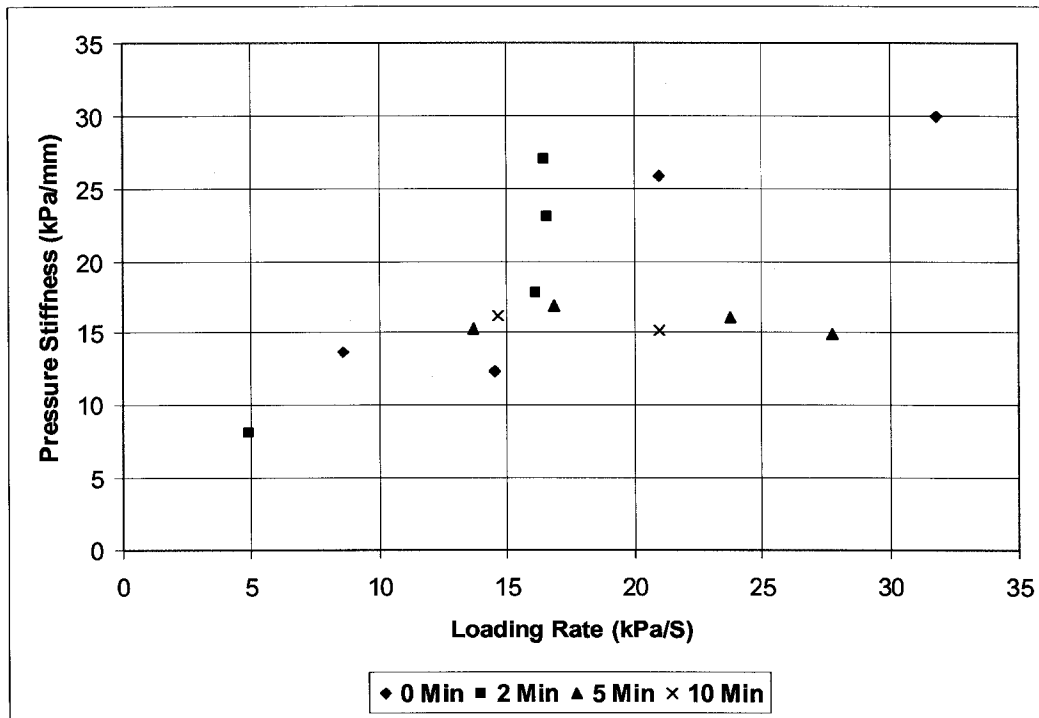


Figure 136: Loading rate vs. pressure stiffness for initial loading

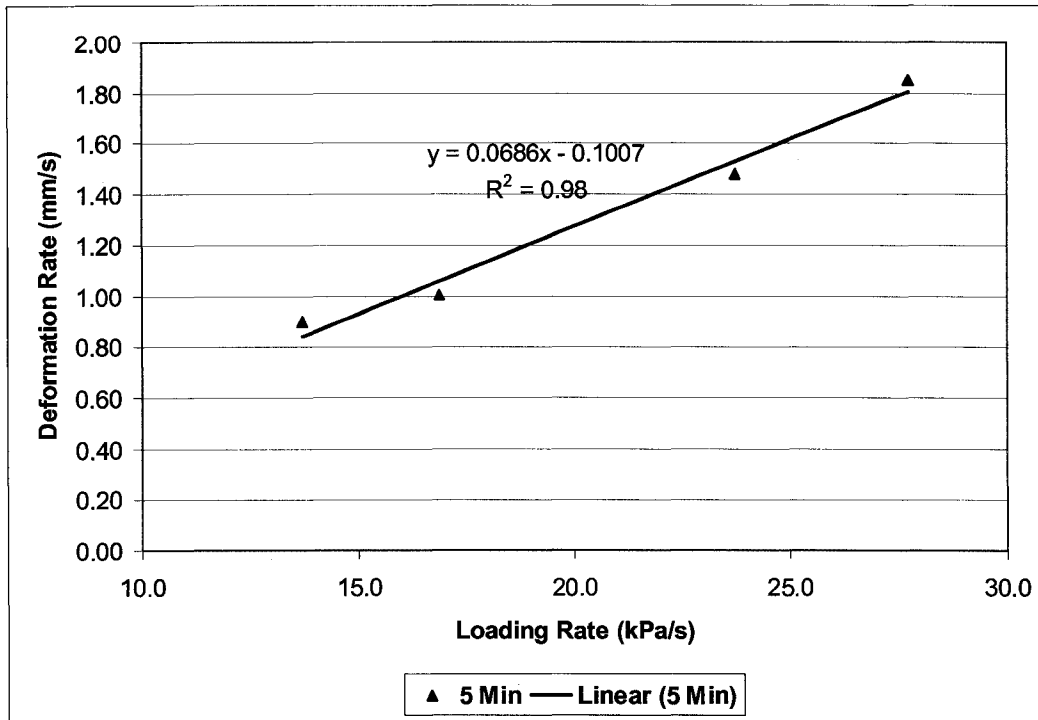


Figure 137: Loading rate and deformation rate for 5 Min test

### 7.3.4 Density

The density and moisture content were measured before and after each test by using a nuclear densometer (Troxler). The initial density measurement with the Troxler unit had a depth of influence up to a maximum of 12 cm; therefore, the density represents a soil bulk density for a zone of influence of ~12 cm. After completing each test, density measurement on both sides of the circular plate was performed, as was mentioned in section 4.9. Density change should be considered the most important parameter in deformation during initial loading. Soil with a high density has less void space than other soils and, therefore, should have less deformation for a given applied load. Measuring the density continuously was difficult. Density changes during the initial loading were observed when the material's behaviour changed from compaction to flowing with time and the magnitude of loading. However, no relationship was found between the initial density and the deformation for initial loading (see Figure 138). The average fluid content of the material (total volume of oil plus water) was 14 to 18

percent. Table 12 shows the density and corresponding deformation and loading rate for Figure 138.

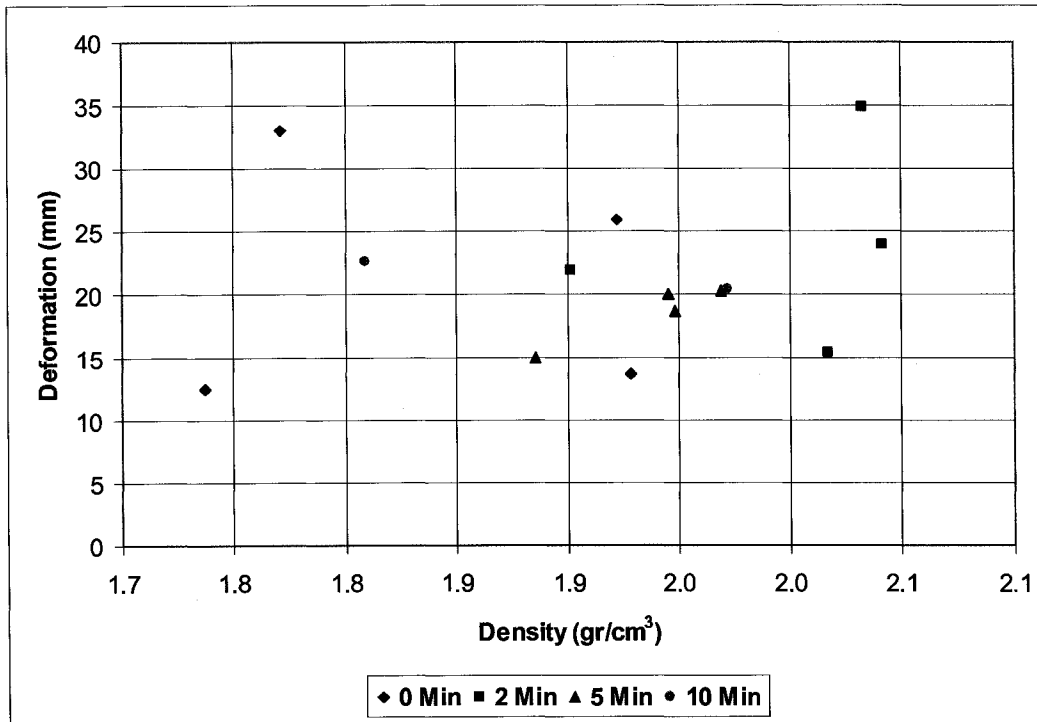


Figure 138: Initial density versus initial loading deformation

Table 12 : Density, deformation and loading rate

Load (kPa)	Test	Deformation (mm)	Loading Rate (kPa/s)	Density (gr/cm <sup>3</sup> )
200	0 Min	13.70	8.57	1.928
400		33.04	31.84	1.771
500		12.52	14.53	1.737
600		25.90	20.98	1.923
200	2 Min	15.39	4.88	2.017
400		34.92	16.50	2.033
500		24.01	16.60	2.042
600		21.83	16.12	1.901
200	5 Min	18.74	13.70	1.948
400		20.22	16.88	1.969
500		14.97	27.74	1.885
600		20.05	23.75	1.945
200	10 Min	-	-	-
400		22.68	20.96	1.809
500		-	-	-
600		20.40	14.66	1.972

## 7.4 Cycling Analysis

The stress-deformation curve was divided into two regions: initial loading and cycling. The analysis of the latter examined the loading and unloading slopes during cycling and predicted the deformation for 20 cycles. The cycling data were divided into the data for deformation, pressure stiffness, and density to study the relationships among the parameters.

### 7.4.1 Deformation

Figure 139 shows the elastic and plastic deformation during cyclic loading for a 2-minute duration. This figure reveals that the elastic deformation after 5 to 8 cycles or 10 to 15 minutes reached a constant value. The deformation of oil sand is a time-dependent phenomenon as oil sand is a viscous material; therefore, the deformation is increased by increasing the stress level.

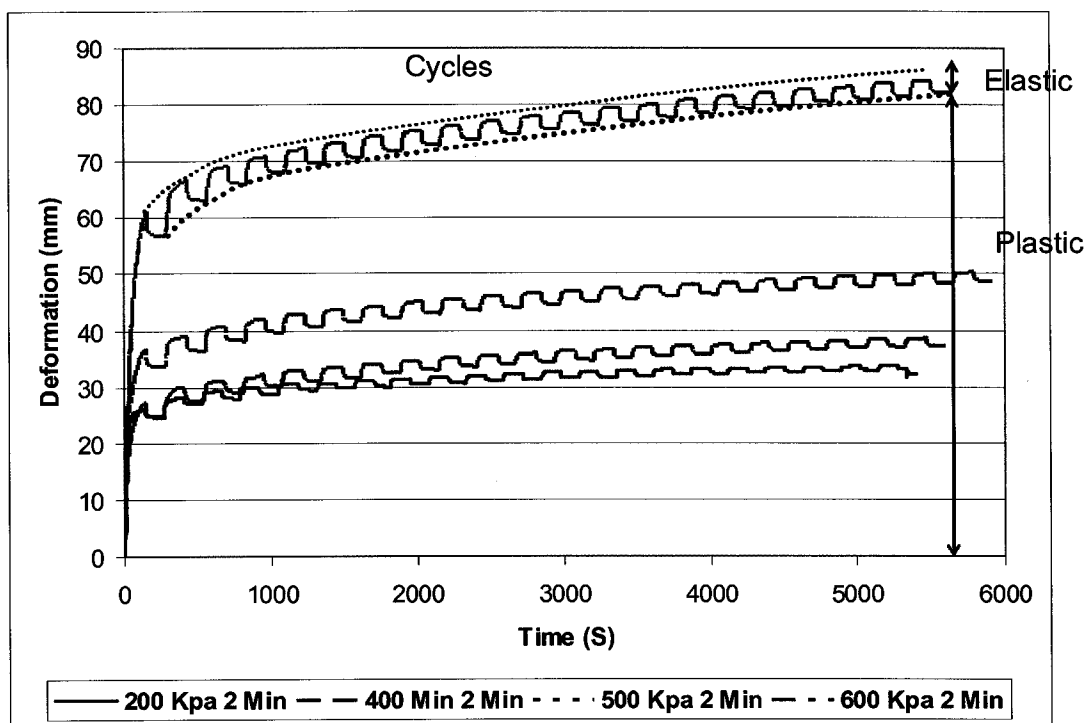


Figure 139: Time deformation curve for loading and unloading at different stresses for 2 min duration test

On initial loading, the oil sand under the plate was compacted and reached a maximum density for oil sand at that pressure. For the 5- and 10-minute duration cycle tests, the cyclic loaded oil sand beneath the plate slowly flowed to the sides of the plate. However, for the 0-minute test, the failure was completely manifest as a punching failure due to the restriction on increasing the density. After removing the points related to the 0-minute test, the pressure deformation plot revealed that a total deformation during 20 cycles exponentially increased with an increase in the stress level (see Figure 140). Figure 140 shows that oil sand deformation was stress-dependent and increased with increasing load levels. For a predictability assessment, the total deformation versus the deformation during 20 cycles was plotted to show the scalable relationship between the two. By removing the points for the 0-minute test, a strong correlation was shown (see Figure 140):

$$\text{Total deformation (mm)} = 4.3 * (\text{total deformation during 20 cycles (mm)}), \quad [38]$$

where the coefficient factor is unitless,

$$\text{and the total deformation} = \text{initial deformation} + \text{deformation during 20 cycles}. \quad [39]$$

By substituting equation [39] into equation [38], it can be shown that

$$\text{Total deformation} = 1.3 * \text{initial deformation}. \quad [40]$$

This method allows us to predict the total deformation for 20 cycles from only the initial deformation after the loading of the oil sands (see Figure 141 and Figure 142).

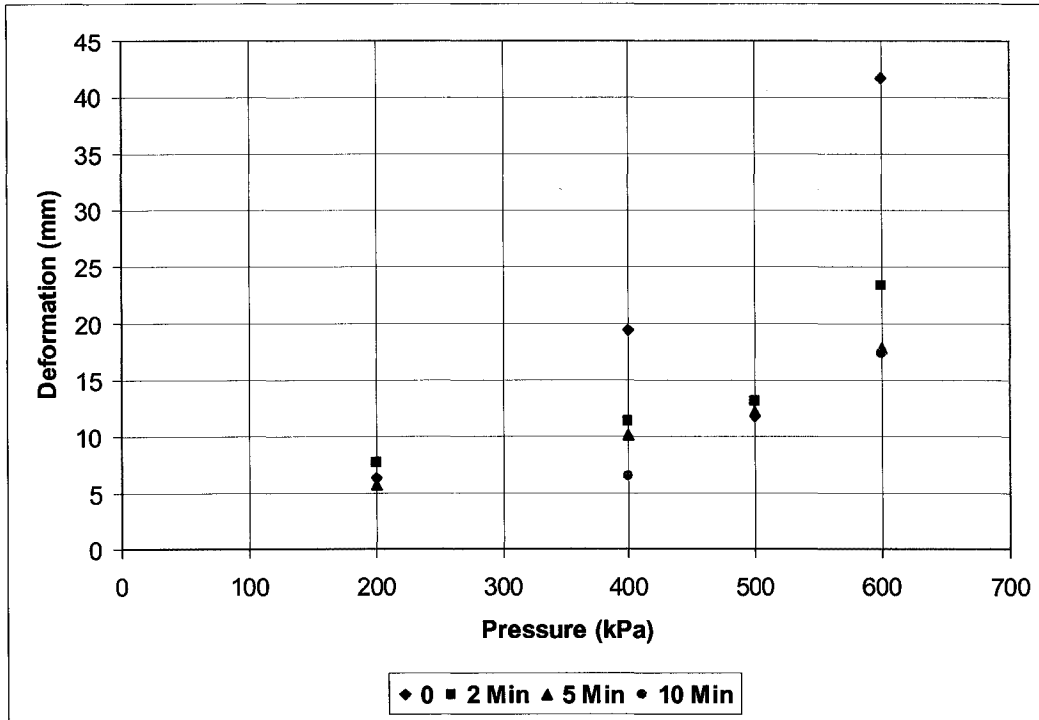


Figure 140: Total deformation at different pressure during 20 cycles

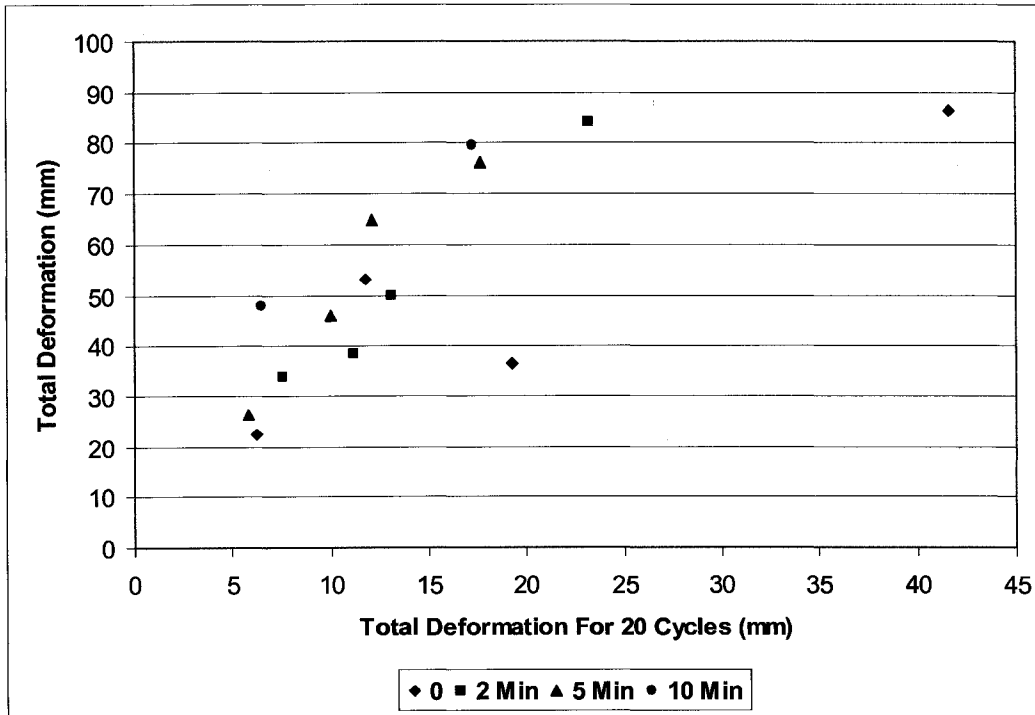


Figure 141: Total deformation versus deformation in 20 cycles for 0-10 min.

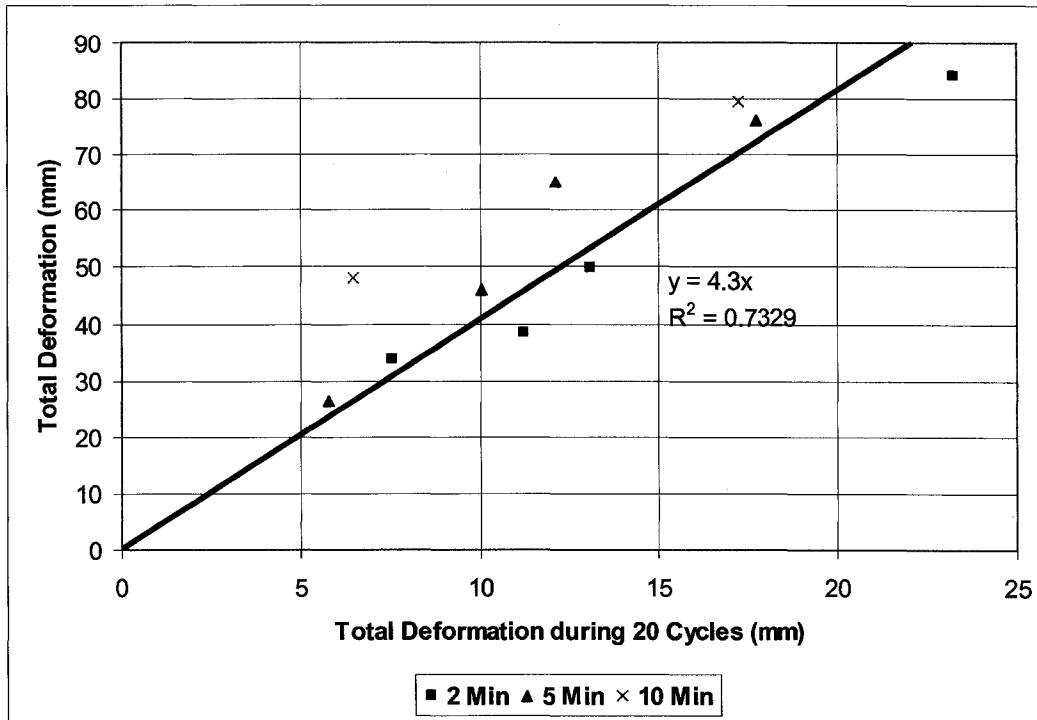


Figure 142: Total deformation versus deformation in 20 cycles for 2-10 min. (on removing the instantaneous 0-min data)

#### 7.4.2 Pressure stiffness

Figure 143 illustrates the total pressure stiffness for varying the duration of the cycle test versus the time. This figure shows the 2-, 5-, and 10-minute duration cycles converge to a similar residual pressure stiffness value of approximately 8 kPa/mm. The 0-minute test value is similar to a compaction test result at a residual value of the pressure stiffness of 5.5 kPa/mm.

Figure 144 and Figure 145 show the local pressure stiffness versus the number of cycles for the 2-minute test and the 0- to 10-minute tests. These figures reveal that an increase in the number of cycles makes the local stiffness increase and converge to a constant value, as shown in Figure 145. After removing the initial cycles for initial loading and averaging the data points in each cycle, a very strong correlation was found between the local pressure stiffness versus the number of cycles (see Figure 146):

Local pressure stiffness=  $106.7 (\text{Number of cycles})^{0.3}$  . [41]

The unit of the coefficient is same as that of the local pressure stiffness (kPa/mm).

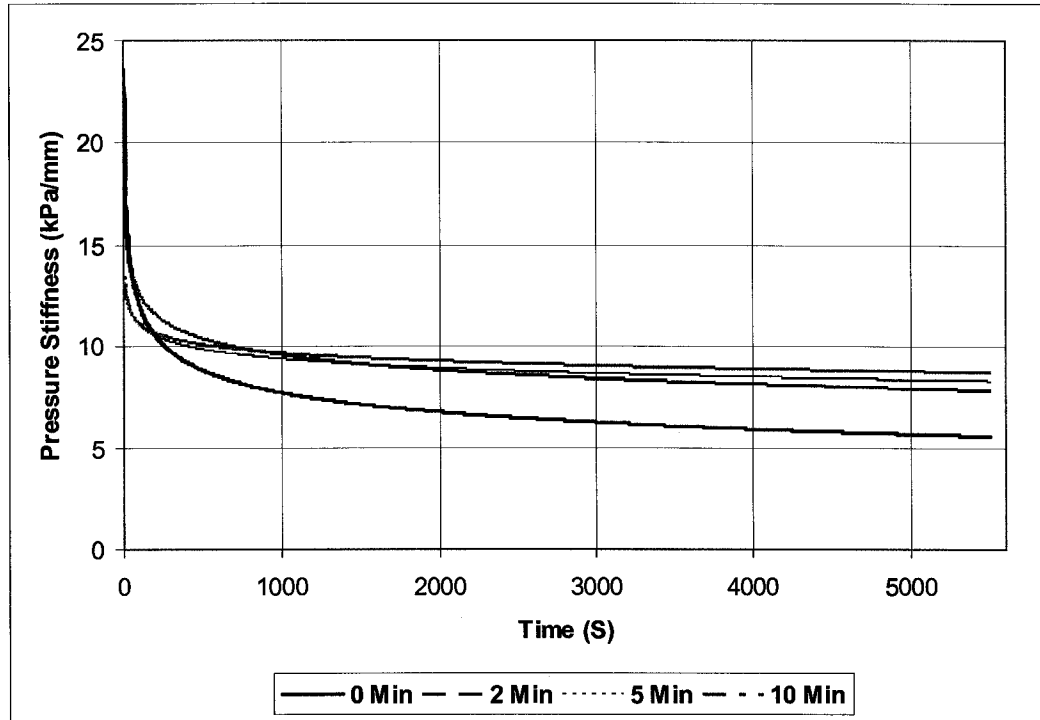


Figure 143: Pressure stiffness for different duration cycles based on averaging curve fit

The bars on the Figure 146 show the variation for the value for each cycle. By using the above equation, deformation may be predicted as a function of the number of cycles. Averaging the data usually smoothes the graph and cancels the error for varying test results. However, the error in our case likely arose from the slow collecting rate of the data-acquisition system, and the inappropriateness of extracting the value from the load-deformation plot of the collected data, and of manually selecting the points when unloading and loading started.

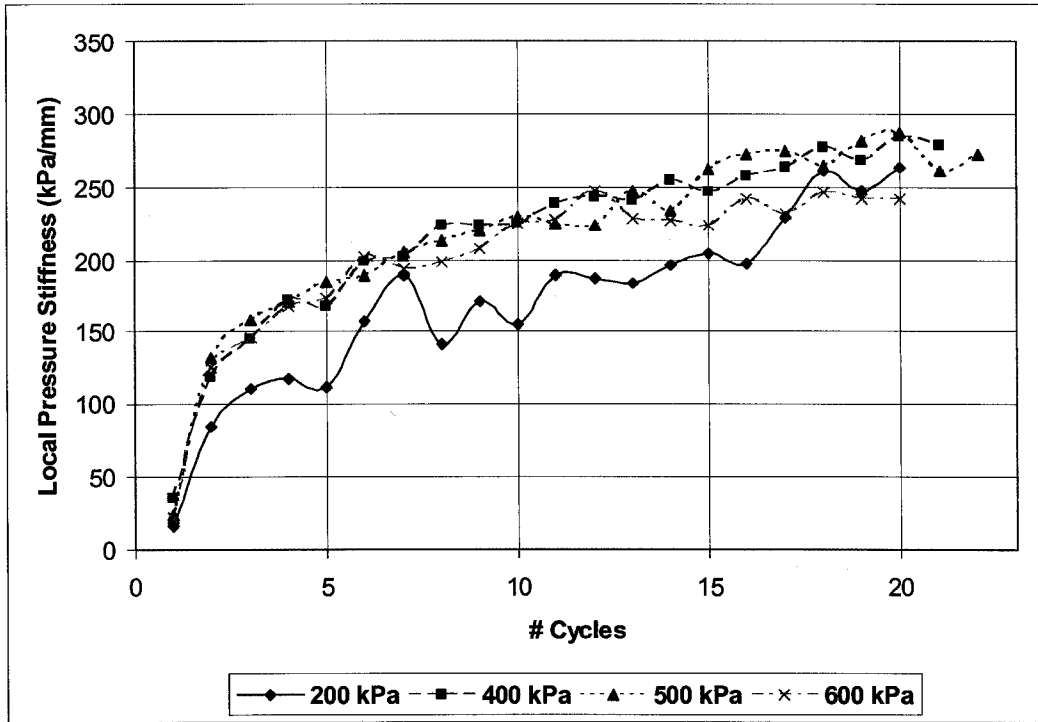


Figure 144: Local pressure stiffness during cycles for 2-min. duration cycles

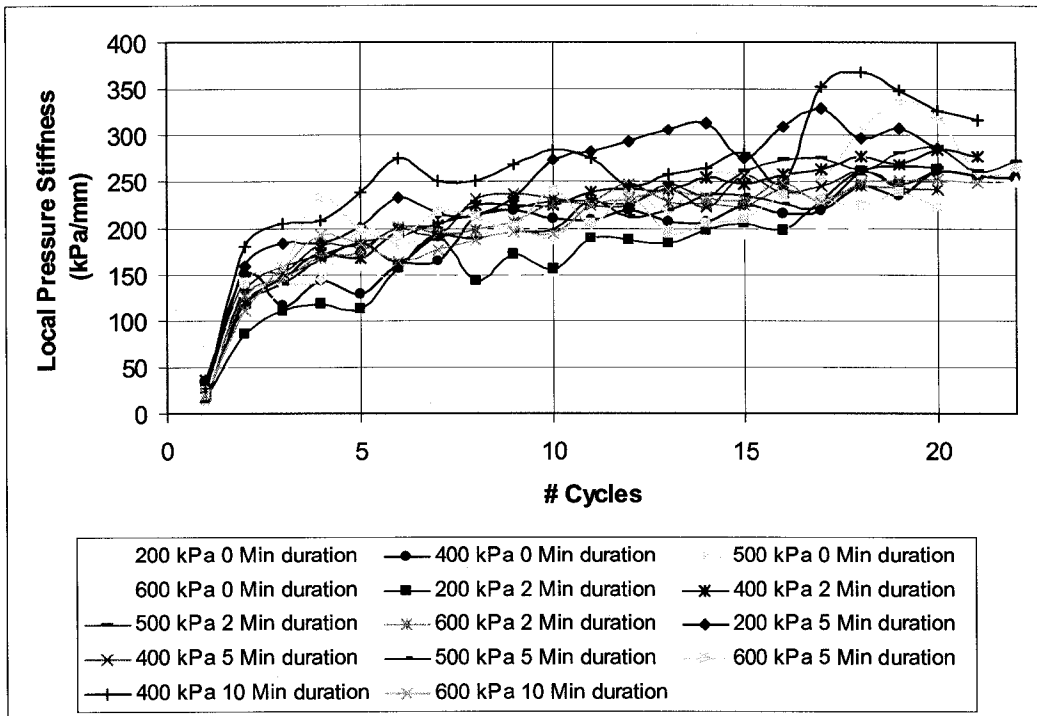


Figure 145: Local pressure stiffness during cycles for 0-10 min. duration cycles

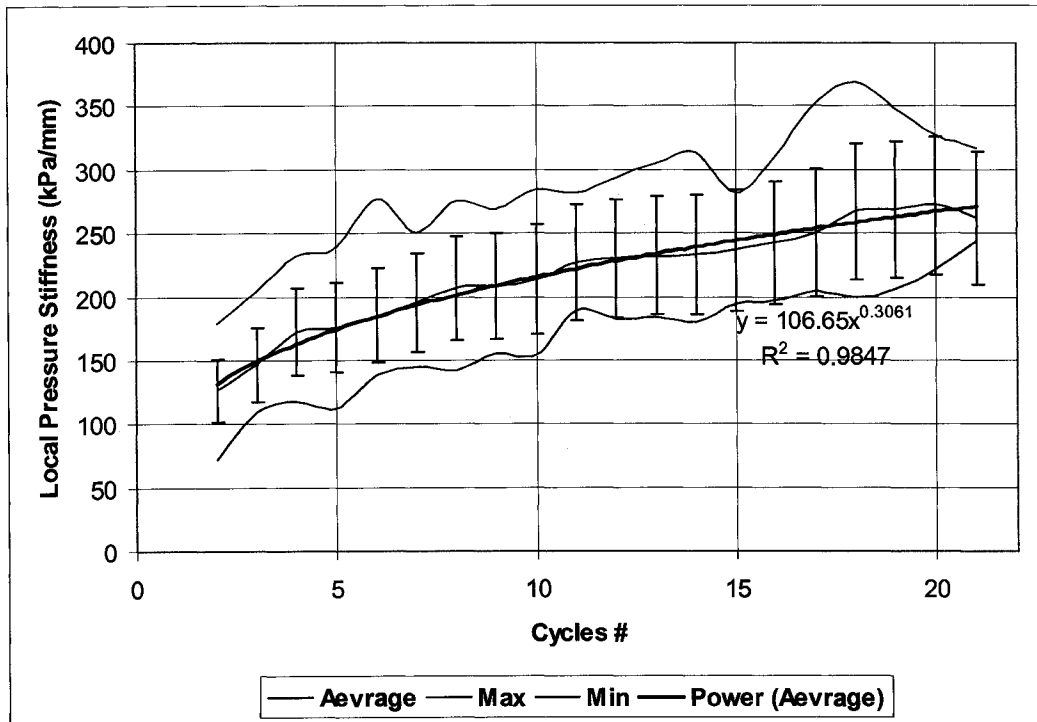


Figure 146: Average of values of local pressure stiffness for 0-10 min. duration cycles

### 7.4.3 Density

Measuring the density during the cyclic loading was a complicated task because of the size of the instrument and the difficulty of continuously measuring the surface. However, no relationship was found between the initial, or the final density and the cyclic deformation. The maximum density achieved during initial loading remained almost constant. Figure 147 and Figure 148 illustrate the initial density versus the deformation during cyclic process, and also the final density. No correlation was found between the initial density or the final density and deformation, during the cyclic activity, just as there was no correlation found during the initial loading. However, in order to change the failure type from punching, to local shear failure, density should be increased beneath the circular plate, by increasing the test duration and cycles. Unfortunately, the final density beneath the circular plate could not be measured due to apparatus restriction.

The density beneath the mobile mining equipment during cyclic loading, should be increased to the maximum density at corresponding pressure. As reported at the literature review, the in situ density of oil sand is between 2-2.1 gr/cm<sup>3</sup>. Therefore, the density beneath mobile mining equipment during activity could not exceed 2.1 gr/cm<sup>3</sup>. Also, the global pressure stiffness, as mentioned previously, drops by increasing the time and cycles that are due to definition of global pressure. Therefore, density increases by decreasing the global pressure stiffness. However, the local pressure stiffness rises by increasing the density and cycles.

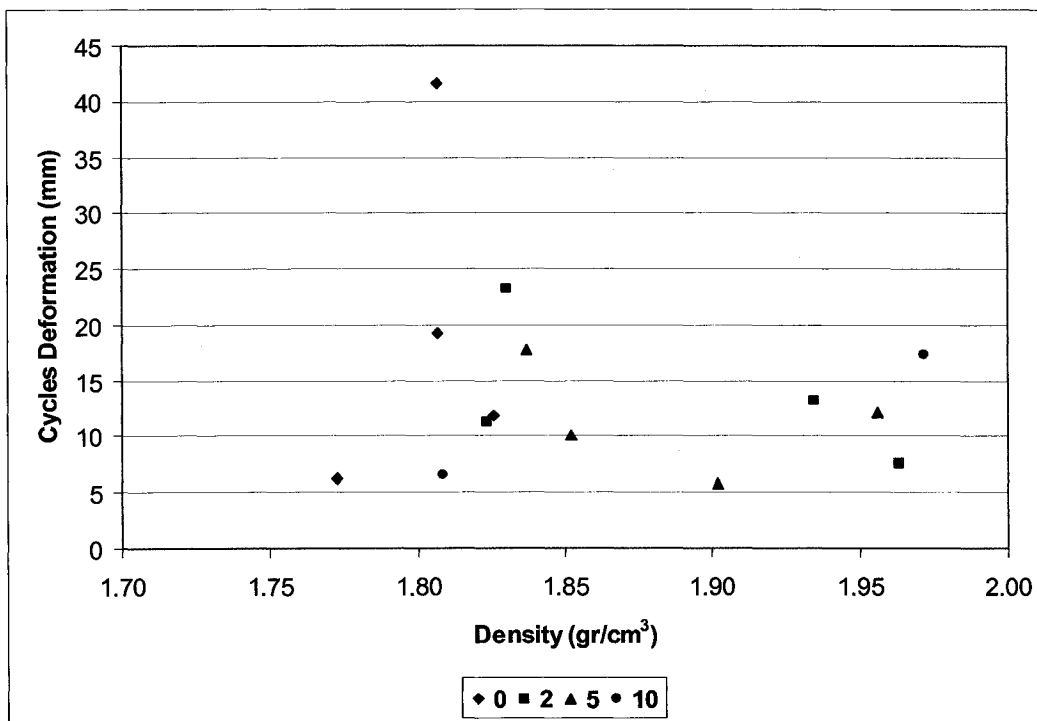


Figure 147: Initial density vs. total cyclic deformation

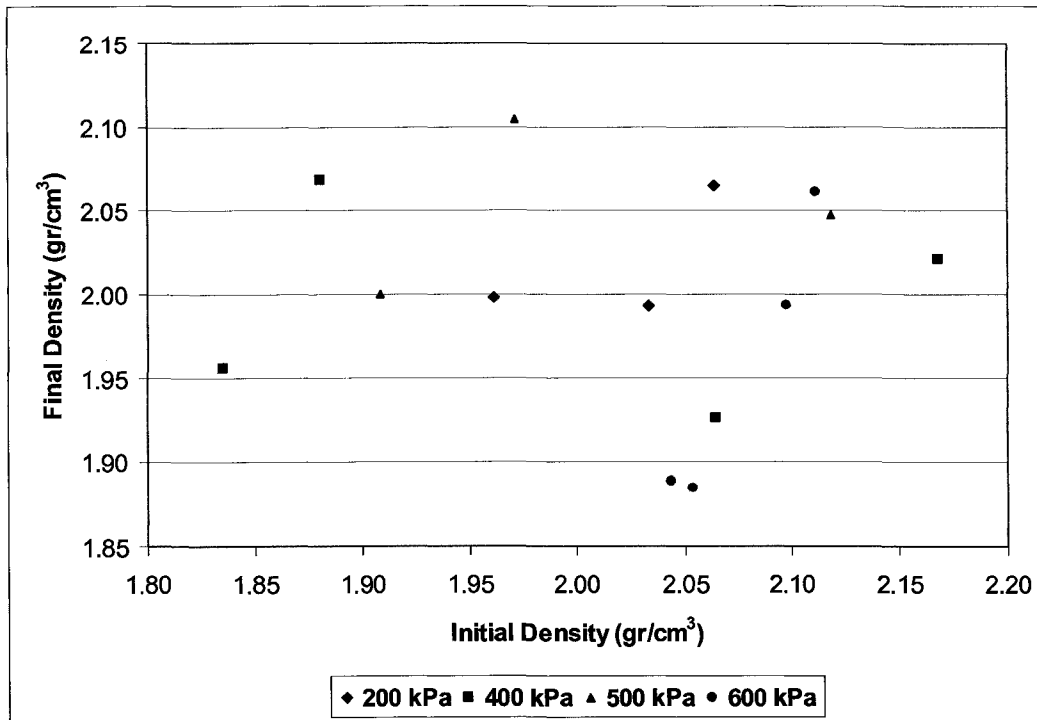


Figure 148: Initial density vs. final density

## 7.5 Total Deformation

By taking the analysis discussed in earlier in section 7.4.1 a stage further, the total deformation may be predicted by adding the deformation due to the constant load for a given duration to the deformation due to a given number of cycles during the cyclic loading. The deformation that occurred during the cyclic loading is a very small portion of the total deformation for a minimum of 20 cycles.

From equation [37],

$$\text{Deformation during constant loading} = \text{Pressure} / A \times t^B \quad [42]$$

$$\text{Local pressure stiffness during cycles} = 106.7 \times (\text{Number of cycles})^{0.3} \quad [43]$$

$$\text{Deformation during cyclic loading} = \text{Pressure} / \sum_{i=1}^{NC} 106.7 \times (NC)^{0.3} \quad [44]$$

where NC is Number of cycles

If Total Deformation = Deformation during cycles + deformation during constant loading,

$$\text{then Total Deformation} = [\text{Pressure} / A \times t^B] + [\text{Pressure} / \sum_{i=1}^{NC} 106.7 \times (NC)^{0.3}], \quad [45]$$

where A and B are the parameters dependent on the cyclic duration, and the unit of pressure is kPa.

### 7.6 Prediction of Coefficient factor for cyclic plate load tests

As explained in pervious section 7.5, the deformation of the oil sand can be calculated by using the following equation:

$$\delta_t = [\sigma / A t^B] + [\sigma / \sum_{i=1}^{NC} 106.7 \times (NC)^{0.3}].$$

A and B in above equation are related to the applied load, as shown in Figure 149:

$$A = 0.0317\sigma + 7.318$$

$$B = -0.0002\sigma - 0.036$$

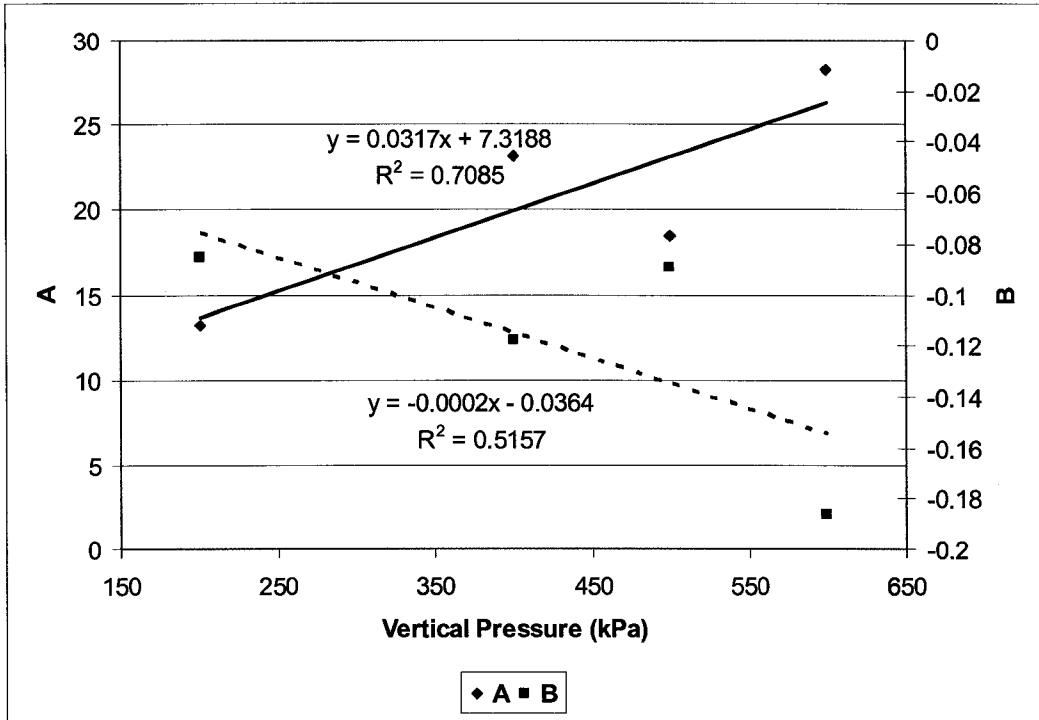


Figure 149: Coefficient factors for different vertical pressure level

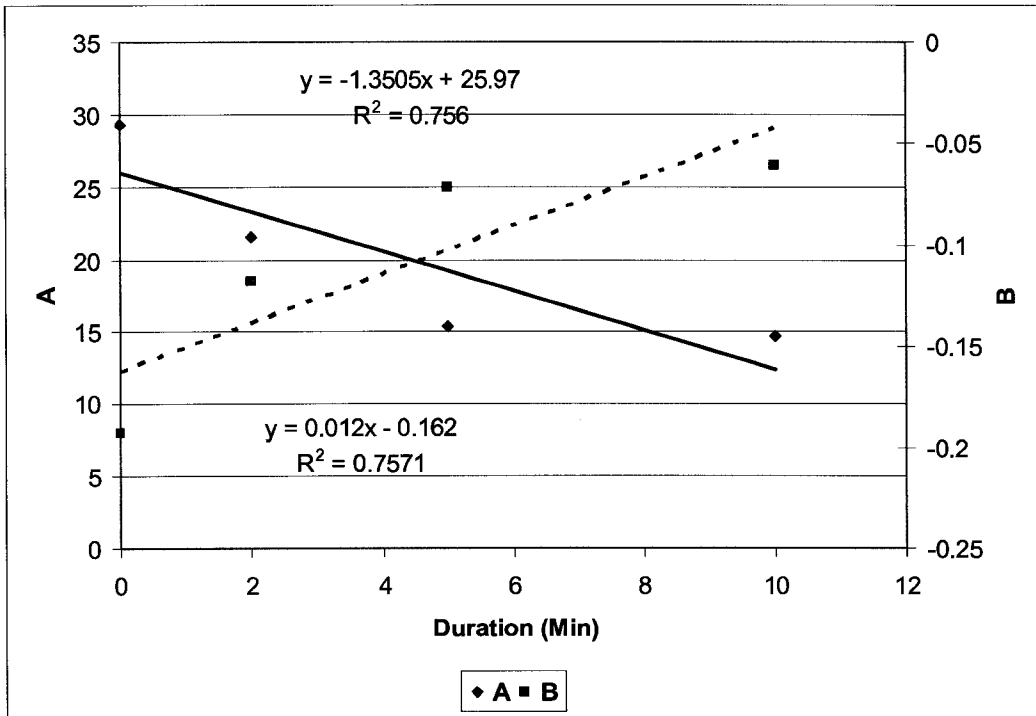


Figure 150: Coefficient factors for different curve duration 0 to 10 Min tests

## 7.7 Effect of cycles on total deformation

In order to investigate the effect of the cycles on the total deformation for the laboratory cyclic plate load test, the 600 kPa and 5 Min test was chosen for an in-depth look at the effect of the cycles on total deformation. Figure 151 shows the stress versus deformation curve and Figure 152 shows deformation versus time for 600 kPa and 5 Min test.

Figure 153 illustrates the in-depth analyses of the effect of two cycles, for 10 mm deformation. The average of the deformation during loading during cycles for each load is approximately 3 mm. Therefore, during the 20 cycles the deformation would be 60 mm. However, approximately 70% of the cycle's deformation recovers during unloading. During the 80 mm deformation of plate load cyclic test, the 20 mm or 25% of total deformation, is due to the cycles. Even though the effects of the cycles are small, under the mobile mining equipment, the ground experienced thousands of cycles. Also, under constant loading of 5 minutes, the deformation is approximately is 2-3 mm.

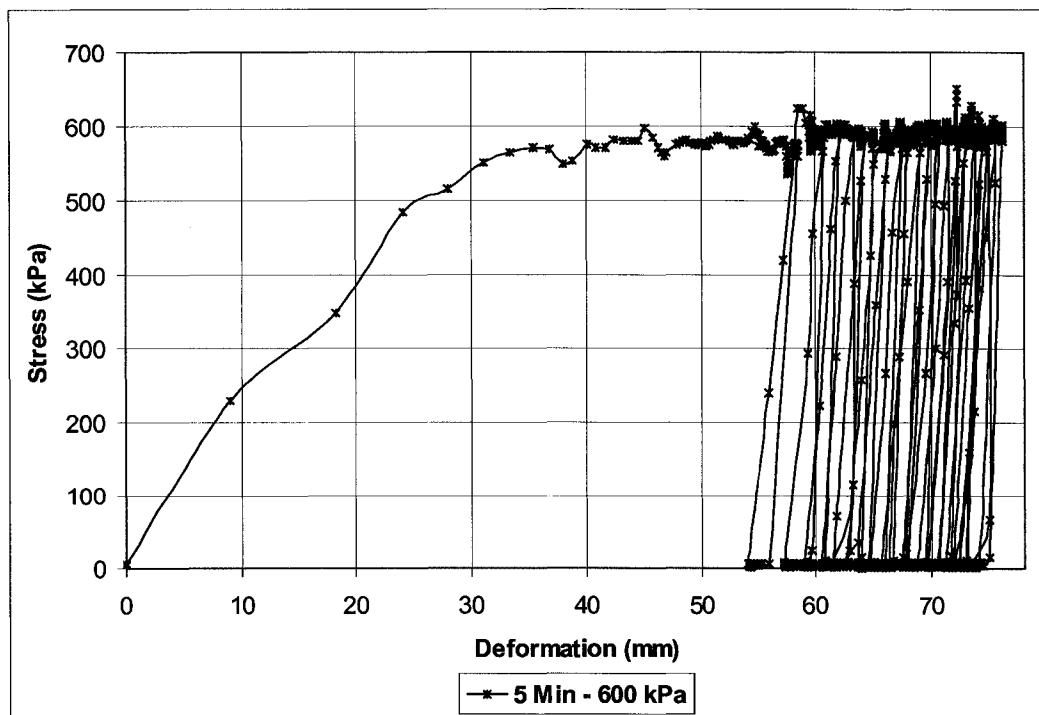


Figure 151: Stress Vs. deformation curve for 600 kPa and 5 Min test

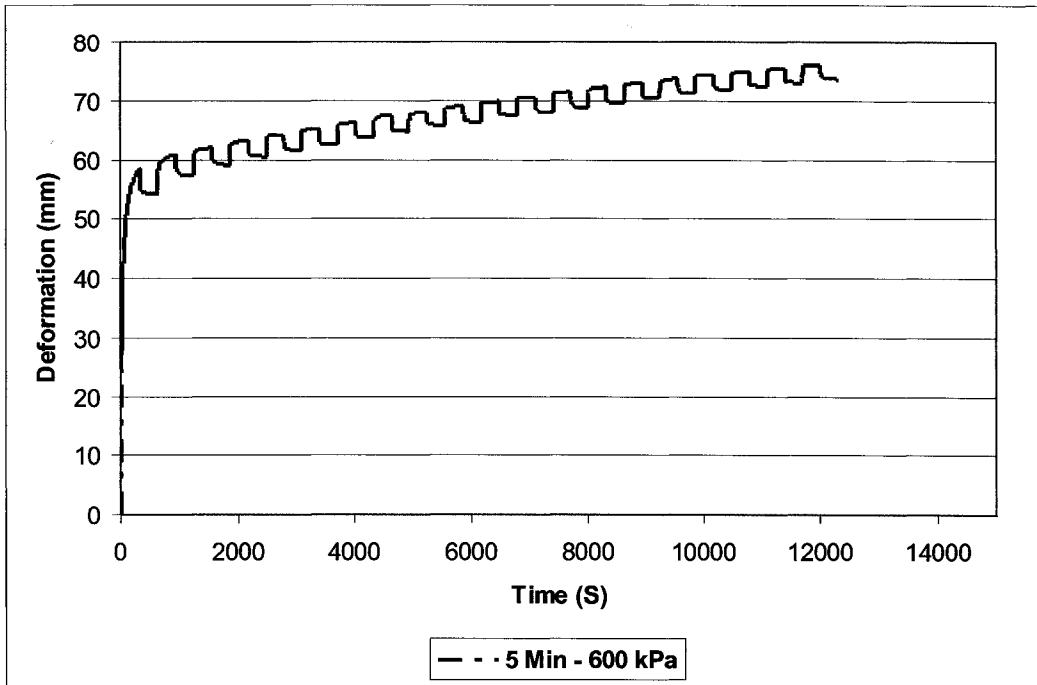


Figure 152: Deformation vs. Time for 600 kPa and 5 Min test

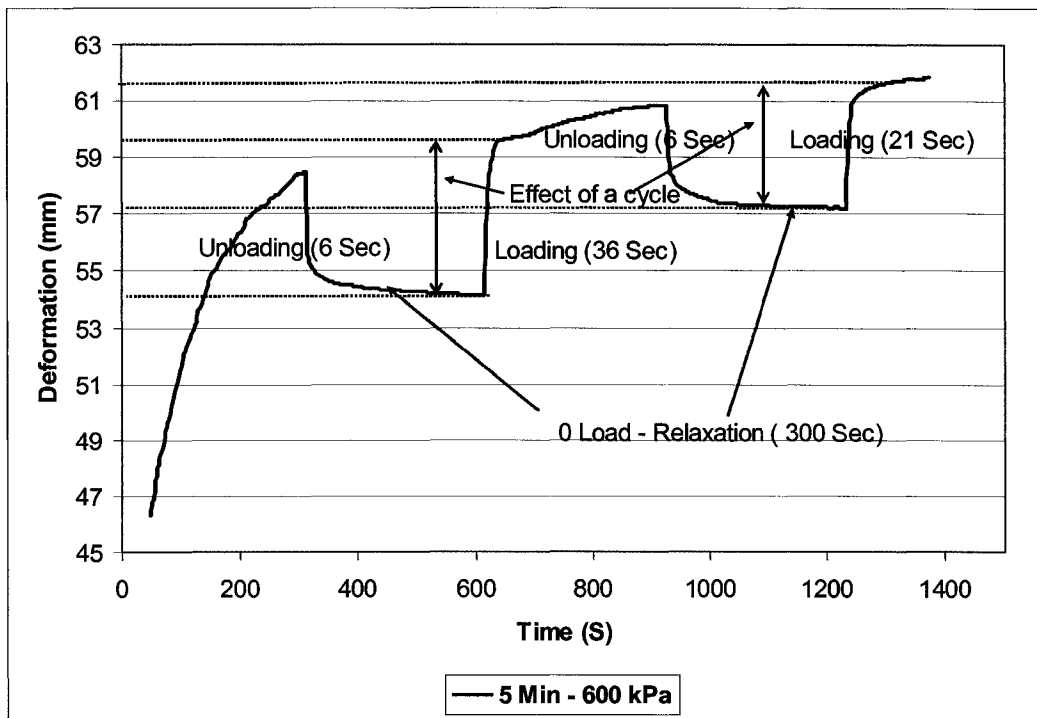


Figure 153: Effect of two cycles on the deformation for 600 kPa and 5 Min test

## 7.8 Remarks

The majority of the deformation occurred in a very short period of time during the initial loading stage. The general structure for a deformation from a constant footprint, during constant loading was expressed as  $P(At^B)$ . For long durations, the pressure stiffness value converged on a residual value.

The total deformation due to 20 cycles, may be predicted solely from the initial deformation.

$$\text{Total deformation} = 1.3 * \text{initial deformation}$$

The total deformation of constant and cyclic loading can be predicted from:

$$\delta_t = [\sigma / At^B] + [\sigma / \sum_{i=1}^{NC} 106.7 \times (NC)^{0.3} ]$$

$$A = 0.0317\sigma + 7.318$$

$$B = -0.0002\sigma - 0.036$$

That A and B parameters are stress dependent.

As the viscosity of the oil sand material highly depends on the temperature, temperature may subsequently have a major impact on the deformation. The proposed deformation equation is valid at a room temperature reading. However, the methodology explained in this chapter, can be used to generate new equations and theories at different temperatures.

Also, the average of the deformation during loading cycles for each load is approximately 3 mm. During shovel activity, hundreds of cycles occur, so even a very small amount of deformation at each cycle can create large differences in total deformation.

## **8 P&H 4100 Boss shovel underfoot testing and deformation prediction**

### **8.1 Introduction**

A full-scale field test was performed to study the ground stiffness behaviour during ground loading by ultra-class mobile mining equipment. The test involved a P&H 4100 BOSS ultra class shovel, which was tested with respect to its loading and ground response on high-grade oil sand. The field test mimicked real conditions while operating a shovel. This test was the first attempt to measure the stiffness of the oil sand environment by using in-place pressure cells and displacement-measurement tools. This test was driven by two goals:

- To use laboratory test results to predict actual field test conditions to understand the effect of parameters such as bitumen content, the loading effects of ground stiffness, and deformation characteristics.
- To provide feedback to mining companies to help them make decisions about purchasing new units, and to help manufacturers to account for this kind of ground scenario in future designs.

Also, the study of shovel performance in a real environment may assist in reducing maintenance time and costs. On October 6-10 2003, underfoot field testing of an 11-84 shovel was performed at one of the oil sand mines in northern Alberta.

### **8.2 Test set-up, equipment and methods**

The equipment, tools, and methods used to acquire data in the field test were

- 12 vibrating wire total pressure cells (to measure the total stress & ground temperature). The model of vibrating wire total pressure cells was 1725 kPa (250 psi) 52608240 from Durham–Geo-Slope-Indicator.
- 4 vibrating wire piezometers (to measure the pore-pressure or fluid pressure response). The model of vibrating wire piezometers was 1725 kPa (250 psi) 52611040 from Durham–Geo-Slope-Indicator.

- Measurement deformation by using a static shovel displacement ground survey of the shovel track
- Power draws from the hoist, swing and crowd motors
- Measurement of the in situ ground density (Troxler)
- Oil water sand (OWS) analysis. Appendix 7 presents the results and the grain distribution,
- Time-stamped video capture.

The pressure cell was formed from two circular plates of stainless steel whose edges were welded together to form a sealed cavity. The cell is 230 mm in diameter and 11 mm thick, and the transducer and connecting tube is 410 mm long. The cavity was filled with a non-compressible fluid (Ethylene glycol, de-aired to 2 ppm). The cell was installed with its sensitive surface in direct contact with the soil. The total pressure applied to that surface was transmitted to the fluid inside the cell and measured with a vibrating wire pressure transducer. The total pressure cell had a low profile (11 mm) to minimize the bridging effect. The modulus of the pressure cell had to be close to that of typical soil to minimize the stiffness effect of the oil sand and the pressure cell. If the pressure cell is stiffer than surrounding soil, it shows less pressure due to the bridging effect and vice versa.

Vibrating wire piezometers were used to monitor the porewater pressure. The vibrating wire piezometers converted the water pressure to a frequency signal via a diaphragm, a tensioned steel wire, and an electromagnetic coil. The piezometer was designed so that a change in pressure on the diaphragm caused a change in the tension of the wire. An electro-magnetic coil was used to excite the wire, which then vibrated at its natural frequency. The vibration of the wire in the proximity of the coil generated a frequency signal that was transmitted to the readout device.

In order to set up the instruments, two shallow trenches were dug with dimensions of 25 metres length and 0.6 metres depth. Below the shovel trench, a thin layer of approximately 10 cm of clean sand was used to cover the piezometers and pressure cells. The trenches were then backfilled and re-

compacted with oil sand. Afterwards, the trenches were flagged to indicate where the shovel needed to be positioned for the test. Figure 154 displays a picture of the instruments installed in one of the trenches while Figure 155 displays a map of the equipment layout from the survey data.

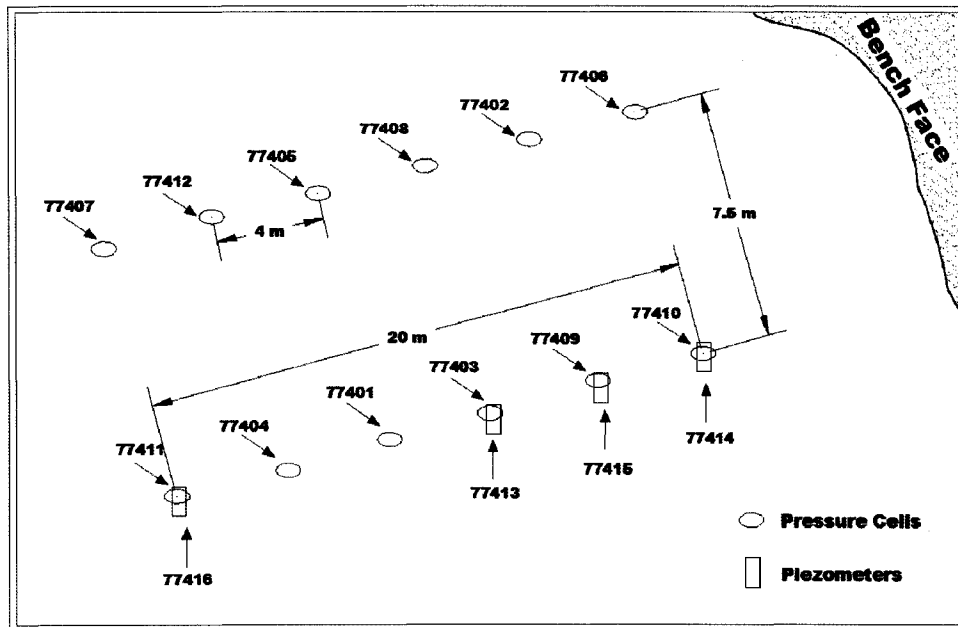


Figure 154: Survey locations for ground sensors

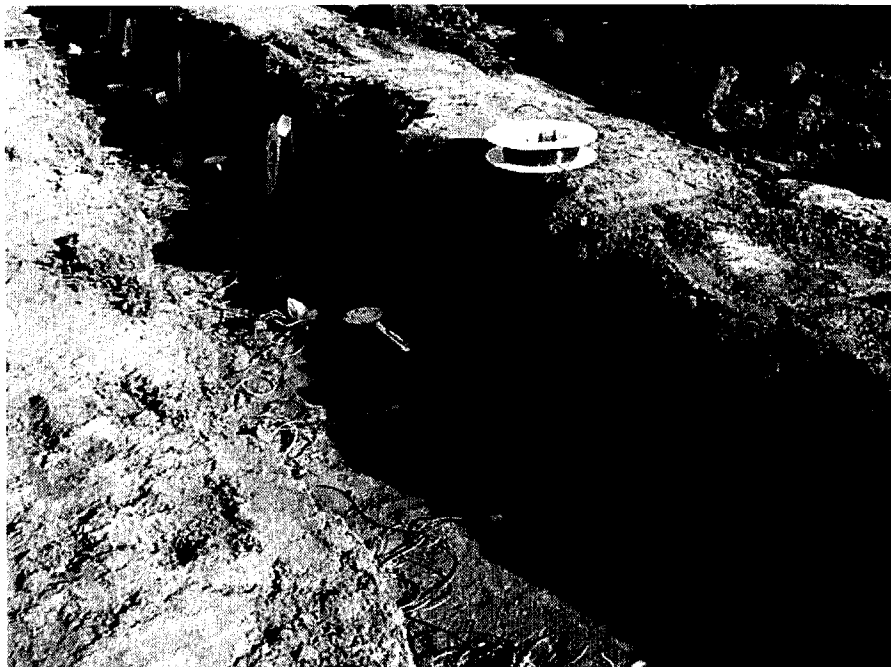


Figure 155: Picture of total pressure cell field installation

The pressure cells were evenly distributed throughout the trenches at intervals of four metres. The piezometers were placed at 0, 4, 8 and 20 metres from the front of the shovel position. The reason for this configuration was to distribute the piezometers with slightly more in front of the shovel since it was thought that the highest pressures would be observed near that location. The piezometers placed 20 metres from the front was used to record the momentary increase in the pore pressure as the shovel passed over that sensor. It also acted as a somewhat remote sensor to record the pore pressure at a known distance from the shovel during operation.

Survey of the track pad, was used as an optical measurement of vertical, and lateral displacement of the shovel. Two targets were used and placed on the front and back of the left hand track. The survey team was then positioned on the left hand side, or non loading side of the shovel where they measured the position of the track at various times during the test. The survey equipment used had a resolution of 1 millimetre.

### **8.3 Test Procedure**

The field test was conducted in 6 different stages: unloaded static tests, mock digging unloaded, loaded static tests, mock digging loaded, truck shovel operation and unloaded static tests. In general, the conditions for the field test were divided into two groups, static and dynamic conditions. The static conditions were designed to study the ground loading and deformation that occurred as the shovel was held at various positions. The dynamic tests were designed to observe the ground-loading conditions as the shovel progressed through a regular range of motions associated with truck loading. Figure 156 presents a diagram of the shovel in position over the sensor grid. Figure 157 illustrates the different parts of the 4100 BOSS shovel.

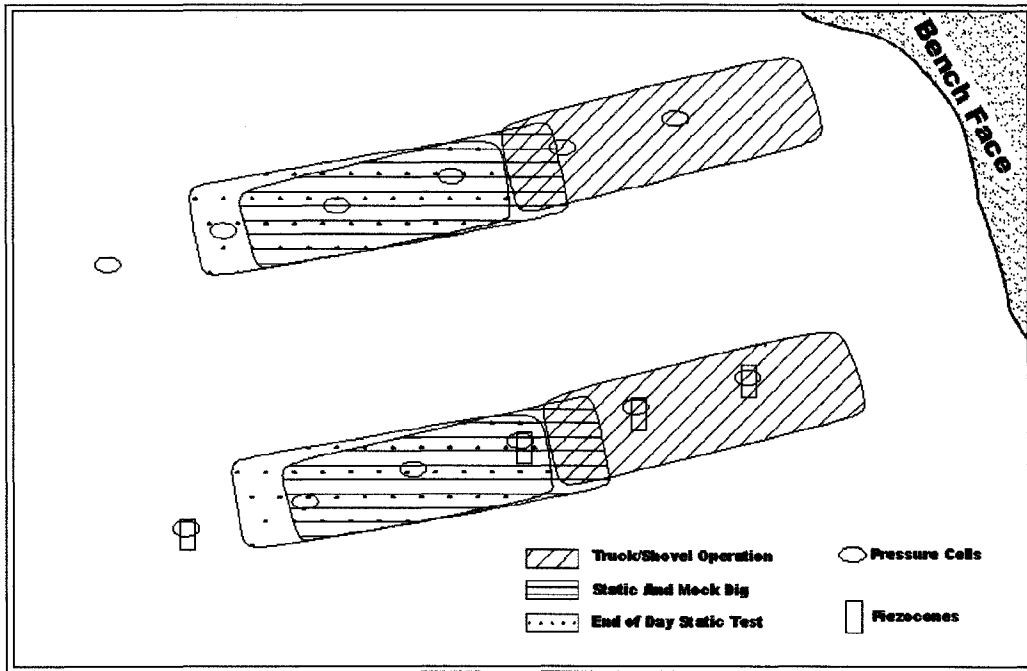


Figure 156: Shovel and active pressure cell locations

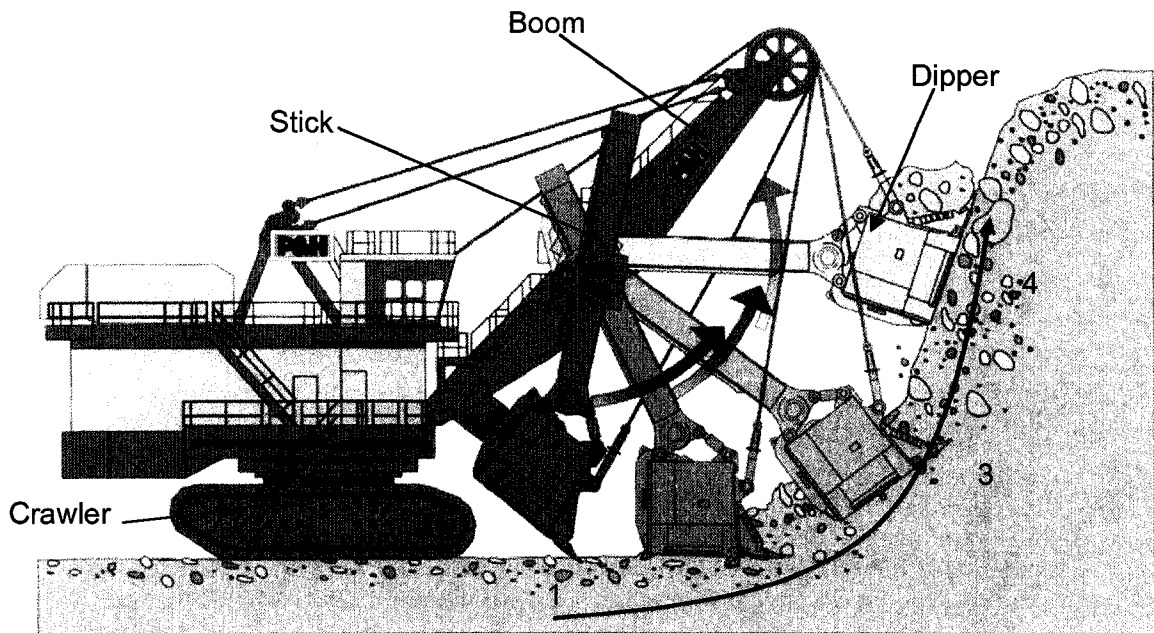


Figure 157: Different parts of the P&H 4100 BOSS shovel (after Harnischfeger 2001)

### 8.3.1 Unloaded static tests

For the unloaded static tests, the shovel was rotated 360 degrees at 45-degree intervals with the stick fully extended and the dipper empty. In between each increment, the shovel was held stationary to allow for ground settling. The average holding time of settling was approximately 1–2 minutes.

### 8.3.2 Mock digging unloaded

The operator was asked to control the shovel as if he were digging into the face and loading a truck. The operator was also instructed to perform this task at a slightly slower rate than normal without any modification of the dipper and with no face penetration. Each position was held constant for measurement. This cycle was repeated 6 times. Figure 158 shows the different positions during the digging action.

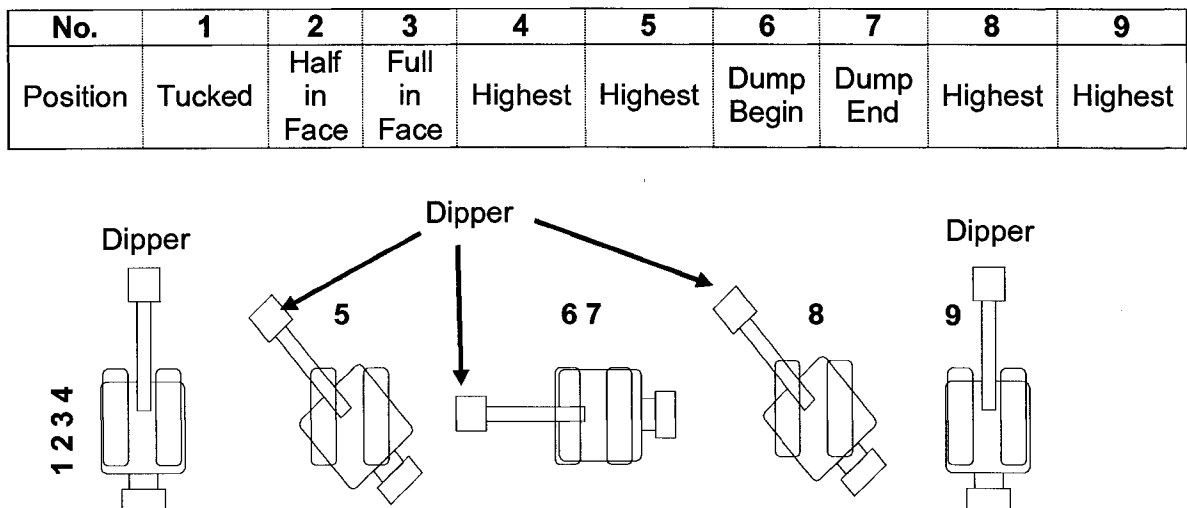


Figure 158: Different digging positions (after Joseph et al. 2003)

### 8.3.3 Loaded static tests

The loaded static tests were identical to the unloaded static test, except that the dipper was filled to capacity during the entire sequence, as shown in Figure 159.

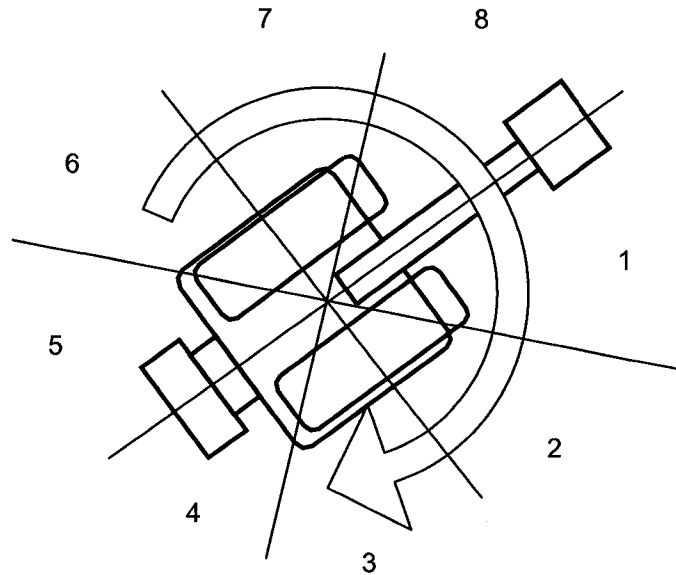


Figure 159: Plan view of shovel unloaded and loaded static tests

### 8.3.4 Mock working face load activity

The mock working face was repeated with a full dipper following the loaded static test. This test was repeated 3 times. Twelve duty cycles were performed with the dipper holding a full load.

### 8.3.5 Truck and shovel operation

During this portion of the test, the shovel was moved close to the bench face in the same position as it would have been in for regular loading operations. The shovel performed regular digging cycles. For this test, a haul truck was dispatched to the pit for loading. After loading, the truck left the pit to dump, and the shovel was relocated closer to the face. The test was repeated 3 times.

### **8.3.6 The end of the loaded static test end**

At the end of the test, the loaded static test was repeated in order to observe how much the ground had softened due to the dynamic testing that had been done. Again, the shovel was centred on the instrumentation grid. The shovel returned as close as possible to the exact position (within 10-20cm) from where the initial static tests had been completed.

### **8.4 Ground and Climate Conditions**

The average bitumen grade of the six oil sand samples was identified by the mine laboratory tests to be 12.7% with an average water content of 2.1%. Appendix 7 presents the grain-size distribution and sample properties. The Aurora mine's geo-technical department was contacted to identify core hole data close to the test location. The closest core hole was approximately 16 metres ahead of the closest pressure cell near the face. This core hole was drilled from a surface depth of 298 metres above sea level (ASL) to a depth of 223 metres ASL. The core hole data suggested that the bitumen grade at the shovel location at 260 metres ASL was about 15-16% and was fairly consistent for several metres below the shovel. This density is higher than that of the sample from the pit, but is not unusual when comparing boreholes to grab sample results. Grab samples were somewhat drained from the surface. Appendix 7 presents the core hole data sheet, which displays the facies and grades at various depths.

The nuclear densometer (Troxler) data measured in-pit during the test gave an average wet density of 1865 kg/m<sup>3</sup> with a standard deviation of 49 kg/m<sup>3</sup> for the 6 measurements. The average fluid content was recorded as 14.7% with a standard deviation of 1.27%. Weather conditions during the test were sunny with cloudy periods, no precipitation, and a temperature of 10-15°C. The oil sand ground temperature at the piezometers was 9.7 to 7.0°C, which, overall, is a fairly consistent ground-air temperature range.

## 8.5 Test Results

Forty per cent of the pressure cells (5 pressure cells) were damaged during the shovel's movement onto its pad. Figure 160 and Figure 161 show the total cell pressures during the test for the NLS (non-loading side) and the LS (loading side) of the shovel. The theoretical static ground pressure, as shown in section 3.4 and Figure 106, was 200 kPa ( $1210 \times 9.8 / 3.5 \times 9 \times 2$ ).

By plotting each test separately, the maximum and minimum loads useful for ground displacement prediction were identified. During the unloaded static test, the maximum pressure reading was 482 kPa when the stick position was 225 degrees away from the original starting point (perpendicular to the face), and the minimum was 422 kPa when the boom position was 45 degrees. The piezometers did not record any significant change in the ground fluid pressure. During the mock digging, the initial ground pressure was 420 kPa, which then decreased to 350 kPa as the shovel stick was lowered to the tuck position to simulate the start of the digging cycle. The difference of the maximum and minimum of the total pressure were approximately 100 kPa. In the loaded static test, the maximum pressure reading was 620 kPa with the shovel stick in a 45-degree position, yielding a 180-degree difference between the unloaded and loaded static tests. During the mock digging test, the corner loading (between 35° to 45° shovel rotation) changed from 333 kPa to a maximum of 537 kPa. However, during the real digging (truck and shovel operation) the pressure cell on the NLS varied from a maximum of 480 kPa to about 75 kPa for the entire three-truck loading operation. The pore fluid pressure during the entire test was relatively low compared to the total pressure cell recording. The peak value was 40 kPa (6 Psi). Appendix 7 presents the pressure cell and piezometers results during the tests. Figure 162 illustrates the ground bearing pressure during the static loaded and unloaded tests.

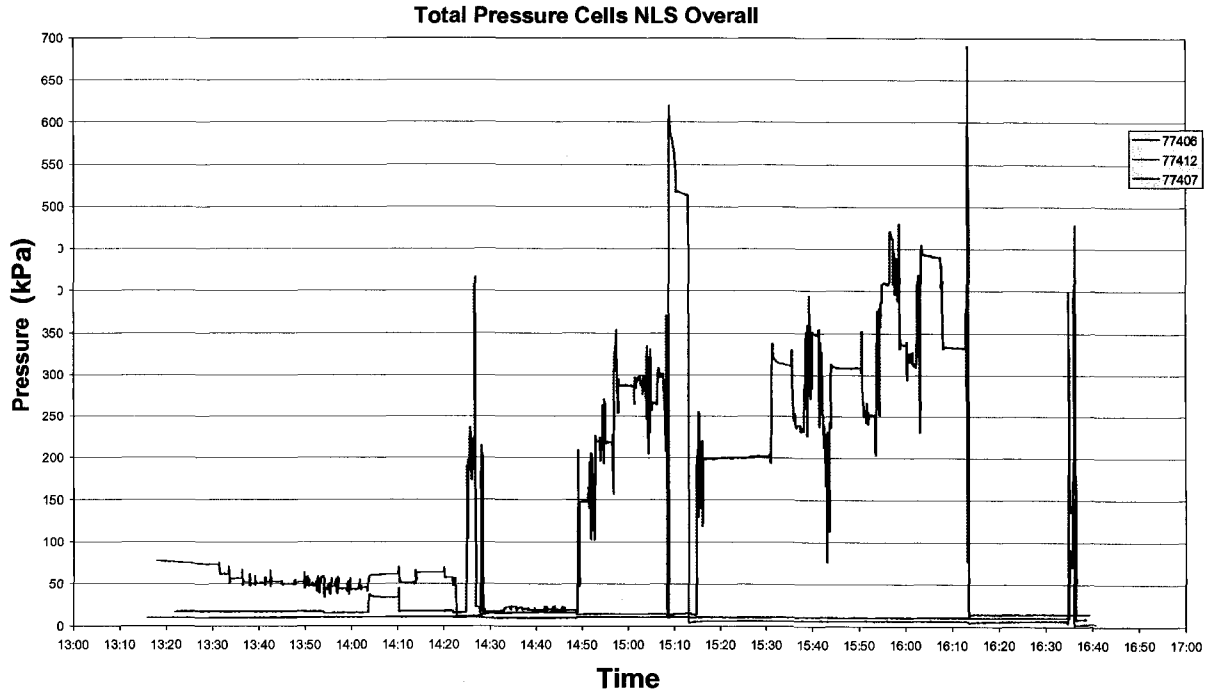


Figure 160: Total pressure cell output of NLS during test

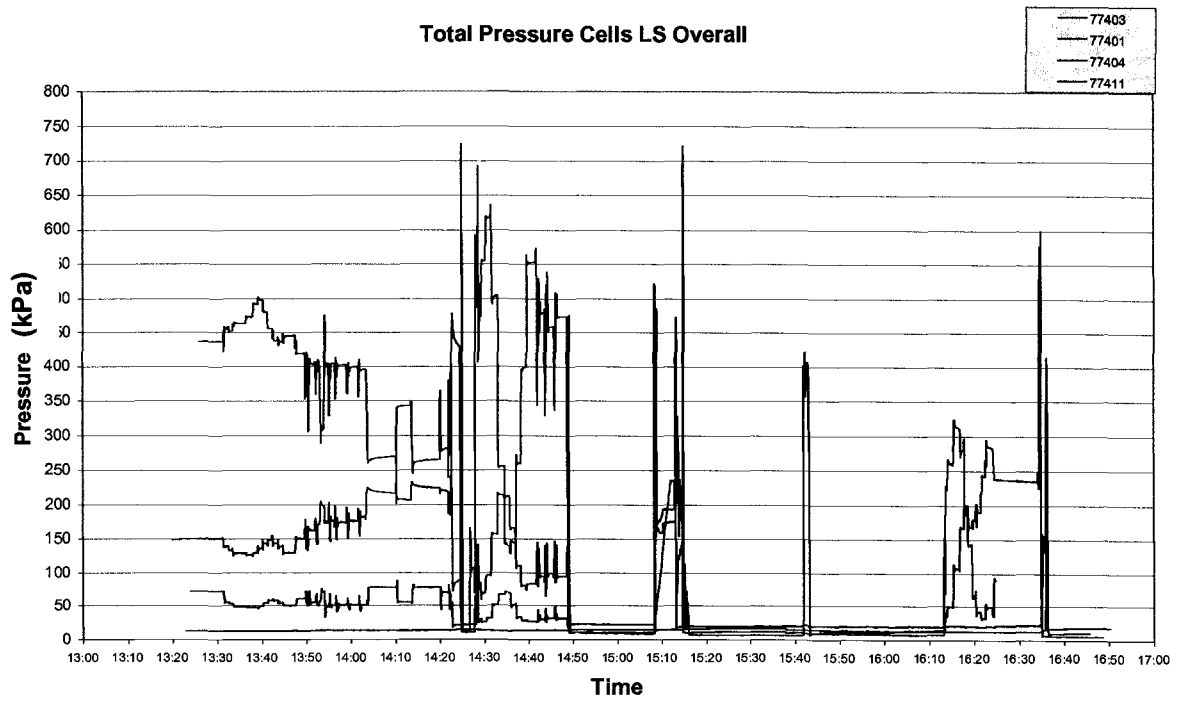


Figure 161: Total pressure cell output of LS during test

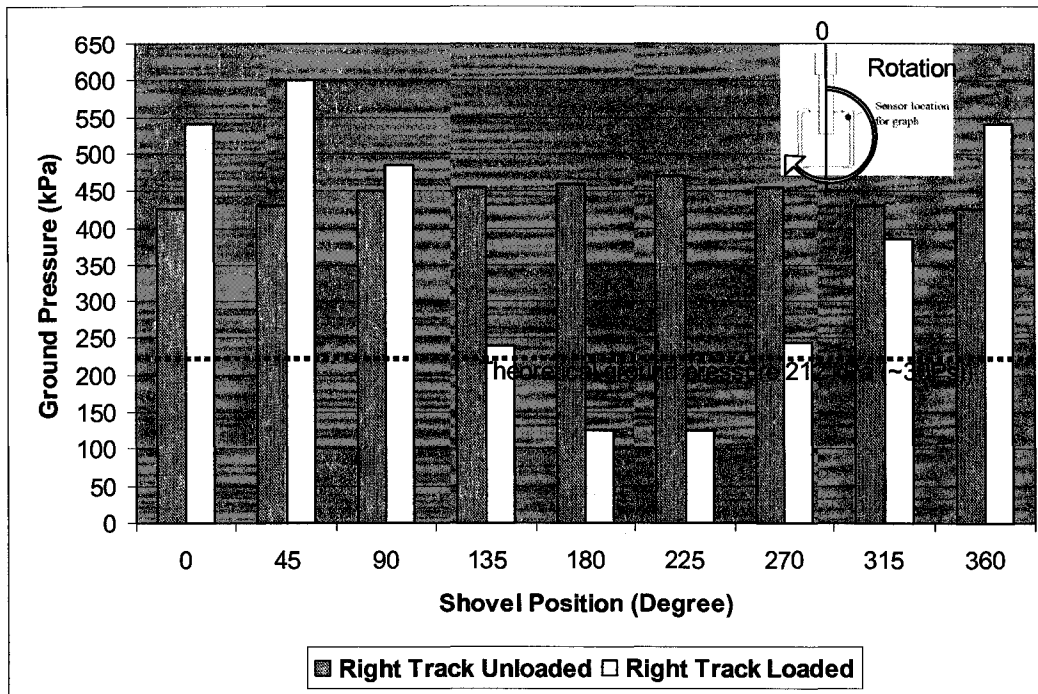


Figure 162: Ground pressures recorded at hold position

The manufacturer claims that the theoretical ground pressure is only possible in ideal conditions: 1) that the track involved is completely rigid and solid, and 2) the ground is flat and not deformable. However in reality, in normal, yet at times unpredictable weather environments, and in especially soft ground conditions, none of the above assumptions are possible. Therefore, the real pressure is much higher than the theoretical ground pressure.

### 8.6 Vertical and horizontal stress modeling beneath shovel track via Boussinesq's approach

A program was written in MATLAB using this approach. Appendix 5 presents the programs for both the shovel and the truck. The model was applied to a shovel and an ultra-class haul truck, the P&H 4100 Boss shovel and Caterpillar 797, respectively, for which the ground contact area is constant. For the shovel, the constant area for each track shovel was  $31.27 \text{ m}^2$  ( $11.58\text{m} \times 2.7\text{m}$ ), and the shovel weight was 13.25MN. However, the stress distribution on the shovel track was dependent on the shovel stick position and the loaded nature of the bucket. This

study considered only a very simple case, with the shovel bucket empty and in the tucked position. Calculating the ground pressure for different shovel positions is not difficult. However, when the ground is not flat, then calculating the ground pressure is not so easy. Figure 163 illustrates the shovel position and the two sections for the stress calculations. The cumulative stresses for projection angles of less than 30 degrees were considered insignificant.

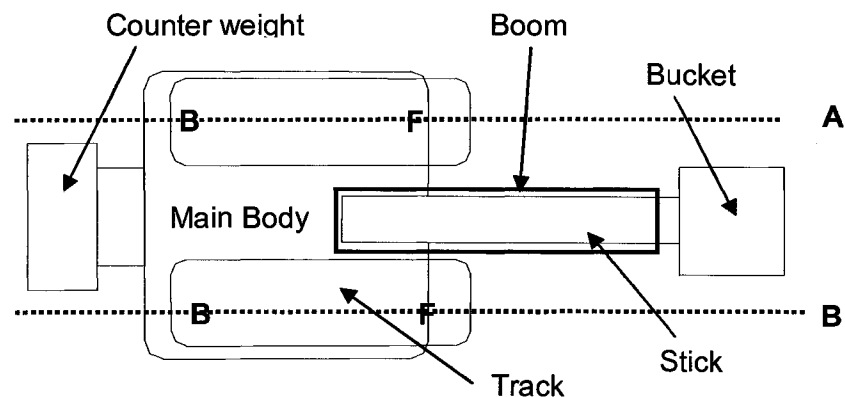


Figure 163: Sections of calculated stress for an ultra-class shovel

Figure 164 through Figure 167 illustrate the principal stresses as well as the vertical and horizontal stresses. As was expected, the maximum vertical stress was at the front of the track, yielding 200 kPa at 50 cm.

The horizontal stress from the Boussinesq's equation provides a reasonable match between the real field shovel test (the P&H 4100 BOSS shovel underfoot test) and the model's outcomes. From the load cell installed 50 cm beneath the shovel track for the 0° shovel position and an unloaded shovel, the ground pressure (Figure 162, previous section) was approximately 400 kPa. In Figure 165,  $\sigma_1$  ground pressure is close to 400 kPa. Only one situation was considered for the Boussinesq approach due to the very complicated ground shovel force. The Boussinesq approach is typically used in geotechnical engineering for shallow foundations; therefore in this case, due to the shallow depth, the Boussinesq approach gave a result very close to that from the real field shovel test.

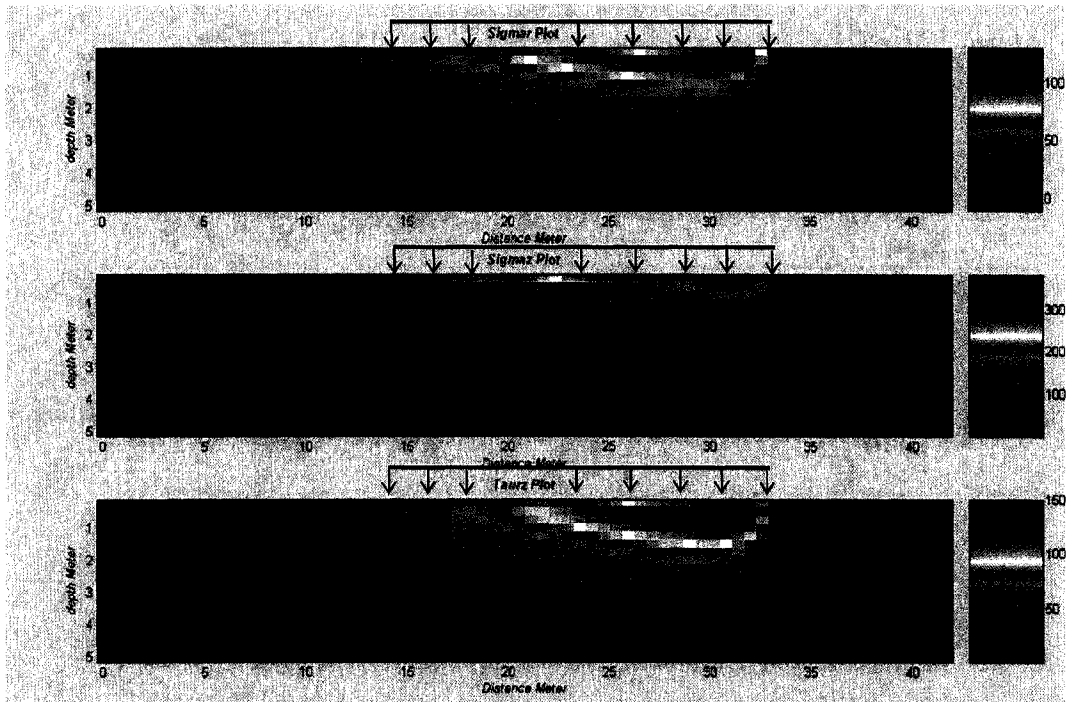


Figure 164: Vertical and horizontal stresses for section B

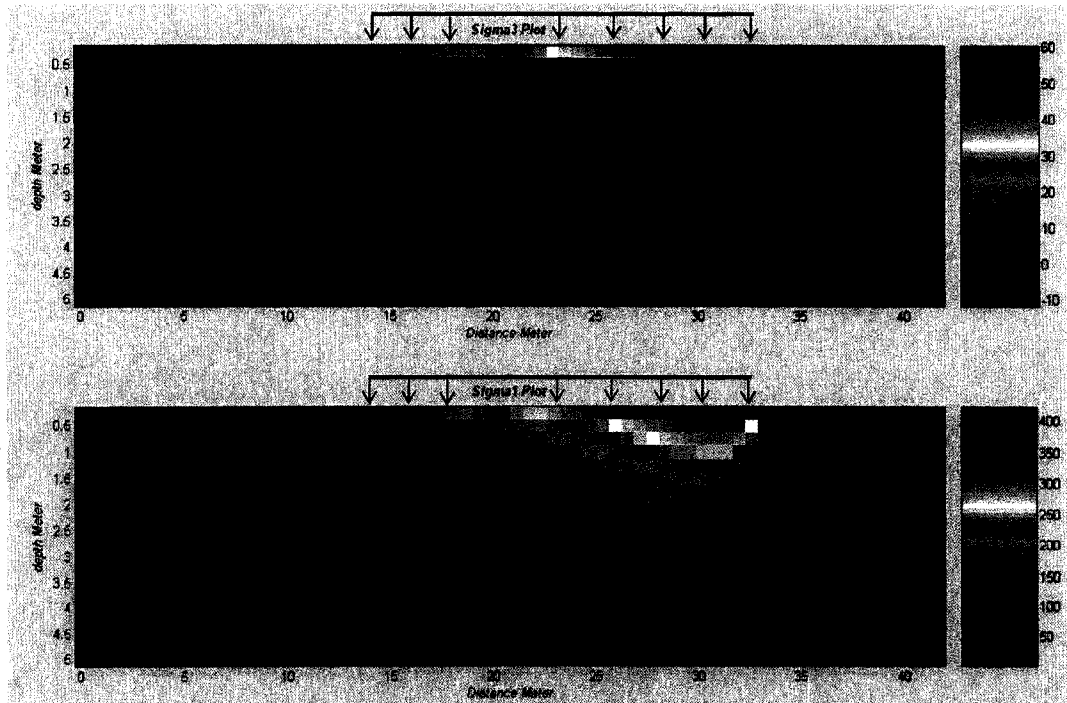


Figure 165: Principal stresses for section B

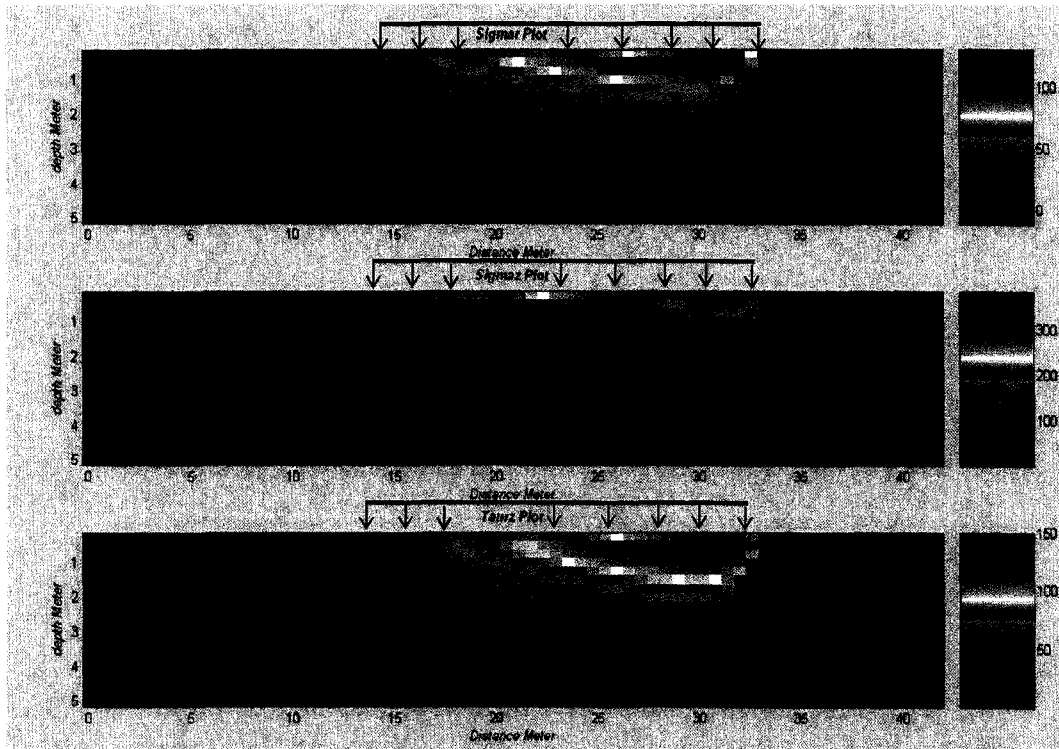


Figure 166: Vertical and horizontal stresses for section A

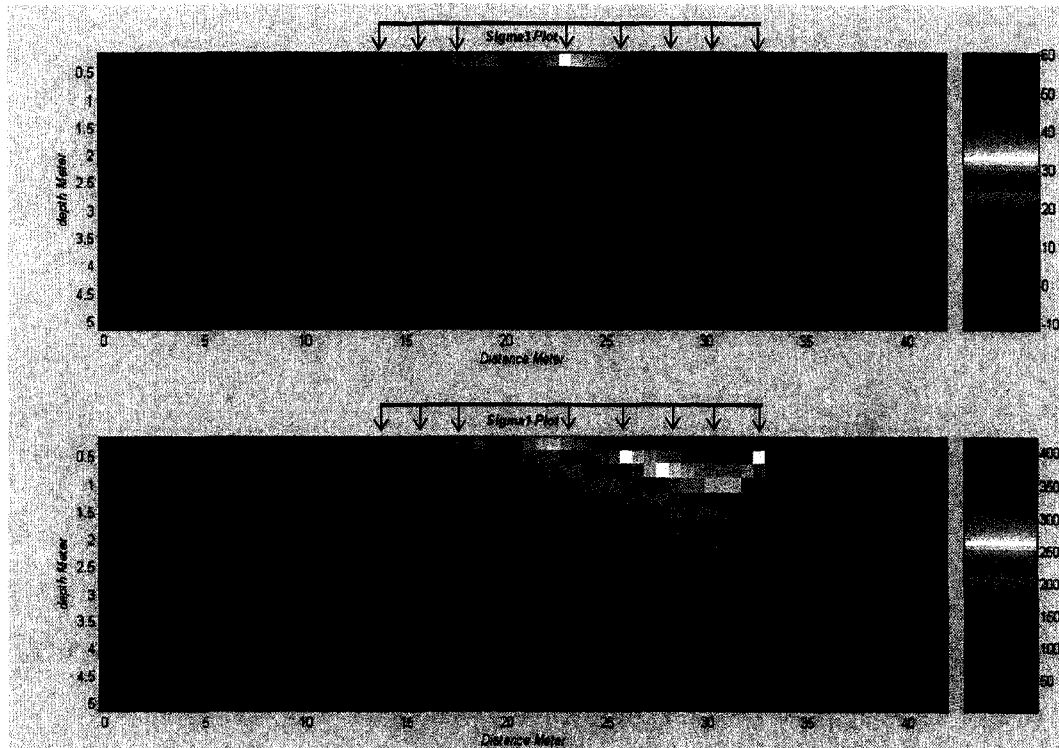


Figure 167: Principal stresses for section A

## 8.7 Deformation Prediction

Deformation data were collected by surveying two fixed locations that were placed on the front and back of the left hand track or on the NLS shovel track (see Figure 168). Figure 169 demonstrates the total displacement of the front and back NLS during the static loading test.

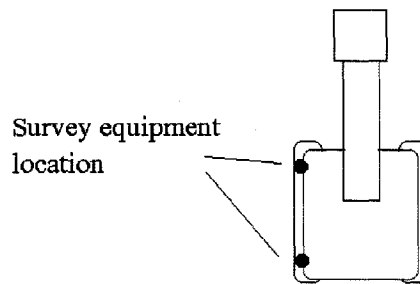


Figure 168: Surveying equipment location

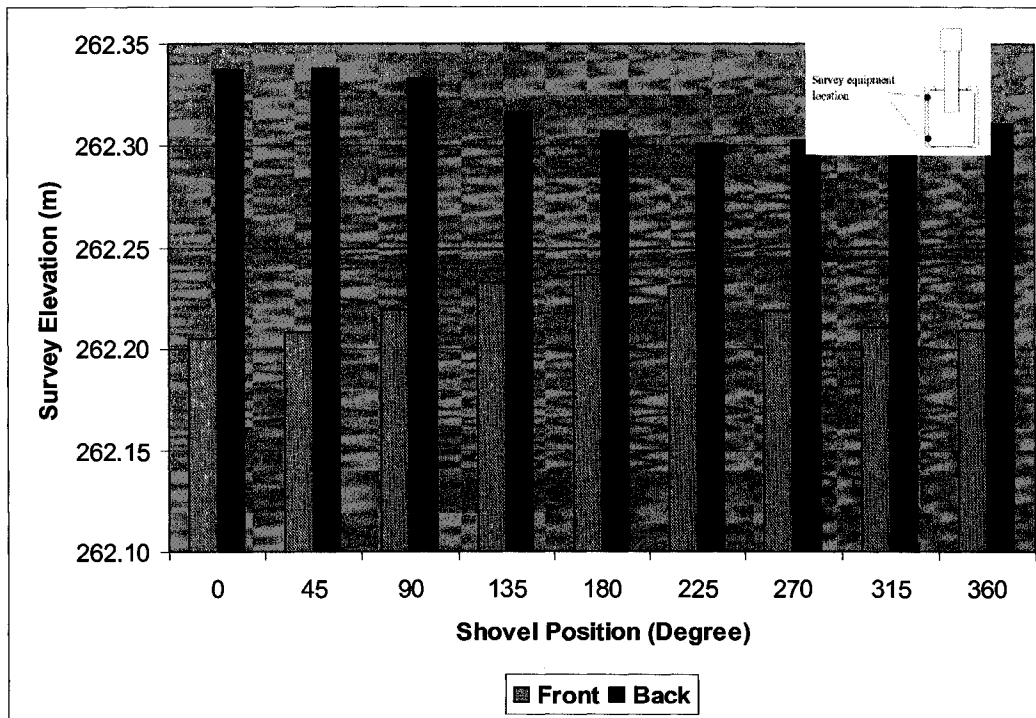


Figure 169: Graph of ground displacement recorded at each hold position

In order to predict the field deformation data, the 10-minute duration curve from section 6.3.2 at Table 11 for pressure stiffness versus time was used ( $\xi_g = 14.609$

$(t)^{-0.0598}$ ). As the test duration was approximately 4 hours, the 10-minute curve was suitable for deformation estimation. Table 13 and Figure 170 display the absolute survey and the predicted laboratory deformation data. In order to accurately predict deformation given the complexity of the loading condition, the following points were considered.

- There were 30 seconds lag time between setting up the shovel in place and the first deformation survey record.
- The time in the deformation equation was set to zero whenever the pressure difference was greater than 100 kPa.
- The time in the deformation equation was set to zero after the shovel was moved to the face to fill the dipper and was back to almost its initial position for the load static test.
- The deformation cycles were not calculated, as the magnitudes were negligible compared to the total deformation measured on surveying.

Table 13: Deformation survey information for shovel-loading conditions

Shovel Positions	Front (mm)		Back (mm)	
	Survey	Predict	Survey	Predict
Shovel Rotated empty	8.67	9.79	1.78	3.17
Simulated Dig Motion, Bucket Empty, Shots taken with bucket raised	9.33	10.99	10.67	3.65
Shovel Rotated Full	82.78	78.59	35	33.12
Simulated Dig Motion, Bucket Full, Shots taken with bucket raised				
Three Bucket Passes, and Then Position Shot	169.50	127.82	62.36	76.69
Truck Loading				
Shovel Rotated Full	196.11	142.01	86.22	62.11

It was observed that a portion of the deformation during the rotation or digging activities was due to the shovel's rocking motion, which was typical of this equipment. Also, the survey data seemed to vary by 20% from the real ground deformation, as Figure 171 through Figure 173 illustrate for the absolute deformation when the shovel was rotating empty, and during the static loading test in the middle of the test and the end of the test, respectively, the maximum and minimum values for the back and front varied by almost by 20%.

The difference between the predicted and real values may be related to the following:

1. Higher bitumen content in the field test compared to that in the laboratory test
2. Lag time between shovel set-up and surveying data.
3. Deformation due to sudden pressure changes caused by shovel movement from its position.
4. Temperature difference in laboratory and field environment.
5. Complexity of the field loading test compared to the laboratory test.

The prediction suggests an error of about 30%:  $(\frac{196.11 - 142.01}{196.11} * 100 = 27\%)$ .

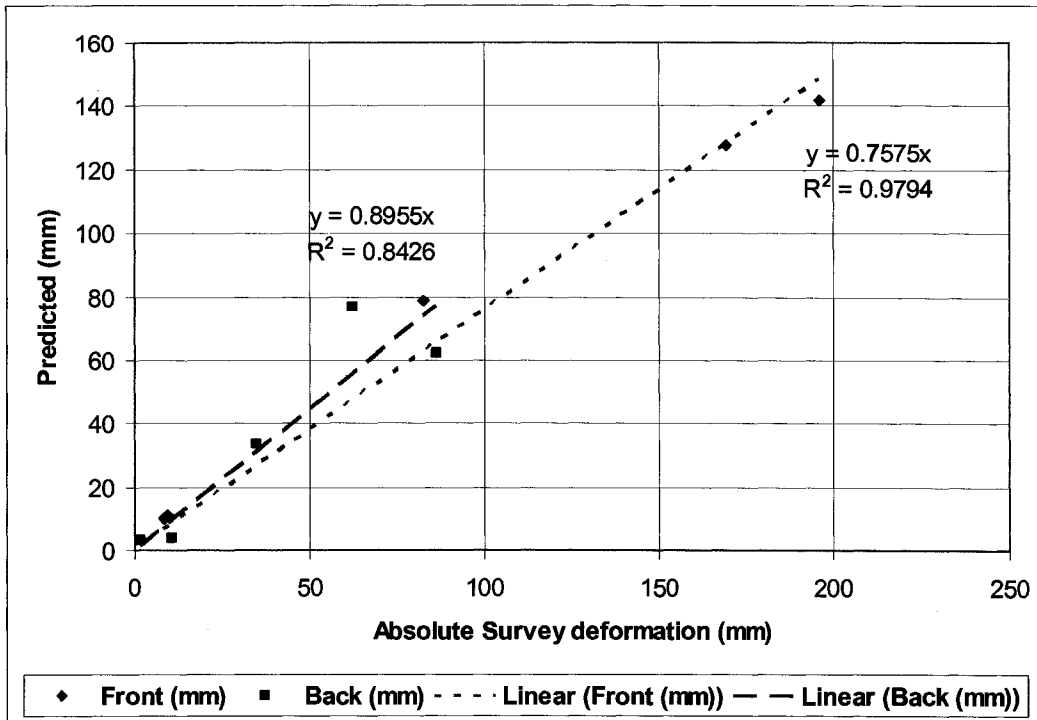


Figure 170: Absolute deformation from survey and prediction deformation

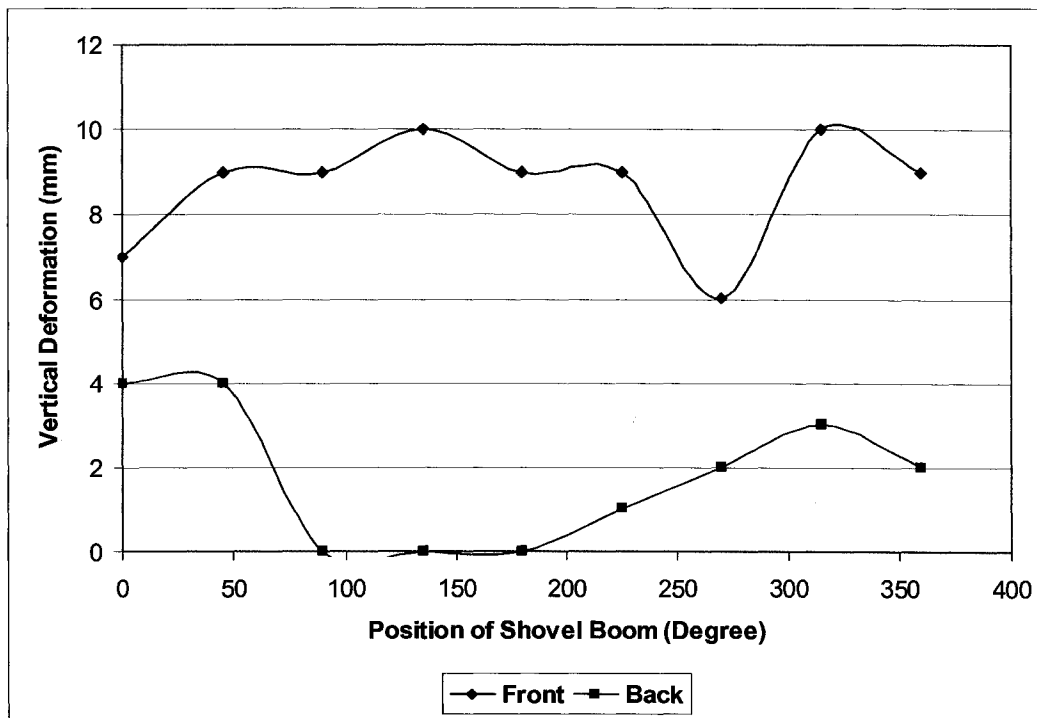


Figure 171: Changing the absolute deformation value during empty-shovel's rotation

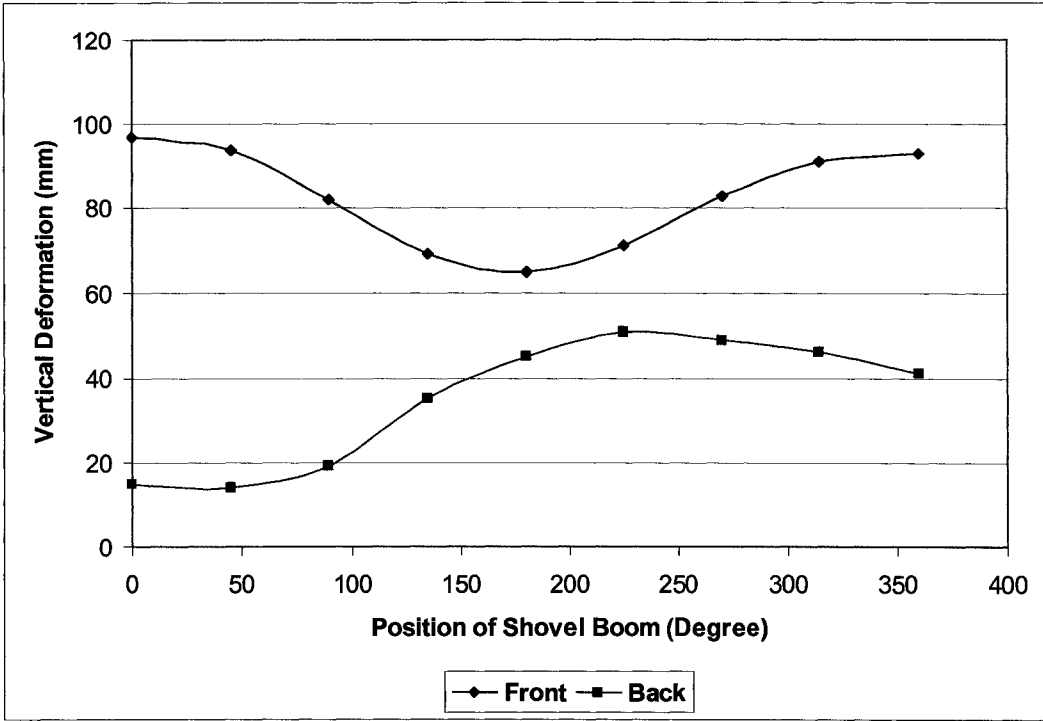


Figure 172: Changing the absolute deformation value during the static loading test

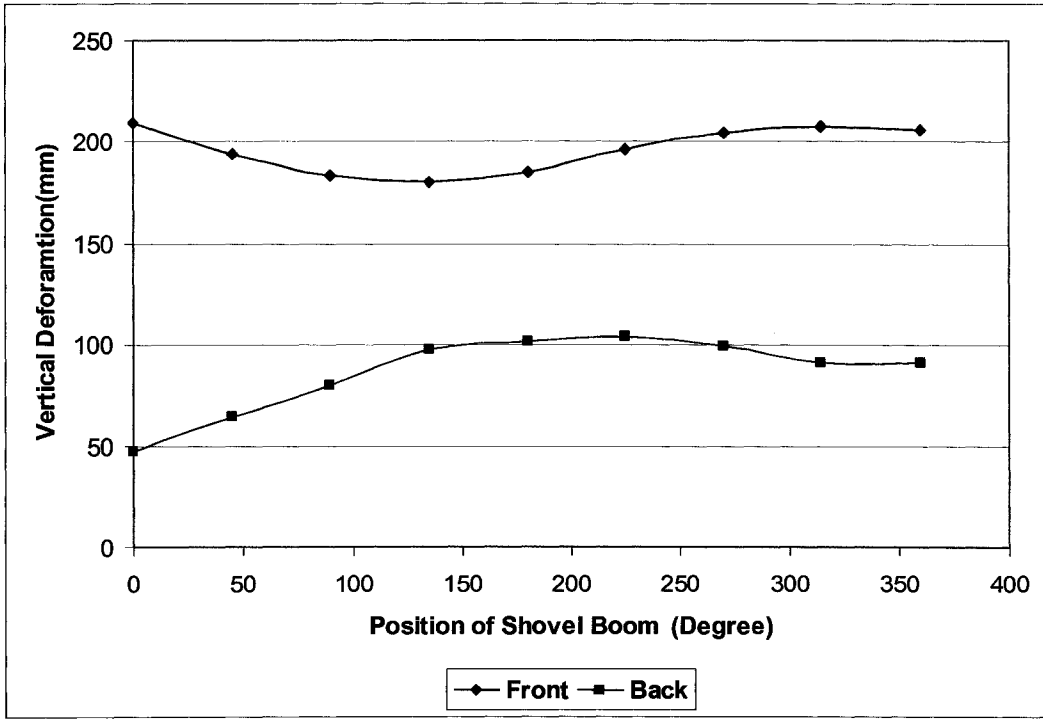


Figure 173: Changing the absolute deformation value during the static loading test (end of day)

## 8.8 Remarks

The results from the pressure cell readings demonstrate that ground loading by the P&H 4100 BOSS shovel during mining operation is highly varied. Also, the pressure cell readings show that the front ground pressures during shovel digging activities are significantly higher than those during the static tests.

The proposed deformation equation has the average of  $\pm 30\%$  accuracy during four hours of shovel activity.

The deformation equation [40] generated from the laboratory tests can be used to predict the ground deformation under mobile mining equipment, with constant footprints during mining activities. This study did not consider the temperature effects on deformation.

The horizontal stress from the Boussinesq's equation provides a reasonable match between the real field shovel test (the P&H 4100 BOSS shovel underfoot test) and the model's outcomes.

## 9 Summary

The objective of this thesis was to investigate oil sand behaviour under dynamic loading conditions due to ultra-class mobile mining equipment, to enable the prediction of the deformation of oil sand under these conditions. Oil sand is a unique material that behaves differently under different conditions. Oil sand samples with 8% and 11% bitumen content were used in triaxial laboratory tests, and samples with 11% bitumen content were used for larger-scale laboratory tests. During the field cyclic plate load tests and the ultra-class shovel underfoot tests, the oil sand quality varied between 8 to 12% bitumen content.

The assumptions that the oil sand beneath mobile equipment is already broken, loose and unlocked, so that oil sand expresses a post-peak behaviour before reaching a residual value and is homogenous and uniform, allowed us to use a pseudo-elastic approach (treating oil sand as elastic, even though it is elastoplastic). It has been shown that Boussinesq's approach to estimating vertical and horizontal stresses beneath an ultra-class shovel provides results very close to those of the real case. From numerical modeling of FLAC and Boussinesq's approach, the induced confining pressure during an applied load can be estimated via

$$\sigma_H = 0.26\sigma_V \text{ (kPa).}$$

This equation is valid for 8 to 11% bitumen oil sand at room temperature (18°C). In winter ( $\geq -40^\circ\text{C}$ ) or summer ( $\leq +40^\circ\text{C}$ ), the relationship may vary. From the laboratory triaxial tests, the residual and peak stress (compressive strength) values of 8% and 11% bitumen oil sand are very similar. However the peak strain values for 8% oil sand are twice that of 11% oil sand. This difference is likely due to greater fluid content. The elastic modulus of 8% oil sand at low confining pressure can be calculated from

$$E = 25\sigma_3 + 1465 \text{ (kPa).}$$

This equation cannot be used for the 11% oil sand, but the peak values (compressive strength) of oil sand at low confining pressures are linear:

$$\sigma_1 = 3.6\sigma_3 + 122 \text{ (kPa)}.$$

This equation may be used for 8 and 11% bitumen content at room temperature.

A standard compaction test has been shown to be inappropriate for determining the density for ultra-class mobile mining equipment loading due to the increased compaction of oil sand under large footprints. Due to the disturbed nature of near-surface oil sand, and the similarity of the load-deformation curves for laboratory versus field evaluations and failure types, the ground interactions of ultra-class mobile mining equipment may be investigated via a large-scale laboratory test under controlled conditions. This test is cheaper than a field test.

The graphs of the global pressure stiffness  $\xi_g$  (pseudo-stiffness) of oil sand, regardless of the duration of loading, converged to a constant value of 8 kPa/mm, observed as a quick estimate of ground deformation. However, the total deformation of oil sand under cyclic loading may be calculated from

$$\delta_t \text{ (mm)} = [\sigma \text{ (kPa)} / A t^B] + [\sigma \text{ (kPa)} / \sum_{i=1}^{NC} 106.7 \times (NC)^{0.3}].$$

where NC is number of cycles and t is time in seconds. The A and B are unitless.

Also, the total deformation of cyclic loading for 20 cycles may be found from

$$\delta_t = 1.3 \delta_0,$$

which shows that cyclic deformation may be calculated via a initial elastic modulus.

## 10 Conclusion and research contribution of new knowledge achieved

The cyclic performance of soft ground was investigated. Oil sand was taken as an example of soft ground. It was shown that due to ultra-class mobile mining equipment activity, oil sand beneath this equipment softens after a few cycles, and deforms. A pseudo-elastic model has been proposed to express the load-deformation behaviour of oil sand. The assumption of homogeneous ground, treated as a pseudo-elastic material, has been proved valid by the agreement between the physical modeling and the numerical approaches employed. The slope of the load-deformation graph versus the time can be predicted with a pseudo-elastic model. The downside of this pseudo-elastic model is that it is sensitive to the interpreted load-deformation behaviour.

A simple cyclic plate load test has been conceived, validated in the field, and mimicked in a large-scale laboratory test. The approach may be used by a mine operator for verifying the suitable stability of soft ground before moving large mobile mining equipment into that vicinity. Such a simple test allows for the determination of the ground deformational response for a known pressure load, and accounts for the equipment footprint size. The results of cyclic loading before equipment movement can be analyzed with the pseudo-elastic model, to predict the deformation according to the number of cycles.

This research was conducted to investigate the cyclic performance of soft ground with oil sand used as an example. Field and laboratory tests showed that the ground pressure stiffness of 11% oil sand at the room temperature in the density range of 1.8-2.0 gr/cm<sup>3</sup> may be approximated by

$$\xi_g = 8 \text{ kPa/mm.}$$

This value may be used for a quick prediction of ground deformation for different static load levels. Moreover, a pseudo-elastic model has been proposed to analyze cyclic plate load test data. Even though the ground behaves in an elasto-plastic fashion, it can be described in pseudo-elastic manner.

Replacing A and B from section 7.6 in the deformation equation yields a solution for the total deformation,  $\delta_t$ , solely as a function of the applied load ( $\sigma$ ), the duration of loading (t) and the number of cycles applied (NC):

$$\delta_t \text{ (mm)} = [\sigma \text{ (kPa)} / \{(0.0317\sigma \text{ (kPa)} + 7.318)t^{(-0.0002\sigma \text{ (kPa)} - 0.036)}\}] + [\sigma \text{ (kPa)} / \sum_{i=1}^{NC} 106.7 \times (NC)^{0.3} ] .$$

The equation allows the user to evaluate, via the field cyclic plate load test in the field, values for  $\sigma$ , t and NC and to predict the deformation  $\delta t$  before moving large mobile mining equipment, such as a 1500-ton GVW oil sand mining shovel, into an area of questionable ground performance. The degree of ground deformation allows the user to make a reasonable decision as to whether the equipment will be in jeopardy during and after such a move.

A unique underfoot ultra-shovel class test at an oil sand mine revealed the ground interaction forces during different duty cycle positions. This test showed how the ground deforms due to cyclic loading. It was shown that the ground pressure changed greatly during the duty cycles of the ultra-class shovel.

## **11 Recommendations for future work**

This thesis showed that cyclic loading due to the motion of large mobile mining equipment softens in-pit soft ground such as oil sand and creates ultra-class equipment instability. More research is needed to fully understand this oil sand behaviour under cyclic loading by specific equipment. Recommendations follow for future work centred on geotechnical and geophysical research and the development of software for equipment ground deformation use.

### **11.1 Geotechnical work in both the laboratory and field**

The major considerations in investigating mobile mining equipment stability and ground interactions are geotechnical. For in-pit high bitumen content (greater than 8%) oil sand, the following work is suggested.

Cyclic and static plate load tests with different footprint shapes such as rectangular and square should be performed to investigate the shape effects on stress-deformation curves. The shape of a shovel track is rectangular and is made up of smaller rectangles. Comparing the results of different-shaped footprints with actual equipment's footprints will help to show if any scaling effects due to shape change occur.

As oil sand has a viscous behaviour, the biggest impact on deformation is temperature. Therefore, investigating the cyclic stress-deformation relative to different temperatures is necessary. By using the current large-scale laboratory set-up with the addition of a heater element to the box, the oil sand cyclic behaviour could be investigated in relation to the temperature.

The majority of deformation occurs during the pre-cycle loading. Unfortunately, the current laboratory and field cyclic loading set-ups are not able to run tests at different loading rates. A hydraulic pump with a controller would be needed to give variable loading rates. Also, the controller should provide the ability to hold a maximum load. Investigating the pre-cycle slope for varying bitumen content while doing the following variables would permit a more extensive investigation:

1. Using variable loading rates.
2. Varying initial ground densities and/or degree pre-compaction.
3. Measuring the deformation profile during pre-cycle loading as well as the pressure bulb beneath the plate via small pressure cells. Doing so would help us to understand density change during loading activity.

During the small-scale shovel field test, a sudden change in the pressure beneath the track was found to cause the majority of the deformation. The total deformation strongly depends on the loading stages. If the load increases until it reaches a constant value, due to compaction, the slope of the loading is not the same as either the initial slope or the cyclic slope. Therefore, the loading slope during the loading steps seems to be worth investigating.

The failure mode changes due to the duration of the test, depending on the oil sand density and the load magnitude. Understanding how confining pressure dissipates in the field during mobile equipment activity will help to explain how plastic deformation increases as a result of decreasing confining pressure;  $\sigma_3$  would be measured by using a push in pressure cells (Model 4830 or a similar model) for shovels and trucks.

## **11.2 Geophysical Work**

The seismic properties of in situ oil sand were measured previously by Joseph (2003). A seismic refraction survey was conducted as part of a passive seismic experiment conducted for three different bitumen grades of oil sand. The aim of the study was to measure the oil sand velocity for 6, 8 and 13.5% bitumen grade oil sands. The data analysis showed that in situ oil sand has a velocity range between 1500 m/s and 1950 m/s. The velocity of oil sand needs to be used in an inversion method to estimate ground stiffness profile.

A preliminary refraction data analysis study performed by the author showed that determining ground stiffness via continuous surface waves is possible. However, the seismic data collection from both the summer and winter were strongly

aliased by both time sampling and geophone positions. An inversion method was performed on the data but did not give a good ground stiffness profile. Nevertheless, this method was a good start for proceeding in a new test direction for future work, including measuring the ground stiffness by season by using the CSW (continuous surface wave) method.

The above ground stiffness evaluation may be used for ground and equipment performance modeling for different times of the year. Section 2.4.1 contains the results and background as a starting point for this kind of analysis.

Before this thesis was written, no geophysical technique had been proposed to determine ground stiffness from passive data. However, the relative ground modulus changes during mining activity can be determined. The preliminary study of passive data revealed that the ground modulus drops after a few truck runs. Section 2.4.2 contains the results and background for the passive data analysis performed to date for summer and winter. By using the winter test set-up described in section 2.4.2, using two lines of geophones at each side of a truck path, and by knowing the ground stiffness for different times of the year, the relative ground stiffness changes during mining activities can be measured.

### **11.3 Software Development**

Currently, no numerical modeling programs are available for analyzing equipment and ground interactions dynamically. Therefore, developing a finite element software for shovel and truck-ground interactions that could analyze ground deformation and equipment interactions dynamically for different ground conditions, such as different materials and different ground profiles, would be advantageous. Any new software should be able to consider the duration of the equipment operation and to update dynamically in small time increments.

## References

- Adalian, C. and Morlier, P., 2001, A model for the behaviour of wood under dynamic multiaxial compression, *Composite Science and Technology* , **61** , 3 , pp 403-408
- Al-Shayea, N.A and Mohib, K.R. and Baluch, M.H., 2003, A plastic-damage model for stress-strain behaviour of soils, *International Journal of Damage Mechanics*, **12**, 4 , pp 305 -329
- Anderson, K.H., 1988, Properties of soft clay under static and cyclic loading, *Publikasjon - Norges Geotekniske Institutt* , **176**, pp 1-20
- American Society for Testing and Materials (ASTM), 2001, Standard test methods for laboratory compaction characteristics of soil using standard effort (600 kN-m/m<sup>3</sup>) , **04.08** section four, soil and rock (I), D698-00a
- Bardet, J.P., 1986, Bounding surface plasticity model for sands, *Journal of Engineering Mechanics, ASCE* , **112**, 11 , pp 1198 -1217
- Beaty, K.S. and Schmitt D.R., 2003, Repeatability of multimode Raleigh-wave dispersion studies, *Geophysics*, **68**, 3 , pp 782-790
- Beaty, K.S., Fall 2000, Determination of near surface variability using Raleigh waves , MSc Thesis, Department of Physics, University of Alberta, Edmonton, Alberta, 208 pages
- Biswas, K. and Jung, S.J. and May, J. ,2001, Behaviour of rock under cyclic loading- some preliminary study , *Rock Mechanics in the National Interest Proceeding of the 38<sup>th</sup> U.S Rock Mechanics Symposium*, pp 375-380
- Butterfield, R. and Georgiadis, M., 1980, Cyclic plate bearing tests, *Journal of Terramechanics*, **17**, 3 , pp 149-160
- Byrne, M.P. and Smith, L.B. and Grigg, F.R. and Stewart, W. P., 1980, A computer model for stress-strain and deformation analysis of oil sand, *Oil Sands Geosciences*, June, pp 11-13
- Chalaturnyk, R and Scott, .J.D and Wong, G. and Chan, D., 2002, Testing dense oil sands from +30°C to -30°C, *Proceedings of the 55<sup>th</sup> Canadian Geotechnical and 3<sup>rd</sup> Joint IAH-CNC and CGS Groundwater Specialty Conferences, Niagara Falls, Ontario, October 20-23* , pp 411-417

- Craig, R.F., 1992, Soil mechanics, London, UK: Chapman & Hall; New York: Van Nostrand Reinhold, 5<sup>th</sup> edition. 427 pages
- Crouch, S.R. and Wolf, P.J. and Dafalias, F.Y., 1994, Unified critical-state bounding-surface plasticity model for soil, Journal of Engineering Mechanics, **120**, 11 , pp 2251-2270
- Campbell Pacific Nuclear Corp., 1980, Operator's manual, MC-1 Moisture/Density Gauge, 25 pages
- Dafalias, Y.F. and Hermann, L.R., 1982, Bounding surface formulation of soil plasticity, Soil Mechanics-Transient and Cyclic Loads, edited by Pande G.N. and Zienkiewicz O.C., John Wiley & Sons Ltd, pp 253-282
- Das, M.B., 2000, Fundamental of geotechnical engineering, Pacific Grove, CA , Brooks/Cole, 2<sup>nd</sup> edition , 593 pages
- Dusseault, M.B.,1977, The geotechnical characteristics of the Athabasca oil sands, PhD Thesis, Department of Civil and Environmental Engineering, University of Alberta, Edmonton, Alberta, 472 pages
- Dusseault, M.B. and Morgenstern, N.R., 1978, Shear strength of Athabasca oil sands, Canadian Geotechnical Journal, **15**, pp216–238
- Ellyin, F., 1997, Fatigue Damage, Crack Growth, and Life Prediction, London, UK; New York: Chapman & Hall, 1<sup>st</sup> edition. 492 pages
- Evett R.S., 2000, In nuclear gauge train-the-trainer course, USDA Radiation Safety Staff, Beltsville, MA.,  
**[http://www.cpri.ars.usda.gov/Soil%20Water%20Papers\\_Presentations/gauge-1.pdf](http://www.cpri.ars.usda.gov/Soil%20Water%20Papers_Presentations/gauge-1.pdf)** [2006-11-28]
- FLAC manual, Second revision April 2002, Itasca Consulting Group
- Ganji, V. and Gucunski, N. and Nazarian, S., 1998, Automated inversion procedure for spectral analysis of surface waves, Journal of Geotechnical and Geoenvironmental Engineering , **124**, 8 , pp 757-770
- Gong, M. and Smith, I.,2003, Effect of waveform and loading sequence on low-cycle compressive fatigue life of spruce, Journal of Material in Civil Engineering , **15**, 1, pp 93-99
- Griffin, D.G., 1986, The heave and settlement of foundation on oil sands : Three Case Histories , MSc Thesis, Department of Civil and Environmental Engineering, University of Alberta, Edmonton, Alberta, 120 pages

- Grozic, J.L.H., 1999, The behaviour of loose gassy sand its susceptibility to liquefaction, PhD Thesis, Department of Civil and Environmental Engineering, University of Alberta, Edmonton, Alberta, 344 pages
- Haegeman, W. and Van-Impe, W.F., 1999, Characterization of disposal sites from surface wave measurements, Journal of Environmental and Engineering Geophysics, 4, 1, pp 27-33
- Haimson, B.C., 1974, Mechanical behaviour of rock under cyclic loading, Proceeding of the Congress of the International Society of Rock Mechanics , 2, pp 373-378
- Harnischfeger Corporation ,2001, Technical communication, P&H Operating Specification
- Harris, M.C. and Hardy, R.M., October 1976, Behaviour of foundation on tar sand at Syncrude plant site capability of analysis and prediction of performance in light of unusual geotechnical characteristic of tar sand, R.M.Hardy & Association, 74 pages
- Hoe, L., and Liu, Z., 2001, Performance of geosynthetic-reinforced asphalt Pavement, Journal of Geotechnical and Geoenvironmental Engineering, 127, 2 , pp 177-184
- Imperial Oil, 2004, Imperial Oil Limited, <http://www.imperialoil.ca> [2004-11-01]
- Ishizuka, Y. and Abe, T. and Kodama, J. ,1990, Fatigue behaviour of granite under cyclic loading, Proceedings of the ISRM International Symposium on Static and Dynamic Consideration in Rock Engineering, pp 139-146
- Joseph, T.G., 2000, Estimation of the post-failure stiffness of rock, PhD Thesis, Department of Civil and Environmental Engineering, University of Alberta, Edmonton, Alberta, 500 pages
- Joseph, T.G., 2001, Syncrude Canada Ltd. Contract year end progress report 2001, Syncrude Canada Ltd Internal Report, 7 pages
- Joseph, T.G. 2001, OsEIP: The oil sand equipment interactions program, Progress report, JPI Ltd. Contract with Syncrude Canada Ltd., 16 pages
- Joseph, T.G. and Welz, M., 2003, Mechanical action and geophysical reaction: Equipment – oil sand interactions (Presentation in Calgary at CIM Conference)

- Joseph, T.G. and Hansen, G., 2002, Oil sand reaction to cable shovel motion, CIM Bulletin, **95**, 1064, pp 62–64
- Joseph, T.G., 2002, OsEIP: The oil sand equipment interactions program, CIM Bulletin, **95**, 1064, pp 58–61
- Joseph, T.G. and Sharif-Abadi, A.D. and Shi, N., 2003, A broken material approach to modeling oil sand under dynamic load (Presentation in Calgary at CIM Conference)
- Kachanov, L.M., 1986, Introduction to Continuum Damage Mechanics, Martinus Nijhoff Publishers, 135 pages
- Kebaili, A and Schmitt, D.R., 1997, Ultrasonic anisotropic phase velocity determination with the radon transformation, The Journal of the Acoustical Society of America, **101**, 6 , pp 3278-3286
- Khalid, H.A., 2000, Evaluation of asphalt fatigue properties in the laboratory, Proceedings of the Institution of Civil Engineers. Transport , **141**, 4 , pp 171-178
- Kosar, K.M. ,1989, Geotechnical properties of oil sands and related strata , PhD Thesis, Department of Civil and Environmental Engineering, University of Alberta, Edmonton, Alberta, 795 pages
- Kosar, K.M. and Scott, J.D., 1987, Testing to determine the geotechnical properties of oil sands, 38<sup>th</sup> Annual Technical Meeting Petroleum Society of CIM , Calgary, Alberta, Canada, pp 995-1010
- Lahlou, K. and Lachemi, M. and Aïtcin, P.C., 1999, Confined high strength concrete under dynamic compressive loading , Journal of Structural Engineering, **125**, 10 , pp 1100-1108
- Lee, H.J. and Daniel, J.S. and Kim, Y.R., 2000, Continuum damage mechanics-based fatigue model of asphalt concrete, Journal of materials in civil engineering , **12**, 2 , pp 105-112
- Lord, E.R.F and Cameron, R., 1985 , Compaction characteristic of Athabasca tar sand, Canadian Geotechnical Conference, 38<sup>th</sup> Canadian Geotechnical Conference: Theory & Practice in Foundation Engineering , pp 359-368
- Louie, N.J., 2001, Faster, Better : Shear-wave velocity to 100 metres depth from refraction micrometre Arrays, Bulletin of the Seismological Society of America **91**, 2 , pp 347-364

- Madshus, C. and Kaynia, A.M., 1999, Dynamic ground interaction; a critical issue for high speed train lines on soft soil, *Geotechnical Engineering for Transportation Infrastructure*, **47**, 7 , pp 1829-1836
- Mao, X. and Fahey, M., 2003, Behaviour of calcareous soils in undrained cyclic simple shear, *Géotechnique*, **53**, 8 , pp 715 -727
- Mater, J.E., 1988, Fatigue, *Journal of Materials Education*, **11**, 1&2 , pp 1-104
- Matthews, M.C. and Hope, V.S. and Clayton, C.R.I., 1996, The use of surface waves in the determination of ground stiffness profiles, *Proceeding of the Institution of Civil Engineering – Geotechnical Engineering* , **119**, 2 , pp 84-95
- Matthews, M.C. and Clayton, C.R.I. and Own, Y., 2000, The use of field geophysical techniques to determine geotechnical stiffness parameters, *Proceeding of the Institution of Civil Engineering – Geotechnical Engineering* , **143**, 1 , pp 31-42
- Moxhay, A.L. and Tinsley, R.D. and Sutton, J.A., 2001, Monitoring of soil Stiffness during ground improvement using seismic surface waves, Article Featured in *Ground Engineering Magazine*, **34**, 1 , pp 34-37
- Myre, J., 1990, Fatigue of asphalt pavements, *Public Road Administration Norwegian Road Research Laboratory*, pp 1-12
- Murthy, V.N.S., 2003, *Geotechnical Engineering: Principles and Practices of Soil Mechanics and Foundation Engineering*, New York, Marcel Dekker, 1029 pages
- National energy Board, 2000, *Canada oil sand, A Supply and Market Outlook to 2015*, 121 pages , <http://dsp-psd.communication.gc.ca/Collection/NE23-89-2000E.pdf> [2006-11-28]
- Pender, M.J.,1982, A model for cyclic loading of overconsolidated soil, *Soil Mechanics-Transient and Cyclic Loads*, Edited by Pande G.N. and Ziekiewicz O.C., 1982 John Wiley & Sons Ltd, pp 283-312
- Plewes, D.H., Spring 1987, *Undrained strength of Athabasca oil sand*, MSc Thesis, Department of Civil and Environmental Engineering, University of Alberta, Edmonton, Alberta , 428 pages

- Ray, S.K and Sarkar, M. and Singh, T.N.,1999, Effect of cyclic loading and strain rate on the mechanical behaviour of sandstone , International Journal of Rock Mechanics and Mining Sciences, **36**, 4 , pp 543-549
- Samieh, M.A. and Wong, C.K.R., 1998, Modeling the response of the Athabasca oil sand in triaxial compression tests at low pressure, Canadian Geotechnical Journal, **35**, 2 , pp 395-406
- Selig, E.T., 1961, Technique for Observing Structure-Soil Interaction, Materials Research and Standards, **1**, 9 , pp 717-719
- Shearer, P.M., 1999, Introduction to Seismology, Cambridge ; New York : Cambridge University Press, 260 pages
- Singh, S.K., 1989, Fatigue and strain hardening behaviour of graywacks from the flag staff formation, Engineering Geology , **27**, 2 , pp 171-179
- Timoshenko, S.P., 1934, Theory of Elasticity, New York and London, McGraw-Hill Book Company, 1<sup>st</sup> edition, 416 pages
- Thorne, L. and Terry, C.W., 1995, Modern Global Seismology, San Diego : Academic Press , 521 pages
- Trombley, N., 2001. Vital information management system. Co-Op Work Term Presentation at Syncrude Canada Ltd., 24 Slides
- Vesic, A., 1963, Bearing capacity of deep foundations in sand, National Academy of Sciences, National Research Council, Highway Research Record, 39 , pp 112-153
- Voyiadjis, G., Abu-Lebdeh, T., 1993, Damage model for concrete using bounding surface concept, Journal of Engineering Mechanics, Proceedings of the ASCE , **119**, 9 , pp 1865-1885
- Welz, M., 2001, Velocities of heavy oil reservoirs from refraction studies, In Situ Rock Physics, Seismic Heavy Oil Consortium (SHOC) at the University of Alberta
- Wohlgemuth, P., 1997, Structural fatigue cracking failure trend. M.Eng. Thesis ,Department of Civil and Environmental Engineering, University of Alberta, Edmonton, Alberta, University of Alberta, 42 pages
- Wu, H.C. and Komarakulnankorn, C., 1998, Endochronic theory of continuum damage mechanics, Journal of Engineering Mechanics, **124**, 2 , pp 200-208

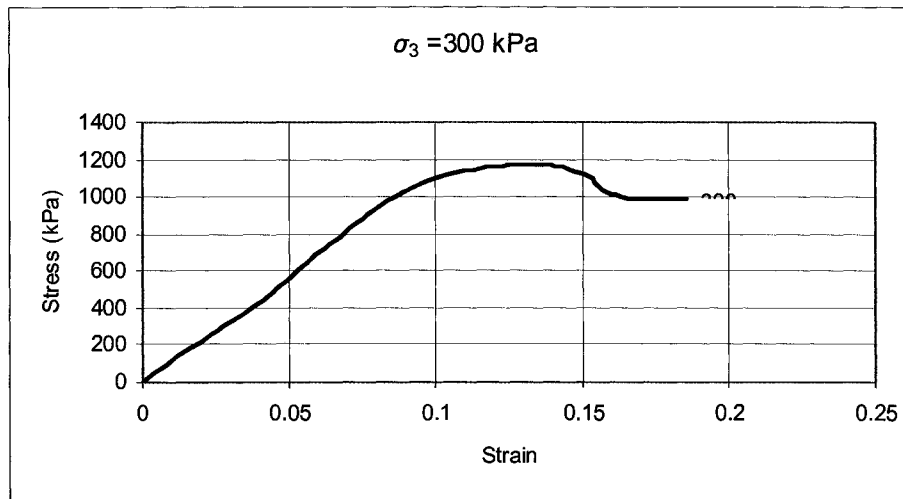
- Zhao, X.H. and Sun, H. and Lo, K.W., 2002, An Elastoplastic damage model for soil, *Géotechnique*, **52**, 7 , pp 533 -536
- Zhenyu, T. and Haihong, M., 1990, Experimental study and analysis of the behaviour of rock under cyclic loading, *International Journal of Rock Mechanics and Mining Sciences & Geomechanics Abstracts*, **27**, 1, pp 51-56

## Appendix 1- Triaxial Test Results

Stress-strain curve for %8 oil sand or Triaxial test (Laboratory tests)

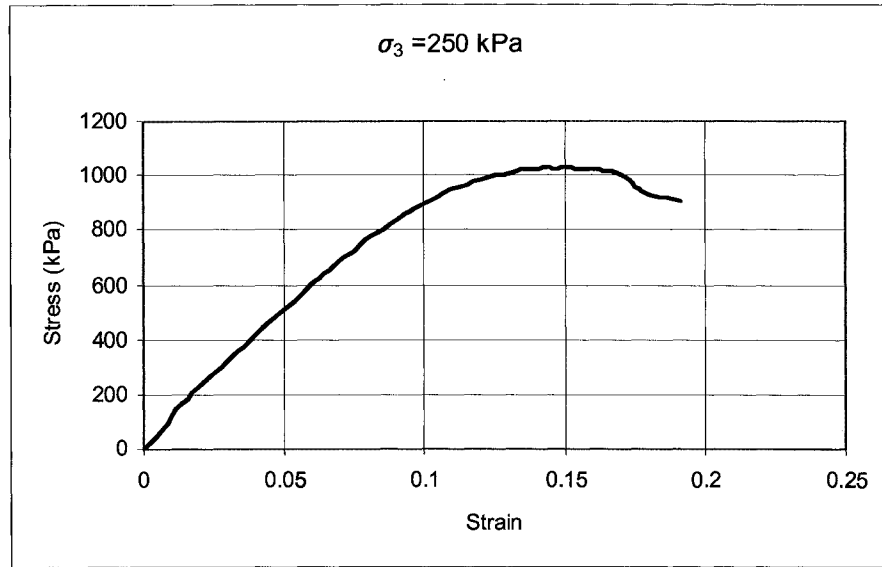
Sample for 300 kPa confining

Diameter(mm)	48.90	L/D	2.18
Length(mm)	106.73	Mass (gr)	404.54
Area (m <sup>2</sup> )	0.001878	Density (gr/cm <sup>3</sup> )	2.02
Volume (m <sup>3</sup> )	0.000200423	Speed (mm/Min)	0.076



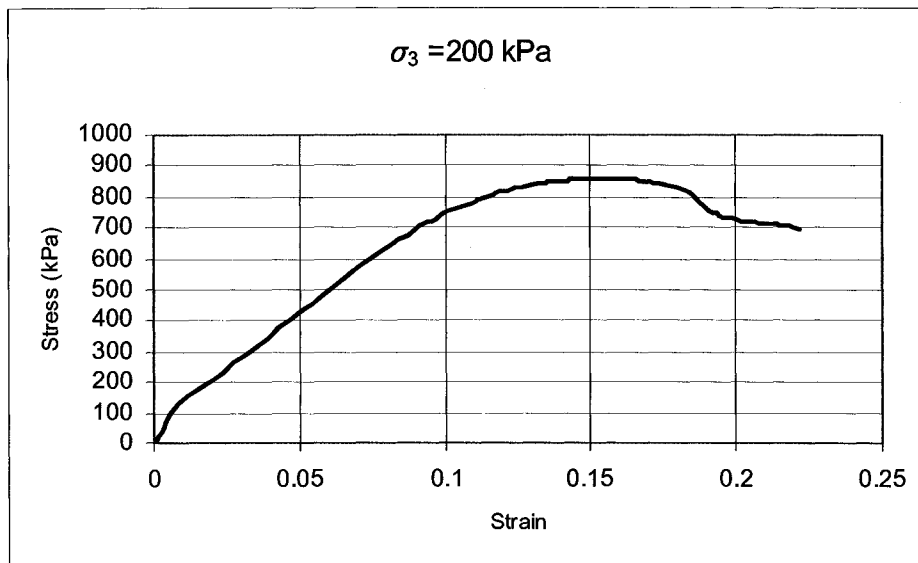
Sample for 250 kPa confining

Diameter(mm)	49.09	L/D	2.18
Length(mm)	106.95	Mass (gr)	400.17
Area (m <sup>2</sup> )	0.001893	Density (gr/cm <sup>3</sup> )	1.98
Volume (m <sup>3</sup> )	0.000202443	Speed (mm/Min)	0.076



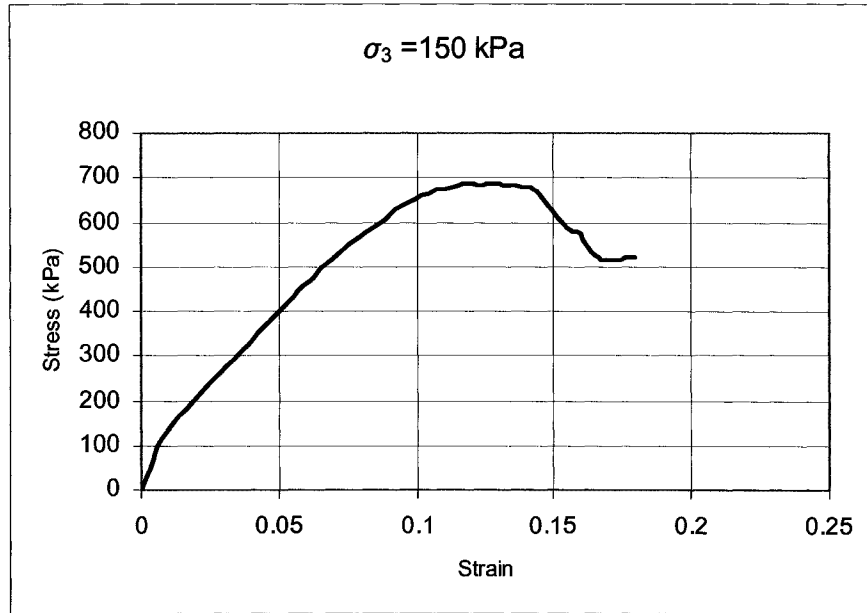
Sample for 200 kPa confining

Diameter(mm)	49.11	L/D	2.23
Length(mm)	109.44	Mass (gr)	417.63
Area (m <sup>2</sup> )	0.001894	Density (gr/cm <sup>3</sup> )	2.01
Volume (m <sup>3</sup> )	0.000207338	Speed (mm/Min)	0.076



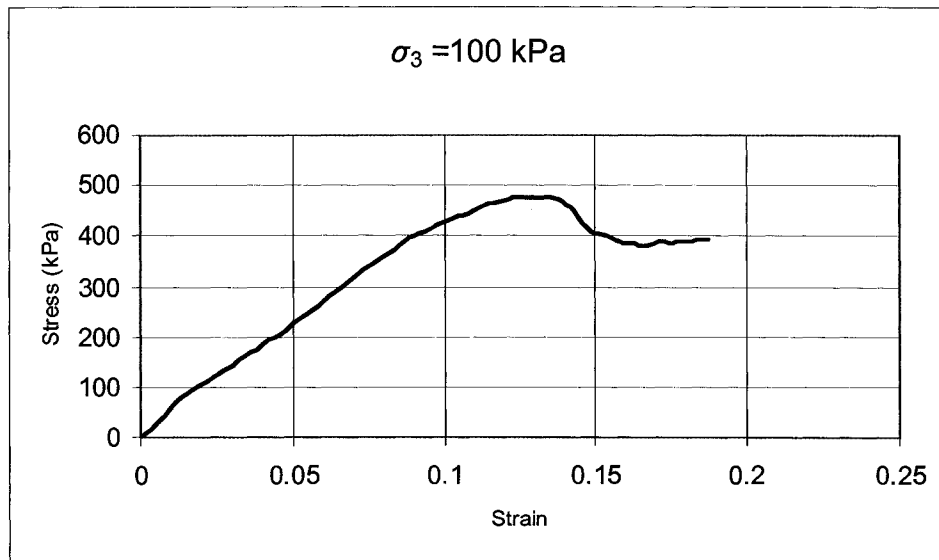
Sample for 150 kPa confining

Diameter(mm)	49.08	L/D	2.20
Length(mm)	107.90	Mass (gr)	405.98
Area (m <sup>2</sup> )	0.001892	Density (gr/cm <sup>3</sup> )	1.99
Volume (m <sup>3</sup> )	0.000204115	Speed (mm/Min)	0.076



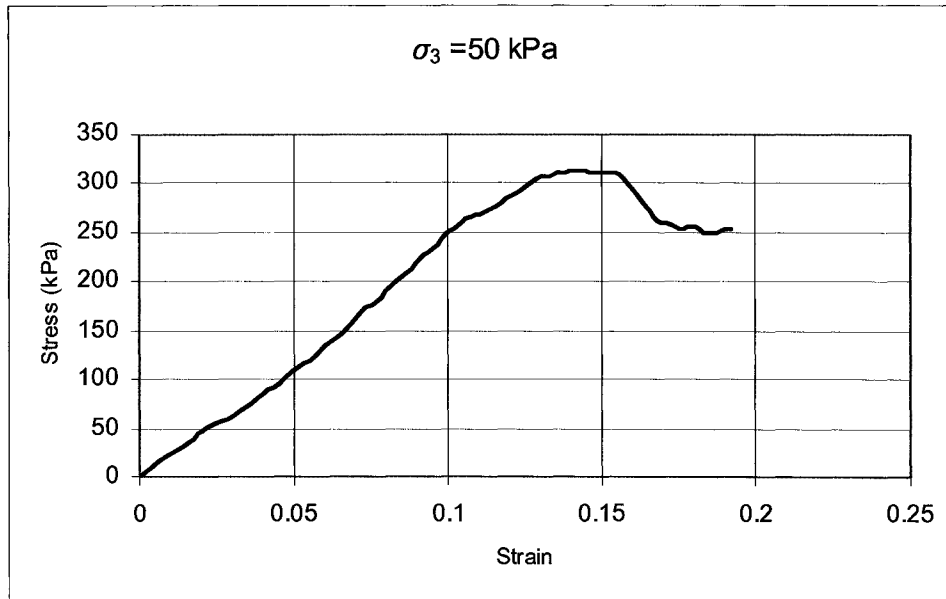
Sample for 100 kPa confining

Diameter(mm)	49.07	L/D	2.12
Length(mm)	104.14	Mass (gr)	393.89
Area (m <sup>2</sup> )	0.001891	Density (gr/cm <sup>3</sup> )	2.00
Volume (m <sup>3</sup> )	0.000196922	Speed (mm/Min)	0.076



Sample for 50 kPa confining

Diameter(mm)	49.11	L/D	2.21
Length(mm)	108.52	Mass (gr)	409.60
Area (m <sup>2</sup> )	0.001894	Density (gr/cm <sup>3</sup> )	1.99
Volume (m <sup>3</sup> )	0.000205526	Speed (mm/Min)	0.076



Stress-strain curve for %11 oil sand

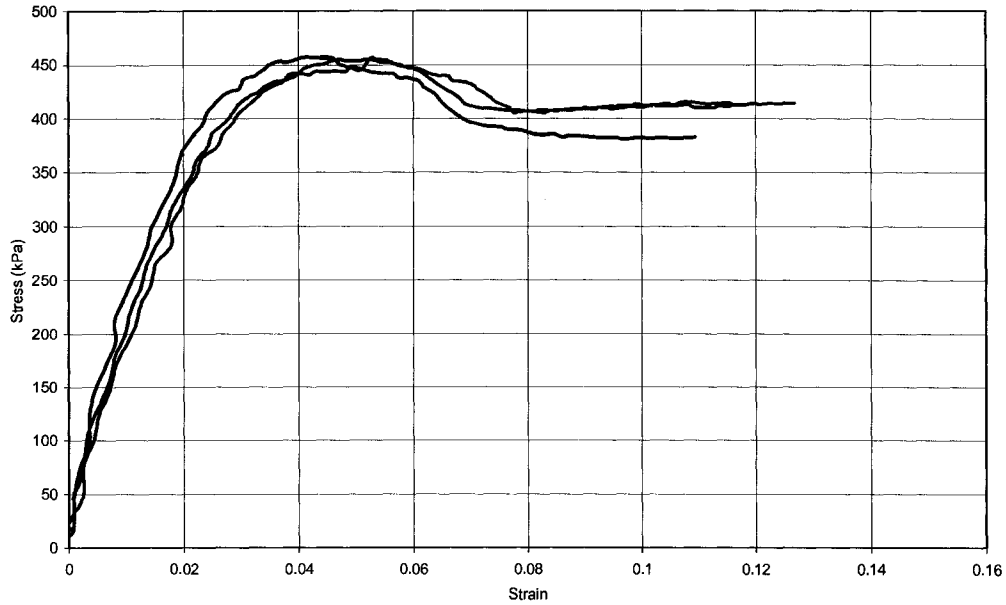
Samples for 100 kPa confining

Diameter(mm)	51.93	L/D	2.04
Length(mm)	105.74	Mass (gr)	455.31
Area (m <sup>2</sup> )	0.002118	Density (gr/cm <sup>3</sup> )	2.03
Volume (m <sup>3</sup> )	0.000224	Speed (mm/Min)	0.076

Diameter(mm)	52.70	L/D	2.00
Length(mm)	105.61	Mass (gr)	455.79
Area (m <sup>2</sup> )	0.002181	Density (gr/cm <sup>3</sup> )	1.98
Volume (m <sup>3</sup> )	0.00023	Speed (mm/Min)	0.076

Diameter(mm)	52.83	L/D	2.00
Length(mm)	105.45	Mass (gr)	454.84
Area (m <sup>2</sup> )	0.002192	Density (gr/cm <sup>3</sup> )	1.97
Volume (m <sup>3</sup> )	0.000231	Speed (mm/Min)	0.076

$\sigma_3 = 100 \text{ kPa}$



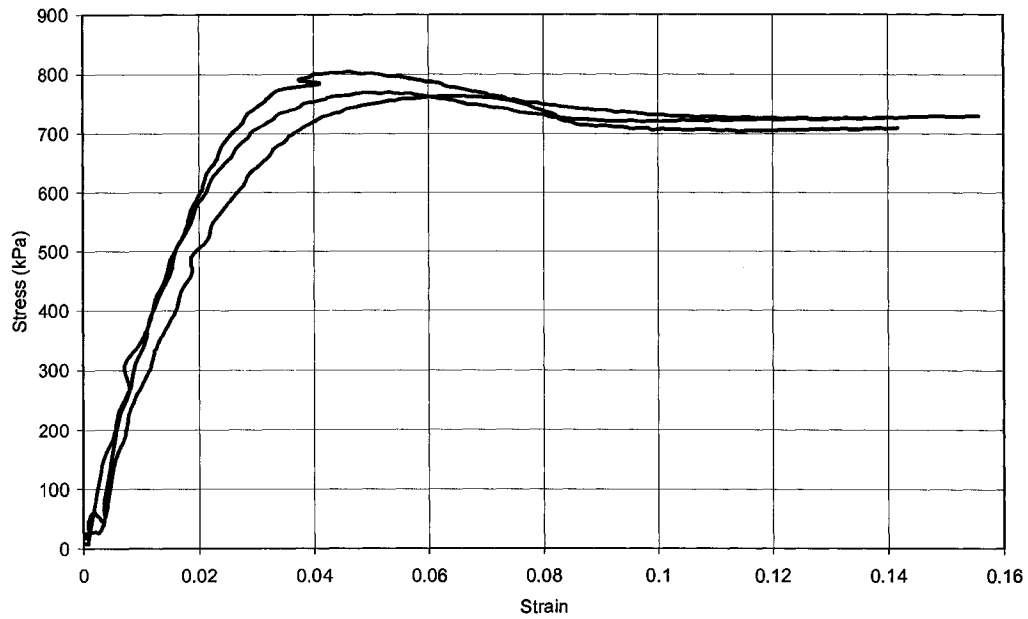
Samples for 200 kPa confining

Diameter(mm)	52.50	L/D	2.03
Length(mm)	106.38	Mass (gr)	452.47
Area (m <sup>2</sup> )	0.002164	Density (gr/cm <sup>3</sup> )	1.97
Volume (m <sup>3</sup> )	0.00023	Speed (mm/Min)	0.076

Diameter(mm)	52.18	L/D	2.03
Length(mm)	106.08	Mass (gr)	454.83
Area (m <sup>2</sup> )	0.002138	Density (gr/cm <sup>3</sup> )	2.00
Volume (m <sup>3</sup> )	0.000227	Speed (mm/Min)	0.076

Diameter(mm)	52.53	L/D	2.01
Length(mm)	105.46	Mass (gr)	454.73
Area (m <sup>2</sup> )	0.002168	Density (gr/cm <sup>3</sup> )	1.99
Volume (m <sup>3</sup> )	0.000229	Speed (mm/Min)	0.076

$\sigma_3 = 200 \text{ kPa}$



Samples for 300 kPa confining

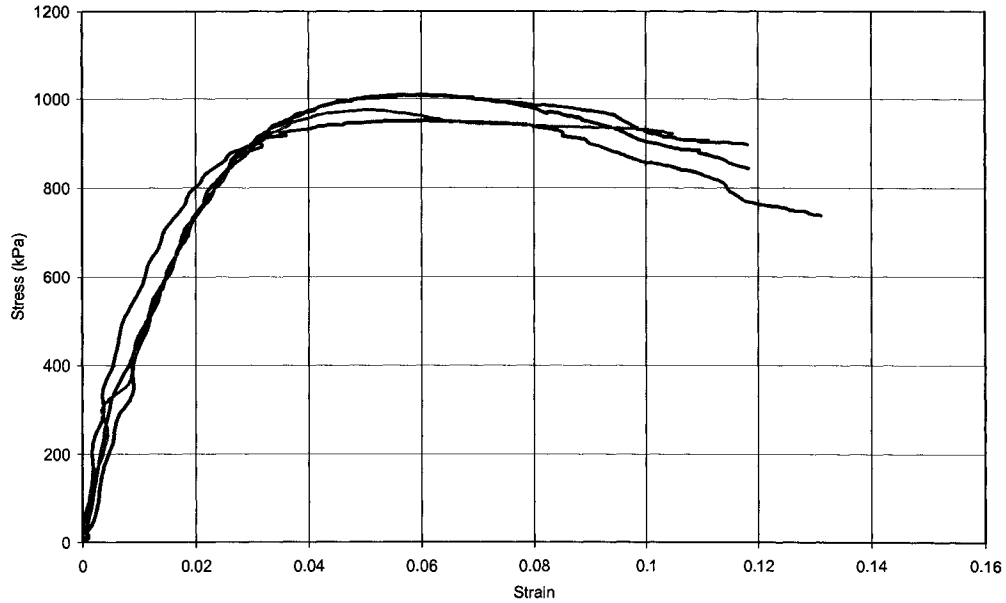
Diameter(mm)	52.22	L/D	2.02
Length(mm)	105.65	Mass (gr)	451.80
Area (m <sup>2</sup> )	0.002142	Density (gr/cm <sup>3</sup> )	2.00
Volume (m <sup>3</sup> )	0.000226	Speed (mm/Min)	0.076

Diameter(mm)	52.29	L/D	2.04
Length(mm)	106.90	Mass (gr)	452.15
Area (m <sup>2</sup> )	0.002147	Density (gr/cm <sup>3</sup> )	1.97
Volume (m <sup>3</sup> )	0.00023	Speed (mm/Min)	0.076

Diameter(mm)	52.22	L/D	2.04
Length(mm)	106.70	Mass (gr)	452.58
Area (m <sup>2</sup> )	0.002142	Density (gr/cm <sup>3</sup> )	1.98
Volume (m <sup>3</sup> )	0.000229	Speed (mm/Min)	0.076

Diameter(mm)	52.21	L/D	2.04
Length(mm)	106.47	Mass (gr)	453.81
Area (m <sup>2</sup> )	0.002141	Density (gr/cm <sup>3</sup> )	1.99
Volume (m <sup>3</sup> )	0.000228	Speed (mm/Min)	0.076

$\sigma_3 = 300 \text{ kPa}$



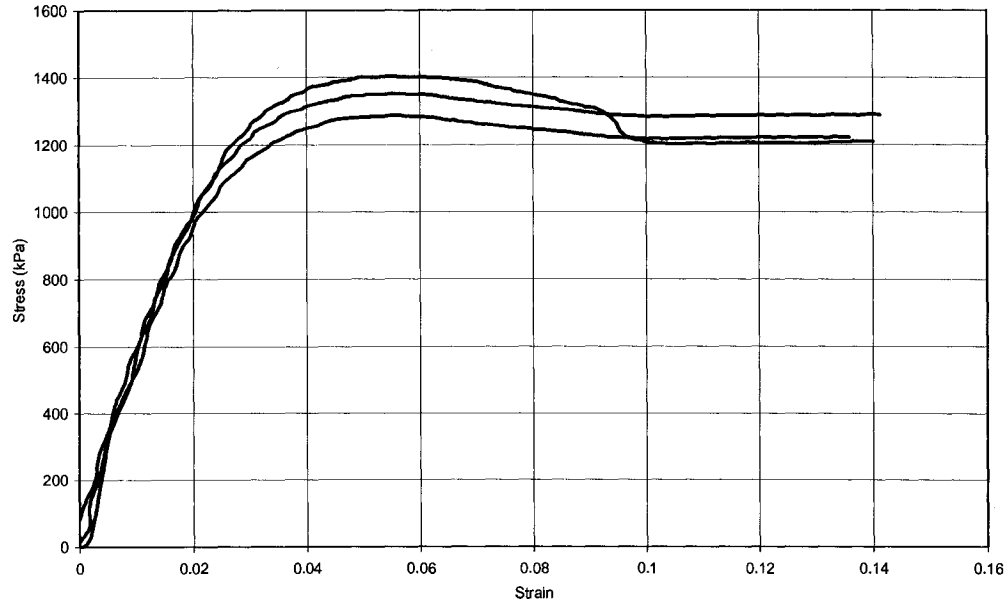
Samples for 400 kPa confining

Diameter(mm)	52.37	L/D	2.02
Length(mm)	105.55	Mass (gr)	454.92
Area (m <sup>2</sup> )	0.002154	Density (gr/cm <sup>3</sup> )	2.00
Volume (m <sup>3</sup> )	0.000227	Speed (mm/Min)	0.076

Diameter(mm)	52.16	L/D	2.04
Length(mm)	106.18	Mass (gr)	454.60
Area (m <sup>2</sup> )	0.002137	Density (gr/cm <sup>3</sup> )	2.00
Volume (m <sup>3</sup> )	0.000227	Speed (mm/Min)	0.076

Diameter(mm)	51.78	L/D	2.04
Length(mm)	105.66	Mass (gr)	453.61
Area (m <sup>2</sup> )	0.002106	Density (gr/cm <sup>3</sup> )	2.04
Volume (m <sup>3</sup> )	0.000222	Speed (mm/Min)	0.076

$\sigma_3 = 400 \text{ kPa}$



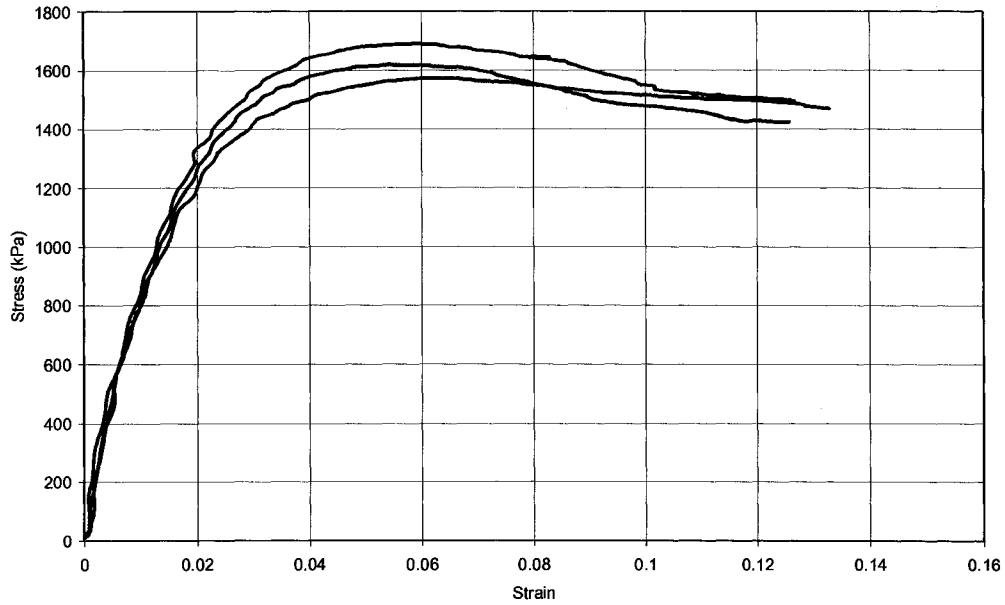
Samples for 500 kPa confining

Diameter(mm)	51.26	L/D	2.08
Length(mm)	106.51	Mass (gr)	455.03
Area (m <sup>2</sup> )	0.002064	Density (gr/cm <sup>3</sup> )	2.07
Volume (m <sup>3</sup> )	0.00022	Speed (mm/Min)	0.076

Diameter(mm)	52.24	L/D	2.03
Length(mm)	105.82	Mass (gr)	454.58
Area (m <sup>2</sup> )	0.002143	Density (gr/cm <sup>3</sup> )	2.00
Volume (m <sup>3</sup> )	0.000227	Speed (mm/Min)	0.076

Diameter(mm)	52.43	L/D	2.02
Length(mm)	106.13	Mass (gr)	453.61
Area (m <sup>2</sup> )	0.002159	Density (gr/cm <sup>3</sup> )	1.98
Volume (m <sup>3</sup> )	0.000229	Speed (mm/Min)	0.076

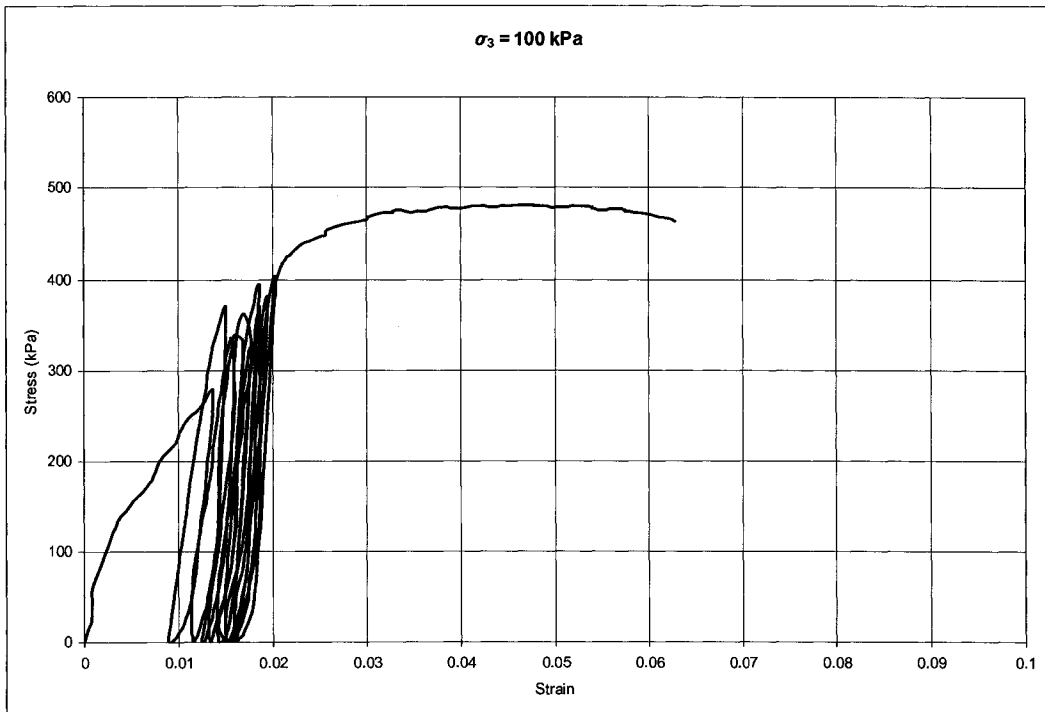
$\sigma_3 = 500 \text{ kPa}$



Sample for 100 kPa confining

Diameter(mm)	51.27	L/D	2.08
Length(mm)	106.43	Mass (gr)	455.09
Area (m <sup>2</sup> )	0.002064	Density (gr/cm <sup>3</sup> )	2.07
Volume (m <sup>3</sup> )	0.00021969	Speed (mm/Min)	0.076

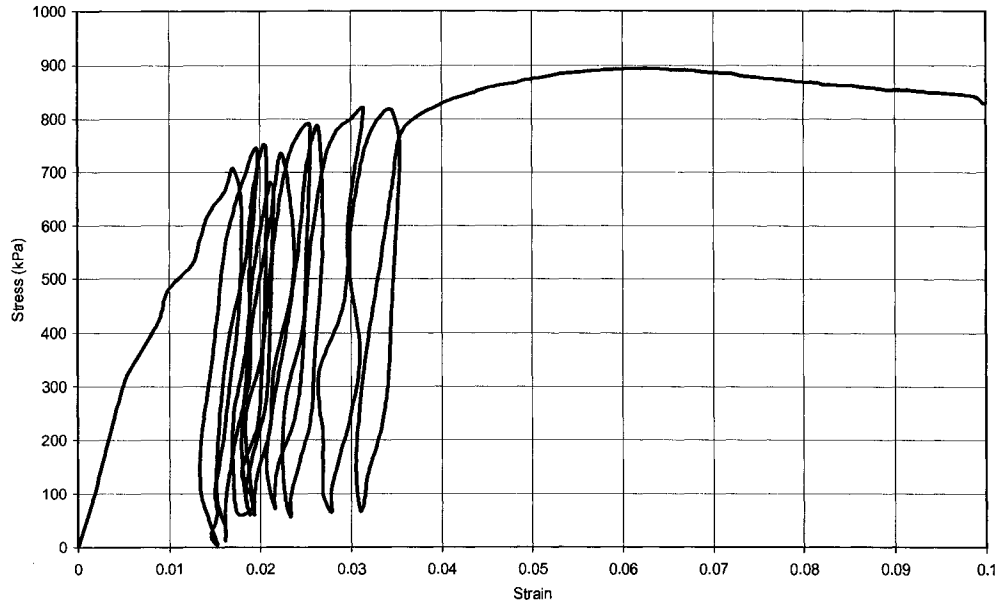
$\sigma_3 = 100 \text{ kPa}$



Sample for 300 kPa confining

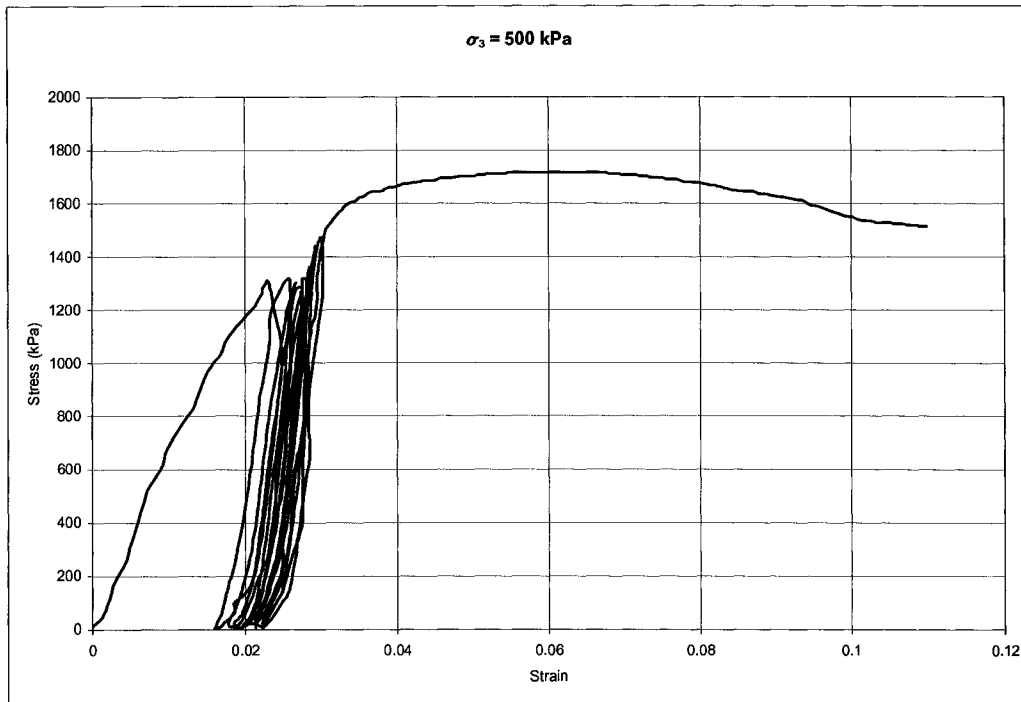
Diameter(mm)	52.11	L/D	2.02
Length(mm)	105.25	Mass (gr)	451.24
Area (m <sup>2</sup> )	0.002133	Density (gr/cm <sup>3</sup> )	2.01
Volume (m <sup>3</sup> )	0.000224497	Speed (mm/Min)	0.076

$\sigma_3 = 300 \text{ kPa}$



Sample for 500 kPa confining

Diameter(mm)	52.21	L/D	2.03
Length(mm)	106.20	Mass (gr)	454.59
Area (m <sup>2</sup> )	0.002141	Density (gr/cm <sup>3</sup> )	2.00
Volume (m <sup>3</sup> )	0.000227393	Speed (mm/Min)	0.076



## Appendix 2 – Summary of Field Plate Load Test

Test No.	Loading condition	Deformation (mm)	Force (kN)	Plate Size	Time (Hour:Min:Sec)	
Test1	Loading	0.00	0	Big plate	0:05:06	
		49.91	5255.38			
	Unloading	61.32	4687.48			0:01:45
		56.46	72.366			
	Decreasing load	49.91	5255.38			0:05:30
		61.32	4687.48			
Test 2	Loading	0	0	Big plate	0:03:18	
		14.04	3229.88			
	Unloading	16.92	3025.43			0:00:27
		16.50	30.711			
	Decreasing load	14.04	3229.88			0:03:51
		16.92	3025.436989			
Test 3	Loading	0	0	Big Plate	0:09:39	
		8.79	5274.31			
Test 4	Loading	0	0	Medium Plate	0:05:03	
		14.34	4301.31			
	Unloading	14.34	4301.31			0:00:33
		13.96	170.79			
Test 5	Loading	0	0	Small Plate	0:03:24	
		17.84	3900.00			
	Unloading	19.5	3967.51			0:00:27
		18.47	375.24			
Test 7	Loading	0	0	Small Plate	0:02:00	
		25.97	4240.74			
	Load kept constant	25.97	4240.74			0:01:33
		61.20	4384.60			
	Unload	61.20	4384.60			0:00:39
		60	0			
Test 8	Loading	0	0	Medium Plate	0:02:11	
		33.14	4142.30			
	Decreasing load	33.14	4142.301			0:01:42
		35.75	3960.57			
	Unload	35.75	3960.57			0:00:27
		34.15	110.22			
Test 9	Loading 1	0	872.97	Big plate	0:00:12	
		11.47	2843.70			
	Loading 2	17	2793.53			0:01:18
		24.53	4059.01			
	Decreasing load	24.53	4059.01			0:00:51
		27.01	3877.28			
	Unloading	27.01	3877.28		0:00:06	

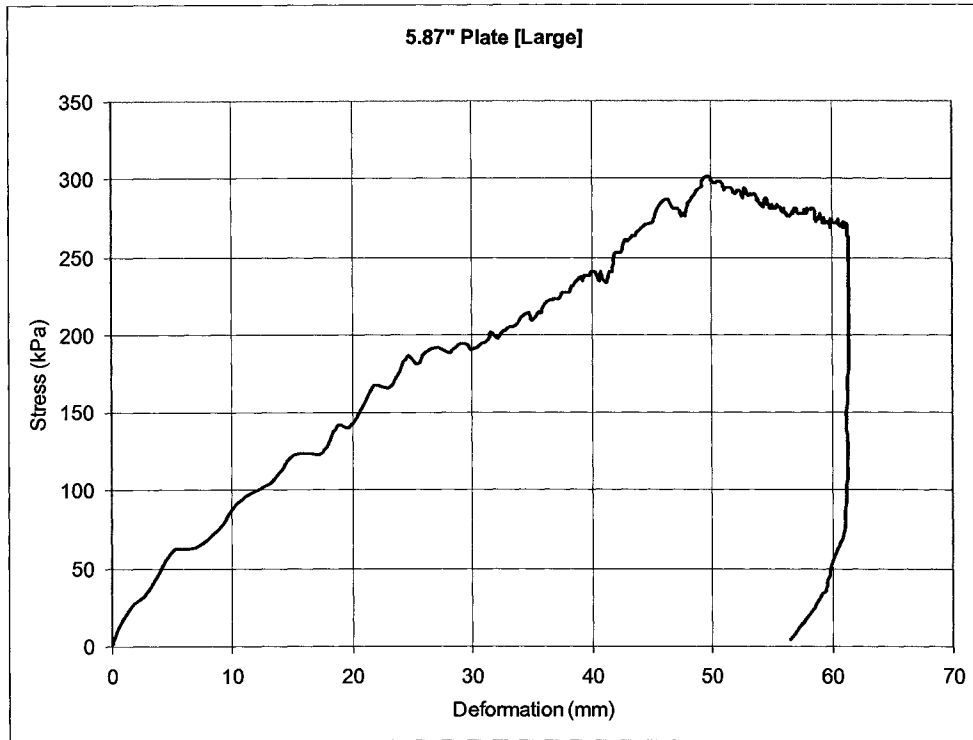
		25.999	151.86		
Test 10	Loading	0	0	Big plate	0:00:30
		28.59	4464.11		0:05:57
	Decrease load	28.59	4464.11		0:04:57
	Unloading	39.22	3593.33		
		38.99	375.24		
Test 11	Loading 1	0	0	Medium Plate	0:00:42
		26.85	2987.57		0:02:15
	Loading 2	39.07	2521.89		0:10:12
		45.02	3756.13		0:11:12
	Decreasing load 1	26.85	2987.57		0:00:36
		39.07	2521.89		
	Decreasing load 2	45.02	3756.13		
	Unloading	51.87	3309.38		
	50.26	170.79			
Test 12	Loading 1	0	0	Medium Plate Cyclic loading	0:01:39
		41.08	3775.06		0:00:36
	Decreasing load	41.08	3775.06		0:00:21
		43.90	3574.40		0:00:09
	Unloading 1	43.90	3574.40		0:01:24
		42.16	110.22		0:00:36
	Holding unload 1	42.16	110.22		0:00:12
		38.32	0		0:00:45
	Loading 2	38.32	0		0:01:03
		50.20	3900.00		0:05:45
	Unloading 2	50.20	3900.00		0:01:21
		49.00	91.29		0:00:45
	Holding unload 2	49.00	91.29		0:00:18
		46.14	0		0:04:48
	Loading 3	46.14	0		0:01:15
		52.83	3309.38		0:00:45
	Unloading 3	52.83	3309.38		0:01:03
		51.42	0		0:05:45
	Holding unload 2	52.64	212.44		0:01:21
		46.62	0		0:00:45
	Loading 4	46.62	0		0:00:18
		58.65	3918.93		0:04:48
	Decreasing load	58.65	3918.93		0:01:15
		59.93	3695.55		0:00:45
	Unload 4	59.93	3695.55		0:00:18
	57.95	49.64	0:04:48		
Holding unload 3	57.95	49.64	0:01:15		
	50.66	0	0:00:45		
Loading 5	50.66	0			
	63.02	3797.77			
Decreasing load	63.02	3797.77			

		64.55	3593.33		
	Unloading 5	64.55	3593.33		0:00:12
		63.30	356.31		
	Holding unload 4	63.30	356.31		0:07:51
		55.52	0		
	Loading 6	55.52	0		0:01:21
		68.95	3937.86		
	Unloading 6	68.95	3937.86		0:00:27
		67.49	0		
	Holding Unload 5	69.19	1408.81		0:01:03
		61.80	0		
	Loading 7	61.80	0		0:00:57
		71.71	3555.48		
	Decreasing Load	71.71	3555.48		0:10:51
		79.71	3188.23		

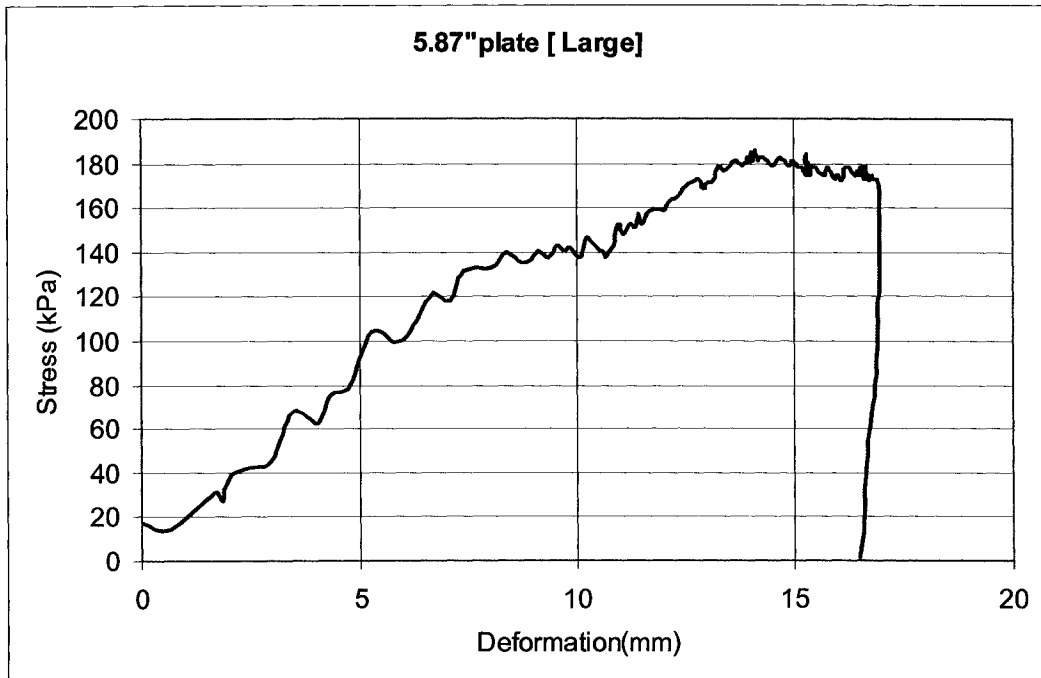
## Appendix 3 – Field Plate Load Test

Plate load test (cyclic and static) – Field test

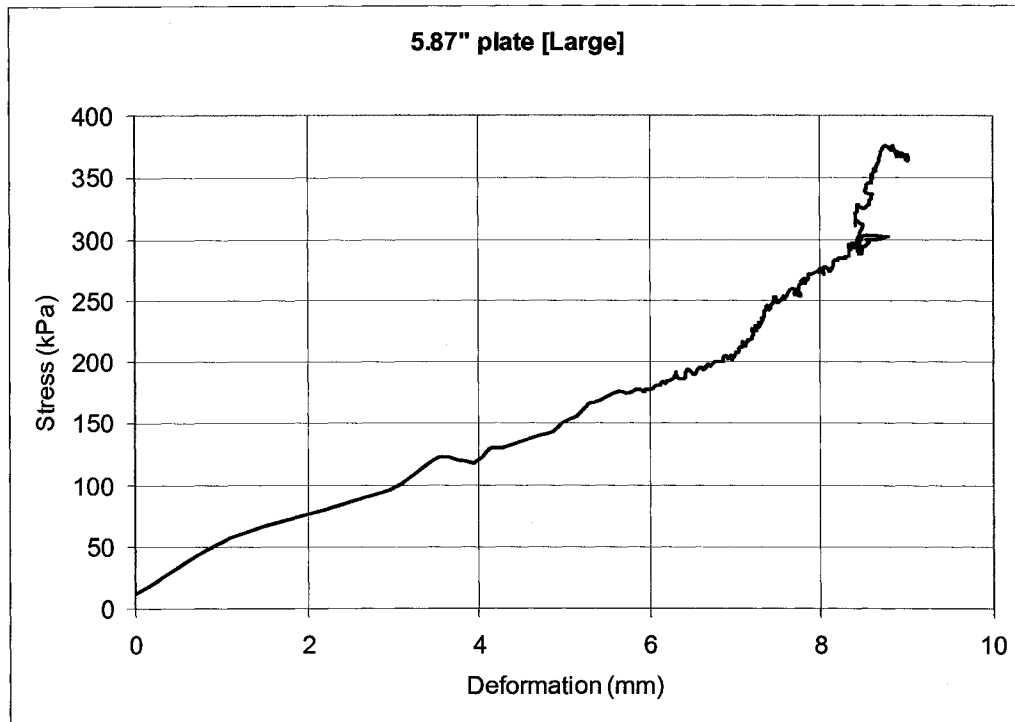
No.1



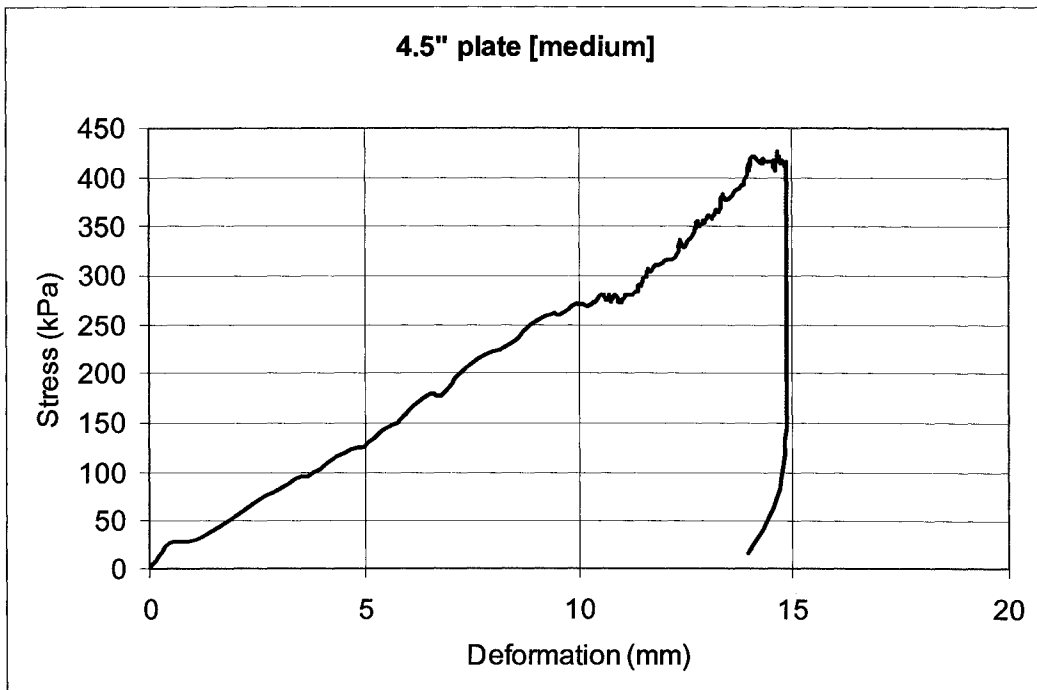
No.2



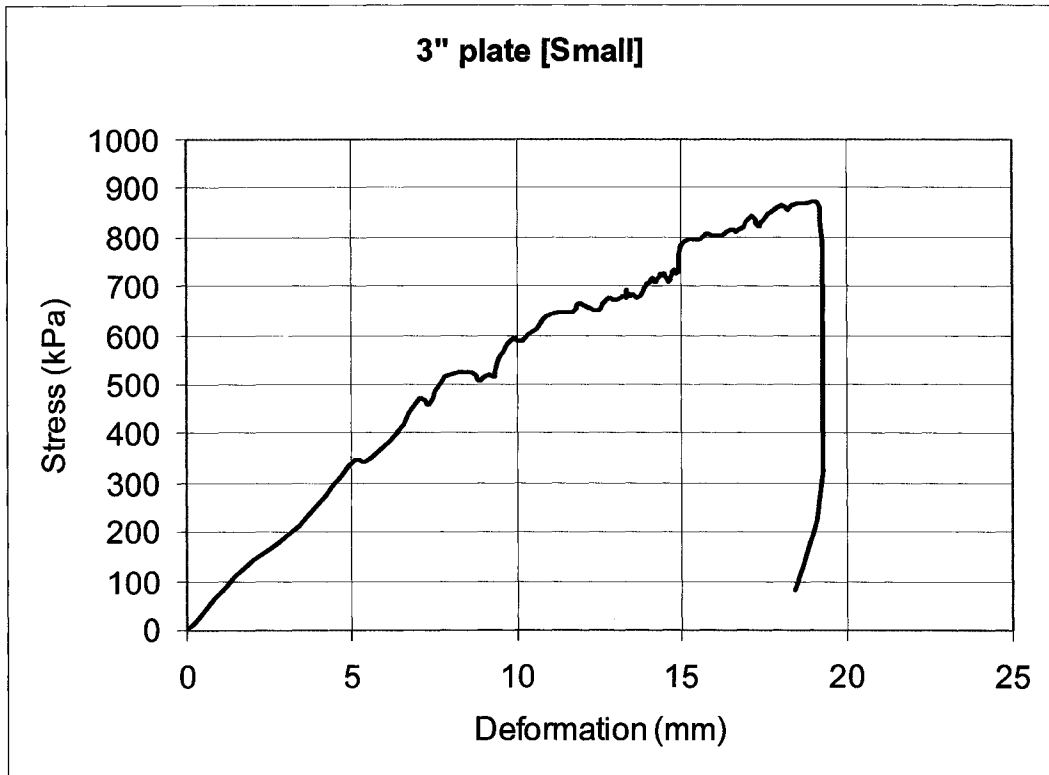
No.3



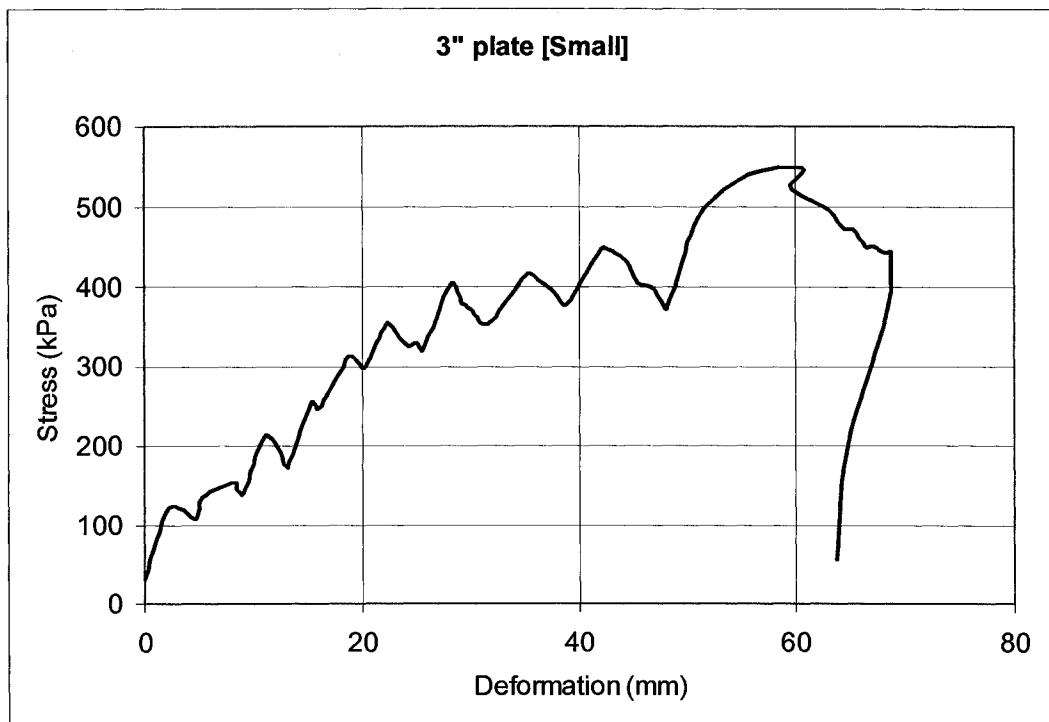
No.4



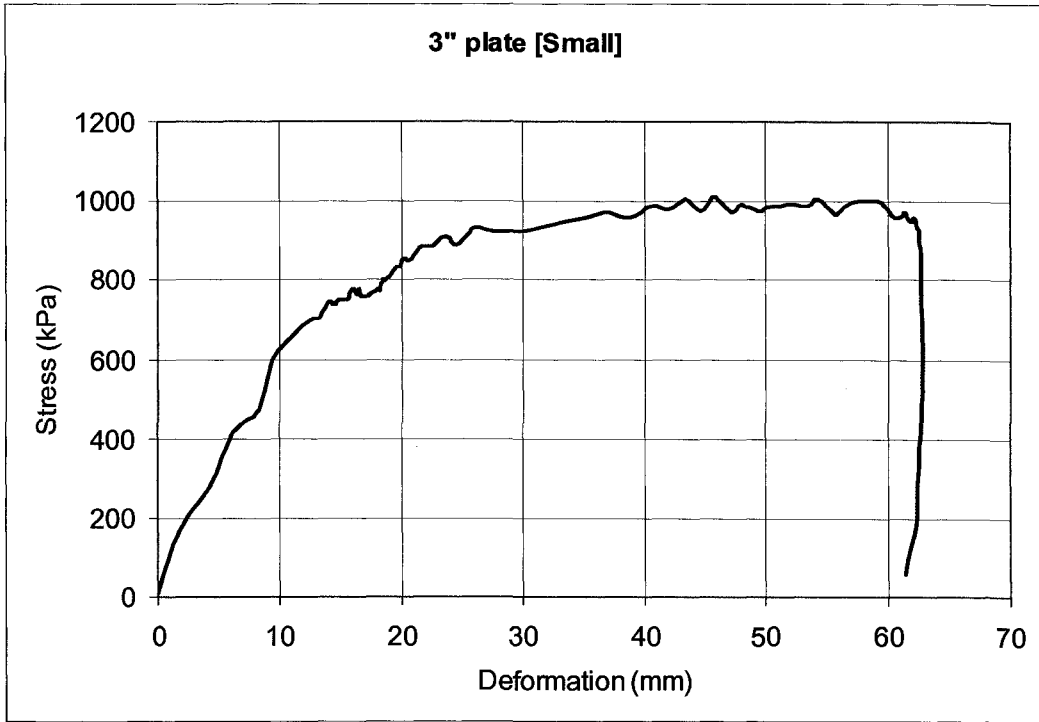
No.5



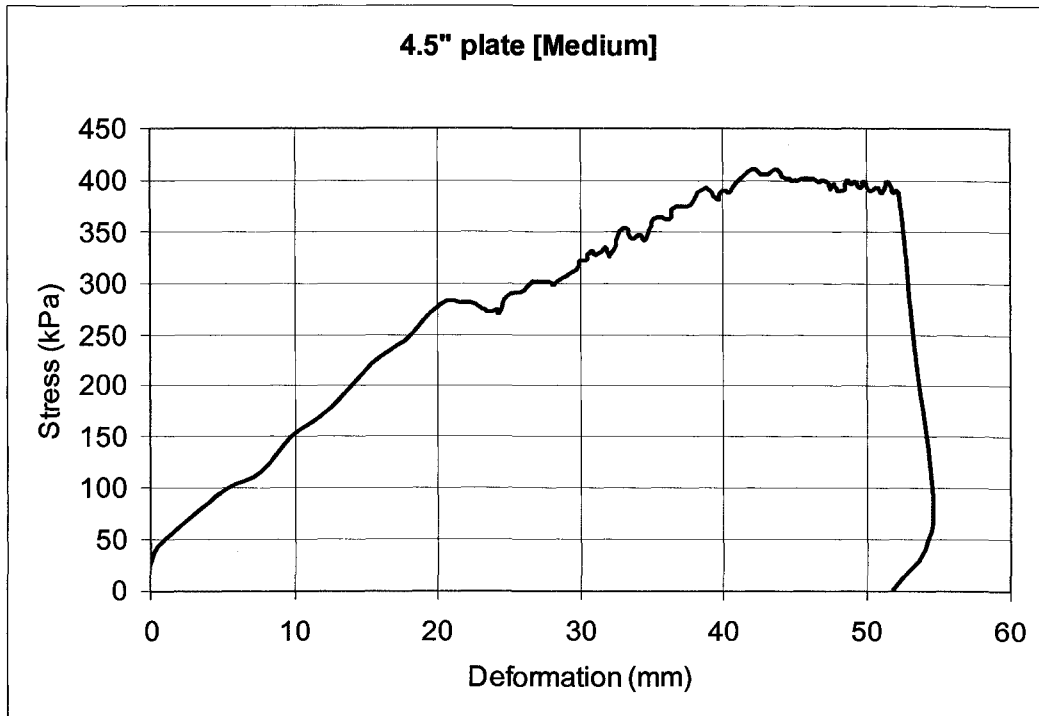
No.6



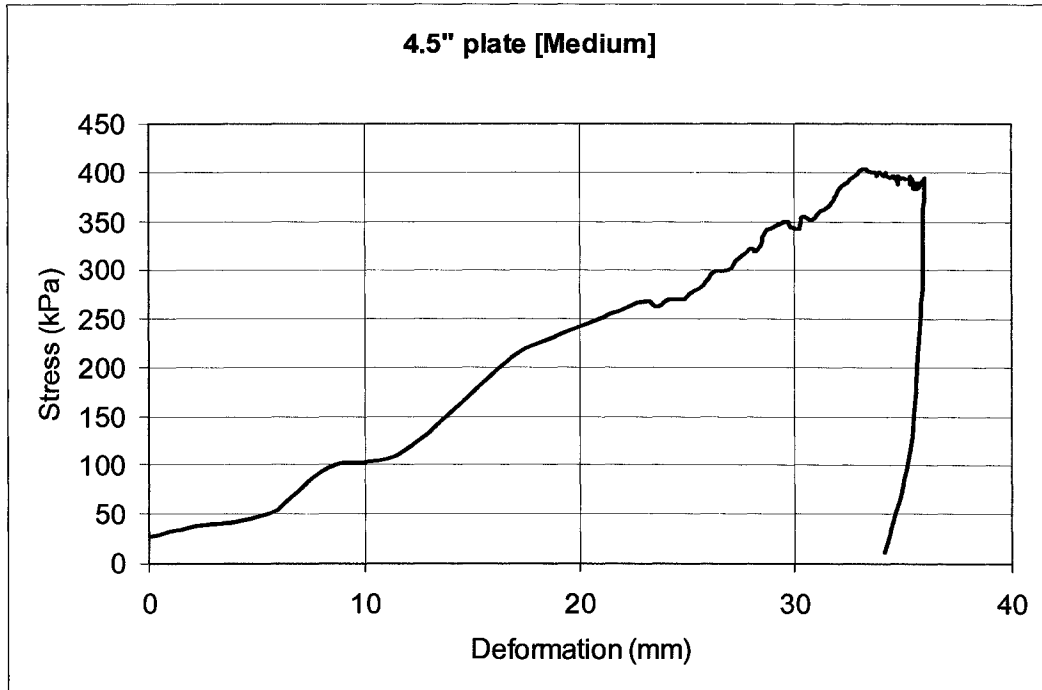
No.7



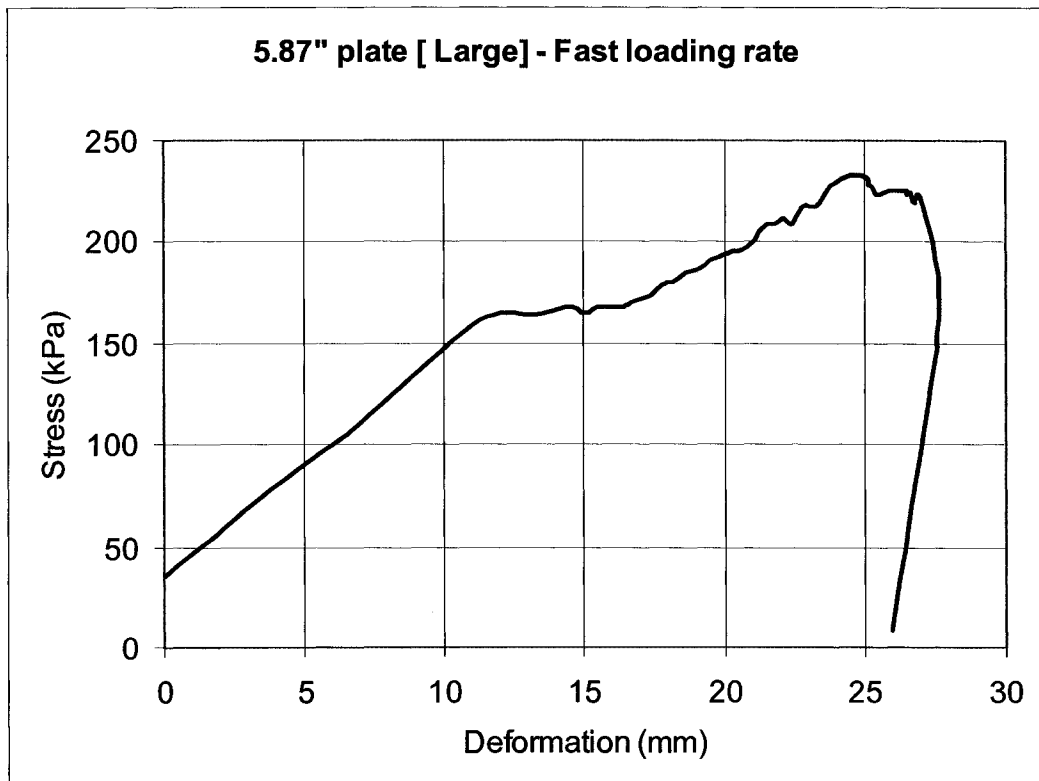
No.8



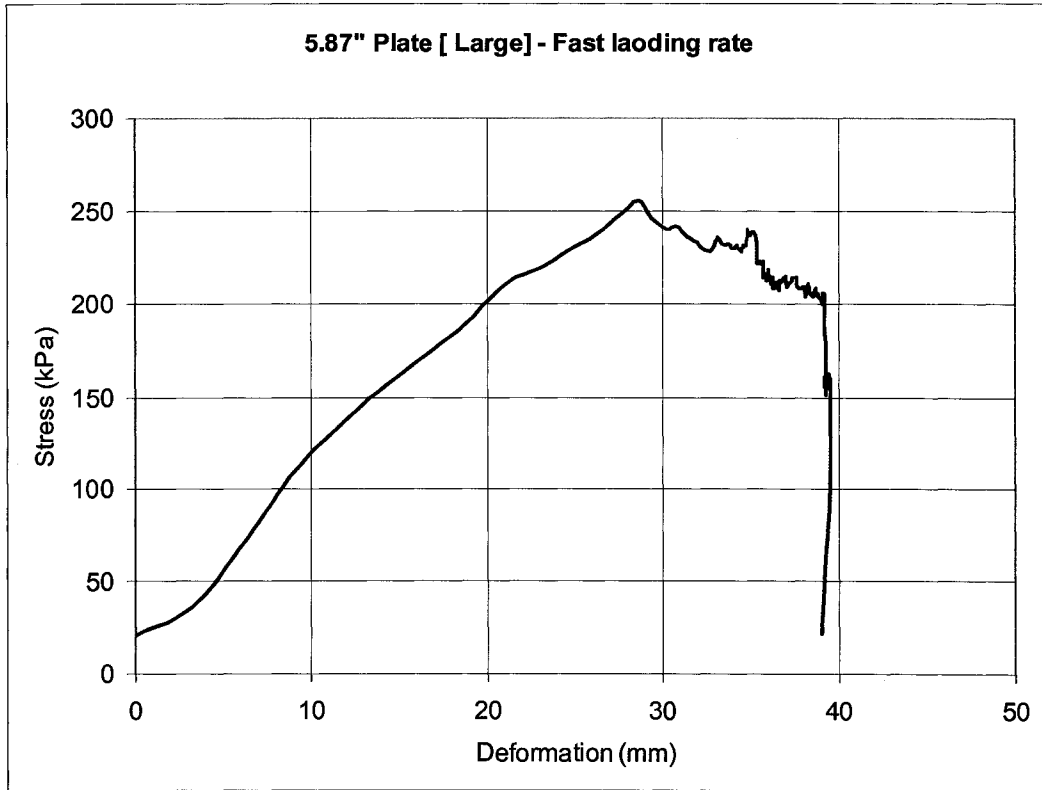
No.9



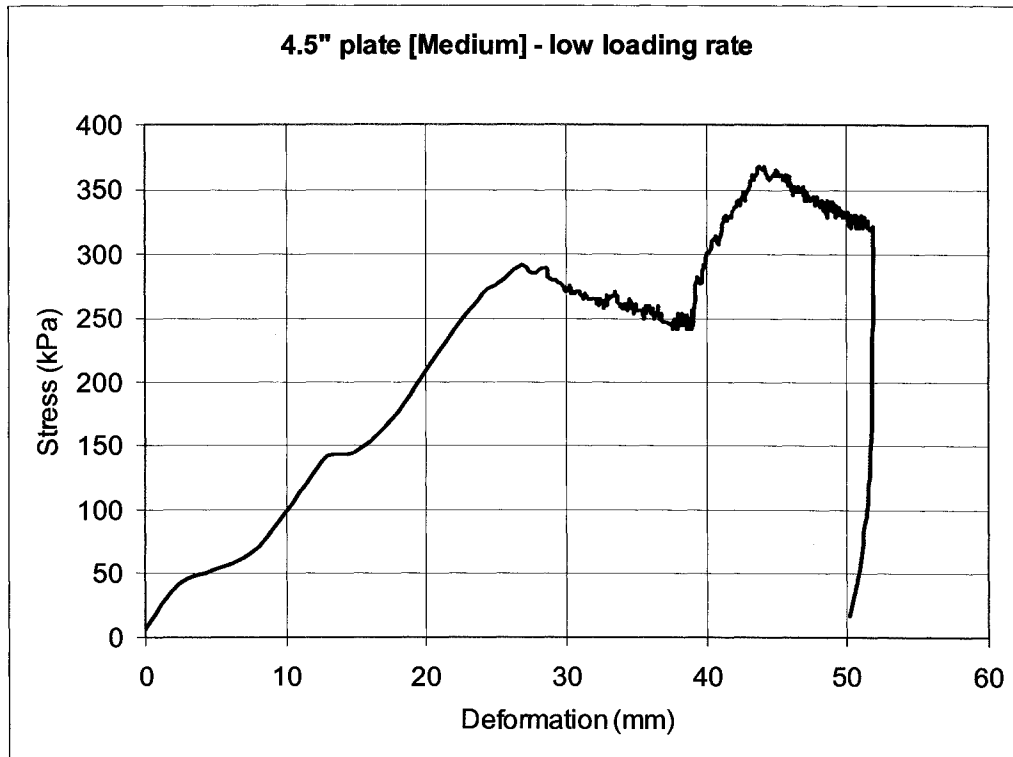
No.10



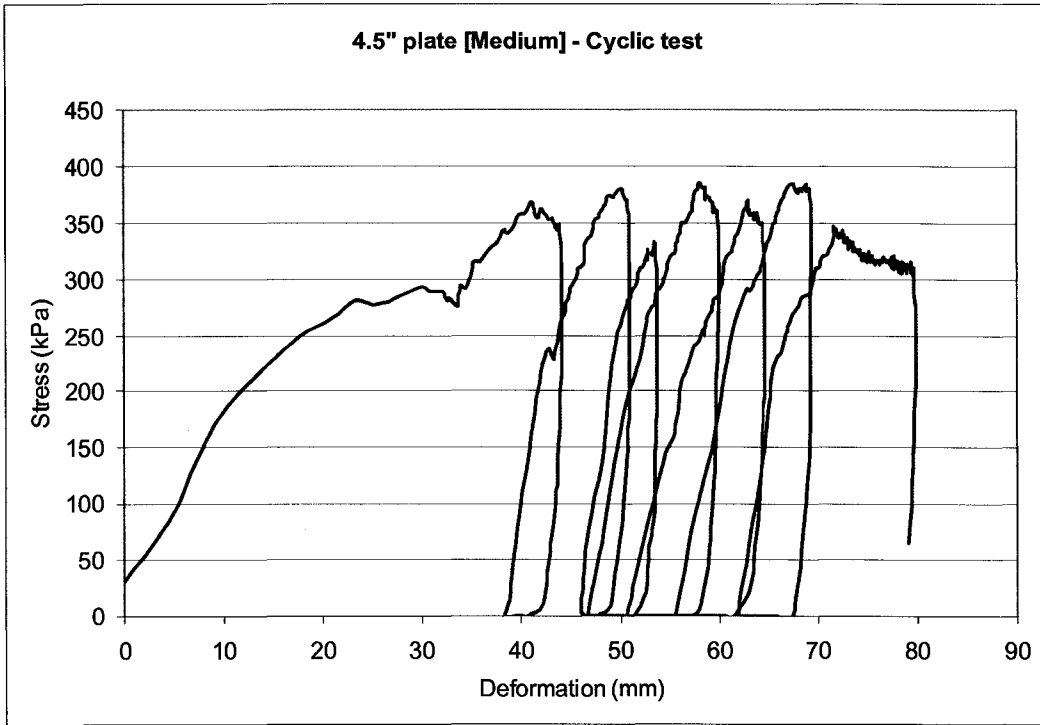
No.11



No.12

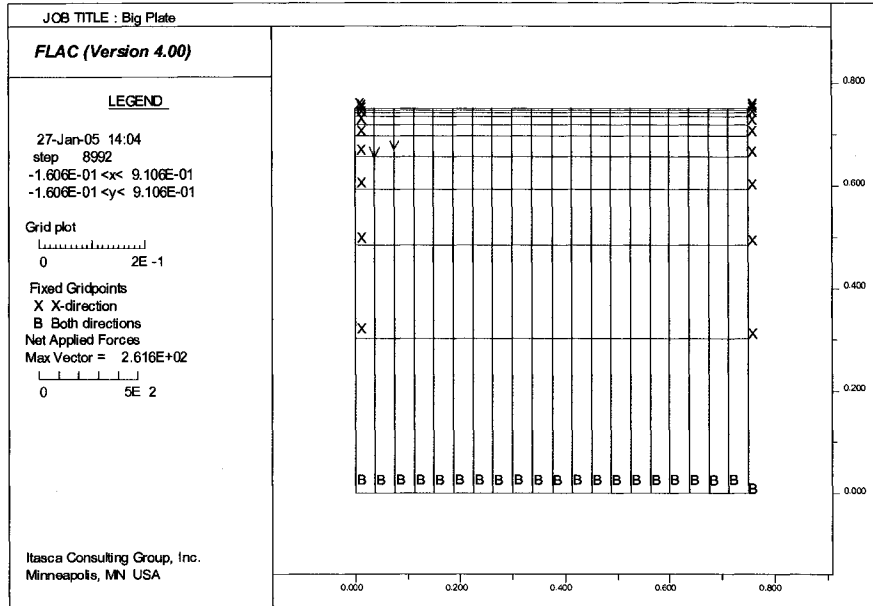


No.13

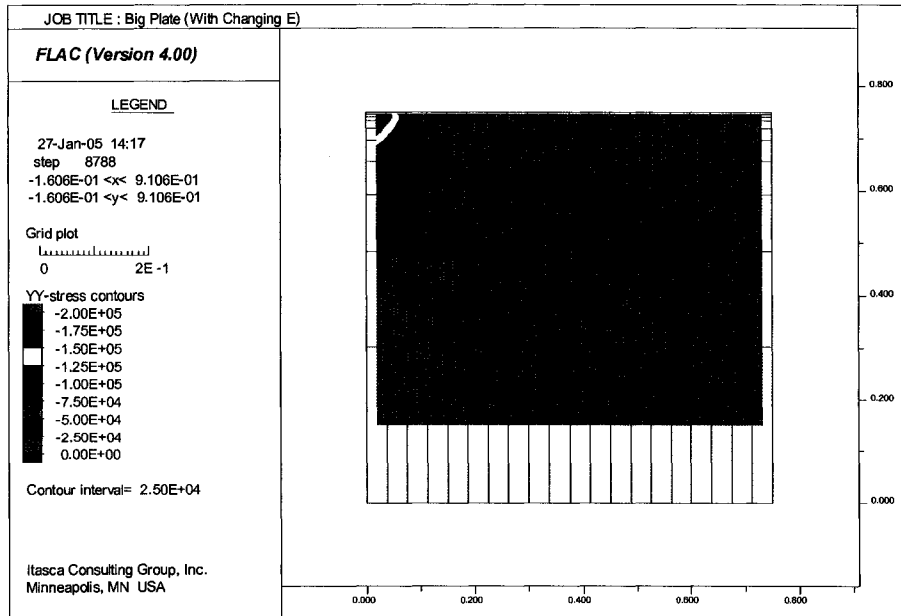


# Appendix 4 – Numerical Modeling Result for Large and Small Plates

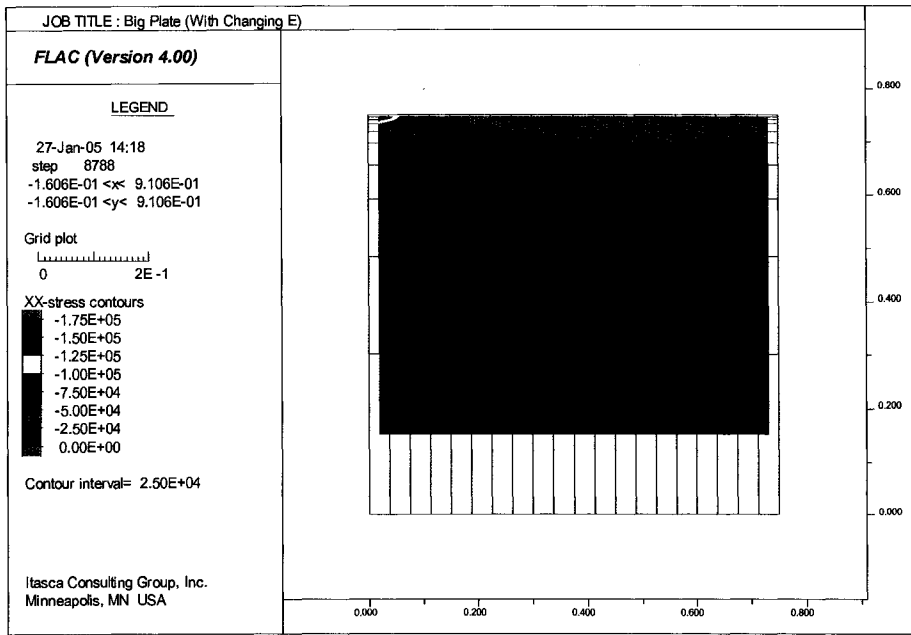
Large Plate



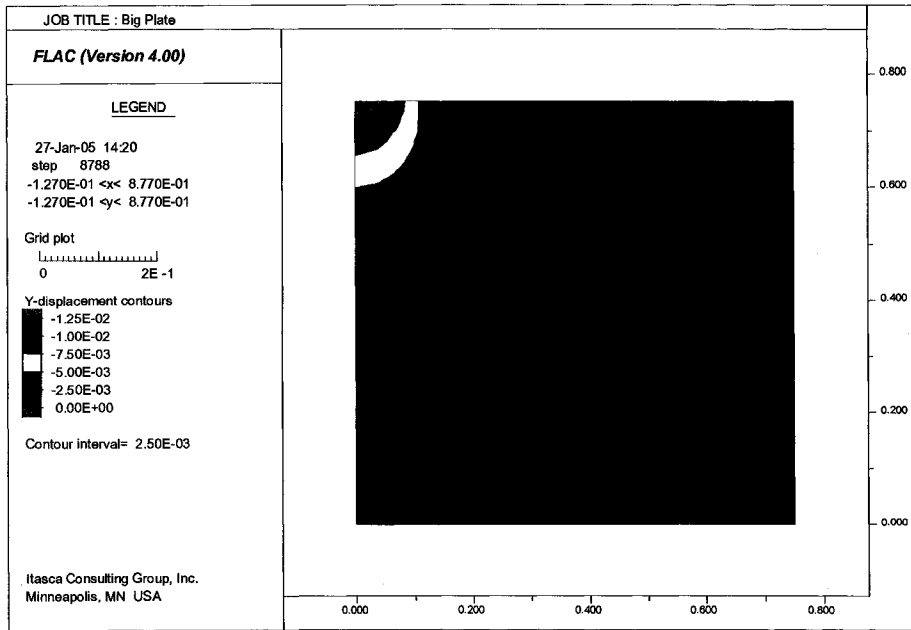
Boundary condition and applied load



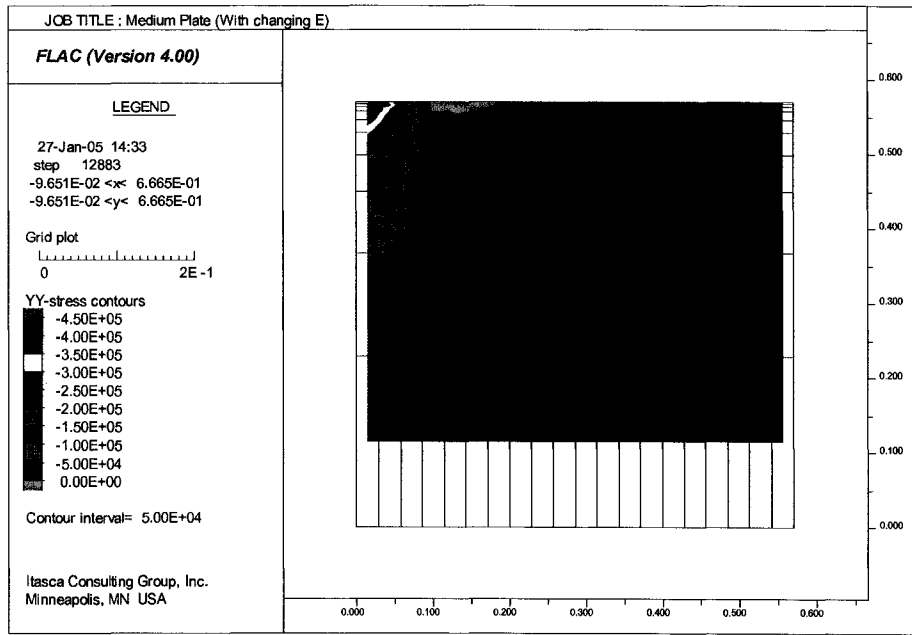
Vertical stress large plate



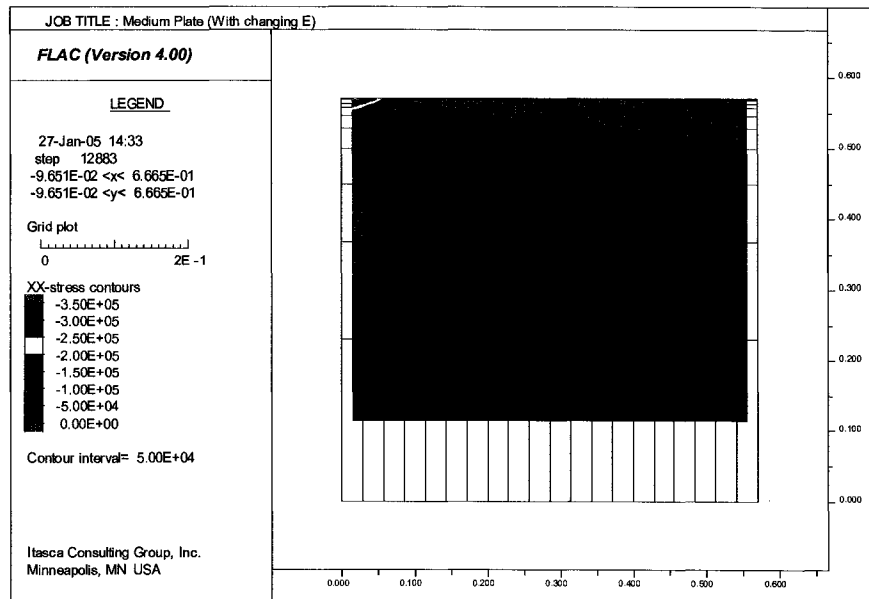
Horizontal stress large plate



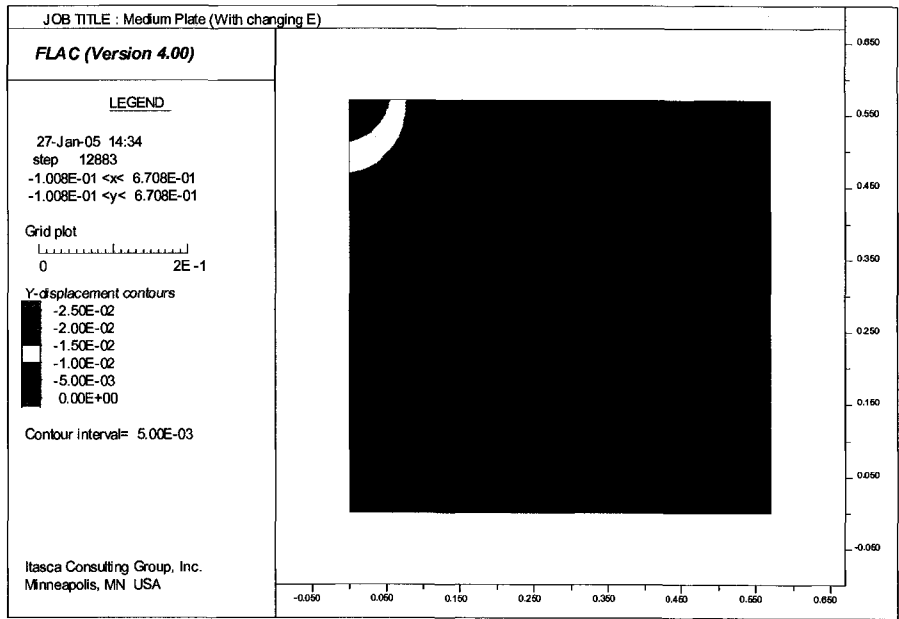
Vertical deformation large plate



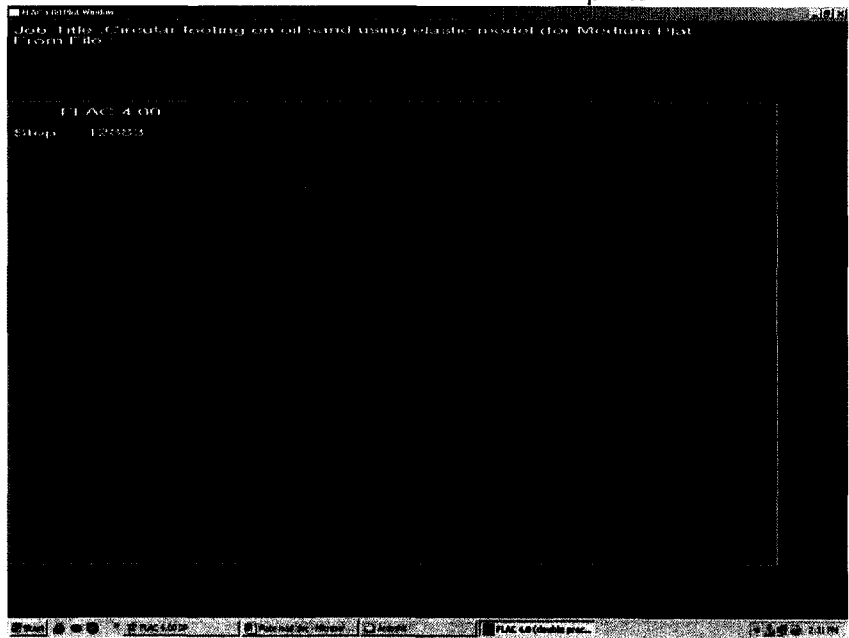
Vertical stress medium plate



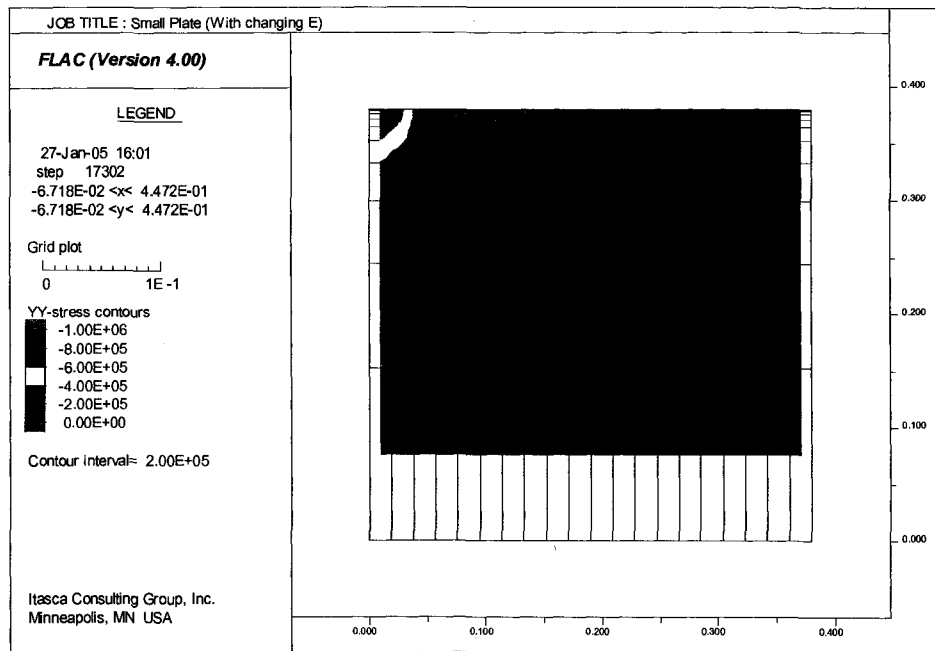
Horizontal stress medium plate



Vertical deformation medium plate



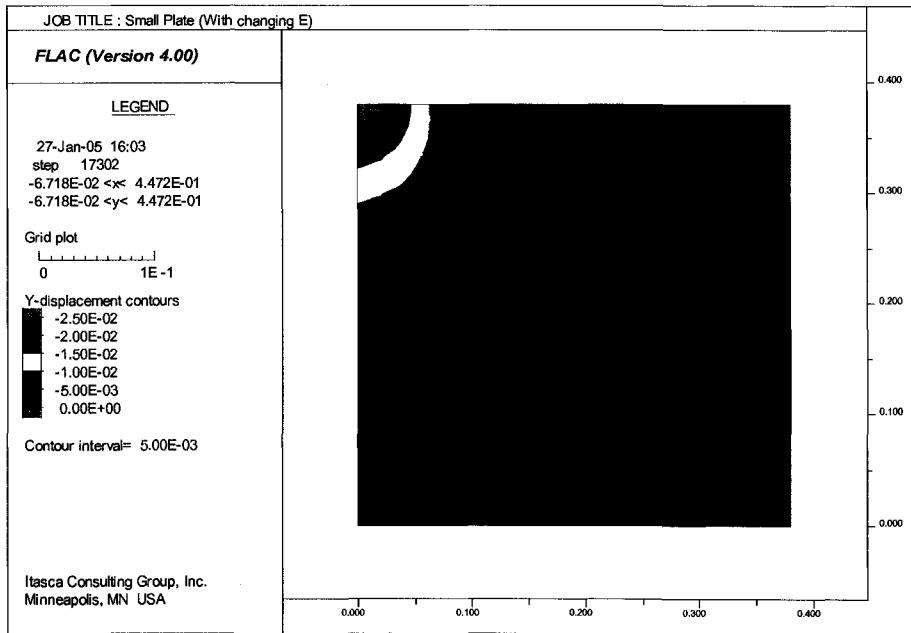
Unbalanced force medium plate



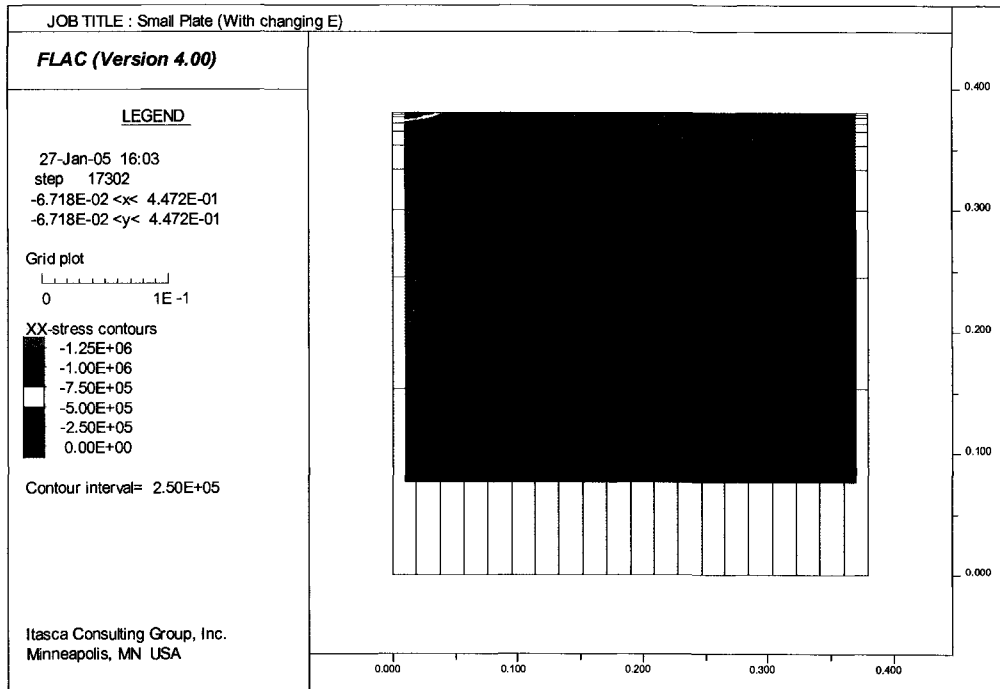
Vertical stress small plate



Unbalanced force small plate

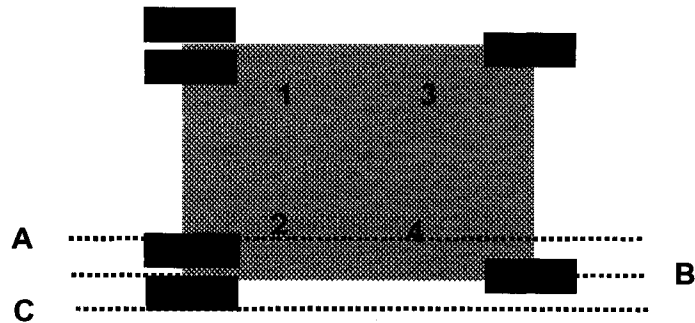


Vertical displacement small plate

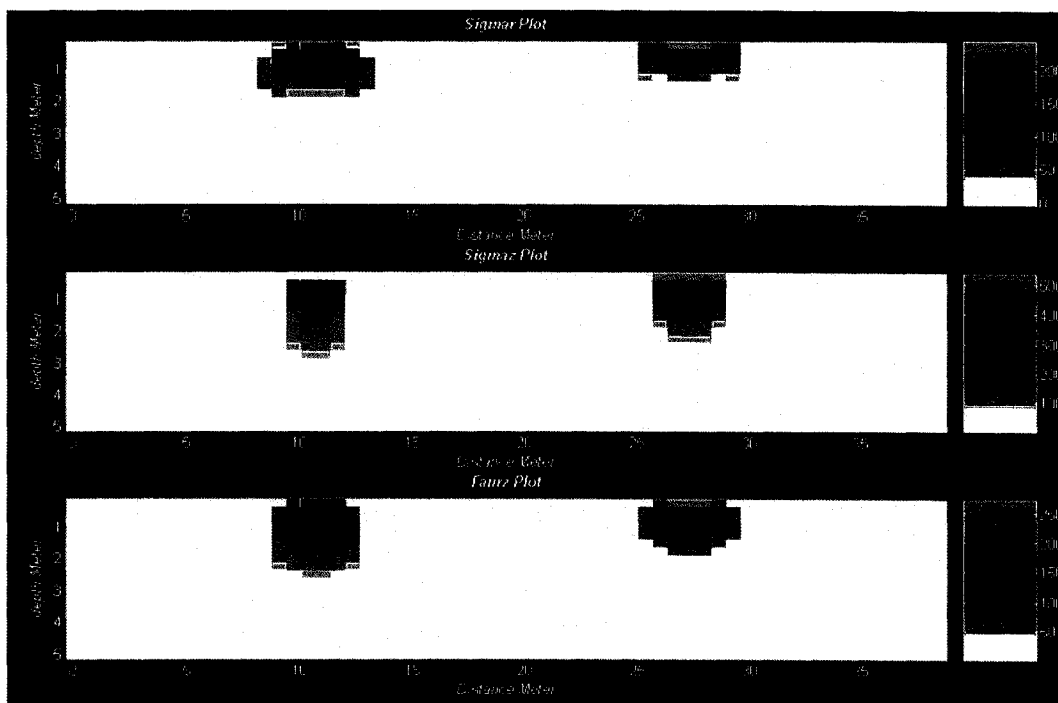


Horizontal stress small plate

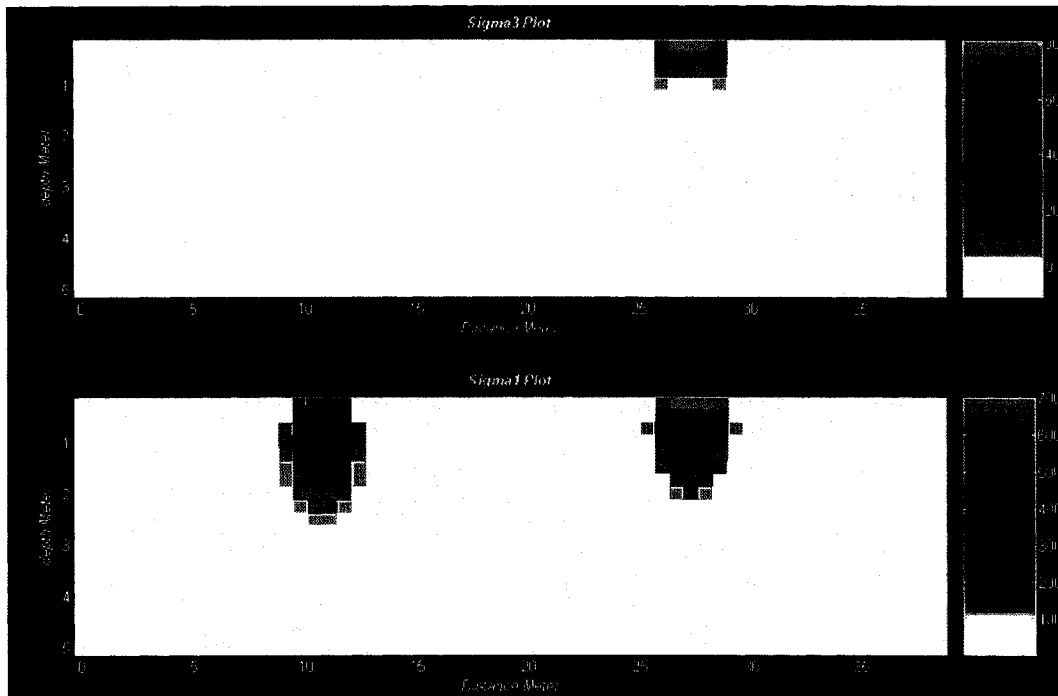
## Appendix 5 – Numerical Modeling Using Boussinesq's Equation for Truck



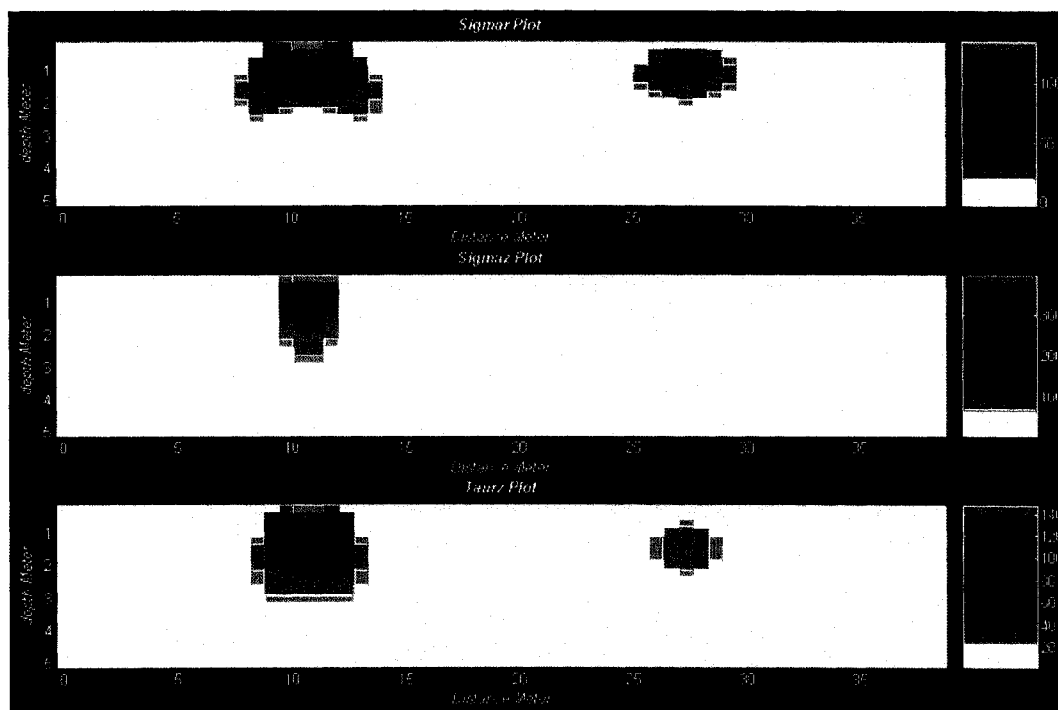
Sections of stress that calculated



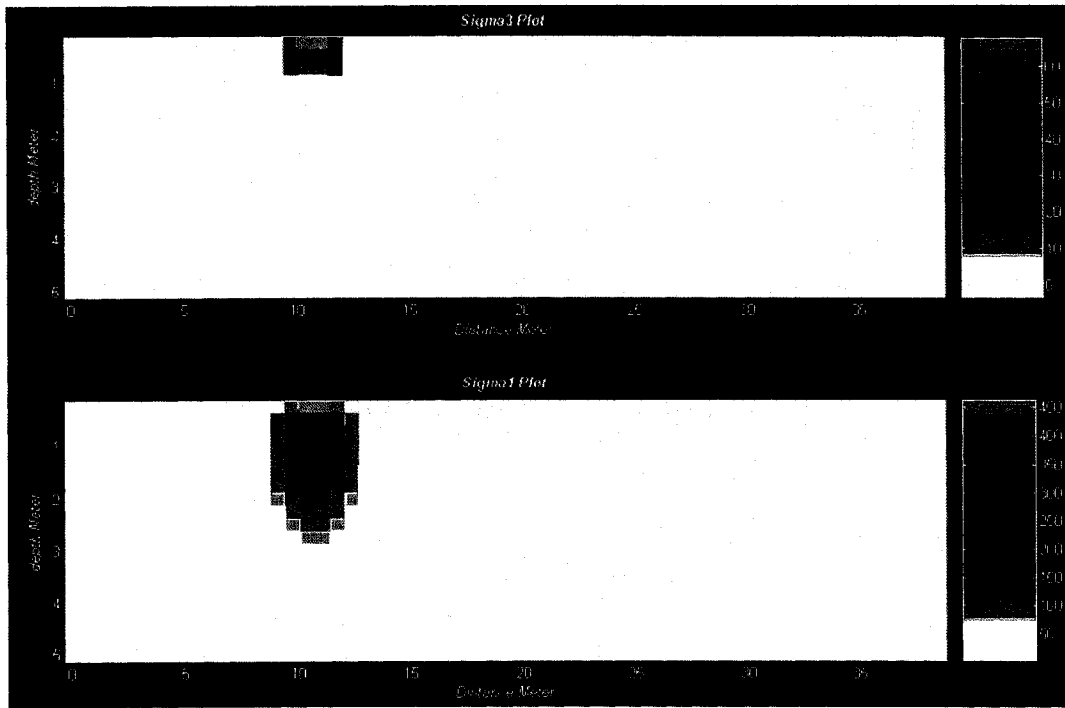
Vertical and horizontal stresses for section B



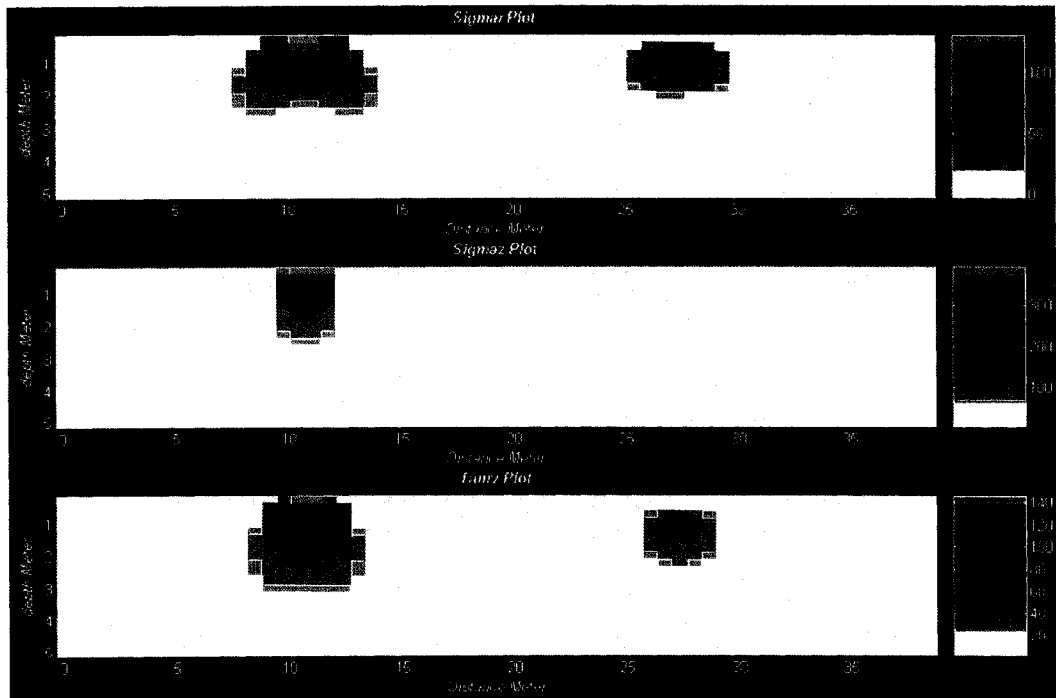
Principal stresses for section B



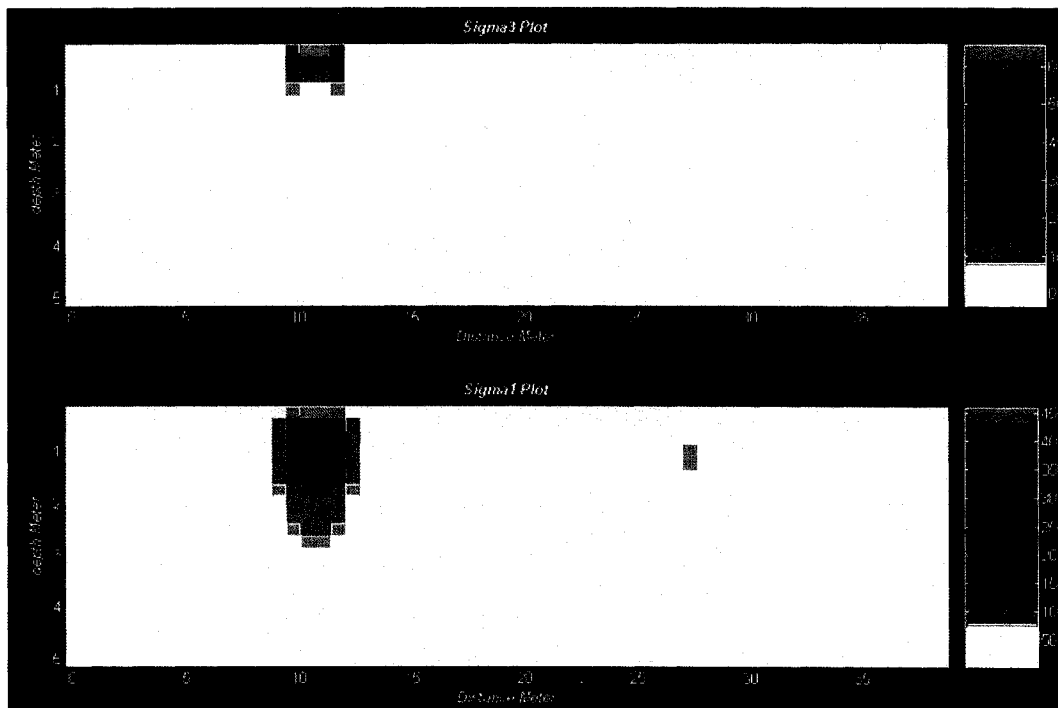
Vertical and horizontal stresses for section C



Principal stresses for section C



Vertical and horizontal stresses for section A



Principal stresses for section A

#### MATLAB code for Truck case

```

%This program is for calculating ground stress based on point load based on
Craig 1974
%this is simple case of one load moving in ground surface
%v is Poisson ratio for oil sand is 0.3
%considering the tire is square and width and length are 1.18m
%Total load under tire q=1019.478 KN
%Max z=5 metres
%Max r=50 metres

clear all
L=1.18 ; %length of tire
D=1.18 ; %width of tire
wheelbase=8.38; %from front tire to rear tire
widthrear=2.944; %width of dual tire in rear
gaprear=0.584; %gap between dual tire
q1=1019.478; %stress for one tire
lmesh=30 ; %divide the length
wmesh=20; %divided the width
frontdist=15
reardist=15
section=20 %Max must be equal to wmesh
smallsquaretire=wheelbase*widthrear/(lmesh*wmesh);
samlltotalsquare=wheelbase*widthrear;
stress=q1/(L*D);
totalstress=zeros(lmesh,wmesh);

```

```

for o=1:lmesh,
    for p=1:wmesh
        if (wheelbase*o/lmesh<=L & p*widthrear/wmesh<=L ) |
            (wheelbase*o/lmesh<=L & widthrear*p/wmesh>=(L+gaprear)) |
            (wheelbase*o/lmesh>=(wheelbase-L) & widthrear*p/wmesh>=((widthrear-L)/2) &
            widthrear*p/wmesh<=(L+(widthrear-L)/2))
                totalstress(o,p)=stress;
            else
                totalstress(o,p)=0;
            end
        end
    end
end

smallforce=totalstress*smallsquaretire ; %calculate force in small square under
tire (tire pressure)
smallforce=[zeros(frontdist,wmesh);smallforce;zeros(reardist,wmesh)]

ldim=[linspace(0,wheelbase+frontdist+reardist,size(smallforce,1))]; %X
coordinate of pressure
ddim=[linspace(0,widthrear,size(smallforce,2))]; %Y Coordinate of pressure

Z=[0.25:0.25:5]; %depth of calculation
R=[0:ldim(2)-ldim(1):reardist+frontdist+wheelbase]; %length of calculation
v=0.31; % Poisson's ratio
n=size(smallforce,1);
m=size(Z,2);
sigmaz=zeros(n,m);
sigmar=zeros(n,m);
taurz=zeros(n,m);
for i=1:n,
    for j=1:m,
        z=Z(1,j);
        for k=1:size(smallforce,1),
            for h=1:size(smallforce,2),
                r=sqrt((ldim(1,i)-ldim(1,k))^2+(ddim(1,section)-ddim(1,h))^2);
                q=smallforce(k,h);
                sigmaz(i,j)=(3*q*(((1/(1+(r/z)^2))^2.5)/(2*pi*z^2)))+sigmaz(i,j);
                sigmar(i,j)=(q*(((3*r^2*z)/(r^2+z^2)^2.5)-((1-
                2*v)/(r^2+z^2+z*(r^2+z^2)^0.5)))/(2*pi))+sigmar(i,j);
                taurz(i,j)=(3*q*(r*z^2/(r^2+z^2)^2.5)/(2*pi))+taurz(i,j);
            end
        end
    end

    sigma1(i,j)=0.5*(sigmaz(i,j)+sigmar(i,j))+sqrt((0.5*(sigmaz(i,j)-
    sigmar(i,j)))^2+taurz(i,j)^2);
    sigma3(i,j)=0.5*(sigmaz(i,j)+sigmar(i,j))-sqrt((0.5*(sigmaz(i,j)-
    sigmar(i,j)))^2+taurz(i,j)^2);
    teta(i,j)=180*(0.5*atan(2*taurz(i,j)/(sigmaz(i,j)-sigmar(i,j))))/pi;
end
end

```

```

subplot (3,1,1)
imagesc(R,Z,sigmar')
xlabel('Distance Metre'); ylabel('depth Metre')
title('Sigmar Plot'), colorbar
subplot (3,1,2)
imagesc(R,Z,sigmaz')
xlabel('Distance Metre'); ylabel('depth Metre')
title('Sigmaz Plot'), colorbar
subplot (3,1,3)
imagesc(R,Z,taurz')
xlabel('Distance Metre'); ylabel('depth Metre')
title('Taurz Plot'), colorbar

figure
subplot (2,1,1)
imagesc(R,Z,sigma3')
xlabel('Distance Metre'); ylabel('depth Metre')
title('Sigma3 Plot'), colorbar
subplot (2,1,2)
imagesc(R,Z,sigma1')
xlabel('Distance Metre'); ylabel('depth Metre')
title('Sigma1 Plot'), colorbar

```

#### **MATLAB code for Shovel case**

```

%This program is for calculating ground stress based on point load based on
Craig 1974
%this is simple case of the constant area
%v is position ratio for oil sand is 0.3
%considering the track is rectangular and width 5.4m length are 11.58 m
%overall crawler

clear all
clc

L=11.58 ; %Length of Crawler
D=2.7 ; %width of Crawler

q1=13256; %Total Force of Shovel
lmesh=40 ; %divide the length
wmesh=40 ; %divided the width
widthrear=3.735; %width of the two crawler from each other
DT=D*2+widthrear*2;
smallsquare=L*DT/(lmesh*wmesh);

frontdist=15;
reardist=15;

```

```

%section=3; %Max must be equal to wmesh (LS)
section=20; %Max must be equal to wmesh (MID)
%section=37; %Max must be equal to wmesh (NLS)
stress=q1/(L*2*D);
totalforce=zeros(lmesh,wmesh);

FNLSP=stress*2.14;
FFNLSP=FNLSP*smallsquare;
BNLSP=stress*0.23;
FBNLSP=BNLSP*smallsquare;
% Front Pressure & Back for LS
FLSP=stress*2.14;
FFLSP=FLSP*smallsquare;
BLSP=stress*0.23;
FBLSP=BLSP*smallsquare;
LS1=abs((FFNLSP-FBNLSP)/(L));
LS2=abs((FFLSP-FBLSP)/(L));
WS1=abs((FFNLSP-FFLSP)/(DT));
WS2=abs((FBNLSP-FBLSP)/(DT));

for p=1:wmesh

    if (DT*p/wmesh>D & DT*p/wmesh<=(2*widthrear+D) |
DT*p/wmesh>=(2*widthrear+2*D))
        totalforce(p,:)=zeros(1,lmesh);
    else
        FNEWLF=(p/DT)*WS1*FFNLSP+FFNLSP;
        FNEWLB=(p/DT)*WS2*FBNLSP+FBNLSP;
        totalforce(p,:)=[linspace(FNEWLB,FNEWLF,lmesh)];
    end

end

Newtotalforce=[zeros(wmesh,frontdist),totalforce,zeros(wmesh,reardist)];
totalpressure=Newtotalforce/smallsquare ; %calcualte presuure in small squire
under track

ldim=[linspace(0,L+frontdist+reardist,size(Newtotalforce,2))]; %X coordinate of
pressure
ddim=[linspace(0,DT,size(Newtotalforce,1))]; %Y Coordinate of
pressure

Z=[0.25:0.25:5]; %depth of calculation
R=[0:ldim(2)-ldim(1):reardist+frontdist+L]; %length of calculation
v=0.25; %pession ratio

n=size(Newtotalforce,2);
m=size(Z,2);

sigmaz=zeros(n,m);

```

```

sigmar=zeros(n,m);
taurz=zeros(n,m);

for i=1:n,
    for j=1:m,
        z=Z(1,j);
        for k=1:size(Newtotalforce,2),
            for h=1:size(Newtotalforce,1),
                r=sqrt((ldim(1,i)-ldim(1,k))^2+(ddim(1,section)-ddim(1,h))^2);
                q=Newtotalforce(h,k);
                sigmaz(i,j)=(3*q*(((1/(1+(r/z)^2))^2.5)/(2*pi*z^2)))+sigmaz(i,j);
                sigmar(i,j)=(q*(((3*r^2*z)/(r^2+z^2)^2.5)-((1-
2*v)/(r^2+z^2+z*(r^2+z^2)^0.5)))/(2*pi))+sigmar(i,j);
                taurz(i,j)=(3*q*(r*z^2/(r^2+z^2)^2.5)/(2*pi))+taurz(i,j);
            end
        end
        sigma1(i,j)=0.5*(sigmaz(i,j)+sigmar(i,j))+sqrt((0.5*(sigmaz(i,j)-
sigmar(i,j)))^2+taurz(i,j)^2);
        sigma3(i,j)=0.5*(sigmaz(i,j)+sigmar(i,j))-sqrt((0.5*(sigmaz(i,j)-
sigmar(i,j)))^2+taurz(i,j)^2);
        teta(i,j)=180*(0.5*atan(2*taurz(i,j)/(sigmaz(i,j)-sigmar(i,j))))/pi;
    end
end

```

```

subplot (3,1,1)
imagesc(R,Z,sigmar')
xlabel('Distance Metre','fontangle','italic'); ylabel('depth Metre','fontangle','italic')
title('Sigmar Plot','fontangle','italic','FontWeight','bold'), colorbar

```

```

subplot (3,1,2)
imagesc(R,Z,sigmaz')
xlabel('Distance Metre','fontangle','italic'); ylabel('depth Metre','fontangle','italic')
title('Sigmaz Plot','fontangle','italic','FontWeight','bold'), colorbar

```

```

subplot (3,1,3)
imagesc(R,Z,taurz')
xlabel('Distance Metre','fontangle','italic'); ylabel('depth Metre','fontangle','italic')
title('Taurz Plot','fontangle','italic','FontWeight','bold'), colorbar

```

figure

```

subplot (2,1,1)
imagesc(R,Z,sigma3')
xlabel('Distance Metre','fontangle','italic'); ylabel('depth Metre','fontangle','italic')
title('Sigma3 Plot','fontangle','italic','FontWeight','bold'), colorbar

```

```

subplot (2,1,2)
imagesc(R,Z,sigma1')
xlabel('Distance Metre','fontangle','italic'); ylabel('depth Metre','fontangle','italic')
title('Sigma1 Plot','fontangle','italic','FontWeight','bold'), colorbar

```

## MATLAB code for field plate load tests

```
% This program is for stress distribution under Circular plate

clear all

bsize=1; %Unit of the each bin for start
r=15; %Number of the bin in the circular plate

cir=zeros(r/bsize,r/bsize);

cc=0; %To count how many bin in the circular plate that has load

for i=1:r/bsize,

    x=sqrt(r^2-i^2); % Find the x distance
    bn=x/1; % How many blocks need in x direction

    for j=1:bn,

        cir(i,j)=1;
        cc=cc+1;
    end

end

tforce=5; % Force in each small square in the circular plate in KN

cir=[flipud(cir);cir];
cir=[fliplr(cir) cir];

rr=5.87*0.0254; %Diameter of the circular plate 5.87" , 4.5" , 3"

[m,n]=size(cir);

force=tforce/(4*cc);

cir=force*cir;

Z=[0.025:0.025:0.5]; %depth of calculation

R=10*r; %length of calculation two times the circular Diameter
v=0.31; %poission ratio

[m,n]=size(cir);
mright=zeros(R/2,n);
mleft=mright;
```

```

mbig=[mleft;cir;mright];

[m1,n1]=size(mbig);    % Building bigger Area for Force
mtop=zeros(m1,R/2);
mbot=mtop;

mbig=[mbot mbig mtop];    % Building bigger Area for Force
[m1,n1]=size(mbig);

sigmaz=zeros(size(Z,2),m1);    % Make the Sigmas equal to zero
sigmar=zeros(size(Z,2),m1);    % Make the Sigmas equal to zero
taurz=zeros(size(Z,2),m1);    % Make the Sigmas equal to zero

for k=1:m1,

    for l=1:size(Z,2),

        for i=1:m1,

            for j=1:n1,

                z=Z(1,l);
                %r=sqrt((k-i)^2+((n1/2)-j)^2)*rr/m;
                r=sqrt(((m1/2)-i)^2+(k-j)^2)*rr/m;

                sigmaz(l,k)=(3*mbig(i,j)*(((1/(1+(r/z)^2))^2.5)/(2*pi*z^2)))+sigmaz(l,k);
                sigmar(l,k)=(mbig(i,j)*(((3*r^2*z)/(r^2+z^2)^2.5)-((1-2*v)/(r^2+z^2+z*(r^2+z^2)^0.5)))/(2*pi))+sigmar(l,k);

                taurz(l,k)=(3*mbig(i,j)*(r*z^2/(r^2+z^2)^2.5)/(2*pi))+taurz(l,k);

            end

        end

        sigma1(l,k)=0.5*(sigmaz(l,k)+sigmar(l,k))+sqrt((0.5*(sigmaz(l,k)-sigmar(l,k)))^2+taurz(l,k)^2);
        sigma3(l,k)=0.5*(sigmaz(l,k)+sigmar(l,k))-sqrt((0.5*(sigmaz(l,k)-sigmar(l,k)))^2+taurz(l,k)^2);
        teta(l,k)=180*(0.5*atan(2*taurz(l,k)/(sigmaz(l,k)-sigmar(l,k))))/pi;

    end

end

R=(linspace(-m1/2,m1/2,m1))*rr/m;

```

```
subplot (3,1,1)
imagesc(R,Z,sigmar)
xlabel('Distance Metre'); ylabel('depth Metre')
title('Sigmar Plot'), colorbar
```

```
subplot (3,1,2)
imagesc(R,Z,sigmaz)
xlabel('Distance Metre'); ylabel('depth Metre')
title('Sigmaz Plot'), colorbar
```

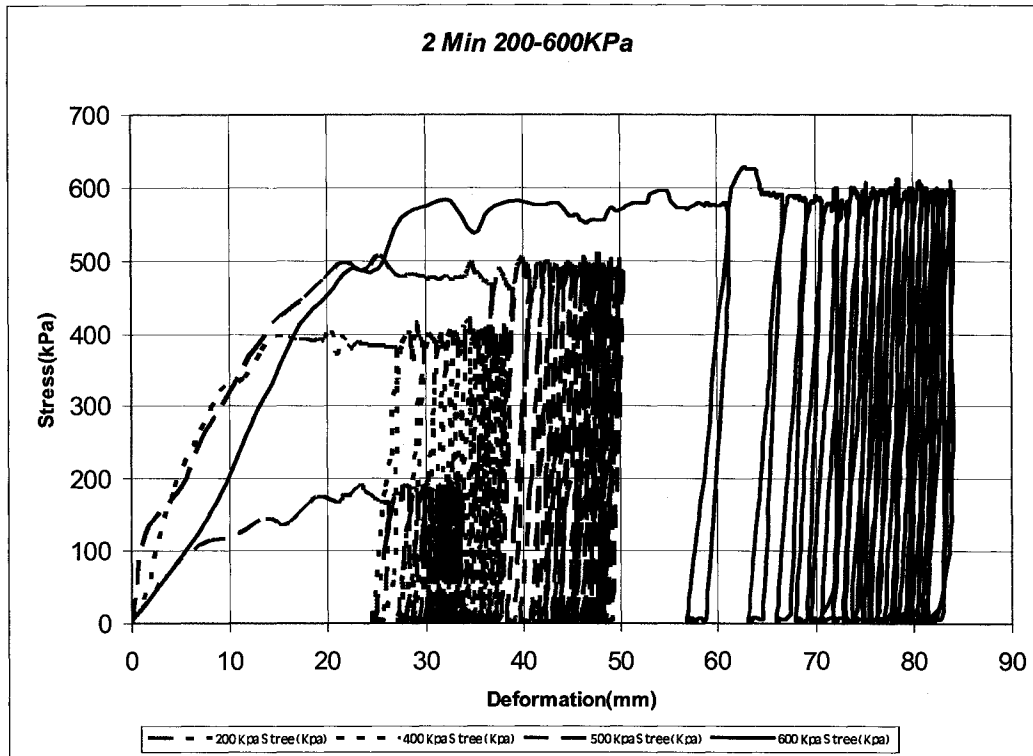
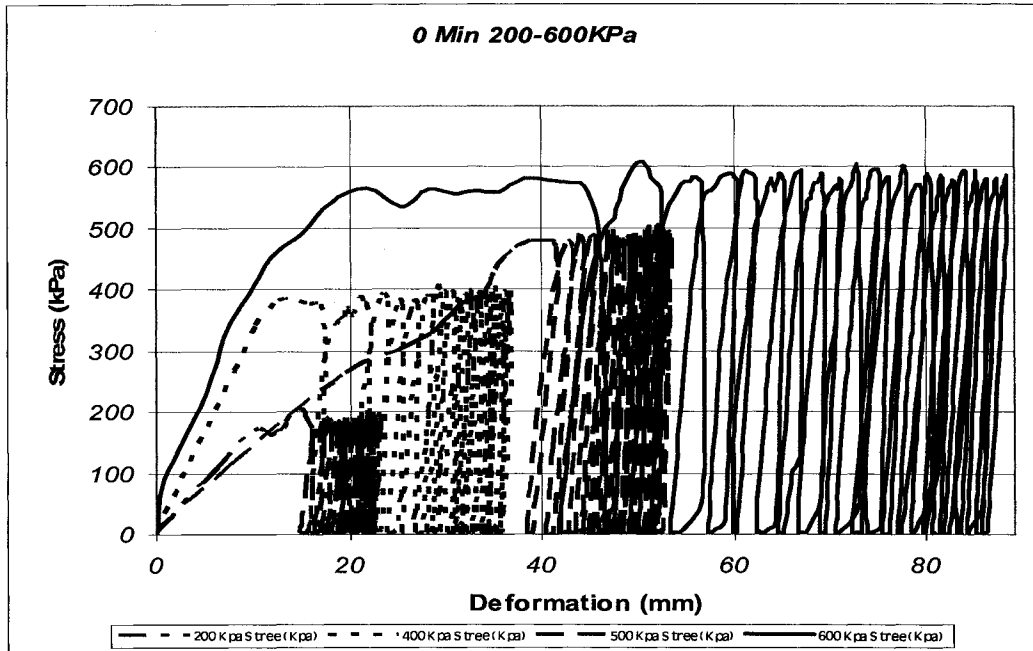
```
subplot (3,1,3)
imagesc(R,Z,taurz)
xlabel('Distance Metre'); ylabel('depth Metre')
title('Taurz Plot'), colorbar
```

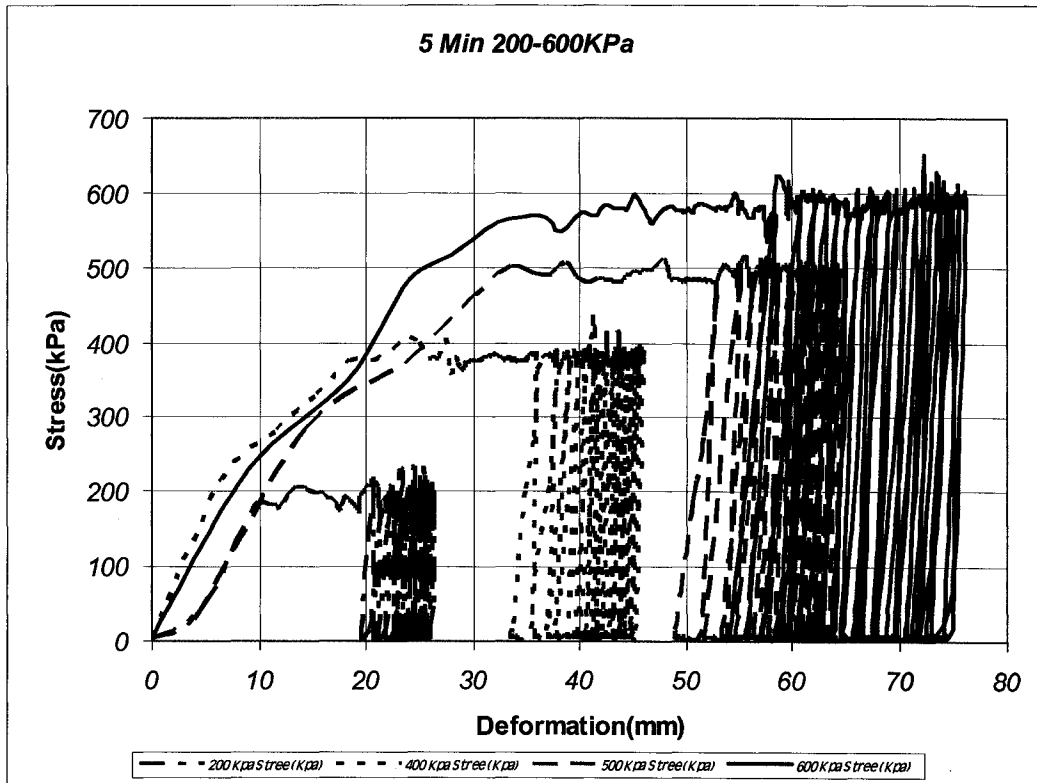
```
figure
```

```
subplot (2,1,1)
imagesc(R,Z,sigma3)
xlabel('Distance Metre'); ylabel('depth Metre')
title('Sigma3 Plot'), colorbar
```

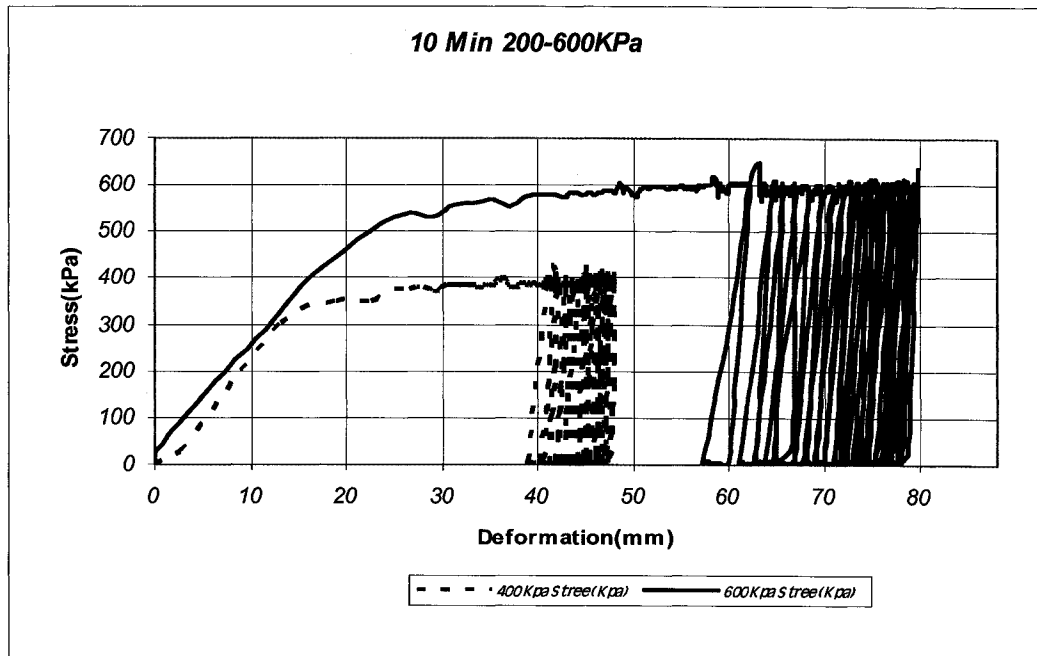
```
subplot (2,1,2)
imagesc(R,Z,sigma1)
xlabel('Distance Metre'); ylabel('depth Metre')
title('Sigma1 Plot'), colorbar
```

# Appendix 6 – Large-Scale Laboratory Plate Load Test



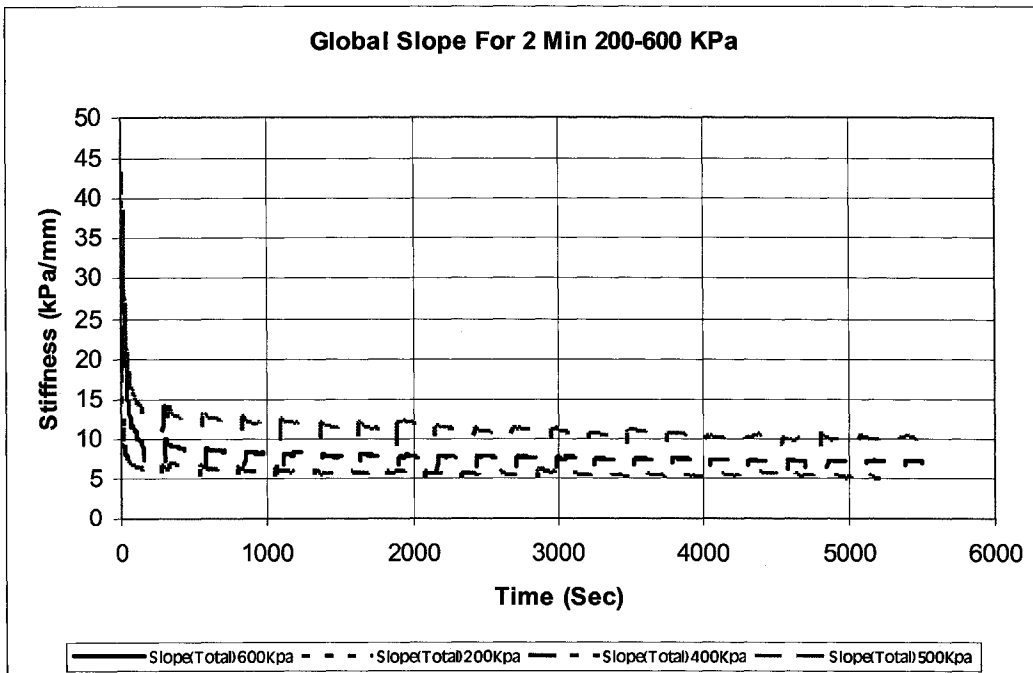
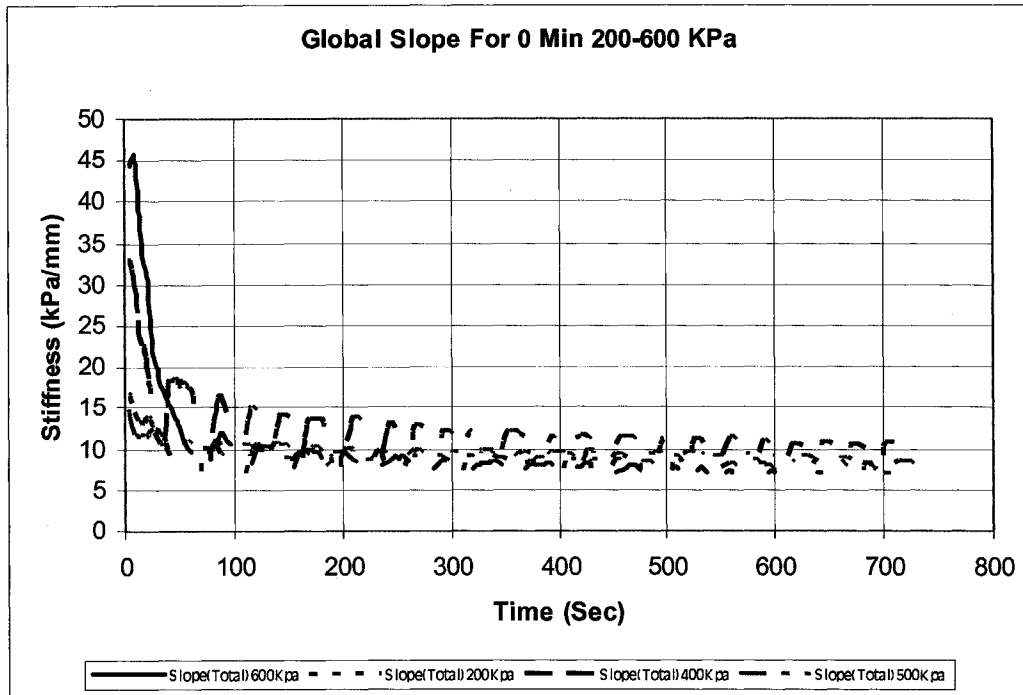


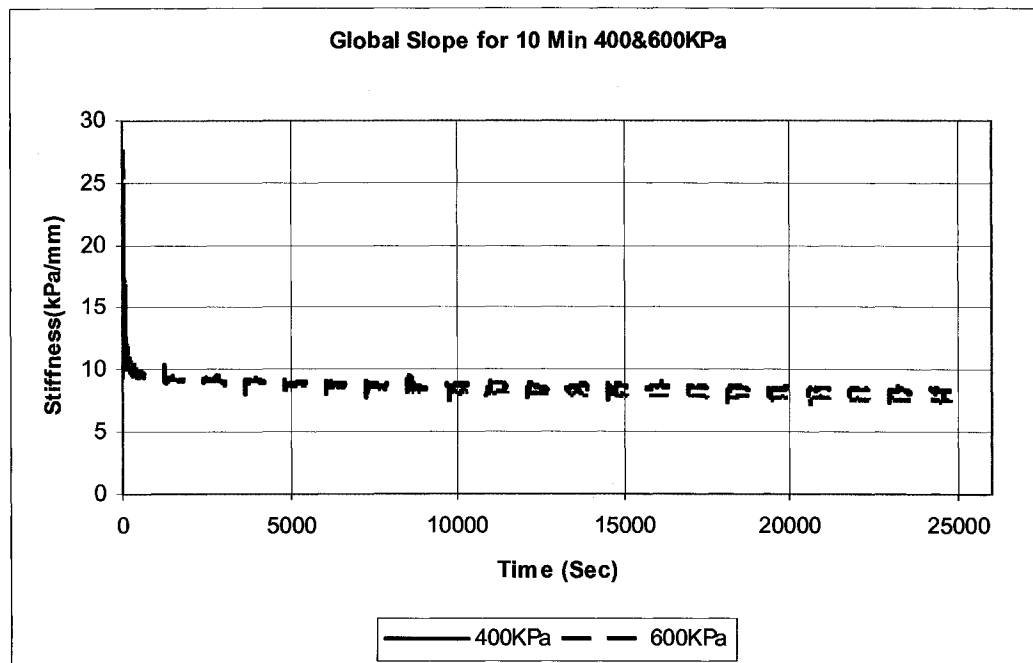
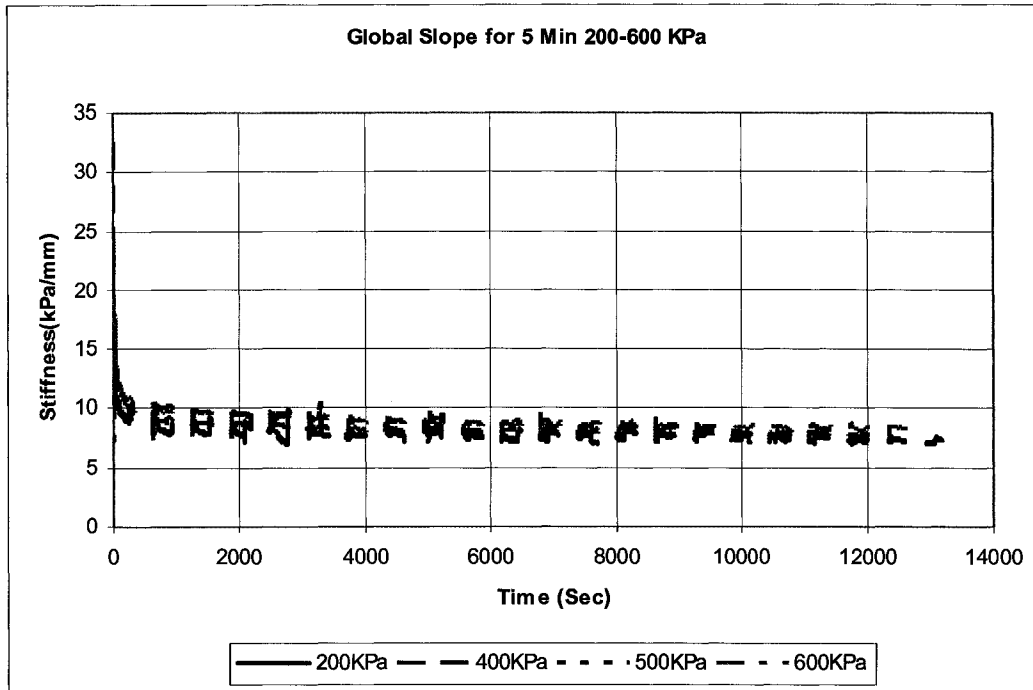
5 Min. duration



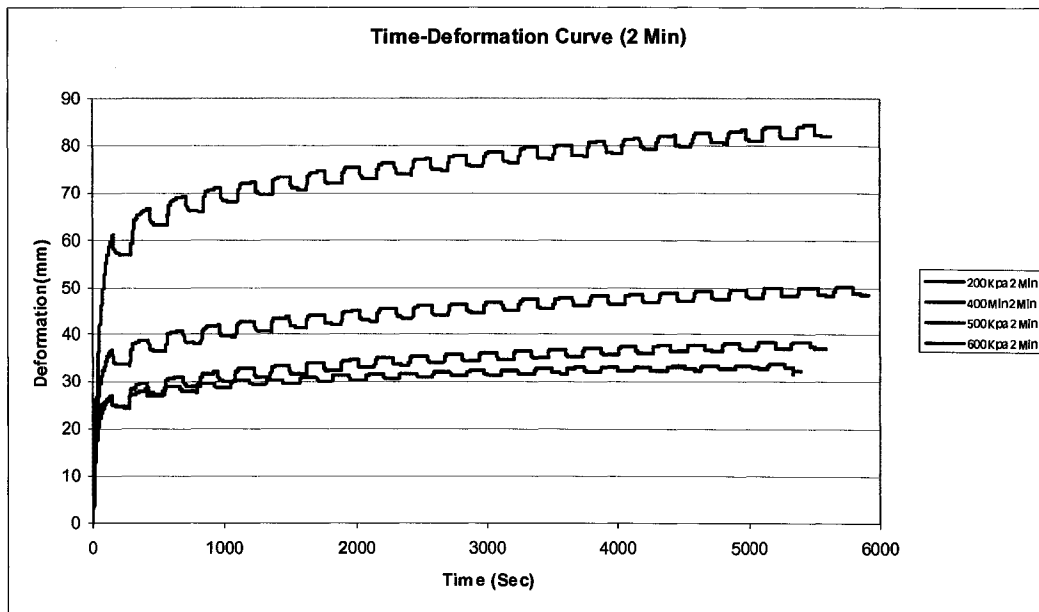
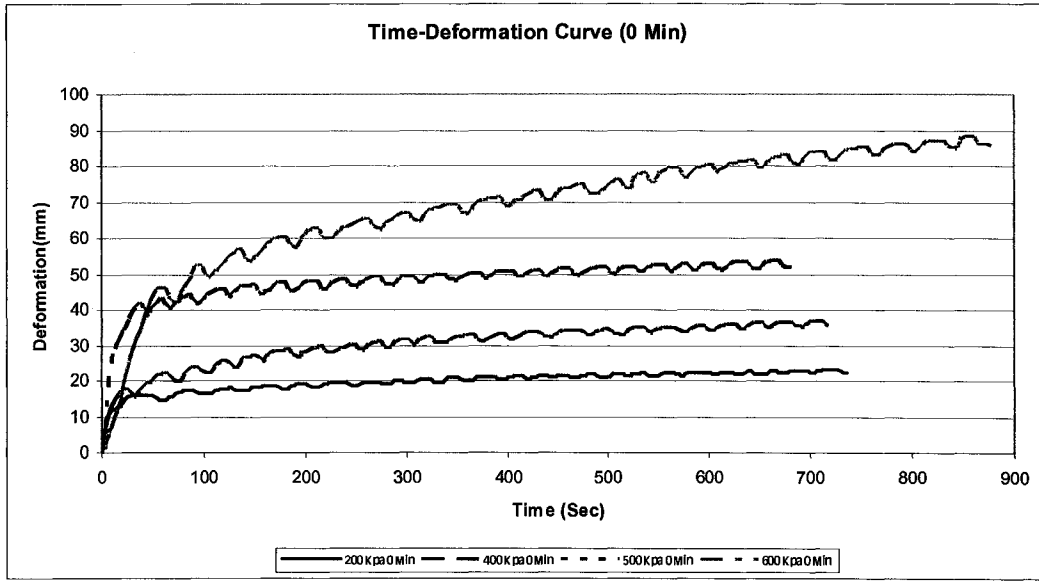
10 Min. duration

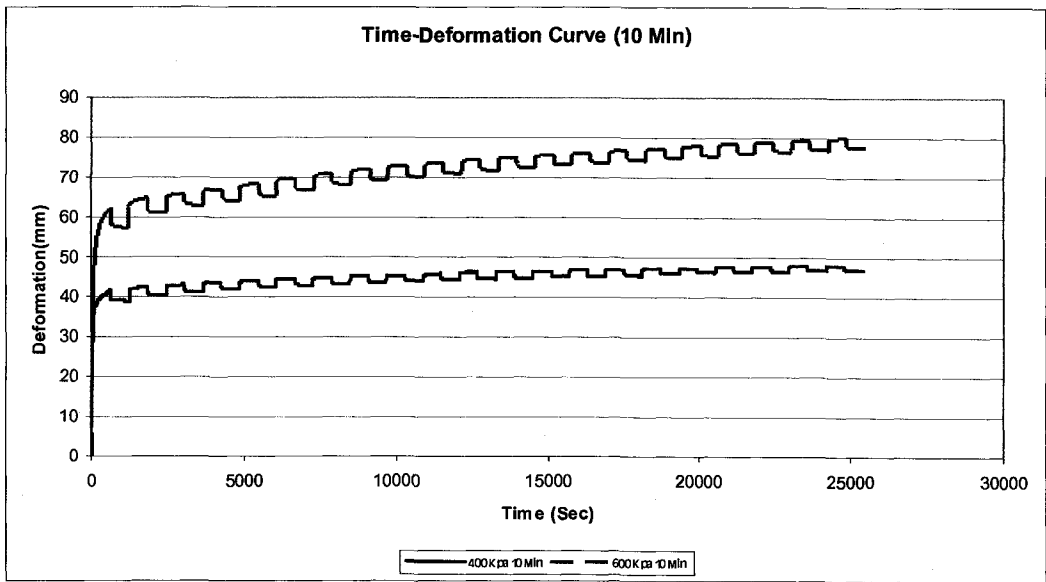
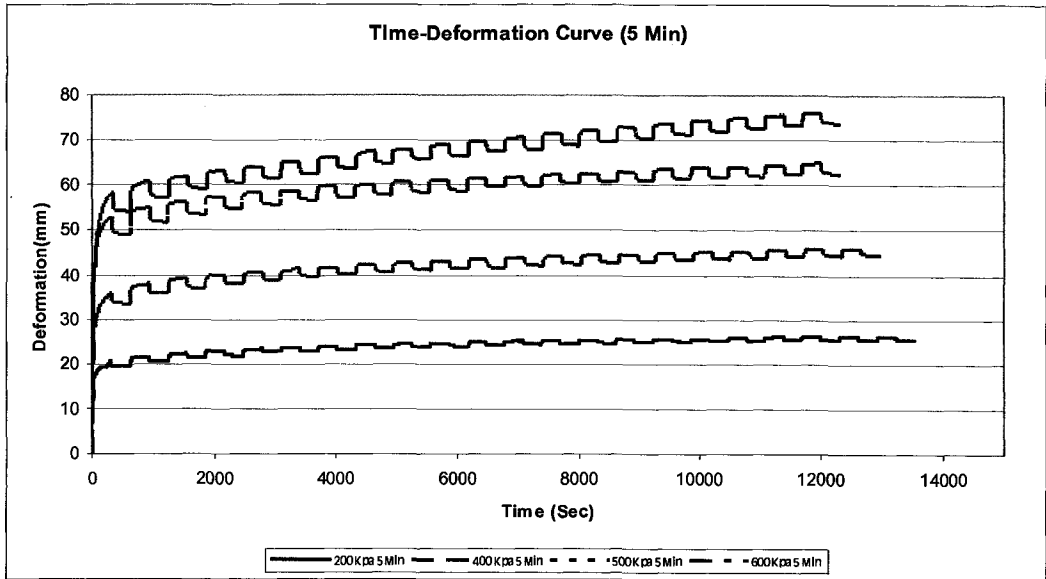
Global slope of pressure stiffness 200-600 kPa with different waiting time





### Time-Deformation curves for 200-600 kPa



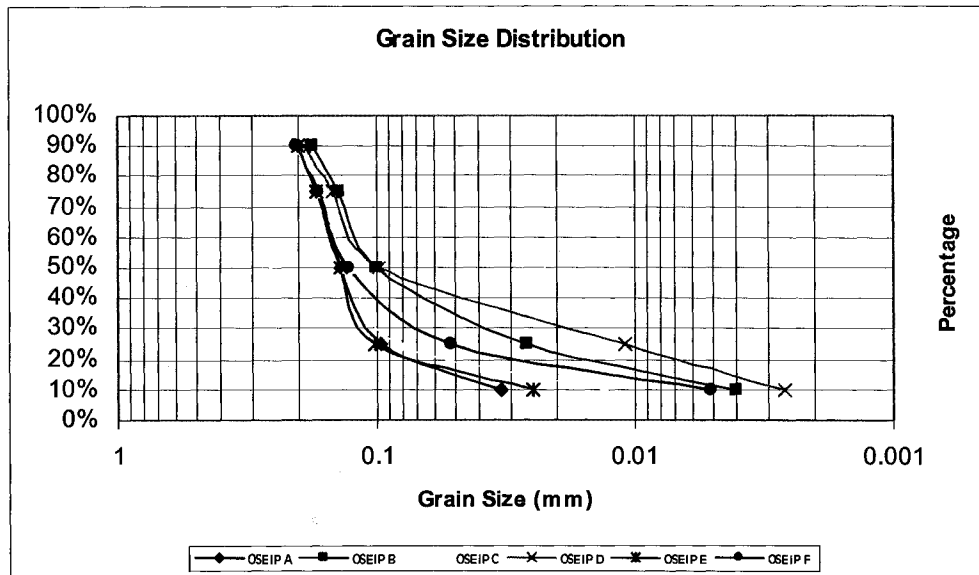


# Appendix 7 – P&H 4100 Underfoot BOSS Test

## Results

OWS of field grab samples

Sample Description	OS&C					Percentages				
	MOISS	MOISS	MOISS	% SOL	SAMPLE	MOISS	MOISS	MOISS	MOISS	MOISS
OSEIP A	100.36	14.8	1.61	83.95	96.001	33.17	97.07	137.8	172.1	204.4
OSEIP B	100.45	10.91	3.14	86.4	101.947	4	26	99.73	141.2	175.8
OSEIP C	99.74	12.91	1.62	85.21	95.426	13.06	82.33	127.4	169	207.6
OSEIP D	100.66	8.82	4.07	87.77	98.249	2.63	10.97	97.38	148	189.9
OSEIP E	100.28	15.14	0.75	84.39	106.463	24.98	101.5	137.1	169.8	201.3
OSEIP F	100.14	13.57	1.31	85.27	99.371	5.12	52.12	128.3	168.3	204
<b>Average</b>	<b>100.3</b>	<b>12.7</b>	<b>2.1</b>	<b>85.5</b>	<b>99.6</b>	<b>13.8</b>	<b>61.7</b>	<b>121.3</b>	<b>161.4</b>	<b>197.2</b>
<b>STD</b>	<b>0.3</b>	<b>2.4</b>	<b>1.3</b>	<b>1.4</b>	<b>4.1</b>	<b>12.6</b>	<b>37.9</b>	<b>18.1</b>	<b>13.3</b>	<b>12.1</b>

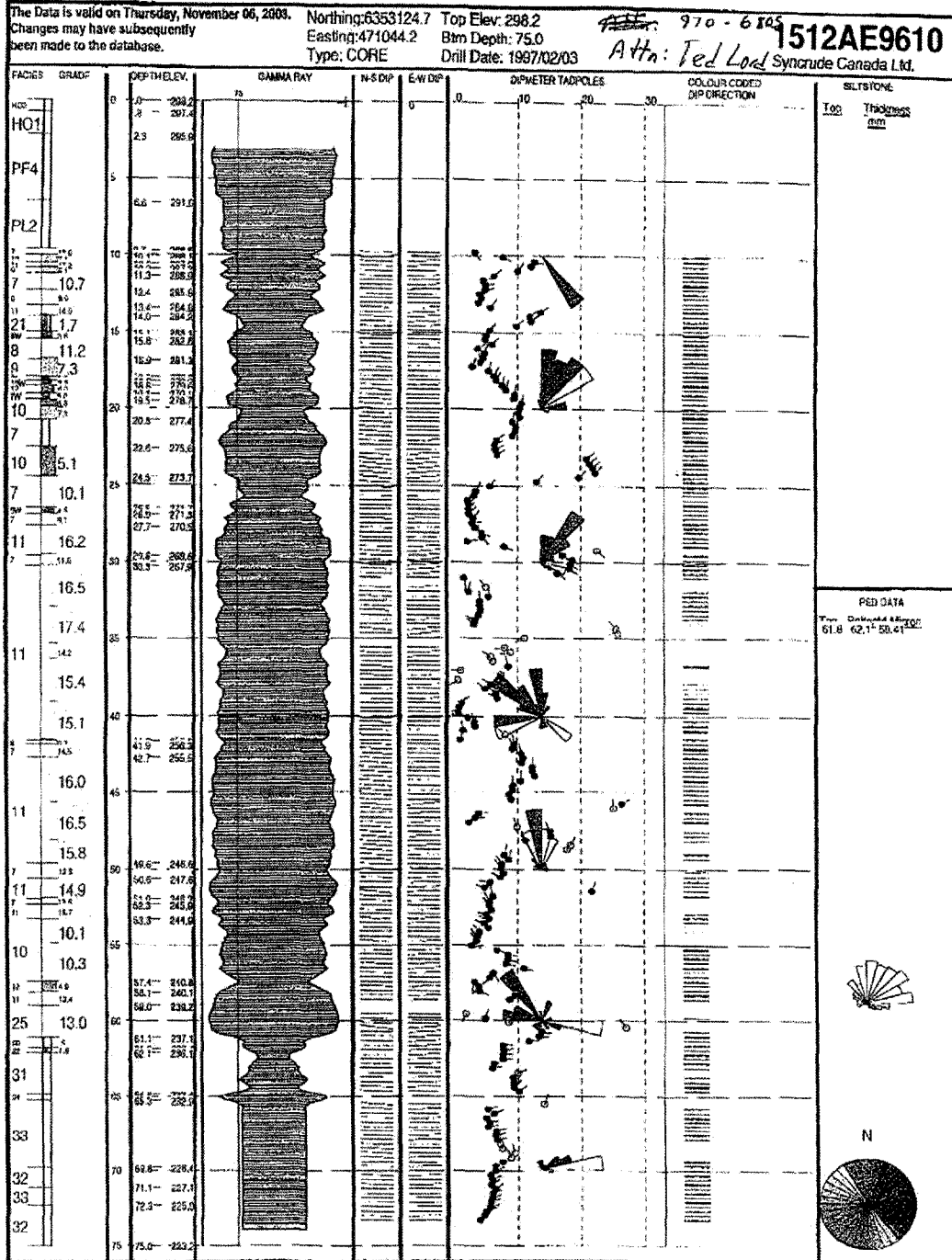


# Core Hole Data

1/06/2003 16:48 FAX

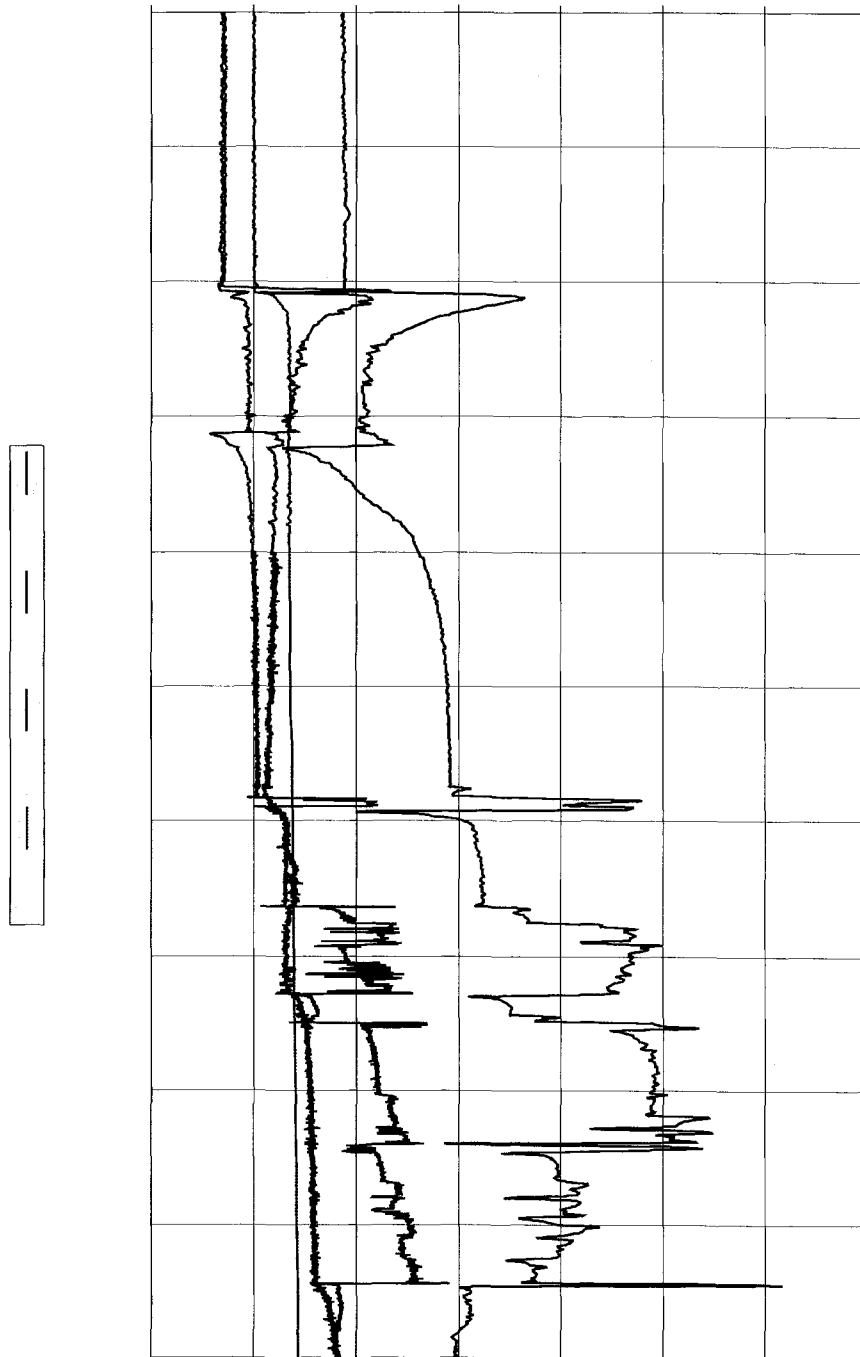
SCL AURORA MINE

001

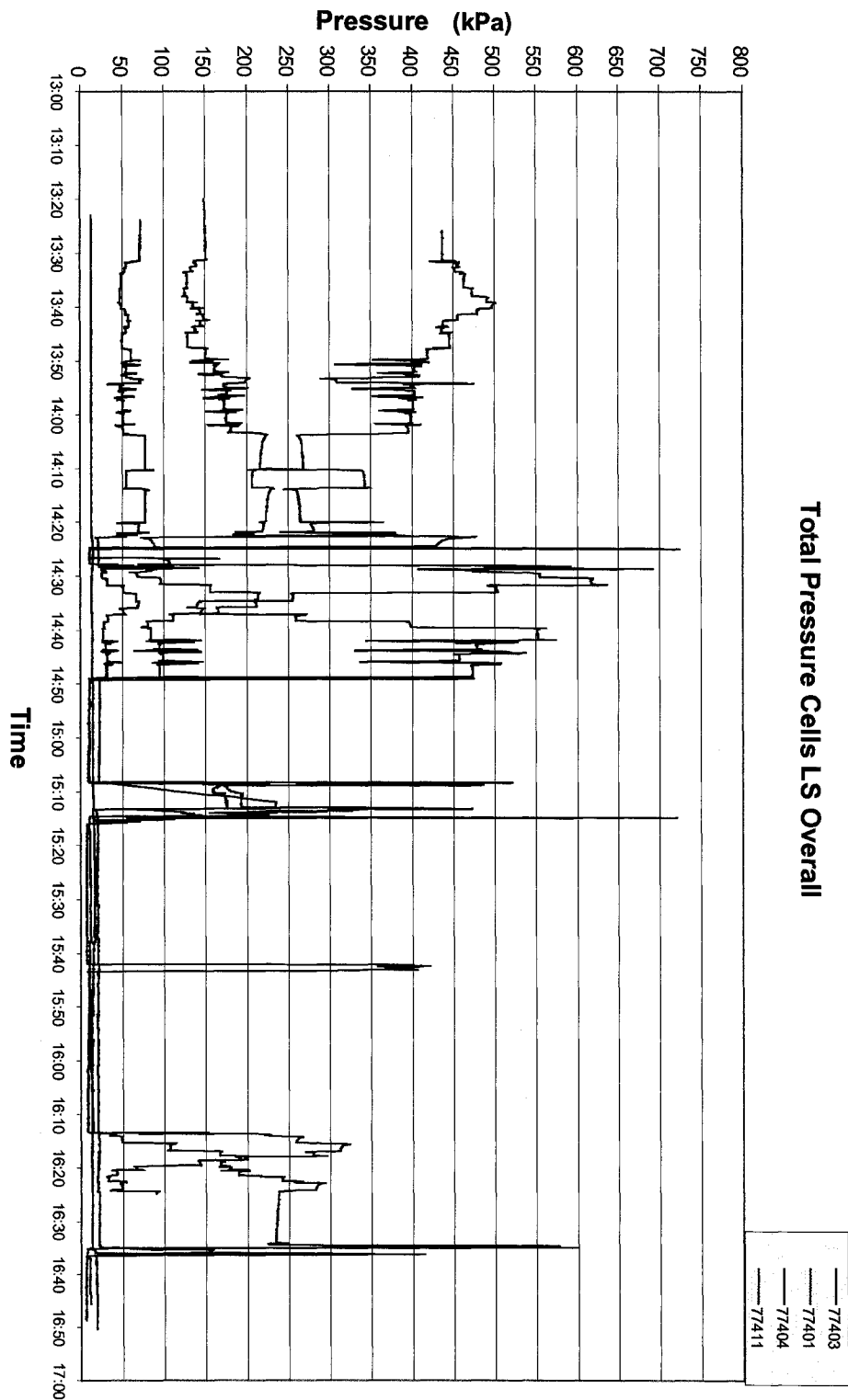


# Piezometer Readings for the Entire Test

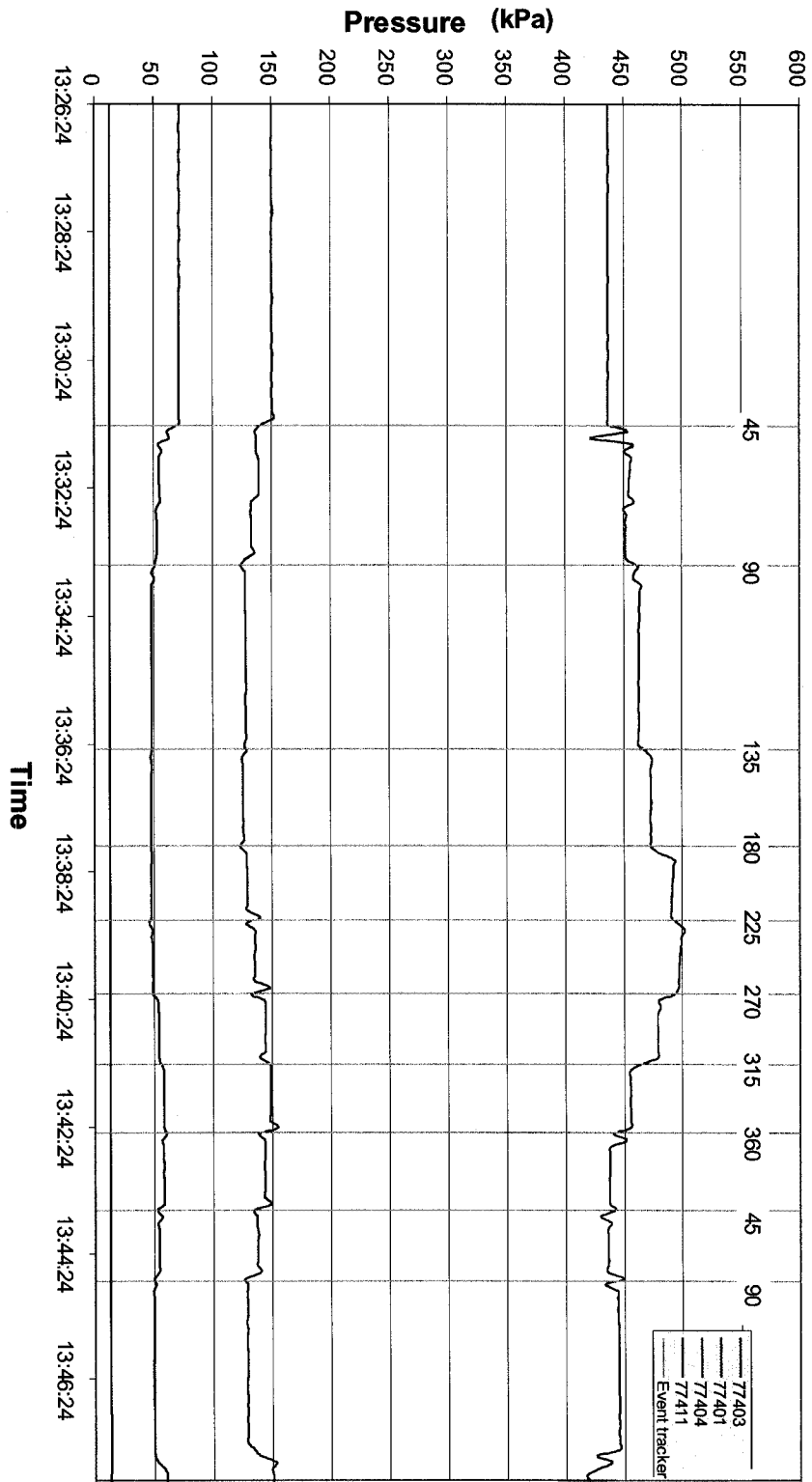
pore pressure (kPa)



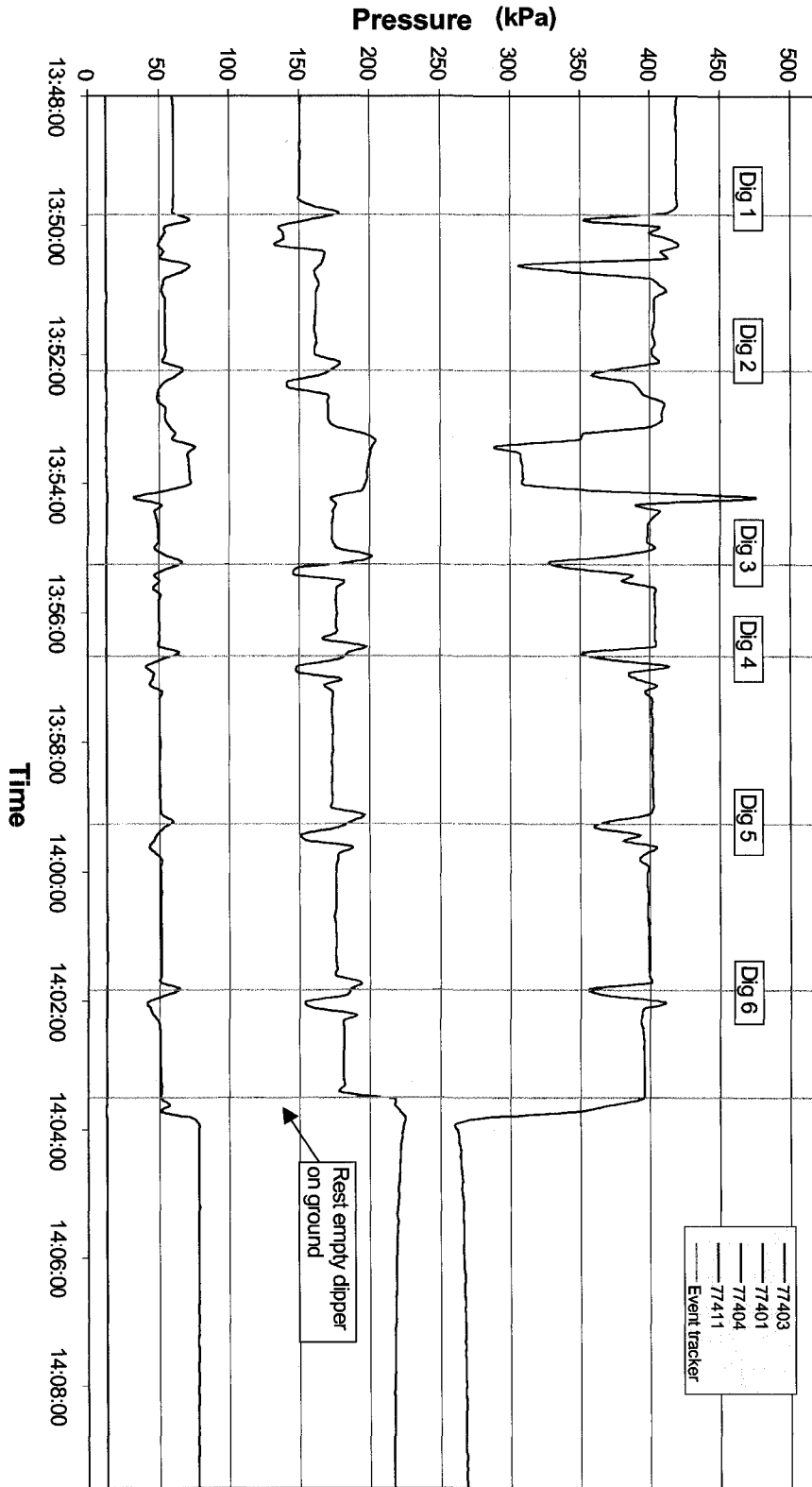
# Total Pressure Cell Readings for the Entire Test (LS)



# Unloaded Static Tests (LS)

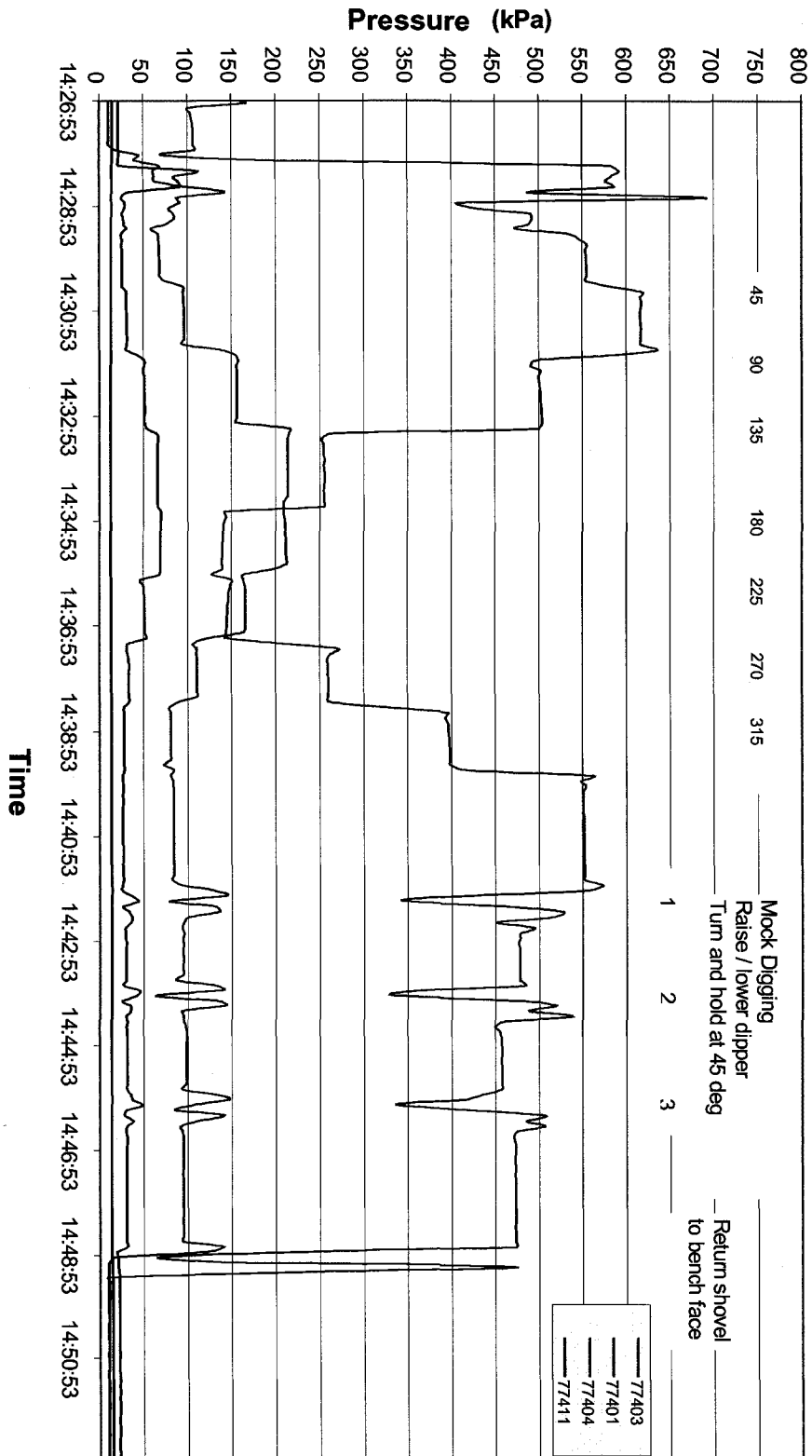


# Unloaded Mock Digging (LS)



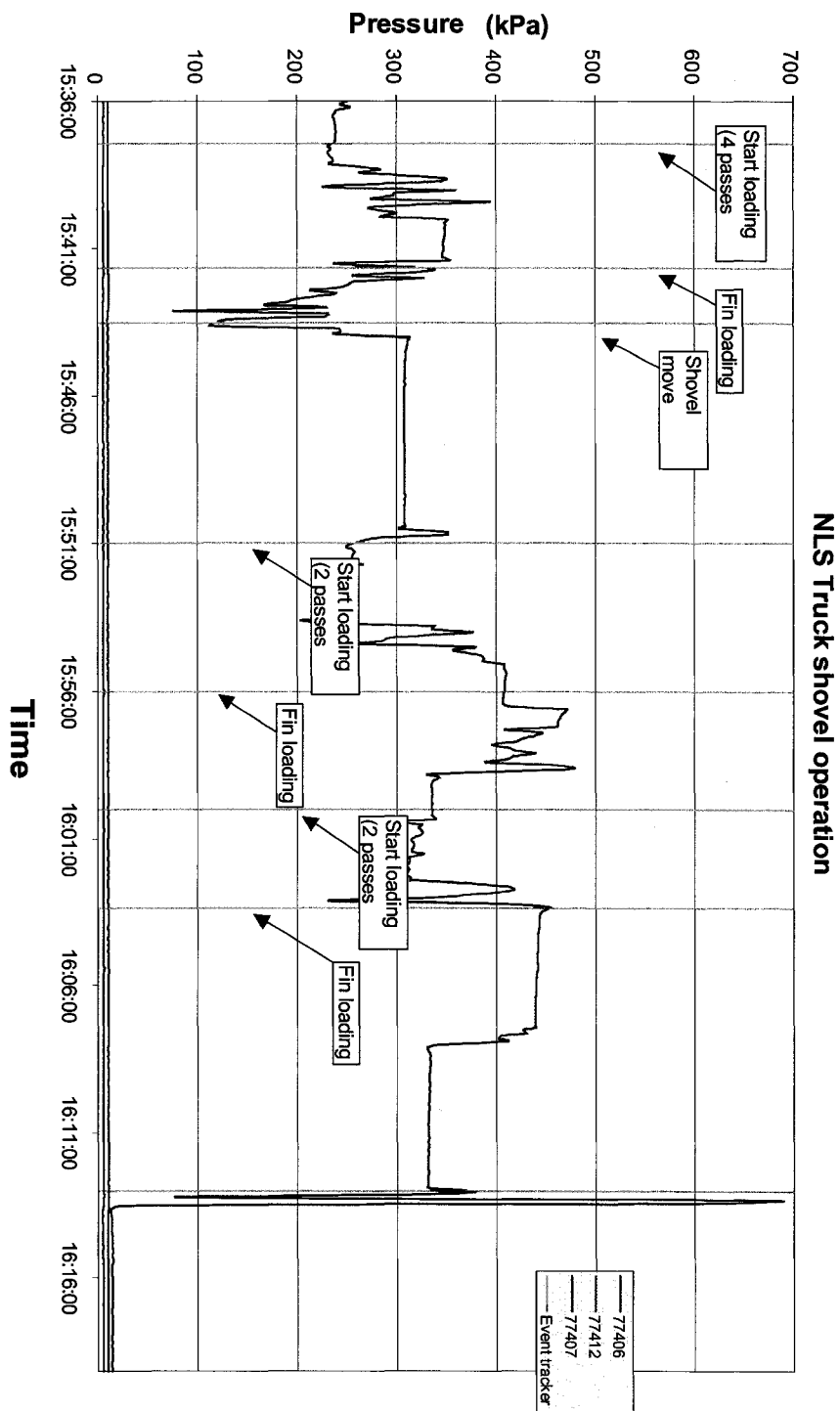
## LS Moc Work Bench Face

# Loaded Static Test (LS) and Mock Digging

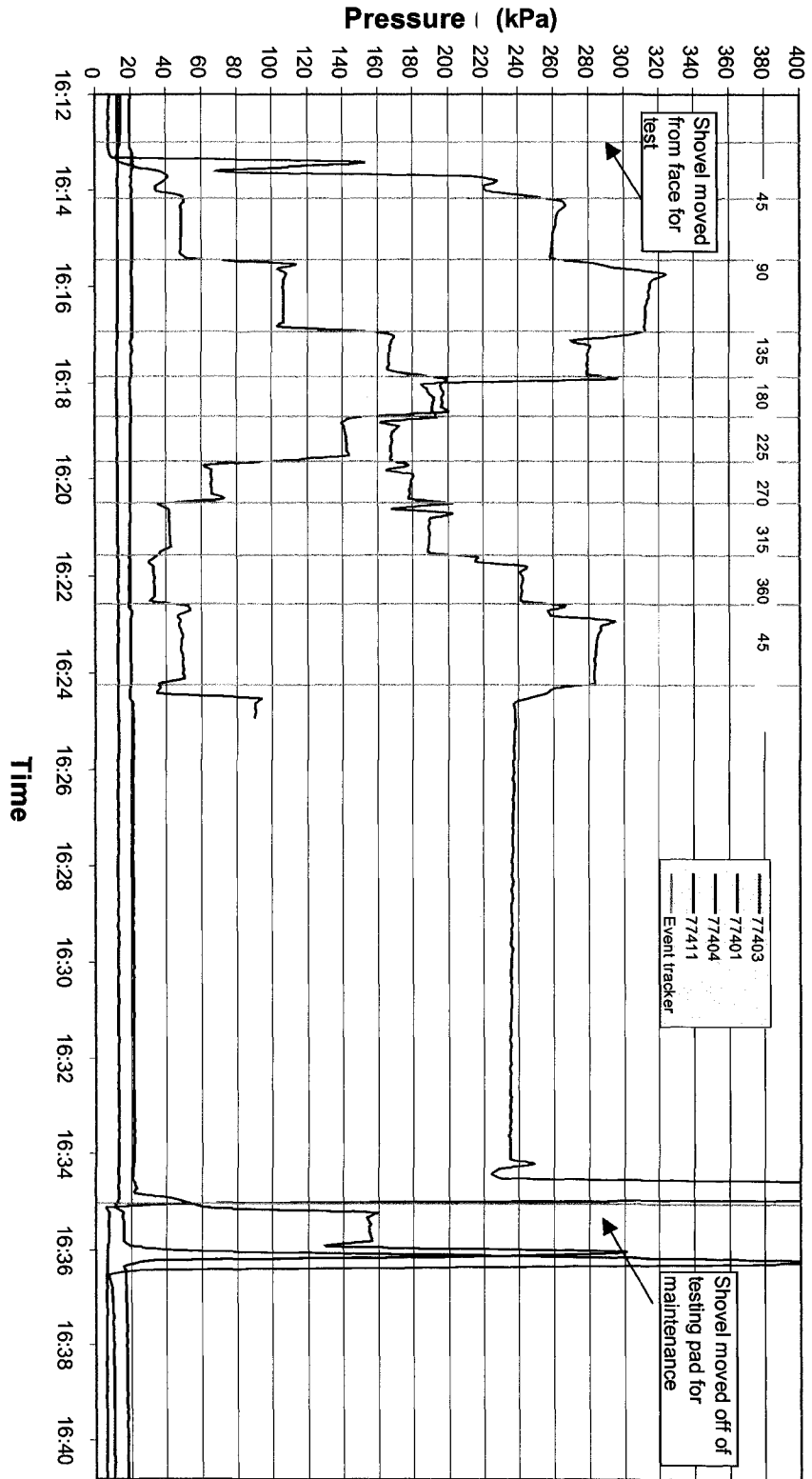


## LS Loaded Static Tests and Mock Digging

# Truck and Shovel Operation at the Face (NLS)



# Loaded Static Test, End of Test (LS)



LS Static Loaded Test End